Stochastic Models of Geodynamo Simulations

by

William Davis

A dissertation submitted in partial satisfaction of the

requirements for the degree of

Doctor of Philosophy

in

Earth and Planetary Science

in the

Graduate Division

of the

University of California, Berkeley

Committee in charge:

Professor Bruce Buffett, Chair
Professor Philip Stark
Professor Nicholas Swanson-Hysell

Summer 2022

Stochastic Models of Geodynamo Simulations

Abstract

Stochastic Models of Geodynamo Simulations

by

William Davis

Doctor of Philosophy in Earth and Planetary Science

University of California, Berkeley

Professor Bruce Buffett, Chair

The Earth's magnetic field originates primarily in the interior of the planet, and represents one of the few signals through which processes of the deep Earth are expressed at the surface. Observations and paleomagnetic measurements of the geomagnetic field therefore provide a valuable means of investigating the state and dynamics of the Earth's core. Fluctuations in the geomagnetic field occur on a wide range of timescales; however, the inaccessibility of the deep Earth means that these fluctuations are poorly understood. To investigate how external magnetic field variability relates to processes in the core, recent studies have constructed stochastic models from direct numerical simulations of the geodynamo. If these stochastic models reflect the underlying dynamics, then they may be used to characterize the paleomagnetic record and investigate the state of the Earth's core. In this thesis, I use geodynamo simulations in conjunction with stochastic models to investigate the expression of internal core processes on external field fluctuations. I examine how changes in the style and vigor of convection are reflected in stochastic models of axial dipole field variability. I find that the magnitude of variability is linked to dipole field generation, whereas the average regression to the mean is associated with turbulently enhanced magnetic diffusion. I also construct a stochastic model from a reversing geodynamo simulation, and find that stochastic models can approximately reproduce the statistics of polarity reversals. Finally, I develop a set of statistical techniques to fit stochastic processes to irregularly sampled time-series data, which are common in paleomagnetic measurements. The overall goal is to investigate the use of stochastic models as a means to relate external magnetic field variability to internal mechanisms in planetary dynamos.

To Kat,

For her advice, patience, and her love

Contents

List of Figures

List of Tables

Acknowledgments

It would be impossible for me to thank all those who have helped me to overcome the challenges of completing this Ph.D. There are a special few that have greatly contributed, and I would like to thank them sincerely.

First, I thank my advisor, Bruce Buffett. He has been a great inspiration throughout my time at Berkeley. I owe him a great debt of gratitude for his guidance. His enthusiasm for scientific research, teaching, and mentoring are qualities that I hope to be able to emulate some day. I thank him for his patience, for showing me understanding when I needed it.

I wish to thank the other members of my dissertation committee, Philip Stark, and Nicholas Swanson-Hysell. Their guidance, comments, and feedback is very much appreciated, and has improved this work. I also want to thank Barbara Romanowicz for advising me in the first few years of my time here at Berkeley. I also thank Michael Manga, David Shuster, Raymond Jeanloz, Roland Bürgmann, and Harriet Lau for their stimulating discussions and encouragement. My collaborators in France, Nathanaël Schaeffer, and Alexandre Fournier, should be mentioned for their contributions and enlightening discussions. Matthias Morzfeld and Cathy Constable at Scripps also deserve thanks for their conversations and advice. I greatly look forward to working with them in the future.

The staff at the Department of Earth and Planetary Sciences also deserves thanks. Rachel Kowalik, Nadine Spingola-Hutton, and Margie Winn have all provided superb support with administrative difficulties. The Earth Science library is one of my favorite places on campus, and I am indebted to the help of librarians Bonita Dyess and Sam Teplitzky. I also thank the staff at the Berkeley Research Computing program, as well as the Texas Advanced Computing Center, for providing helpful technical support.

I have made a great many friends here at Berkeley, and many of them have inspired me scientifically. Despite the outbreak of a global pandemic making social interactions difficult, I will sorely miss the community that I found. It would be impossible for me to list everyone, but I especially thank Andrew Turner, Chase Chandler, Nicholas Knezek, Maggie Avery, Dan Frost, Tushar Mittal, Andy Tholt, Drew Gorin, Sarina Patel, Sevan Adourian, Manar Al Asad, Rodrigo Chi, Tom Smart, and Jiwoon Hwang. I have been honored to know these people as colleagues and as friends.

It is hard to describe how indebted I feel to my family. They have encouraged me to explore my scientific interests from a young age. Without their confidence in me, I would not be who I am today. Finally, I dedicate this work to Kat Armstrong. I owe more to her than anyone else. I am so grateful that science brought us together. She has always believed in me and supported me, and helped me through the hardest times. Her unending patience, advice, and love, have made all of this possible.

Chapter 1

Introduction

The Earth has a global magnetic field, which originates in the interior of the planet and extends into space. This field is primarily generated in the liquid iron outer core, passing through 3000 kilometers of silicate mantle before reaching the Earth's surface (see Fig. 1.1). Fluctuations of the geomagnetic field have been recorded throughout history, and this variability is governed by complex dynamics within the core. Fluid motions and the magnetic field interact in a self-exciting manner, resulting in a complex interplay of forces, fluxes, and processes that are collectively referred to as the geodynamo. Although the detailed state of the core is inaccessible, some of the generated magnetic field can be observed at the Earth's surface. Direct observations of this geomagnetic field have been possible for the past few centuries. Further back in time, certain conditions permit some geological (and archaeological) materials to record a snapshot of the local field at the time of their formation, as internal remanent magnetization. From the compilations of these indirect measurements, we can piece together a record of field behavior extending back billions of years though Earth's history, with higher resolution for the recent field and sparser inferences further back in time. These paleomagnetic records indicate that the geomagnetic field exhibits a staggering range of variability. The morphology and intensity of the surface field change over millennia. On longer timescales, the dominantly dipolar field has reversed polarity hundreds of times, with a frequency that is tremendously variable. These variabilities likely reflect changes in the style and vigor of convection, which are ultimately governed by the state of the core and the bounding effects of the mantle. However, the inaccessibility of the deep Earth leaves these relations poorly understood.

One approach to investigating the internal dynamics of the core is through direct numerical simulation of the magnetohydrodynamic action within the core, also known as geodynamo simulations (Christensen and Wicht, 2015). The goal is to produce simulations that reproduce the dynamic properties of the observable field, with the benefit of having the details of internal field and fluid motions directly accessible. Although numerical limitations prevent simulations from being conducted at Earth-like conditions, many properties of the external field can be reproduced (Wicht and Sanchez, 2019).

Another method of investigating field variability is through statistical models. An exam-

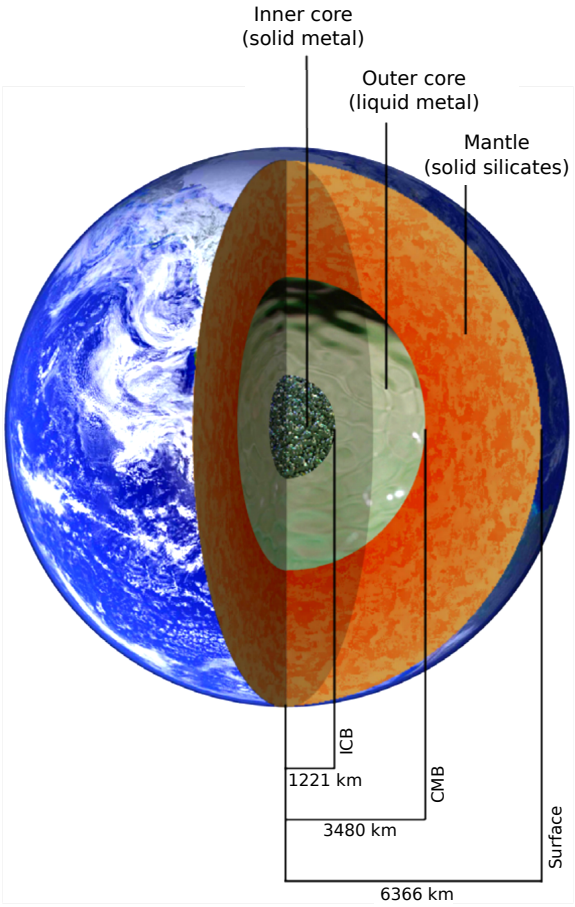

Figure 1.1: Cutaway view showing the main layers of the Earth. Adapted from Roberts and King (2013).

ple is given by Constable and Parker (1988), where the authors derive statistical descriptions of the components of a spherical harmonic expansion of the field. This model and further extensions are able to reproduce variabilities of the magnetic field; they are also able to reproduce comparable variability from dynamo simulations (Bouligand et al., 2005). While these models provide convenient representations of statistical properties, physical interpretations of parameters within these statistical models have not been directly established.

An alternative statistical approach is to use stochastic models to represent geomagnetic field variability. Studies have generally described the variability of axial dipole intensity as a stochastic processes (Brendel et al., 2007). These include a deterministic and a random component, known as the drift and noise terms, respectively. These models were able to reproduce the variability of the recent geomagnetic field, estimated from paleomagnetic models (Buffett et al., 2013). Recently, Buffett et al. (2014) applied this approach to the output from a geodynamo simulation, enabling an investigation of the links between the external field and internal field generation mechanisms. However, these connections were only

made for a single dynamo simulation, and how these connections respond to changes in the boundary conditions or the vigor and style of convection were not investigated. The main aim of this thesis is to explore connecting these stochastic models to underlying physical processes. This entails investigating how drift and noise functions change across a range of dynamo simulations, and whether these functions continue to reflect internal core processes. The overarching goal is to investigate the use stochastic models as a tool to link external field variability to internal mechanisms in fluid dynamos.

One first-order property of geomagnetic field variations inferred from paleomagnetic records is the presence of polarity reversals. As such, the presence and frequency of polarity reversals in numerical geodynamo simulations are often quantities of interest (Sprain et al., 2019). Although numerous studies have been able to produce dynamo simulations that reverse, accurate estimates of statistics such as reversal rates commonly requires long, costly simulations (Lhuillier et al., 2013), that are rarely conducted. If stochastic models are able to reproduce the statistics of stable-polarity dynamo simulations, then it is possible that might also be able to reproduce the statistics—specifically the reversal rates—of reversing simulations. Although stochastic models have been previously explored in the context of reversing dynamo simulations (Meduri and Wicht, 2016), their capacity to reproduce reversal rates was not investigated. If stochastic models can accurately reproduce the statistics of reversals, then perhaps they can be used to predict asymptotic statistics whilst being built from high-resolution simulations of a short length. This would greatly aid systematic searches for Earth-like geodynamo simulations (e.g., Kutzner and Christensen, 2002; Christensen and Aubert, 2006; Christensen, 2011). Hence another goal of this thesis is to explore: (1) whether stochastic models can reproduce reversal statistics of numerical simulations, and (2) whether the reversal rates be estimated from stochastic models built from short lengths of data.

A final consideration is how stochastic models might be fitted from paleomagnetic records. Fitting stochastic models to empirical data requires the careful application of appropriate statistical methods (Friedrich et al., 2011). However many of these methods encounter difficulties with paleomagnetic records, due to complications of geological sampling (Buffett and Puranam, 2017). In particular, the irregular sampling of some records renders many methods impracticable. In order to enable future analysis of paleomagnetic records, another goal of this thesis is to develop a set of techniques enabling the fitting of stochastic models to irregularly sampled data.

This thesis aims to explore each of these topics, and attempts to integrate them together in the context of stochastic models of the geodynamo and geomagnetic field. I begin by providing a brief review of the necessary fundamentals of the geodynamo in Chapter 2. In Chapter 3, I give an extensive literature review of previous work concerning stochastic models of the geodynamo. In Chapter 4, I address the main focus of this thesis and use stochastic models to investigate the internal field generation mechanisms of a set of numerical geodynamo simulations. Work appearing in this chapter has subsequently been published in Davis and Buffett (2021). In Chapter 5, I extend the previous analysis to a numerical geodynamo simulation that exhibits polarity reversals, with specific attention paid to the

statistics of reversals. In Chapter 6, I develop a set of statistical methods for fitting stochastic models to irregularly sampled data, such as paleomagnetic records. Work appearing in this chapter has subsequently been published in Davis and Buffett (2022). Finally, Chapter 7 concludes with a summary of this work, and an outlook for future directions of this research.

Chapter 2

Principles of the Geodynamo

The Earth's magnetic field, and the internal geodynamo process which generates it, have both been areas of interest since the early beginnings of the field of geophysics. In this chapter, I provide a short summary of the basic principles that are relevant to this thesis. More extensive reviews can be found in Roberts and King (2013) and Olson (2015), while the mathematical fundamentals are rigorously covered in Braginsky and Roberts (1995). I begin with a brief account of historical developments, which gives context for the study of the geodynamo. I then summarize some common methods of quantitatively representing the field. These are used to give a short summary of the observed and inferred phenomena of the field, for both recent history as well as through geologic time. I then give a short summary of the mathematical formulation of the governing equations for the geodynamo. Finally, I outline the requirements for numerical geodynamo simulations, as well as recent investigations on how "Earth-like" these simulations are.

2.1 Introduction

Before the geodynamo was studied as an entity to itself, initial work mainly was concerned with the geomagnetic field present at the surface of the Earth. This was largely motivated by the need for reliable nautical navigational methods. Early observations showed that a magnetic compass needle would point almost, but not exactly, in a northerly direction. This discrepancy, with respect to "true North," was termed "declination," and denoted by D. Another observation was that a suspended compass needle would orient itself steeply relative to the horizontal plane. This angle was termed "inclination," and denoted by I. Global variations in declination and inclination were useful for locally determining longitude, and were used in ocean navigation. One of the first hypotheses for the origins of the geomagnetic field came from William Gilbert, who, in his 1600 Treatise *De Magnete*, proposed that the source of this field was internal to the Earth. However, further investigation into this hypothesis made little progress for the next few hundred years (Chapman and Bartels, 1940), as the necessary tools were only available after the development of the field of electrodynam-

ics in the 19th Century. This, together with sound mathematical descriptions of the field (provided by Gauss in 1838) initiated the field of geomagnetism.

Following from Gilbert's initial work, the source of the geomagnetic field was originally thought to be a permanent magnet in the interior of the Earth. However, later experiments showed that magnetic minerals lose their permanent magnetization when heated beyond their Curie temperatures. This excluded the possibility of a permanent magnet as the origin for the Earth's field, except for small-scale fields originating from the top few kilometers of the crust. An alternative explanation for the geomagnetic field was through electrodynamics, which relied on free electric currents rather than permanent magnetization. This idea was proposed in 1919 by Joseph Larmor, with reference to both the Earth and the Sun. This "dynamo hypothesis," supposed that electric currents and magnetic fields in the centers of astrophysical objects interacted in a self-sustaining way, requiring no permanent magnetism. This perspective eventually led to the development of the theory of magnetohydrodynamics (MHD) (Elsasser, 1946, 1950; Bullard and Gellman, 1954), which is now widely accepted as the mode of magnetic field generation in the Earth.

The field of geomagnetism has developed in parallel to other areas of Earth sciences, and a large amount of complementary knowledge has come from seismology and mineral physics. From the study of seismic waves that penetrate the deep Earth, we now know that the Earth is distinctly segregated radially, comprising a metallic core and an overlying silicate mantle (Oldham, 1906). Furthermore, the core is itself separated into a liquid outer shell and a solid center (Lehmann, 1936). The composition of the core is thought to be an iron-nickel alloy, as inferred from meteoritic evidence, seismic observations, and experimental mineral physics (Birch, 1952; Bullen, 1954; Birch, 1964). The outer core has long been understood to be slightly less dense than a Fe-Ni alloy, indicating a small component of lighter elements. Oxygen, sulfur, silicon, hydrogen, and carbon are the most likely candidates, though their precise relative abundance remains poorly understood and the subject of much ongoing research (e.g., Poirier, 1994; McDonough, 2003). These light elements are important, as they might provide a buoyancy source for fluid motions and the overall energetics of the core (see Nimmo, 2015, for an extensive review).

Description of the Geomagnetic Field

In order to quantitatively describe the geomagnetic field, an adequate mathematical representation is necessary. The description, in terms of potential theory, dates back to the early work of Gauss in 1838. It involves a decomposition of the magnetic field exterior to the Earth's surface onto a sphere. As the atmosphere at the Earth's surface has very low electrical conductivity, one can assume a negligible current flow in this region. Then Amperè's law and the lack of magnetic monopoles gives a magnetic field $\mathbf{B}$ with

$$\nabla \times \mathbf{B} = 0, \qquad \text{and} \qquad \nabla \cdot \mathbf{B} = 0. \tag{2.1.1}$$

This leads to a magnetic field that is conservative, and can be represented by a "geopotential" field V, with

$$\mathbf{B} = -\nabla V, \tag{2.1.2}$$

which obeys Laplace's equation

$$\nabla^2 V = 0. \tag{2.1.3}$$

Given this, the field at a point can be expressed in spherical coordinates (r, θ, ϕ), where θ is the colatitude, ϕ is the longitude, r is in the radial direction, and the origin is at the center of the Earth. Hence:

$$B_r = -\frac{\partial V}{\partial r}, \tag{2.1.4}$$

$$B_\theta = -\frac{1}{r}\frac{\partial V}{\partial \theta}, \tag{2.1.5}$$

$$B_\phi = -\frac{1}{r\sin\theta}\frac{\partial V}{\partial \phi}. \tag{2.1.6}$$

From this, declination, inclination, and field intensity F can be represented as

$$D = \tan^{-1}\left(\frac{B_\phi}{-B_\theta}\right), \tag{2.1.7}$$

$$I = \tan^{-1}\left(\frac{-B_r}{\sqrt{B_\theta^2 + B_\phi^2}}\right), \tag{2.1.8}$$

$$F = \sqrt{B_r^2 + B_\theta^2 + B_\phi^2}. \tag{2.1.9}$$

This potential is typically partitioned into sections concerning the field interior and exterior to the core. Assuming negligible external magnetic sources, a general solution for the external potential V_{ext} can be expanded as (e.g., Backus et al., 1996),

$$V_{\text{ext}}(r, \theta, \phi, t) = a\sum_{\ell=1}^{\infty}\left(\frac{r}{a}\right)^{\ell} \times \sum_{m=0}^{\ell}\left[g_\ell^m(t)\cos m\phi + h_\ell^m(t)\sin m\phi\right] P_\ell^m(\theta) \tag{2.1.10}$$

where a is the radius of Earth's surface, $P_\ell^m(\theta)$ is the Schmidt normalized Legendre function with degree ℓ and order m, and a is the radius of the Earth. In this expansion, the terms g_ℓ^m and h_ℓ^m are called the Gauss coefficients. The term g_1^0 represents the axial dipole, which combines with g_1^1 and h_1^1 to give the full dipole field. The Gauss coefficients have the units of teslas, so scaling by $4\pi a^3/\mu_0$ gives the dipole moment in units of Am^2, where $\mu_0 = 4\pi \times 10^{-7}\ \text{Hm}^{-1}$ is the permittivity of free space. This decomposition enables for a convenient, concise description of the external magnetic field.

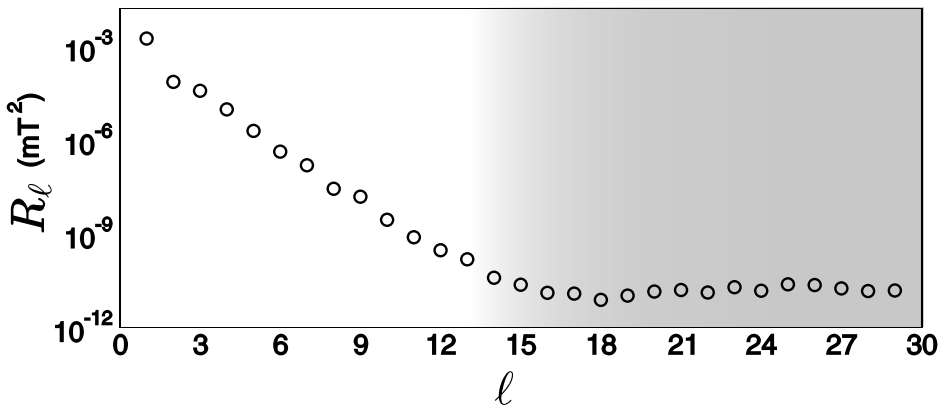

Figure 2.1: The spectrum of the modern geomagnetic field at Earth's surface as a function of spherical harmonic degree (2.2.1). Gauss coefficients are taken from a combination of satellite observations and ground-based observations between 1999 and 2007 (Olsen and Mandea, 2008). The shading illustrates the field that is thought to be generated by crustal magnetism. Modified from Roberts and King (2013).

2.2 Observations of the Geomagnetic Field

The modern external magnetic field can be analyzed through recent observations. Here, "modern" refers to the field during the last few hundred years. This field may be considered separately to the paleofield, as direct data from ground-based observatories and ship logs are available. More recently, observations from satellite missions have also become available (e.g., Swarm, CHAMP, and Ørsted). These enable high-resolution inversions of the external magnetic field (e.g., see Olsen et al., 2006, and subsequent studies). Together, these allow for the accurate estimation of Gauss coefficients up to high spherical harmonic degrees (Olsen et al., 2007).

The modern field is mostly dipolar, with a tilt of about 9° relative to Earth's rotation axis (Gubbins and Herrero-Bervera, 2007). In addition to the dipole field, the full field shows a wide range of spatial complexities. One way of expressing this is through the spatial power spectrum (Mauersberger, 1956; Lowes, 1966). This spectrum, defined as

$$R_\ell(r,t) = \left(\frac{a}{r}\right)^{2\ell+4} (\ell+1) \sum_{m=0}^{\ell} \left[\left(g_\ell^m(t)\right)^2 + \left(h_\ell^m(t)\right)^2 \right], \tag{2.2.1}$$

is a function of harmonic degree ℓ, radius r, and time t, is shown for Earth's surface field in Fig. 2.1. The field is dominated by the dipole ($\ell = 1$), which comprises more than 90% of the amplitude. The power of the other degrees decreases steadily until about $\ell \sim 13$, after which the spectrum flattens. This has been interpreted to reflect the large scale fields produced in the core being obscured by crustal magnetism (Olsen and Mandea, 2008).

Variations in the geomagnetic field are referred to as "secular variation" or "paeleomagnetic secular variation," for the historical or geologic field, respectively. Satellite observations

reveal small changes in the modern field, which have been attributed to fluid flows and waves at the very top of the core (e.g., Holme and Olsen, 2006; Finlay et al., 2010a; Chi-Durán et al., 2021). In addition, historical records from observatories and maritime logbooks indicate a small, westward drift of magnetic features (Jackson et al., 2000). Rapid changes in the derivative of secular variation, commonly referred to as "geomagnetic jerks" (Backus, 1983; Courtillot and Le Mouël, 1984; Mandea et al., 2010), have also been observed.

On timescales beyond historical records, estimates of the geomagnetic field can be gathered from archaeomagnetism. This is the study of archaeological objects that have a remanent magnetization—for example, recorded in iron-rich clay pottery or bricks as they cool through their Curie point (e.g., Gubbins and Herrero-Bervera, 2007).

The Paleomagnetic Field

Beyond human records, we have no direct observations of the geomagnetic field. Instead, the paleofield is inferred through measurements of various geologic materials, which have preserved a natural remanent magnetization at the time of their formation. These remanent magnetizations may be measured in laboratory settings through various demagnetization techniques (see Tauxe, 2010; Dunlop and Özdemir, 2015, for extensive reviews). These paleomagnetic measurements have been invaluable for the study of the Earth through deep geological time, and were key in the development of the theory of plate tectonics (McElhinny and McFadden, 1999).

Magnetism of igneous rocks is one source of paleomagnetic data. These rocks often contain (anti)ferrimagnetic minerals such as magnetite, hematite, or other Fe-Ti variants. As these minerals cool through their Curie temperature, a remanent magnetization is recorded. This is called thermal remanent magnetization (TRM) (Merrill et al., 1998). Extrusive igneous rocks often cool rapidly, and essentially provide point measurements of the magnetic field at a specific time and location. Multiple episodic volcanic events may record an irregular, discrete sampling of the field. Intrusive igneous rocks, by contrast, cool slowly and therefore record averaged magnetic fields. It must be noted, however, that reheating events may create complications such as secondary magnetization and overprinting the original records.

Another type of remanent magnetization is found in sedimentary rocks. Magnetic grains that can rotate freely will orient themselves in the direction of the local magnetic field. This is known as detrital (or depositional) remanent magnetization (DRM) (Merrill et al., 1998). As opposed to extrusive igneous rocks, these records provide continuous records of local magnetism, although absolute intensities are not easily attained (Tauxe, 2010). However, post-depositional geological, geochemical, and biological processes can transform or otherwise distort this remanent magnetization. TRM and DRM are often used in complementary settings, with deep-sea ocean cores providing long, continuous DRM measurements, which are calibrated against TRM point measurements (e.g., Ziegler et al., 2011).

Paleomagnetic observations indicate that the Earth's external magnetic field varies on geologic timescales. This is commonly referred to as "paleomagnetic secular variation," or "paleosecular variation." Numerous reviews describe this in detail (e.g., see Merrill et al.,

1998; Gubbins and Herrero-Bervera, 2007; Kono, 2015). Paleomagnetic observations taken from a single site are often interpreted as resulting from a single geocentric dipole field. The point where the axis of this dipole meets the Earth's surface is called the virtual geomagnetic pole (VGP). If intensity measurements are possible, then the magnitude of the inferred dipole field is referred to as the virtual dipole moment (VDM). These are "virtual," because non-dipole field components are not considered. This is based the assumption that, over timescales of 10^3 years, the non-dipole field averages to zero (see Constable and Korte, 2015, for details). On longer timescales of 10^4–10^5 years, VGPs are averaged to produce "paleomagnetic poles." Compilations of paleomagnetic poles suggest that the field is predominantly aligned with the Earth's rotation axis. This is referred to as the geocentric axial dipole (GAD) hypothesis, under which the averaged dipole field intensity is represented by a virtual axial dipole moment (VADM).

Paleomagnetic studies often indicate small fluctuations in VGP positions and VDMs, on timescales of $\sim 10^4$ years. These typically constitute fluctuations in intensity of the dipole moment by about 50% of its average value (Gubbins and Herrero-Bervera, 2007; Tauxe and Yamazaki, 2015). Occasionally these small fluctuations appear to become larger, reflecting a VGP diverging from axial alignment (Roberts, 2008). VGP fluctuations that are larger, but do not cross the equator, are called "excursions." Some authors define excursions as times when a VGP appears to move within 45° of the equator (e.g., Laj and Channell, 2015). These events are often associated with a weakening of the dipole field.

Occasionally, a paleomagnetic pole will cross the equator and become anti-parallel with its original orientation. These events are referred to as "polarity reversals," and are widely accepted to have happened many times throughout geologic history (Merrill et al., 1998). For example, over the last ten million years, the field is estimated to have reversed 47 times (Cande and Kent, 1995). If a paleomagnetic pole is in the same predominant direction as the present field for a period of time, that period is referred to as a "normal" polarity state. Otherwise, that period is referred to as a "reversed" polarity state. If the paleomagnetic pole remains within one polarity state for 10^6–10^7 years, that period of time is referred to as a "polarity epoch," or "chron." Shorter polarity durations of 10^5–10^6 years are referred to as "sub-chrons," and polarity durations on the edge of detectability are called "cryptochrons" (Laj and Channell, 2015). The geological history of dipole polarity inferred from paleomagnetic records is commonly referred to as the geomagnetic polarity time series (GPTS). For the most recently updated version of this compilation, see Ogg (2020). Transitions between polarity states are not instantaneous; the duration of reversals is estimated to be 10^3–10^4 years, however this is a debated topic (e.g., Clement, 2004; Valet et al., 2012). Another observation is that VGP paths appear to have preferred longitudinal paths during reversals (Clement, 1991; Valet et al., 2012).

Polarity reversals occur non-periodically, seemingly randomly, but with a mean rate that appears to change over geologic history (Constable, 2000; Lowrie and Kent, 2004). Within stationary intervals, the distribution of chron durations appears to follow an exponential distribution (Cox, 1968, 1969), however this is strongly debated (Naidu, 1971; McFadden and Merrill, 1984; Marzocchi, 1997; Carbone et al., 2006). Rarely, a period of stable polarity

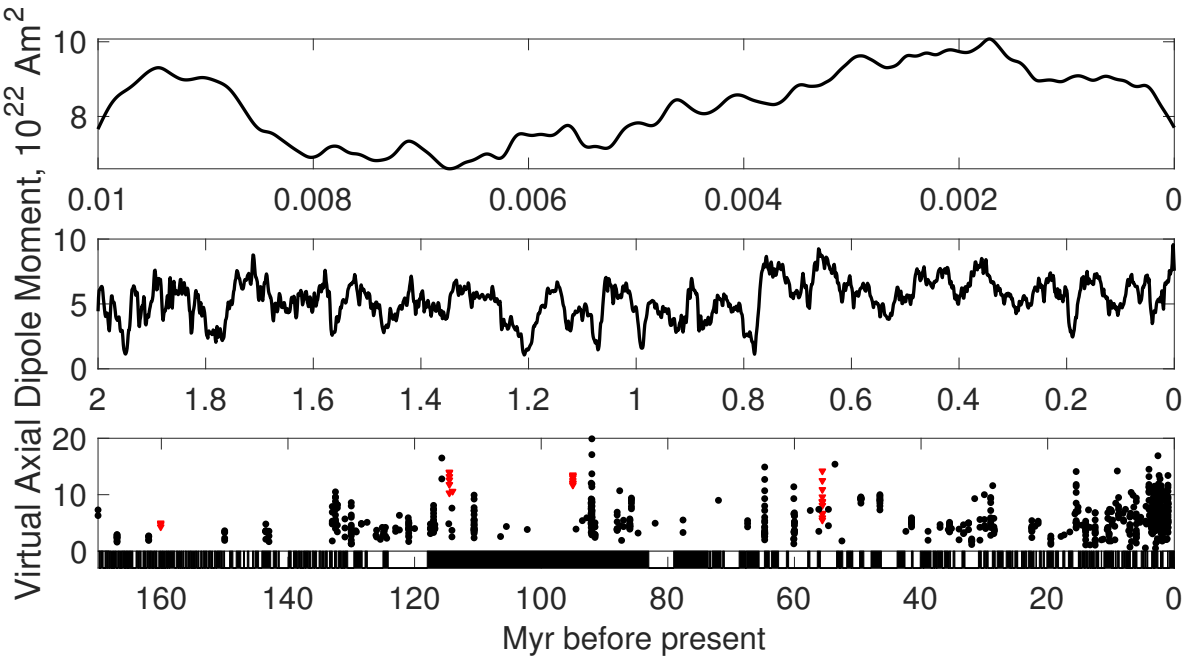

Figure 2.2: Paleomagnetic models of virtual axial dipole moment through geologic time. The top panel shows estimates of the VADM for the last ten thousand years, from the paleomagnetic model CALS10k.2 (Constable et al., 2016). The middle panel shows estimates of the VADM for the last two million years, from the paleomagnetic model CALS10k.2 (Ziegler et al., 2011). The bottom panel shows a compilation of paleomagnetic estimates of VADM, spanning the last 170 million years (Biggin et al., 2010). Triangles and circles indicate measurements made from single crystals and whole rocks, respectively. The lowermost edge shows the axial dipole polarity, from the GPTS (Ogg, 2020). Normal and reversed polarities are marked in black and white, respectively.

endured for an unusually long period of time, approximately 10^7–10^8 years. These events are called "superchrons." Examples include the Cretaceous normal and Permo-Carboniferous reversed superchrons, lasting approximately 38 and 50 million years, respectively. There is also evidence for an increase in the overall field strength during these superchrons (Prévot et al., 1990; Tarduno and Cottrell, 2005; Biggin et al., 2012).

Paleomagnetic studies have indicated that the Earth's magnetic field has been present for much of Earth's history (Merrill et al., 1998). These records, along with modern observations, indicate that the field has exhibited spatial and temporal variability. An illustration of different scales of variations inferred from various paleomagnetic models is shown in Fig. 2.2. Investigation into the origin of the Earth's magnetic field, as well as the source of its variations, motivates the study of the geodynamo.

2.3 The Geodynamo

Today, it is widely-accepted that the geomagnetic field originates from the magnetic field that accompanies the flow of electric current created by a self-excited dynamo operating within the Earth. Following early work by Elsasser, Bullard and Gellman, two varieties of geodynamo theory were developed: kinematic, and magnetohydrodynamic. In kinematic theory, the velocity field is prescribed. The magnetic field responds in reaction to it, and there is no allowance for the fluid flow responding to the magnetic field. This framework has largely been superseded by magnetohydrodynamic theory, which accounts for the full interactions between flows of electrically conducting fluids and magnetic fields. As evidence from seismology and mineral physics suggests that the Earth's outer core is a liquid iron alloy, we can reasonably conclude that magnetohydrodynamics is the mechanism for the geodynamo. Details of the development of this theory can be found in Roberts and King (2013) and Roberts (2015), and the mathematical fundamentals are covered in Braginsky and Roberts (1995).

Magnetohydrodynamics describes the interaction between magnetic fields and an electrically conducting fluid. This defines the dominant forces for magnetic field generation in the geodynamo. Thermal and/or compositional convection is thought to be the most likely mechanism driving fluid flow in the Earth's core (Olson, 2015). These convective motions of the electrically conducting fluid induce magnetic fields, which are twisted and stretched such that the original field is reinforced. The magnetic field also exerts a Lorentz force back on the fluid flow, and the generation of magnetic field is counteracted by ohmic dissipation, which removes power due to electrical resistance.

The full complexity of these interacting components makes the dynamo difficult to study. Therefore, a number of simplifications are commonly made for components that are not thought to play primary roles (Roberts, 2015). The most reasonable approximation is that of non-relativistic fluid flow. Another common assumption is the Boussinesq approximation. This assumes that density changes due to temperature and/or compositional variations are only considered through a buoyancy term in the momentum equation. This also implies an incompressible flow, and uniformity of properties such as thermal and electrical conductivities. Through these simplifications, the governing equations of MHD and thermal convection for fluid flow $\mathbf{u}$, magnetic field $\mathbf{B}$, and temperature T, can be derived (Roberts and King, 2013).[1] The first governing equation is for fluid flow $\mathbf{u}$, and is the Navier-Stokes equation in a rotating reference frame:

$$\frac{\partial \mathbf{u}}{\partial t} + \mathbf{u}\cdot\nabla\mathbf{u} + 2\Omega\left(\hat{z}\times\mathbf{u}\right) + \nabla\Pi = \nu\nabla^2\mathbf{u} + \alpha T g(r_o)\frac{r}{r_o} + \frac{1}{\rho}\mathbf{J}\times\mathbf{B}, \tag{2.3.1}$$

where Ω is the angular velocity about the $\hat{z}$ rotation axis, Π is the non-hydrostatic pressure, ν is the kinematic viscosity, α is the coefficient of thermal expansion, $g(r)$ is acceleration due

[1] Here the source of buoyancy is assumed to be purely thermal, for simplicity. This restriction can be relaxed, giving equations for thermo-chemical convection, (e.g., Glatzmaier and Roberts, 1996).

to gravity at radius r, r_o is the radius of the outer core, ρ is the fluid density, and $\mathbf{J}$ is the current density. The presence of rotation gives rise to a Coriolis force $2\Omega\,(\hat{z} \times \mathbf{u})$, as well as a centrifugal acceleration which is absorbed into the pressure term Π. The first term on the right-hand side describes viscous dissipation forces. The next term represents the effect of thermal buoyancy force per unit mass. Finally, the Lorentz force $\mathbf{J} \times \mathbf{B}$ gives the force per unit volume exerted on the fluid by the magnetic field.

Next, the evolution of the magnetic field $\mathbf{B}$ is governed by the induction equation:

$$\frac{\partial \mathbf{B}}{\partial t} = \nabla \times (\mathbf{u} \times \mathbf{B}) + \eta \nabla^2 \mathbf{B}, \tag{2.3.2}$$

where η is the magnetic diffusivity. The first term on the right-hand side represents electromagnetic induction, whereas the second term represents ohmic dissipation. The evolution of temperature is governed by the transport equation:

$$\frac{\partial T}{\partial t} + \mathbf{u} \cdot \nabla T = \kappa \nabla^2 T + \frac{q}{\rho C_p}, \tag{2.3.3}$$

where κ is the kinematic viscosity, q is the heat source, and the quantity ρC_p is the volumetric heat capacity. Finally, fluid flow is assumed to be incompressible, and magnetic continuity gives

$$\nabla \cdot \mathbf{u} = 0, \quad \text{and} \quad \nabla \cdot \mathbf{B} = 0. \tag{2.3.4}$$

From the two equations (2.3.1)–(2.3.2), one can see that the magnetic field and velocity components are not independent. The flow, magnetic field, and temperature are also influenced by boundary conditions, imposed by the overlying mantle and underlying inner core. For the magnetic field, all components are continuous across the boundary. For the velocity field, a common requirement is no flux across the boundaries of the fluid shell,

$$\mathbf{u} \cdot \mathbf{r} = 0. \tag{2.3.5}$$

A second condition usually imposed is either a no-slip or (viscous) stress-free boundary condition. In the no-slip case, all the components of the velocity vanish at the boundary, representing viscous coupling. On the other hand, stress-free conditions only require the tangential components of stress to vanish at the boundary, assuming the viscous boundary layer is thin (Kuang and Bloxham, 1999). Finally, boundary conditions on the temperature are typically either set at fixed values or fixed flux.

Toroidal-Poloidal Decomposition

A useful tool for analyzing the internal magnetic field is the toroidal-poloidal decomposition, pioneered by Bullard and Gellman (1954).[2] It provides a framework for representing

[2]Sometimes referred to as the "torpol" or "Mie" representation (Backus, 1986; Backus et al., 1996; Roberts and King, 2013).

divergenceless fields such as the magnetic field (or an incompressible velocity field). This formalism is widely used in dynamo studies. It consists of separating the field into two components,

$$\mathbf{B} = \mathbf{B}_{\mathcal{T}} + \mathbf{B}_{\mathcal{S}}, \tag{2.3.6}$$

where $\mathbf{B}_{\mathcal{T}}$ and $\mathbf{B}_{\mathcal{S}}$ are the toroidal and poloidal fields, respectively. The toroidal field is defined as

$$\mathbf{B}_{\mathcal{T}} = \nabla \times (\mathcal{T}\mathbf{r}), \tag{2.3.7}$$

where $\mathcal{T}(r, \theta, \phi, t)$ is the toroidal scalar field. Likewise, the poloidal field is defined as

$$\mathbf{B}_{\mathcal{S}} = \nabla \times \nabla \times (\mathcal{S}\mathbf{r}), \tag{2.3.8}$$

where $\mathcal{S}(r, \theta, \phi, t)$ is the poloidal scalar field. The toroidal and poloidal scalar fields can be further decomposed by spherical harmonic order and degree,

$$\mathcal{T}(r, \theta, \phi, t) = \sum_{\ell=1}^{\infty} \sum_{m=-\ell}^{\ell} \mathcal{T}_m^{\ell}(r, t) Y_{\ell}^{m}(\theta, \phi), \tag{2.3.9}$$

$$\mathcal{S}(r, \theta, \phi, t) = \sum_{\ell=1}^{\infty} \sum_{m=-\ell}^{\ell} \mathcal{S}_m^{\ell}(r, t) Y_{\ell}^{m}(\theta, \phi), \tag{2.3.10}$$

where Y_{ℓ}^{m} are the spherical harmonics of degree ℓ and order m, and $\mathcal{T}_m^{\ell}$ and $\mathcal{S}_m^{\ell}$ are scalar functions of r. The toroidal field does not possess a component in the radial direction, whereas the poloidal field lines circulate in meridional planes. This decomposition is useful because the toroidal and poloidal parts are orthogonal to each other on integration over the sphere's volume (see Backus et al. (1996) for an in-depth description).

Field Generation Mechanisms

One area of interest in dynamo theory concerns the mechanisms by which the magnetic field is generated. An inspection of the induction equation

$$\frac{\partial B}{\partial t} = \nabla \times (\mathbf{u} \times \mathbf{B}) + \eta \nabla^2 \mathbf{B}, \tag{2.3.11}$$

reveals that a constant $\mathbf{B} = 0$ field is always a valid solution. Therefore, the generation of magnetic field can only be possible when this solution becomes unstable. Furthermore, dynamo action can only be maintained when the inductive effects of $\nabla \times (\mathbf{u} \times \mathbf{B})$ are larger than diffusive effects. The relative importance of these effects is typically measured by the magnetic Reynolds number

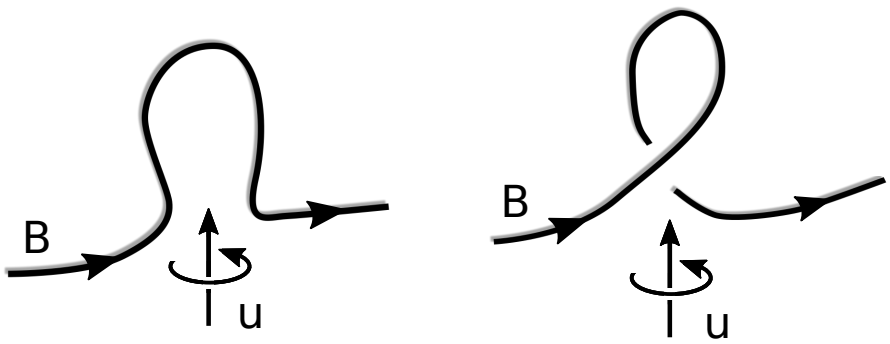

Figure 2.3: A schematic illustration of magnetic induction due to helical convection. Helical flow lifts (left) and twists (right) an initial magnetic field B to produce a loop of magnetic field with both positive and negative B_z components.

$$\mathrm{Rm} = \frac{\overline{U}L}{\eta}, \tag{2.3.12}$$

where L and $\overline{U}$ are the characteristic length and flow velocity scales, respectively. The value of the magnetic Reynolds number where the magnetic field starts to self-sustain is called the "dynamo onset."

The non-linearities in the induction equation (2.3.11) often preclude direct analysis. One alternate option is to consider the typical mechanisms of magnetic field generation arising from (2.3.11). Induction mechanisms are often described in the context of the frozen flux theorem, where field lines are swept along with the flow, and reconnect where field gradients are large (Gubbins and Herrero-Bervera, 2007). One example of a magnetic field generation mechanism is the α-effect. Originally investigated by Parker (1955), and further explored in the context of mean field electrodynamics (e.g., Moffatt, 1978), it describes the response of magnetic field lines to localized helical fluid motions. As an eddy with helicity—both a velocity and vorticity—approaches a magnetic field line, both the velocity and the vorticity act to induce a new magnetic field. The fluid motion lifts the flux line, which is fixed to the surrounding fluid, creating a region of increased curvature. At the same time, the vorticity of the eddy applies a twisting motion to the flux line. This process is illustrated in Fig. 2.3. Large field gradients at the point of intersection cause the flux loop to detach and become independent of the original field line. This loop creates a current $\mathbf{J}$ that is anti-parallel to the original mean magnetic field $\overline{\mathbf{B}}$. On average, this current has a strength of

$$\overline{\mathbf{J}} = \alpha\overline{\mathbf{B}}, \tag{2.3.13}$$

with a constant of proportionality of α (Steenbeck et al., 1966). Overall this process involves a transfer of kinetic energy—required to bend and rotate the flux line—into the magnetic energy of the loop.

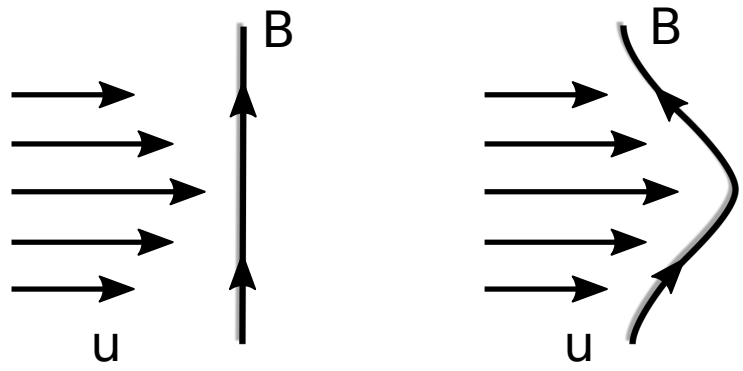

Figure 2.4: A schematic illustration of magnetic induction due to shear flow. Spatially varying flow interacts with a magnetic field line (left). As a result of shearing, the field line is bent (right), inducing a net magnetic field in the direction of mean flow.

Another proposed mechanism for magnetic induction is the ω-effect.[3] This effect describes zonal shearing motions associated with differential rotation, which drag azimuthal magnetic fields (Roberts, 2015). The magnetic stress grows as the field lines become increasingly stretched, eventually self-limiting the field amplification. This process is illustrated in Fig. 2.4.

It is hypothesized that the dipole field in the core is mainly a result of the α-effect, maintained by helical-flowing axial convection cells (Kageyama and Sato, 1997; Olson et al., 1999). In these cells, a strong axial vorticity is combined with a secondary axial flow, inducing a net helicity necessary for the α-effect. This mechanism is illustrated in Fig. 2.5.

2.4 Numerical Simulations

The complexities, non-linearities, and interdependencies of the dynamo equations (2.3.1)–(2.3.4) present tremendous challenges for direct analysis. As such, the majority of recent advances in understanding core dynamics have come from numerical simulations of dynamo processes (Olson et al., 2010). As several theorems prohibit 2D solutions of the dynamo problem, (Cowling, 1933; Bullard and Gellman, 1954; Braginskii, 1964), the full 3D fluid motions and magnetic fields in a spherical-shell geometry must be simulated. Extensive reviews of this approach can be found in Christensen and Wicht (2015) and Matsui et al. (2016).

Simulation of magnetohydrodynamics in the core starts with a numerical discretization of the dynamo equations (2.3.1)–(2.3.4). These equations are usually specified in non-dimensional form. However, there is no generally accepted standard way to scale the variables (Kono and Roberts, 2002). To give an example, I show one scaling option for

[3]Sometimes referred to as the Ω-effect.

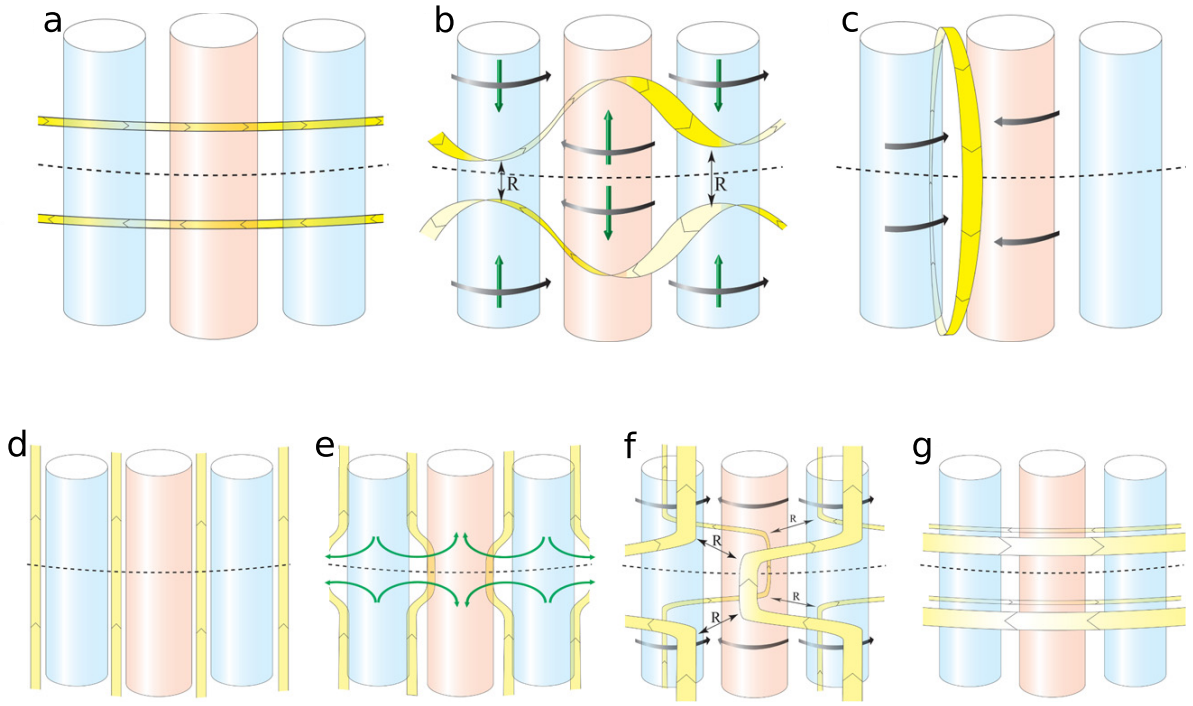

Figure 2.5: Schematic illustrations of the α-effect in the presence of axial convection columns. Subplots a-c show the generation of the poloidal field from the toroidal field. Subplots d-g show the generation of the toroidal field from the poloidal field. Magnetic field lines are shown as yellow ribbons. The primary columnar flows are shown as black arrows, and the secondary axial flow is shown as green arrows. Reconnection points of the field lines are indicated with an "R" symbol. Adapted from Roberts and King (2013)

convection-driven dynamos, which will be used for the simulations in Chapter 4. Four characteristic scales are set:

- The characteristic length scale is the thickness of the outer core, L.
- Time is scaled by the viscous diffusion time L^2/ν.
- Temperature is scaled by the average temperature difference between the inner and outer core boundaries, ΔT.
- The magnetic field is scaled by $\sqrt{\rho\mu\Omega\eta}$, where μ is the magnetic permeability.

These scaling choices lead to the non-dimensional governing equations:

$$\mathrm{Ek}\left(\frac{\partial \mathbf{u}}{\partial t}+\mathbf{u}\cdot\nabla\mathbf{u}\right)+2\hat{z}\times\mathbf{u}+\nabla\Pi=\mathrm{Ek}\nabla^2\mathbf{u}+\mathrm{Ra}\frac{r}{r_o}T+\frac{1}{\mathrm{Pm}}\left(\nabla\times\mathbf{B}\right)\times\mathbf{B}, \qquad (2.4.1)$$

$$\frac{\partial \mathbf{B}}{\partial t} - \nabla \times (\mathbf{u} \times \mathbf{B}) = \frac{1}{\mathrm{Pm}} \nabla^2 \mathbf{B}, \tag{2.4.2}$$

$$\frac{\partial T}{\partial t} + \mathbf{u} \cdot \nabla T = \frac{1}{\mathrm{Pr}} \nabla^2 T + \mathrm{Qt}, \tag{2.4.3}$$

$$\nabla \cdot \mathbf{u} = 0, \quad \text{and} \quad \nabla \cdot \mathbf{B} = 0, \tag{2.4.4}$$

where $\mathbf{u}$, $\mathbf{B}$, and T are now dimensionless, and Qt is the volumetric heating rate. Four non-dimensional control parameters have been introduced. The relative importance of buoyancy forces to viscous diffusion, and hence the vigor of convection, is specified by the modified Rayleigh number[4]

$$\mathrm{Ra} = \frac{\alpha g(r_o) \Delta T L}{\nu \Omega}. \tag{2.4.5}$$

The Ekman number

$$\mathrm{Ek} = \frac{\nu}{\Omega L^2}, \tag{2.4.6}$$

describes the ratio of viscous forces to the leading-order Coriolis force. The Prandtl number

$$\mathrm{Pr} = \frac{\nu}{\kappa}, \tag{2.4.7}$$

describes the ratio of viscous diffusion to thermal diffusion. Finally, the magnetic Prandtl number

$$\mathrm{Pm} = \frac{\nu}{\eta}, \tag{2.4.8}$$

describes the ratio of viscous diffusion to magnetic diffusion. Typical values for these parameters estimated for the Earth and used in typical dynamo simulations are listed in Table 2.1. Due to computational limitations, numerical dynamo simulations cannot reach Earth-like parameters. The main challenge is resolving small-scale flows in Ekman boundary layers. These boundary layers have a thickness of $\sim \mathrm{Ek}^{\frac{1}{2}} \times L$, requiring fine grid spacing and small timesteps for accurate numerical solution. Despite this limitation, many simulations are able to reproduce magnetic fields similar to that of the Earth (see Section 2.4).

Equations (2.4.1)–(2.4.3) give nine equations with eight unknowns, however there is some redundancy between (2.4.2) and $\nabla \cdot \mathbf{B} = 0$. If the initial field satisfies $\nabla \cdot \mathbf{B} = 0$, then later solutions ensure that $\nabla \cdot \mathbf{B} = 0$ continues to hold. The magnetic field is usually decomposed into a finite set of poloidal and toroidal components (see Section 2.3). Similar decompositions are used for the velocity field, allowing for the calculation of some derivatives in the spectral

[4]This compares with the traditional Rayleigh number, $\mathrm{R} = \alpha g(r_o) \Delta T L^3 / \kappa \nu$, which describes the ratio of thermal diffusion time to viscous buoyant rise time. This definition is less useful for the geodynamo, due to the strength of the Coriolis force. The traditional and modified Rayleigh numbers are related with $\mathrm{Ra} = \mathrm{R} \cdot \mathrm{Ek}/\mathrm{Pr}$.

domain. Other derivatives may be calculated locally on grid points with methods such as finite differences (e.g., Matsui et al., 2014). Time-stepping can be implemented a number of ways, however a common method is to use the Crank-Nicolson method for the linear diffusive terms, and the second-order Adam-Bashforth method for the Coriolis force and the other non-linear terms (Glatzmaier, 2013; Matsui et al., 2014). Time stepping must be done such that the Courant condition remains valid (Christensen et al., 1999). This limits the time step to be smaller than advection time between two grid points, and requiring very small time steps to resolve thin boundary layers resulting from low Ekman numbers.

How Realistic are Simulations?

Ever since the first dynamo simulations of Glatzmaier and Roberts (1995) and Kageyama et al. (1995), a key question has been: Are these simulations relevant to the Earth? Many dynamo simulations have been able to reproduce some individual properties of the observable geomagnetic field, such as its strength (e.g., Glatzmaiers and Roberts, 1995), secular variation timescale (e.g., Christensen and Tilgner, 2004), shape of the power spectrum (e.g., Davies and Constable, 2014), westward drift of magnetic structures (e.g., Sakuraba and Roberts, 2009), and the occasional presence of reversals (e.g., Driscoll and Olson, 2009). However, other studies have proposed more detailed assessments of geodynamo simulations (e.g., Sprain et al., 2019).

One approach for the assessment of realistic dynamo conditions involves analysis of the morphology of the simulated magnetic fields. Christensen et al. (2010) introduced a set of morphology criteria that assessed the similarity between simulation results and the historical geomagnetic field. Earth-likeness was measured in a quantitative manner, by relying on well-established structural quantities of the geomagnetic field estimated from historical observations (Jackson et al., 2000; Finlay et al., 2010b) and paleomagnetic models (Korte et al., 2005; Khokhlov et al., 2006). The criteria included: dipole dominance, equatorial symmetry, axial symmetry, and a measure of patchiness of the field. These criteria were investigated with respect to two identifying parameters. The first parameter described characteristic timescales, indicated by the magnetic Ekman number $\mathrm{Ek}_\eta = \mathrm{Ek}/\mathrm{Pm}$, which reflect the ratio of the rotation time scale to magnetic diffusion time scale. The second param-

Table 2.1: Order of magnitude parameters in the core, and typical values used in numerical dynamo models. Here the Rayleigh number is normalized by a critical value Ra_c which defines the onset of convection without a magnetic field. Estimates for Earth values arise from thermodynamic and transport properties inferred from laboratory experiments, and observations of the Earth's field. See Olson (2015) for an extensive summary.

	$\mathrm{Ra}/\mathrm{Ra}_c$	Ek	Pm	Pr
Core	$\gg 1$	10^{-15}–10^{-14}	10^{-6}–10^{-5}	0.1–1
Dynamo models	10–100	10^{-6}–10^{-3}	10^{-1}–10^{3}	0.025–10^{3}

eter described the vigor of convection, indicated by the magnetic Reynolds number, Rm. The compliances of a large number of dynamo simulations were tested by Christensen et al. (2010), spanning several orders of magnitude in control parameters. Fig. 2.6 shows these results. Simulations that produced fields agreeing well with the proposed Earth-like criteria formed a wedge shape, which extended below magnetic Ekman numbers of about $\sim 10^{-4}$. There were a range of magnetic Reynolds numbers that produced Earth-like fields, and this range changed with magnetic Ekman number. Later studies have continued to find that simulations in this wedge-shaped region of parameter space yield Earth-like fields (Wicht and Sanchez, 2019).

The findings of Christensen et al. (2010) show that some dynamo simulations produce external field morphologies that are similar to the Earth. However these fields may simply appear correct for the "wrong" reasons. Another indication for Earth-like simulations comes from analysis of the dominant force balances within the simulations. The goal is to investigate whether dynamo simulations are operating in a force-balance regime that is thought to operate in the Earth. In particular, this refers to the balance between terms in the Navier-Stokes equation. Simulations are mostly restricted by the Ekman number, with too large Ekman numbers translating to increases in the viscous force, which are in turn counteracted by stronger convective driving, resulting in excessively large inertial effects. A small Ekman number in the core suggests that the pressure gradient, Lorentz or Magnetic force (M), buoyancy or Archimedean force (A), and Coriolis force (C) are first-order balanced. This is referred to as the "MAC" force balance, with viscous and inertial contributions being much smaller (Christensen, 2010; Jones, 2011; Roberts and King, 2013). Davidson (2013) estimated the magnitude of these forces for the vorticity formulation of the Navier-Stokes equation (2.3.1), and predicted non-dimensional scaling laws for the flow velocity and magnetic field strength. The scaling for the flow velocity, represented by the Rossby number

$$\mathrm{Ro} = \frac{\overline{U}}{\Omega L}, \tag{2.4.9}$$

was predicted to scale with the total available power $\mathcal{P}$ and dissipated power f_{Ohm}. A similar scaling was predicted for the magnetic field strength, represented by the Lehnert number

$$\mathrm{Le} = \frac{\overline{B}}{\Omega L \sqrt{\rho \mu}}, \tag{2.4.10}$$

where $\overline{B}$ is the characteristic magnetic field strength. See Davidson (2013) for detailed descriptions. These proposed scalings were tested against a collection of dynamo simulations from Christensen et al. (2010). Later analysis in Wicht and Sanchez (2019) also included simulations from Aubert et al. (2017). Fig. 2.7 shows these hypothesized scalings, and the empirical scalings apparent in the dynamo simulations.

The dynamo simulations appear to follow the hypothesized scalings, suggesting that the primary force balance is MAC. This also extrapolates to estimates of values for the Earth

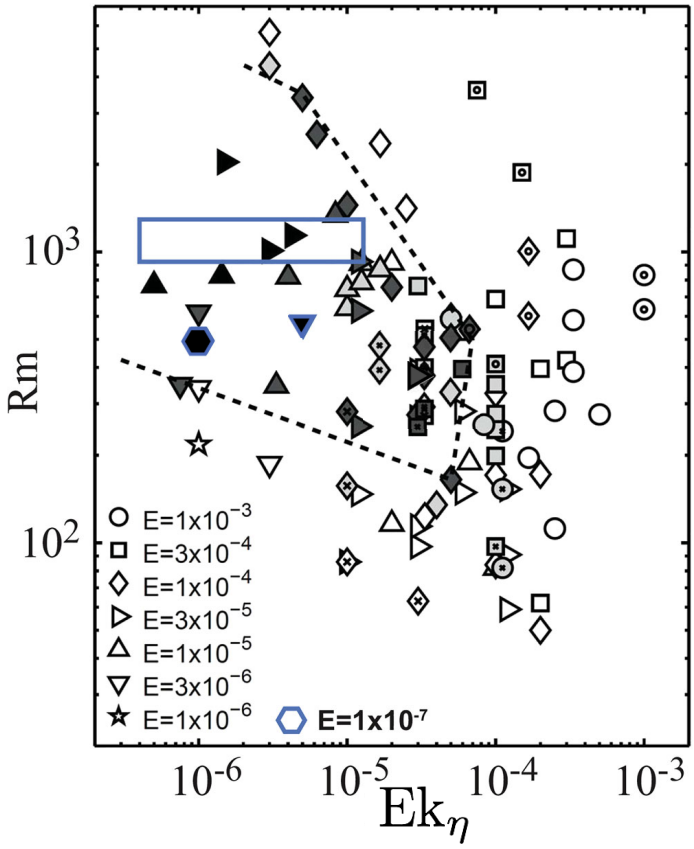

Figure 2.6: Parameter regimes of Earth-like numerical geodynamo simulations, based on the field morphology criteria from Christensen et al. (2010). Scattered symbols represent values taken from numerical geodynamo simulations, with the symbol shapes corresponding to different Ekman numbers (see legend). The symbol face colors indicate the compliance of the field morphology based on the criteria from Christensen et al. (2010), with black = excellent, dark grey = good, light grey = marginal, and white = bad. This includes 155 simulations from Christensen et al. (2010), indicated with black edges. Also included are two simulations from Schaeffer et al. (2017), indicated with blue edges. The blue rectangle indicates 17 simulations from Aubert et al. (2017), which range from Ek = 3×10^{-5} to Ek = 10^{-8}, and all have excellent field morphologies. The Earth-like "wedge" has been outlined by dashed lines. Modified from Wicht and Sanchez (2019).

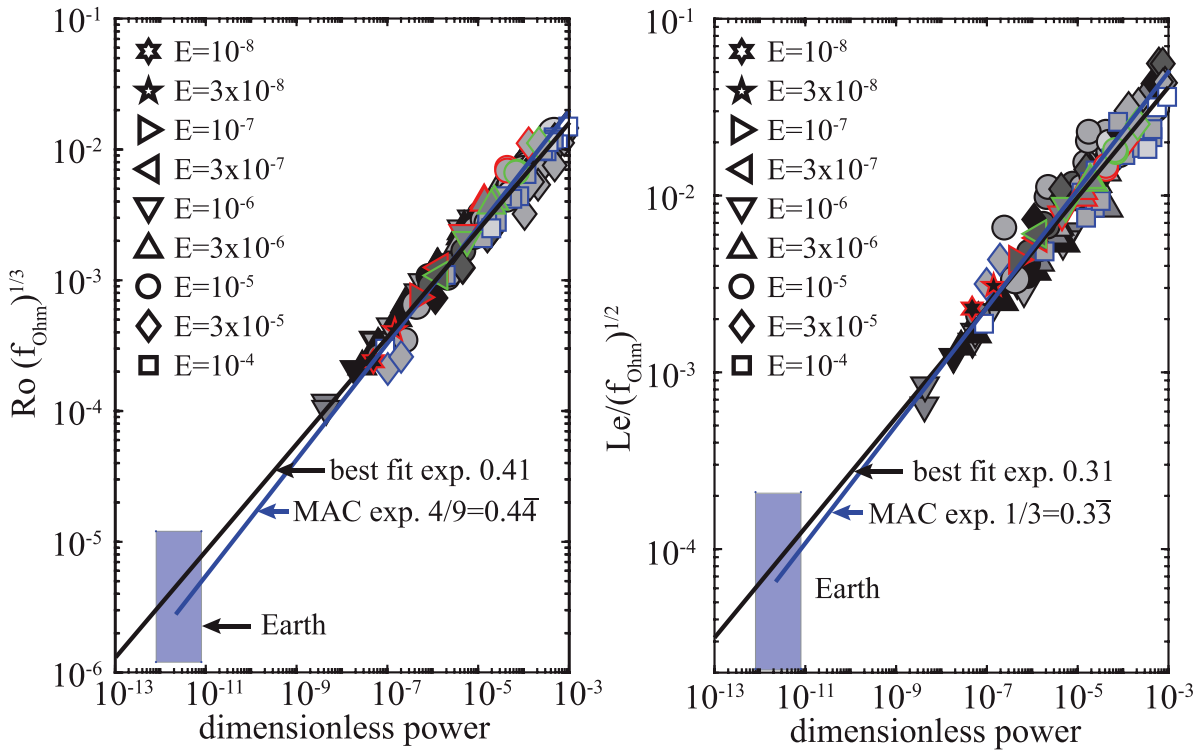

Figure 2.7: Dependence of flow velocity (left) and magnetic field strength (right) on the dimensionless convective power, expressed in non-dimensional quantities. Scattered symbols represent values taken from numerical geodynamo simulations, with the symbol shapes corresponding to different Ekman numbers (see legends). This includes 133 simulations from Christensen (2010), with thermal and compositional convection cases indicated with black and blue edges, respectively. Also included are 17 simulations from Aubert et al. (2017), with fixed codensity and "coupled Earth" cases indicated with red and green edges, respectively. The symbol face color indicates the magnetic Prandtl number, ranging from Pm $\geq$ 10 in white to Pm $\leq$ 0.1 in black. The predicted scalings for MAC balance are shown as blue lines, whereas linear least squares fit scalings from the data are indicated as black lines. The exponents of these scalings are indicated. Estimates for the power requirement of the Earth's geodynamo come from Christensen and Tilgner (2004). Estimates for Earth values for the magnetic field strength come from surface observations and predicted torsional oscillation frequencies (Gillet et al., 2010). Estimates for the Earth values for flow velocity come from the typical secular variation timescale (Gillet et al., 2010). Modified from Wicht and Sanchez (2019).

inferred from Gillet et al. (2010) and Christensen and Tilgner (2004), indicating that dynamo simulations and the Earth are in the same force-balance regime. Recent work also suggests the MAC balance is expressed in dynamo simulations through a high magnetic to kinetic energy ratio (Schwaiger et al., 2019). When this ratio is above unity, it indicates that the Lorentz forces are stronger than inertia or viscosity, suggesting the models are in the regime for MAC balance.

In summary, scaling behavior and force balance analysis suggests that the primary force balance in some modern dynamo simulations is indeed Earth-like. Secondary forces are not as small as they should be, but may nevertheless have only negligible impacts on the dynamo process.

Chapter 3

Stochastic Models of the Geomagnetic Field

With the fundamentals of the geodynamo covered, I now focus on giving a comprehensive literature review of stochastic models of the geodynamo. I also address their context with other abstract and statistical models.

3.1 Abstract Models of the Geodynamo and Geomagnetic Field

As discussed in the previous chapter, the geodynamo is a very complex system. The fluid motion of the liquid iron alloy interacts with the magnetic field in a self-sustaining way, and further complexities arise from chemical and physical processes occurring at the interfaces between the outer core and the mantle and inner core. As a result, analytical modeling of the magnetic and velocity fields with partial differential equations is challenging. Even with computational fluid simulations of the full 3D velocity and magnetic fields, linking observations of the external magnetic field to interior processes is difficult. Many studies have thus sought to derive simpler "toy" descriptions of the geodynamo. Although these descriptions are highly idealized, they may provide a path toward understanding the full nature of the system (Laymon, 1985, 1995).

Some of the first attempts at idealized models of the geodynamo were "disk dynamos." Originally proposed by Bullard (1955), this model considers an abstract electrically conductive disk rotating about a perpendicular axle. A wire attached to the axle is in sliding contact with the edge of the disk by means of a conductive brush. In the presence of a magnetic field parallel to the axle, an electric current is induced, which then drives a self-exciting dynamo. A popular extension of the model was presented in Rikitake (1958), wherein a configuration of two disks was considered. Critically, this latter setup was able to accommodate a magnetic field of either normal or reversed polarity, and was also able to produce polarity reversals. These early disk dynamos were popular for investigating the geodynamo

as well as other astrophysical objects (see Jacobs, 1994, for a review), as they were simple enough to work with, either analytically or computationally, yet also contained sufficient chaos and complexity to plausibly imitate the dynamics of the geodynamo (e.g., Ito, 1980). Many modified configurations have since been proposed. One example produced a model with fast and slow magnetic modes (Nozières, 1978). Other generalizations have considered N coupled disks arranged in complicated fashions (Shimizu and Honkura, 1985; Ito, 1988). Although these models may be able to reproduce some of the observed features of the geomagnetic field, they represent extreme idealizations of the magnetohydrodynamic nature of the core. More recent work has attempted to merge the disk approach with mean field magnetohydrodynamics, replacing elements of the disk dynamo model with more physically realistic mechanisms (Ryan and Sarson, 2007).

Another approach is to model local regions in the core as distinct but interacting subsystems (e.g., Mazaud and Laj, 1989; Seki and Ito, 1993; Dias et al., 2008). These numerical models are analogous to the Ising model of ferromagnetism used in statistical mechanics (Ising, 1924). These models partition the outer core into a number of regions, and each unit is assigned a scalar state of either $+1$ or -1. These elementary units are typically assumed to be point dipoles aligned either parallel or antiparallel with the Earth's rotation axis (Mazaud and Laj, 1989). The probability of any one unit switching to the opposite state is influenced by the combined states of all the other units with which it interacts. The combined behavior of these units gives rise to an emergent, time-varying magnetic field. The field also exhibits transitions between different states of behavior (e.g., from a frequently-reversing state to a stable-polarity state) depending on how strongly the elemental units interact with each other. Some studies have modified this approach by producing dynamo models which combine elements of the disk and Ising models (Seki and Ito, 1999). Others have permitted the dipole units to deviate from a binary parallel or antiparallel orientation (Nakamichi et al., 2012; Mori et al., 2013), or attempted to model the effects of interacting fluid vortices in these regions (Narteau et al., 2000). These "Ising-like" models are capable of reproducing some of the reversal statistics in the paleomagnetic record (Seki and Ito, 1993; Dias et al., 2008). However, these models represent deliberate distortions of geodynamo mechanisms. It has yet to be shown whether these highly idealized models represent any physical processes or governing forces in the core.

A final class of toy models of the geodynamo are simple deterministic systems. These models are composed of a small number of non-linear ordinary differential equations, inspired by classic chaotic systems such as the Lorenz 63 model (Lorenz, 1963). These models typically postulate that the typical dynamics of the full magnetic field can be partitioned into a small number of modes (Pétrélis et al., 2009), or alternatively, magnetic modes that interact with particular components of velocity fields (Gissinger et al., 2010; Gissinger, 2012). Although these models quantitatively reproduce some observed properties of the geomagnetic field (e.g., Gwirtz et al., 2021a), the simplifications bring any physical interpretations into question. On the other hand, some deterministic models do not aim to reflect any physical processes in the core (e.g., Gwirtz et al., 2021b). Such examples only seek to be "proxy models" that behave like the geomagnetic field, and are used for testing field forecasting

techniques.

Although many of these abstract models have been successful at mimicking the behavior of the geodynamo, and may in some cases reproduce certain features of the field, they are often difficult to link to conventional magnetohydrodynamic theory. It may be argued that many of these models are simply phenomenological, as they are independent of theory (e.g., McMullin, 1968); however, these models demonstrate more serious flaws when they predict unrealistic field behavior. In such a case, the model "floats" untethered to either theory or observation (Redhead, 1980). This motivates finding more credible frameworks for modeling the geodynamo, that: (1) accurately and reliably reproduce empirical observations; and (2) have firm grounding in realistic magnetohydrodynamic theory. If these two goals are met, then it may be possible to connect observations and underlying processes in meaningful ways.

3.2 Statistical Models of the Geomagnetic Field

Statistical models are widely employed in many areas of geophysics, including the study of the geomagnetic field (Stark, 2004). Such models aim only to represent statistical properties of the field, rather than individual empirical observations. Often only broad-scale statistics—such as means, variances, or covariances—of the field are considered. The goal of such models is to represent or reproduce statistical quantities of the external magnetic field, with the acknowledgement that these may or may not reflect physical properties or processes of the geodynamo.

One of the simplest statistical models of the geomagnetic field describes the polarity as a two-state stochastic variable: either normal or reversed. This approach is motivated by the geomagnetic polarity timescale (GPTS), which is a frequently-updated compilation of paleomagnetic observations (for the most recent iteration, see Ogg, 2020). Early studies posited that the frequency of polarity reversals follows a Poisson distribution (Cox, 1968, 1969). This hypothesizes that reversals are random events with a constant rate and an exponential waiting time. This model lacks any memory, meaning that the probability of a reversal in a given time span is independent of previous history. Extensions of these models have been used to investigate possible polarity biases between normal and reversed states (Cox, 1981), although no consensus has yet been reached as to whether a bias is present. Early models described reversals occurring at a single unchanging rate, which is not compatible with the paleomagnetic record; the GPTS shows drastic changes in reversal rates over geologic time(e.g., McFadden and Merrill, 1984; Constable, 2000). To better match the paleomagnetic record, extensions of the Poisson model have been made, for example, by varying the mean reversal rate throughout the history of the Earth (e.g., Merrill et al., 1998; Lowrie and Kent, 2004).

For the variability of the geomagnetic field on shorter timescales, a popular statistical model is that of Constable and Parker (1988). This model, referred to as a "Giant Gaussian Process" (GGP), describes variations of the spherical harmonic components of the field over

the past five million years. The amplitude of the spherical harmonic components were modeled as zero mean Gaussian distributions for non-dipole components, and a pair of Gaussian distributions at opposite polarities for the axial dipole. The model provides complete descriptions of the probability distributions of magnetic field directions and intensities at any point on the Earth's surface. This model has proved to be incredibly useful for interpreting paleomagnetic measurements. Many refinements of the original model have been proposed, including: updates to the original dataset (e.g., Quidelleur and Courtillot, 1996; Bono et al., 2020); refined covariance descriptions of the non-dipole components (Constable and Johnson, 1999); and symmetry based considerations (Hulot and Bouligand, 2005). GGPs have also been fitted to external magnetic fields which were generated by numerical geodynamo simulations (Bouligand et al., 2005). For a comprehensive review of GGPs, their applications, and an updated model for the recent geomagnetic field, see Bono et al. (2020).

Although GGPs provide useful descriptions of the time-averaged field, they are stationary. To introduce nonstationarity into the GGP framework, Constable (1990) added autoregressive temporal structure to the first few spherical harmonic components of the field. Specifically, the discrete evolution of the field components was set by a first-order autoregressive process

$$g_\ell^m(t_i) = a \cdot g_\ell^m(t_{i-1}) + \varepsilon(t_i), \tag{3.2.1}$$

where $g_\ell^m(t_i)$ is the Gauss coefficient with degree ℓ and order m at time t_i, a is a constant that controls the characteristic timescale of the process, and $\varepsilon(t_i)$ is Gaussian white noise. The value of a was fit to observations, to reflect the natural temporal variability of the field. Furthermore, it was found that if the axial dipole component was forced to transition through a polarity reversal, the model was able to reproduce the qualitative features of global paleomagnetic measurements. A similar approach to temporal variability was taken by Hulot and Le Mouël (1994), where the field components were modeled as a Gaussian process. There, a "two scale" treatment was proposed, in which a nearly stationary axial dipole field was combined with a secular field that varied faster and had characteristic timescales described by the Gaussian processes. Further refinements to this model have been made, both for the simulated fields created by numerical geodynamo models (Lhuillier et al., 2011), as well as the more recent field from 1840–2010, revealed through observatory and satellite data (Gillet et al., 2013).

While these models provide convenient representations of statistical properties of the geomagnetic field, their main utility is description and prediction. Possible links between these statistical representations and physical mechanisms in the core have not been established.

3.3 Stochastic Models of the Geomagnetic Field

Stochastic models of the geomagnetic field attempt to describe the changes in the field within a specific statistical framework. They establish a probability model for coefficients of the geomagnetic field, with specified constraints on the form of time dependence. The stochastic

models in the geomagnetic literature mainly take the form of stochastic differential equations (SDEs). The fundamentals of SDEs are covered in Pavliotis (2014), and their applications in the physical sciences are covered in Gardiner (1985), Van Kampen (1992), and Risken (1996). As these models are built from differential equations, they are more amenable to interpretation and may more accurately reflect physical processes in the core.

One justification for the stochastic differential equation perspective comes from the field of complex dynamical systems and the study of self-organization (Haken, 1989, 2006, 2013, 2020). Complex systems often have a large number of interacting modes, or components, with different characteristic timescales. However, the phenomenon of self-organization can sometimes give rise to slow dynamics of "order parameters" that control the dynamics of faster-scale subsystems.[1] This separation of time scales between the slow and fast dynamics can lead to a dramatic reduction of the relevant degrees of freedom in the system (Majda et al., 2005). The behavior of complex systems which comprise a large number of degrees of freedom can thus often be described by low-dimensional stochastic equations (Van Kampen, 1992), and in some cases a Fokker-Planck equation (Risken, 1996). The interpretation is that the stochastic component is not just an external forcing; rather, that it is an intrinsic part of the dynamics of the system. Analyzing a complex system such as the geodynamo in this manner can be approached in two ways. In some cases it is possible to start by considering the interactions of subsystems, and deduce the governing equations for the macroscopic order parameters (e.g., Haken, 1985). Alternatively, one can construct a phenomenological model for macroscopic observables by calculating specific averages from experimental or observational data (e.g., Haken et al., 1985; Haken, 2006; Peinke et al., 2019). These two strategies describe "bottom-up" and "top-down" approaches, respectively. The bottom-up approach has previously been popular in physics and chemistry (e.g., Van Kampen, 1992), and in astrophysics (see, e.g., Chandrasekhar, 1943; Knobloch, 1980, for reviews). The top-down approach, motivated by the original work of Haken (Borland and Haken, 1992a,b,c, 1993), did not find popularity until later work by Siegert et al. (1998). Since then, the top-down approach has been applied to many areas in physical sciences (see Friedrich et al., 2011, for a comprehensive review).

For stochastic models of the geomagnetic field, as with GGPs, the purpose of the model depends on the kind of observation upon which it is based. Models constructed from numerical simulations provide an opportunity to connect the emergent stochastic properties to internal physical mechanisms. On the other hand, models constructed from geomagnetic field observations provide simple statistical descriptions of the variability of the geomagnetic field. If both of these points of connection can be made, then quantitative links between geomagnetic observations and physical processes in the geodynamo might be possible. If a model can achieve both, then stochastic models of geomagnetic field variations may have the potential to go beyond the phenomenological toy models, and provide a route towards

[1] In the original literature, Haken and others refer to this structure as the "slaving principle", between the "Master modes" and the "enslaved modes". In order to adopt more conscientious and inclusive naming practices, I will use alternate terminology (Graur, 2021; I.N.I., 2022).

estimating core processes through geological time.

Stochastic models that have been presented in the literature can be broadly divided into two classes—deductive models and inductive models—reviewed in this section.

Deductive Stochastic Models

One way of building a stochastic model of the geodynamo is to start from an existing theoretical deterministic model, and through the use of domain knowledge, intuition, or experience, extend it with a stochastic component. This deductive approach must be validated through testing hypotheses (usually in the form of statistical predictions) against empirical data (either paleomagnetic measurements, geodynamo simulations, or both). In the past, this approach has been particularly popular in astrophysics (e.g., Chandrasekhar, 1943; Knobloch, 1980). However, only recently has this been applied to the Earth's geodynamo.

One of the first examples of this approach is presented in Hoyng et al. (2001). There, the authors approach began with a 1D $\alpha\omega$-type mean field dynamo model (Schmitt and Schüssler, 1989), which was extended by considering a randomly fluctuating efficiency of the α-effect. Taking averages over fast-scale fluctuations of overtone modes resulted in a equation for the evolution of the transition probability of the amplitude of the dipole mode, $p(a,t)$, of the form

$$\frac{\partial p}{\partial t} = -\frac{\partial}{\partial a}S(a)p + \frac{1}{2}\frac{\partial^2}{\partial a^2}D(a)p. \tag{3.3.1}$$

This follows the form of a Fokker-Planck equation, where $S(a)$ is the drift term and $D(a)$ is the noise term (Risken, 1996).[2] Furthermore, the drift and noise functions follow the structure

$$S(a) \approx \Lambda(1-a^2)a, \tag{3.3.2}$$

and

$$D(a) \approx \Delta_0 a^2 + \Delta_1, \tag{3.3.3}$$

respectively, where Λ, Δ_0, and Δ_1 are constants determined by parameters of the mean field model. These theoretical predictions for the drift term, the steady state distribution, and other statistics were compared against empirical results obtained from numerical simulation of the mean field model, and a good agreement was found.

Analysis of this specific stochastic mean field model was continued in Schmitt et al. (2001), where the effect of control parameters on the fitted drift and noise functions (3.3.2)–(3.3.3) was investigated. The drift function was interpreted to be linked to the linear growth of the dipole mode (most present at low dipole amplitudes), and balanced by quadratic

[2]This implicitly assumes a Lanegvin-type model for variations in the dipole, with almost surely continuous sample paths.

α-quenching at higher amplitudes. This started to link externally observable statistics to internal physical properties of the geodynamo.

To make the desired connection to the geodynamo, Hoyng et al. (2002) analyzed the Sint-800 model, a paleomagnetic record of virtual axial dipole moment (VADM) for the last 800 thousand years (Guyodo and Valet, 1999). This record was interpreted in the stochastic mean field framework (Hoyng et al., 2001; Schmitt et al., 2001), under the presumption that the connection from external stochastic representation to internal physics is valid for the Earth. From this analysis, the authors inferred fluctuations in the amplitude of the α-effect in the core on the order of 250%, and a ratio of turbulent to molecular diffusion on the order of 20–30. However, despite multiple attempts at forward modeling, the stochastic model of VADM fluctuations could not be completely aligned with all the observed statistics from the Sint-800 record, calling into question either the validity of the theoretical mean field mechanisms, or the analysis and interpretation of the paleomagnetic record.

A similar attempt to use a stochastic model to investigate physical processes in the geodynamo was conducted by Brendel et al. (2007). The authors studied a longer palaeomagnetic model—Sint-2000, a record of VADM variations over the past two million years (Valet et al., 2005)—in the context of the mean field interpretation (Hoyng et al., 2001). Critically, rather than presuming the stochastic model of (3.3.2)–(3.3.3), a non-parametric fit for the drift and noise functions was employed.[3] The fitted drift function agreed fairly well with the mean field prediction of (3.3.2), and a linear growth rate of ~ 20 kyr was determined (Schmitt et al., 2001). However, fits for the noise function from Sint-2000 did not follow the quadratic prediction (3.3.3) from the mean field theory. Instead, the amplitude noise was found to be approximately constant for most high VADM values, but increasing by a factor of three below dipole amplitudes of about $\sim 2 \times 10^{22}$ Am^2. The authors were unable to reconcile this observation with the mean field framework, reducing the plausibility of proposed physical links.

A subsequent study built up from the mean field framework of Hoyng et al. (2001) came from Kuipers et al. (2009). There, a set of 3D magnetohydrodynamic geodynamo simulations were analyzed in order to investigate the validity of a stochastic mean field framework. Three simulations taken from Wicht et al. (2009) were considered, representing characteristic end-members of typical dynamo dynamics:

1. A strongly dipolar field, exhibiting no reversals,

2. A strongly dipolar field, exhibiting rare reversals, and

3. A weakly dipolar, rapidly-reversing field.

[3]The Fokker-Plank equation was explicitly discretized, and the unknown coefficients of the drift and noise functions were found through optimization against a numerical estimate of the transition probability distribution, at a small but finite lag time. This was under the assumption that the process is driven by white noise, and is therefore Markov. This method was successfully verified on the simplified mean field model of Hoyng and Duistermaat (2004).

The drift and noise functions were fitted using the methods developed in Brendel et al. (2007), and are reproduced here in Fig. 3.1.

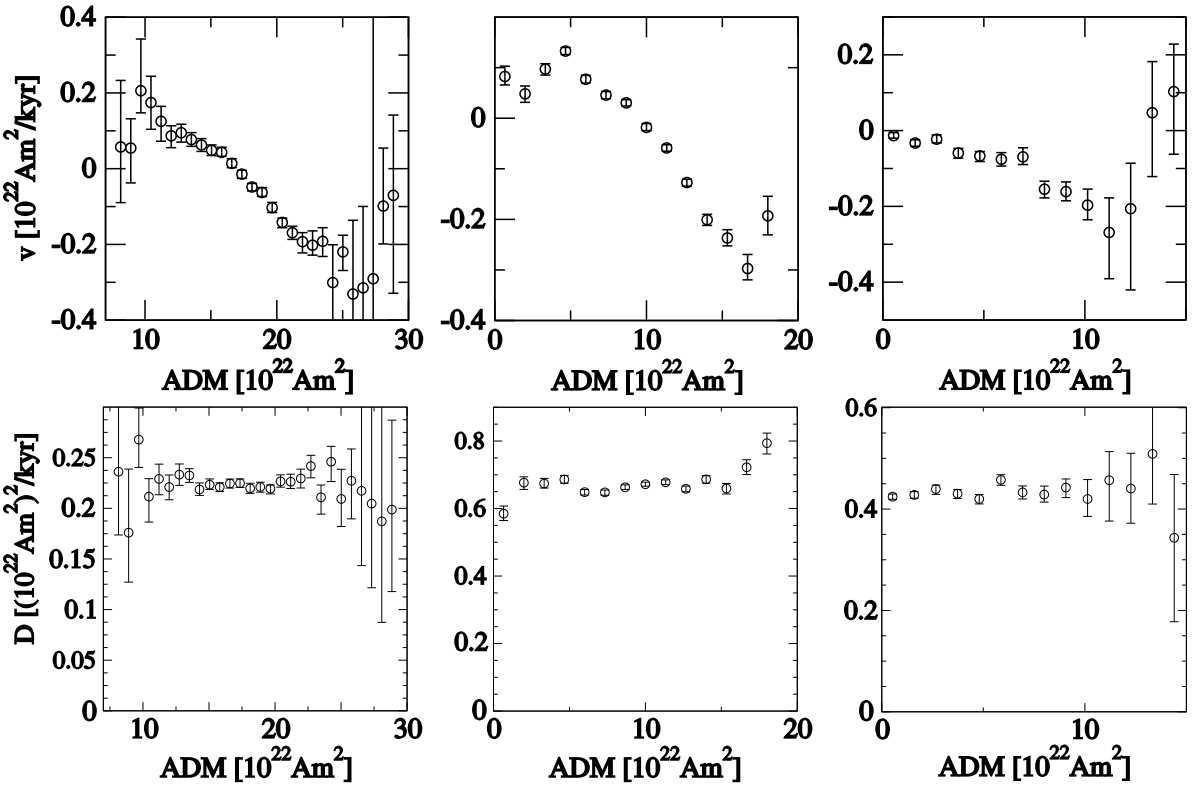

Figure 3.1: Fitted drift (top) and noise (bottom) functions, here $v(x)$ and $D(x)$, respectively, from three numerical geodynamo simulations (Wicht et al., 2009). The left, middle, and right plots show results for the strong non-reversing dynamo, the strong reversing dynamo, and the weak rapidly-reversing dynamo, respectively. Adapted from Kuipers et al. (2009).

The previous drift prediction of equation (3.3.2) was found to apply well only to the strong reversing dynamo. The noise functions were all found to be approximately constant, similar to fits from paleomagnetic records in Brendel et al. (2007), and contrary to the prediction of equation (3.3.3). Together, these discrepancies implied that the particular mean field model of Hoyng et al. (2001) was not readily applicable to these non-reversing or weak simulations. In an attempt to reconcile this finding with the quadratic noise predicted by Hoyng et al. (2001), the authors suggested that variations in the field are suppressed by a magnetic quenching of the convective flow. An important aspect of this study, however, is that the numerical nature of the geodynamo models allowed for a direct inspection of the internal processes. All three simulations showed that, on average, the root mean squared velocity field was anti-correlated with the magnetic field. The authors hypothesised that, with stronger fields, the amplitude of variations in convective turbulence becomes smaller by some quenching process, and that this decrease is just sufficient to balance the increase

in noise from turbulent diffusion. Alternatively—or additionally—they posit that this phenomenon could be attributed to changes in the correlation time of the velocity field. This conclusion seems questionable, since it rests upon a particular balance between amplification and quenching across a large span of control parameters and three end-member regimes of behavior. An alternative conclusion is that the particular assumptions of the mean field model in Hoyng et al. (2001) are not applicable. This argument also extends to the Earth, calling the conclusions of Brendel et al. (2007) into question.

These studies feature stochastic models of the geodynamo that are deduced from an existing idealized theoretical model, namely, mean field dynamo theory (Moffatt, 1978; Krause and Raedler, 1980). While both numerical simulations and paleomagnetic observations were demonstrated to be expressible in a Fokker-Planck interpretation, links to physical processes were possible only for mean field simulations (Hoyng et al., 2001; Hoyng and Duistermaat, 2004; Brendel et al., 2007). Nevertheless, the authors note that the general stochastic interpretation is worthwhile, and propose that a similar analysis could be readily applied to more complicated dynamo models (Hoyng et al., 2001; Hoyng, 2009). Perhaps without the restriction of the mean field interpretation of Hoyng et al. (2001), a stochastic model and underlying physical properties can be reconciled, allowing quantitative insights into the geodynamo from geomagnetic records.

One other study that should be mentioned in the context of deductive reasoning is Scullard and Buffett (2018). Rather than appealing to mean field theory, the authors consider a more general case of augmenting the induction equation with random sources. The thought is that the large scale poloidal and toroidal fields are forced by the fast-scale, high-order harmonics imposed by convective fluctuations. When considering a combination of Gaussian white noise and weak Poisson distributed jumps, the probabilistic dynamics of the fields could be interpreted as a Fokker-Planck equation. This analysis found the drift function to reflect the balance between ohmic dissipation and the average contribution of convective events. This framework has so far been underutilized in the literature; however, it has great potential for analyzing empirical observations, and deserves further investigation.

Inductive Stochastic Models

An alternative approach to constructing a stochastic model of the geodynamo is to start from observations, rather than an existing theory. If a set of observations—either from a simulation or an empirical geomagnetic dataset—appears to have "stochastic" behavior, a tentative hypothesis to account for this behavior can be constructed. For this hypothesis to be accepted, it must be verified that the stochastic model is a representative model; i.e., that it both reproduces statistical properties of the original data and generalizes well to other observations. Although this approach requires an element of pattern recognition—and hence the initial search may suffer from confirmation of bias (e.g., Nickerson, 1998)—it allows for a top-down approach to complexity (Peinke et al., 2019).

One of the first examples of this "empirical first" approach to constructing stochastic models of the geomagnetic field appears in Buffett et al. (2013). The paleomagnetic models

of PADM2M (Ziegler et al., 2011) and Sint-2000 (Valet et al., 2005) were considered, but without an *a priori* physical framework. These records were presumed to be well-represented by a stochastic differential equations, and the drift and noise functions of this assumed model were fitted to the empirical observations. This was accomplished through calculation of conditional moments, see Fig. 3.2.

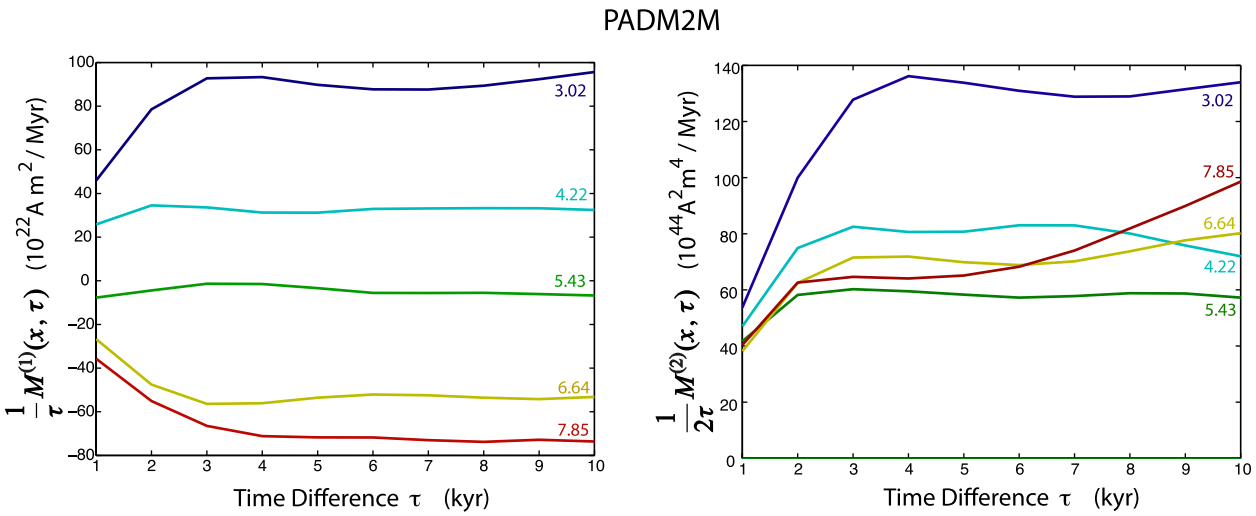

Figure 3.2: Scaled conditional moments calculated from the time-series PADM2M model of Ziegler et al. (2011). The scaled first and second moments are shown as a range of τ values in the left and right plots, respectively. Each colored line represents a different x-conditioning, which is accomplished by binning. The bin centers for each x-condition are indicated on the right of each line. Similar moments where also found for the Sint-2000 model of Valet et al. (2005). Adapted from Buffett et al. (2013).

To connect these moments to the drift and noise functions, the authors employed the "direct estimation" technique of Siegert et al. (1998). Similar results were found for both PADM2M and Sint-2000. The drift function was determined to be approximately linear, crossing zero approximately at the mean VADM state of $\sim 5 \times 10^{22}$ Am^2. The noise term was found to be approximately constant above dipole amplitudes of about $\sim 4 \times 10^{22}$ Am^2, with a factor of two increase for lower dipole amplitudes (see Fig. 3.3).

To validate the stochastic model, the authors calculated the steady state distribution and reversal rate of the VADM, and found a good agreement with the original data. Finally, a hypothesis was proposed for the physical origins of the drift and noise functions. To link the full magnetohydrodynamic action of the core to the observable axial dipole field, the authors analyzed the total magnetic field projected onto the $n = 1$ term of the vector spherical harmonic expansion, $\overline{\mathbf{B}}$, (e.g., Chandrasekhar, 1981). The induction equation for $\overline{\mathbf{B}}$ is written as

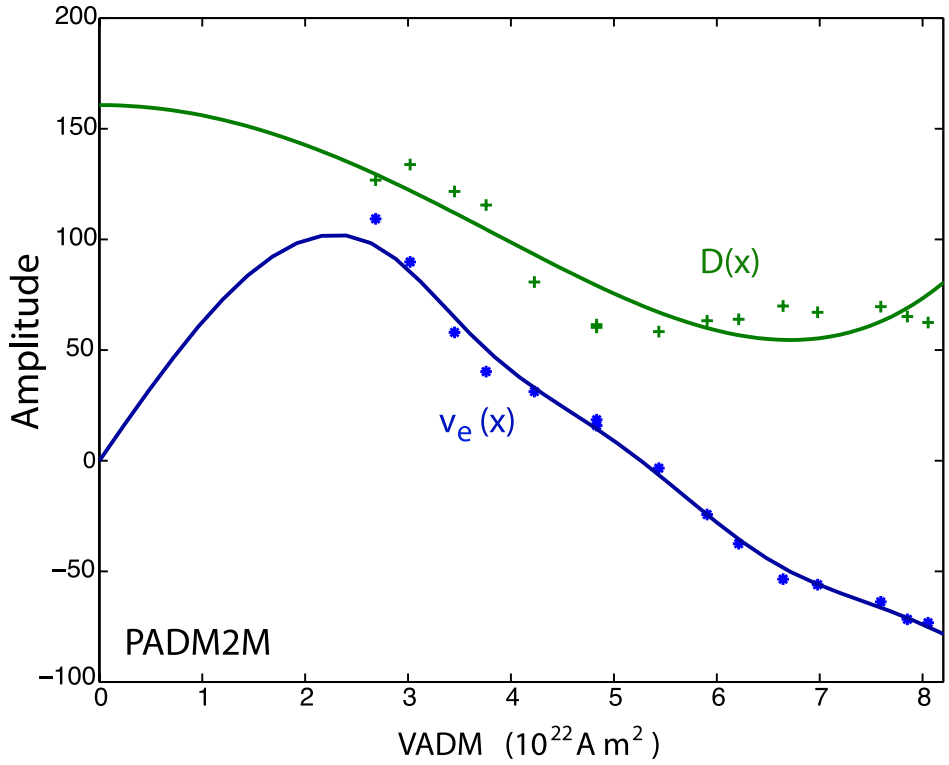

Figure 3.3: Fitted drift and noise functions, here $v_e(x)$ and $D(x)$, respectively, from the PADM2M model of Ziegler et al. (2011). Fits from binning for the drift function and noise function are shown as blue stars and green plusses, respectively. Smooth spline fits are indicated for each function with solid lines. The ordinate amplitudes are 10^{22} Am^2 Myr^{-1} and 10^{44} A^{2}m^4 Myr^{-1} for the drift and noise functions, respectively. Similar fits where also found for the Sint-2000 model of Valet et al. (2005). Adapted from Buffett et al. (2013).

$$\frac{d\overline{\mathbf{B}}}{dt} = \overbrace{\nabla \times \overline{(\mathbf{v} \times \mathbf{B})}}^{\text{Induction}} + \overbrace{\eta \nabla^2 \overline{\mathbf{B}}}^{\text{Diffusion}} . \tag{3.3.4}$$

When averaged over the whole core, this expression reflects changes in the axial dipole moment (ADM) (e.g., Jackson, 1998; Davidson, 2013). Changes to the ADM are then partitioned into slow, average balances and fast, non-equilibrium imbalances. The resulting expression that describes the rate of change of the ADM is analogous to a stochastic differential equation,

$$\frac{dx}{dt} = -\frac{1}{\tau_d}\Big(x(t) - \langle x \rangle\Big) + \Delta S(t), \tag{3.3.5}$$

where x is the ADM, τ_d is the characteristic time-scale of relaxation, and $\Delta S(t)$ represents variations in induction that are not balanced by ohmic dissipation over short timescales.

This conceptual model thus allowed linking the fitted drift and noise functions to physical properties of the geodynamo. The authors suggested that the gradient of the drift reflects the dipole diffusion time, allowing for a prediction of the electrical conductivity of the core, and that the noise reflects the effect of fast-scale helical convective fluctuations that contribute to the dipole field (Moffatt, 1970). However, without a comparison to the internal details of the core, these hypotheses remained untested.

To substantiate the proposed physical mechanisms of Buffett et al. (2013), Buffett et al. (2014) analyzed the output of a numerical geodynamo simulation. The simulation, performed using the 3D implementation "Calypso" from Matsui et al. (2014), produced a stable but time-varying, non-reversing, dominantly dipolar field. It was assumed that the ADM variations could be modeled by an SDE, and the drift and noise functions were fitted to the ADM time-series data from the simulation. These functions indicated a linear drift and constant noise, following a similar form to that of the paleofield from Buffett et al. (2013), except without an increase in the noise at low dipole amplitudes. As the internal details of the fluid flow and magnetic field could be directly accessed in the simulation, the hypothesized physical mechanisms of Buffett et al. (2013) could be investigated. For the drift term, the authors found that the corresponding characteristic timescale (i.e., the gradient of the drift) was shorter that the slowest dipole decay mode. This was surprising, because the time-averaged poloidal field closely matched that of the slowest decay mode. The authors interpreted this faster-than-expected decay rate as a consequence of fluctuations of the first few non-fundamental decay modes, which would augment the average relaxation. The noise term was interpreted to be the manifestation of variations in fast-scale convective action that contribute to magnetic induction. This mechanism, previously invoked in Buffett et al. (2013), was quantified as

$$\overline{\mathbf{v} \times \mathbf{B}} \approx \epsilon B_\phi V_{\text{rms}}^2 l/\eta, \tag{3.3.6}$$

where l is the length scale of a convective column, B_ϕ is the azimuthal magnetic field, V_{rms} is average fluid velocity, and η is the magnetic diffusivity. Variations in the quantities on the right-hand side of (3.3.6) were extracted directly from the simulation, and compared with the fitted amplitude of the noise $\Delta S(t)$ in (3.3.5). The amplitude of the noise term predicted fluctuations in V_{rms} of about $\sim 5\%$, which was consistent with the measured variations of V_{rms}. This empirical verification supported the hypothesized links from the stochastic model to internal core processes. Together with the fits of the drift and noise functions from paleomagnetic models (Buffett et al., 2013), this enabled a quantitative investigation of core processes. Although no direct connection between the drift and a particular mechanism in the core was made, a few interpretations were possible. The characteristic timescale of the drift implied either a low electrical conductivity of the core, diffusion involving the interaction of many decay modes, or alternatively a contribution from turbulent diffusion. As for the noise term, the fitted average amplitude implied velocity variations of approximately 70%, with the hypothesis that these large variations must be necessary for driving polarity reversals. Although the study only analyzed a single numerical geodynamo simulation, it was a key step

towards the investigation of physical processes in the geodynamo using stochastic models.

Validation of the conceptual SDE model of ADM variations was explored in Buffett and Matsui (2015), through analysis of the power spectrum. The authors considered a simplified stochastic model similar to those found in Buffett et al. (2013) and Buffett et al. (2014), i.e., a linear drift and constant noise

$$\frac{dx}{dt} = -\gamma\big(x(t) - \mu\big) + \sqrt{D}\Gamma(t), \tag{3.3.7}$$

where γ is the slope of the drift function (which relates to the characteristic timescale of the process), μ is the zero crossing of the drift (corresponding to the time-average for non-reversing dynamos), D defines the amplitude of noise variations, and $\Gamma(t)$ is Gaussian white noise. This process has a spectrum (after removing the time average) of

$$S_x(f) = \frac{2D}{(\gamma^2 + 4\pi^2 f^2)}, \tag{3.3.8}$$

where f is the frequency. Although this form agreed well with numerical spectra calculated from a sample geodynamo simulation at low frequencies, a discrepancy was found at high frequencies; see Fig. 3.4. Replacing the Gaussian white noise $\Gamma(t)$ with exponentially correlated noise gave a spectrum of

$$S_x^C(f) = \frac{2D\alpha^2}{(\gamma^2 + 4\pi^2 f^2)(\alpha^2 + 4\pi^2 f^2)}, \tag{3.3.9}$$

where $1/\alpha$ is the correlation time of the new, exponentially correlated noise. This resulted in a more accurate representation of the calculated spectra; see Fig. 3.4. In these examples, the stochastic models were fitted from information on short timescales, i.e., conditional moments with a very short time difference. Despite this, the long-scale power spectra were predicted very well. This indicates that the stochastic models are able to reproduce features of the data which were not explicitly used to construct the model.

The validation of the power spectrum reinforced the idea that SDEs are able to adequately reproduce the behavior of axial dipole field variations. Similar comparisons were made between the observed spectrum of the paleofield (e.g., Constable and Johnson, 2005), and the corresponding stochastic models (e.g., Buffett et al., 2013). Buffett and Matsui (2015) also illustrated the necessity of correlated noise to ensure the validity of the model at short time intervals.[4] This SDE perspective for the power spectra has been extended further for the dipole (Sadhasivan and Constable, 2022), as well as for non-dipole field components (Gillet et al., 2013; Bouligand et al., 2016). The addition of correlated noise increased the scope of the stochastic model, allowing for a wider range of situations to which it is applicable. However a physical mechanism for the correlated noise was not investigated.

[4]The presence of correlated noise in both paleomagnetic observations and numerical simulations was also apparent in the calculated conditional moments (e.g., Fig. 3.2, as well as the fact that one expects the rate of change of the ADM to be well-defined at all times.)

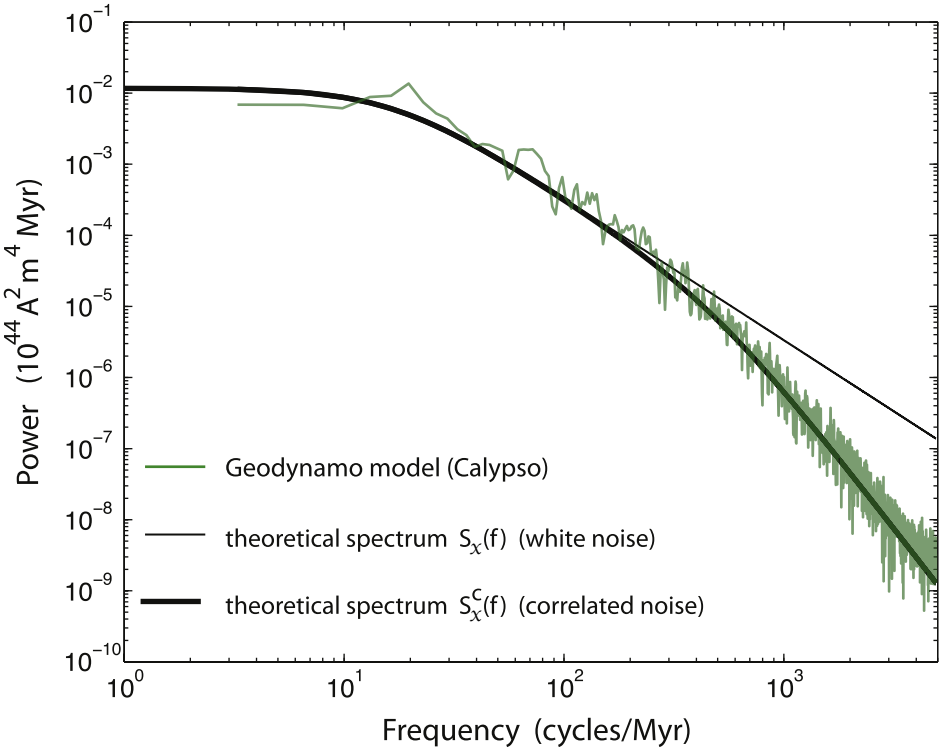

Figure 3.4: Power spectra of axial dipole moments. The numerical spectrum calculated from a sample geodynamo simulation is shown in green. The theoretical spectra for a white noise process and a correlated process are shown as thin and thick black lines, respectively. Adapted from Buffett and Matsui (2015).

Another consideration regarding the connection of stochastic models and paleomagnetic models was considered in Buffett and Puranam (2017). There, two paleomagnetic models covering a range of timescales were considered. These included a record of VADM over the last two million years, PADM2M (Ziegler et al., 2011), and a shorter but finer-resolution record over the last ten thousand years, CALS10k.2 (Constable et al., 2016). The nature of magnetic acquisition in the records was investigated, revealing that the slow processes of sedimentation effectively smoothed out fast-scale variations, adversely impacting the drift and noise functions fitted to the paleomagnetic models. This effect was taken into account in the comprehensive study of Morzfeld and Buffett (2019), where multiple paleomagnetic data sources were used to construct a composite stochastic model for ADM variations. In the future, effort should be made to investigate the use of more diverse paleomagnetic (and archeomagnetic) data sources, especially irregularly sampled observations, in stochastic models.

One other inductive investigation into stochastic models of dipole variations came from Meduri and Wicht (2016). There, the authors extended a set of numerical geodynamo simulations from Kuipers et al. (2009) to investigate the physical origins of the drift and

noise functions. These functions were fitted to the output ADM for each simulation, as in previous studies (e.g., Buffett et al., 2013, 2014). The drift functions were found to be similar to the results from previous numerical simulations Kuipers et al. (2009). However the authors found evidence of increases in the amplitudes of the noise functions at high ADM values. To investigate the physical causes, contributions towards induction and diffusion (governed by the induction equation) were extracted directly from the simulations. The mean action of induction was found to increase linearly at low dipole amplitudes, eventually reaching a quadratic turnover, and decline at larger amplitudes. This form was qualitatively similar to the proposed quenching model of Brendel et al. (2007). This proposed mechanism for the drift term suggested a qualitative behavior of dipole variations aligned similarly to the mean field interpretation of Hoyng et al. (2001). However, a corresponding physical explanation for the amplitude of the noise term was not explored.

These outlined studies illustrate the deductive approach towards constructing stochastic models of the geomagnetic field, for both numerical simulations and paleomagnetic models. Stochastic models are fitted to empirical time-series geomagnetic data, and may be verified through comparison with statistics of the original data that were not used to construct the stochastic model. If the stochastic models are found to reflect the underlying dynamics in simulations, then they may be used to characterize the paleomagnetic record and investigate the state of the Earth's core. Further work should test whether stochastic models generalize to other numerical geodynamo settings and regimes. This is important both for the validity of SDEs as accurate statistical descriptions of field variations, but also for the testing of proposed physical interpretations of the form of the drift and noise functions. Additionally, when attempting to interpret paleomagnetic records, one should bear in mind that these records are not perfect reflections of the geomagnetic field. Further studies should continue to consider the effects of measurement errors, and the physical nature of paleomagnetic recording processes on the fitted stochastic models. Finally, the nature of temporal uncertainty and the effects of smoothing and regularization in paleomagnetic records should be considered carefully.

3.4 Applications of Stochastic Geomagnetic Models

If stochastic models are able to accurately describe statistical variations of geomagnetic field, they may be used to test various hypotheses.

As variations in the dipole field effectively behave like a bistable oscillator (Hoyng et al., 2001), stochastic models provide a method of investigating the properties of reversals. For example, the durations of reversals were considered in Buffett (2015). A stochastic model was able to reproduce the statistics of reversal duration and recovery time, but this model also suggested a change in the efficiency of dipole field generation during reversals. Following from this, Buffett and Avery (2019) considered the effects of temporal resolution in geomagnetic measurements from marine magnetic anomalies (Gee and Kent, 2007; Ogg, 2020). Similar polarity duration statistics were found when the resolution of the stochastic

model was lowered to that of the marine magnetic anomalies. This suggests that many short polarity intervals may be concealed by the effects of slow acquisition. Alternatively, this might reflect the detection limits of ship-tow magnetic surveys.

Stochastic models have also been employed to investigate field phenomena during periods of stable dipole polarity. Buffett et al. (2022) investigated paleomagnetic records that indicated slow, gradual decreases in dipole amplitude punctuated with infrequent, intense periods of amplification, e.g., Fig. 3.5, (Ziegler and Constable, 2011; Avery et al., 2017). It was found that a Langevin-type SDE could not reproduce these asymmetries. However, this feature could be replicated by extending the stochastic model to include discontinuous jumps—or equivalently, noise with non-zero skewness. This skewness was hypothesized to reflect the recurrence statistics of helical convective events (Buffett et al., 2014; Scullard and Buffett, 2018).

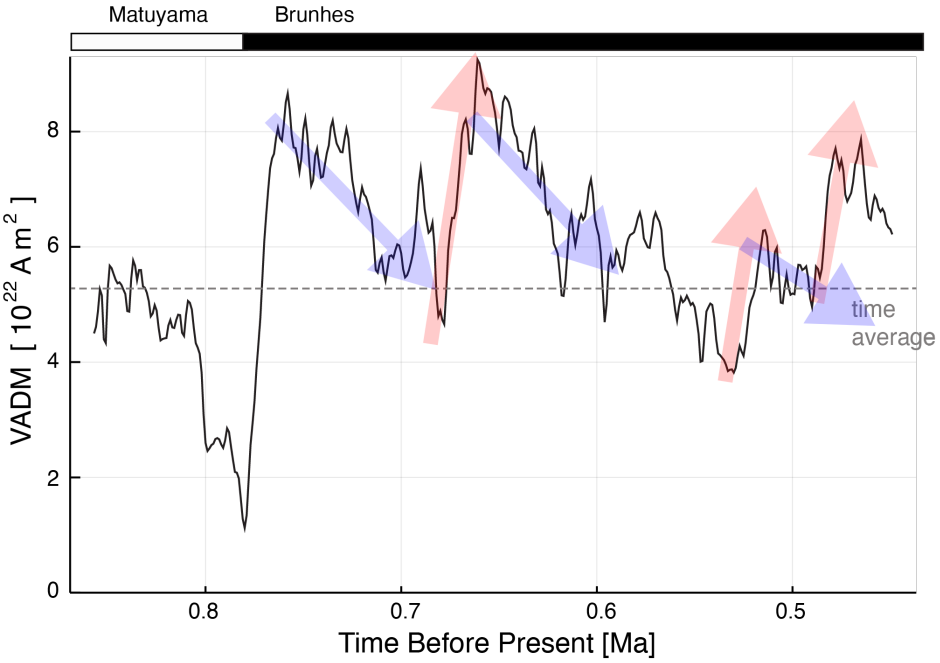

Figure 3.5: The time dependence of axial dipole moment from a section of the PADM2M model (Ziegler et al., 2011). Abrupt increases in VADM (red arrows) are often followed by slower decreases (blue arrows) when averaged over short-period fluctuations. Adapted from Buffett et al. (2022).

As stochastic models give a statistical description of field evolution, they can be used to forecast future states of the geomagnetic field (e.g., Morzfeld et al., 2017; Gwirtz et al., 2021a). One area of interest is an assessment of the likelihood of the next geomagnetic reversal (Constable and Korte, 2006; De Santis et al., 2013; Laj and Kissel, 2015). An example of this appears in Buffett and Davis (2018). From the stochastic model of ADM fitted in Buffett et al. (2013), the evolution of the transition probability backwards in time was in-

vestigated using an adjoint Fokker-Planck equation. In particular, the evolution towards a target set of final conditions was considered. This target set comprised all ADM states of the opposite polarity, i.e., for some unknown initial condition, the final condition corresponds to the ADM being in the target set (reversed). The probability distribution of initial conditions was determined through a numerical solution of the adjoint Fokker-Planck equation. In the context of the modern field, the initial condition is known: the current axial dipole moment is $X = 7.6 \times 10^{22}$ Am^2. With this initial condition, the probability of ending in a reversed polarity after a specified amount of time could be calculated. Considering 20 000 years in the future, this probability was calculated to be very low: a little less than 2%. Extending this interval to 50 000 years increased the likelihood to $\sim 11\%$. These results indicated that an imminent magnetic reversal is unlikely.

The likelihood of reversals was also explored in Buffett et al. (2019), with regard to the variability of the dipole field. In particular, this study investigated the likelihood of sustaining ADM extreme trends. Using the procedure of Nijsse et al. (2019) and considering a stochastic process with a given window length, the expected variance of the slope of that processes was expressed as a function of the window length (Nijsse et al., 2019). This procedure only holds true for a certain class of stochastic processes, namely, Ornstein-Uhlenbeck processes (Uhlenbeck and Ornstein, 1930). At high dipole intensities, ADM variations approximately follow this form; however, at low dipole intensities the drift function drops in amplitude and this model becomes less accurate (Buffett et al., 2013). These differences were determined to be negligible, as the predicted variance compared well with calculations from the paleomagnetic record CALS10k.2 (Constable et al., 2016), a record that was not used in Buffett et al. (2013) to determine the stochastic model. See Fig. 3.6 for an illustration. This analysis allowed for the calculation of the likelihood of the dipole sustaining or exceeding trends of a given slope for a fixed length of time. This was used to assess the historical trend in dipole strength, which has been decreasing since 1840 CE (Malin, 1987). It was determined that the chance of sustaining this trend, given the dipole variations over the last two million years, corresponds to a 2.1σ event—or approximately $\sim 3.6\%$. Extending this trend 1.66 kyr to let it cross into the opposite polarity corresponds to a 6.7σ event—a vanishingly small probability. This suggested that the historical trend is a uncommon but not particularly rare event. Additionally, the chance that this trend might progress unimpeded into a reversal was argued to be very unlikely.

Overall, stochastic models representing variations in the geomagnetic field have been useful tools for testing hypotheses. This is due to the simple, interpretable, and versatile nature of stochastic models. However, their validity as statistical representations of field variations relies on their ability to accurately reproduce observations. So far, numerical and observational studies have indicated that stochastic models are able to reproduce field statistics—regardless of the validity of proposed links to physical mechanisms. This emulative power has been shown both qualitatively and quantitatively (e.g., Buffett et al., 2013; Buffett and Matsui, 2015; Bouligand et al., 2016; Buffett et al., 2022), and long-time-scale statistics are reproduced well even when only short increments are used to construct the model.

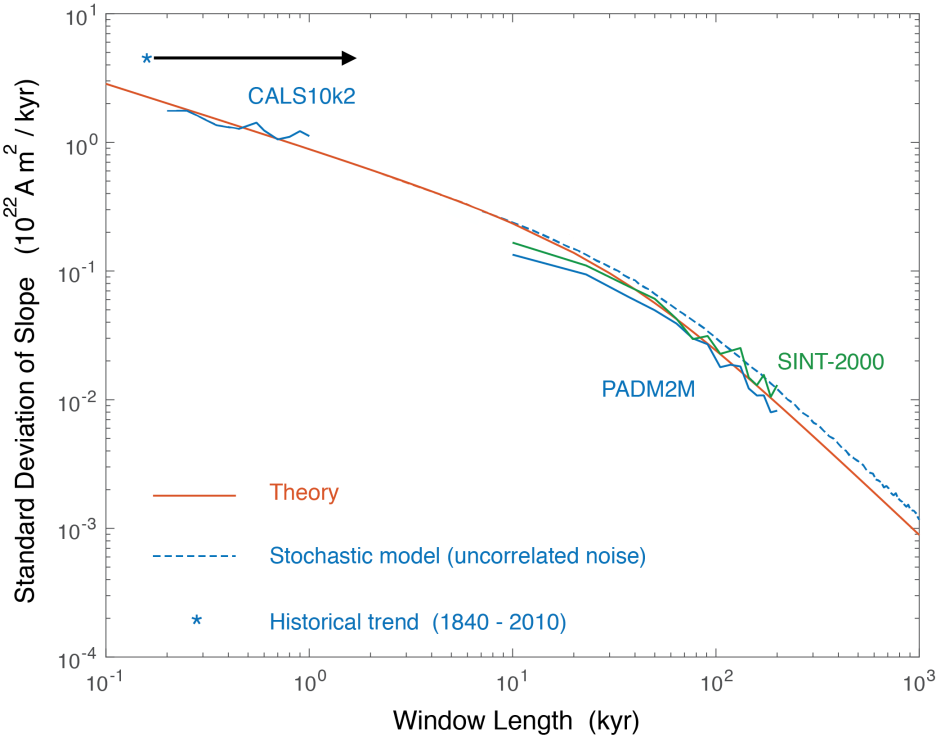

Figure 3.6: Theoretical predictions for the standard deviation of trends, as a function of window length. The analytical prediction and calculated values from a stochastic realization are shown by solid orange and blue dashed lines, respectively. Calculations from several paleomagnetic models (CALS10k.2, PADM2M and Sint-2000) are also included for comparison (Constable et al., 2016; Ziegler et al., 2011; Valet et al., 2005). The historical trend over the last 170 years is shown with a blue star. Extending this trend by 1.66 kyr is indicated by the black arrow. Adapted from Buffett et al. (2019).

3.5 Summary and Proposed Extensions

Stochastic models have been useful for both describing and interpreting geomagnetic field variations. They have been employed as extensions to prior statistical models, and have been used to describe averaged properties of the magnetic field (Gillet et al., 2013; Bouligand et al., 2016). Links from these models to processes in the core have been be proposed and investigated, hypothesizing physical interpretations of external field variations. In the literature, stochastic models have been constructed deductively from mean field dynamo theory (e.g., Hoyng et al., 2001, and subsequent studies), as well as magnetohydrodynamic theory (Scullard and Buffett, 2018). Alternatively, they have been fitted inductively from empirical observations (e.g., Buffett et al., 2013), and links to physical processes have been hypothesized though comparisons with numerical simulations (e.g., Buffett et al., 2014, and subsequent studies). The validity of these models has been investigated though comparisons

with independent statistics (e.g., Buffett and Matsui, 2015). As such, stochastic models attempt to go beyond "toy models" of the geodynamo, providing an interpretable framework with testable, plausible physical foundations.

Although simple SDE models can reproduce many of the statistics of geomagnetic field variations, there is scope for these models to be improved. The majority of examples have been scalar Langevin models, driven by Gaussian white noise. One problem with white noise models is that they do not reproduce the behavior of conditional moments at low time-lags (e.g., Friedrich et al., 2002). To account for the correlation of the noise, the Gaussian white noise may be replaced with a correlated noise source; for example, an exponentially correlated noise (Lehle and Peinke, 2018). Further extensions include the possibility of non-Gaussian noise, which has been proposed by Buffett et al. (2022). The justification of the scalar nature of the stochastic models relies on a separation of timescales between the slow and fast modes in physical systems (Haken, 2013). For the geodynamo, this translates to the idea that the slowest mode of the magnetic field, the fundamental poloidal mode, is a representative "order parameter" which dominates the other, faster fluctuating field components. The validity of this perspective relies on the relative timescales of the magnetic decay modes in the core. Although the timescales for the individual poloidal and toroidal modes both fall off quickly after the fundamental, the ratio between the slowest toroidal and poloidal modes is only $\sim 1/3$ (Gubbins and Roberts, 1987), calling the validity of single-variable Langevin models into question. One option is to extend the dimensions of the stochastic model to explicitly include the toroidal component (e.g., Scullard and Buffett, 2018). Although the toroidal magnetic field cannot exit the core and must be inferred from weak electrical currents (Elsasser, 1947; Roberts and Lowes, 1961), this direction may be promising for the analysis of numerical simulations. Alternatively, another option is to consider the interaction of spatially distinct regions of (or events in) the core (e.g., Narteau et al., 2000; Molina-Cardín et al., 2021). Such an approach represents conceptual or analogical simplifications of processes in the geodynamo. As such, care should be taken to avoid deliberately introducing unrealistic distortions to the model (McMullin, 1985). Adding sufficient complexity to a model can often enable a good fit to empirical observations; however, more complicated stochastic models with additional dimensions or free parameters may not necessarily lead to a better understanding of the underlying mechanisms. As such, future research should continue to verify the physical validity of links between stochastic models of the external field and interior core processes. One way of exploring this is to extend numerical studies, such as Buffett et al. (2014), to wider ranges of geodynamo parameters. If stochastic models can continue to be useful over a wide range of geodynamo regimes, then this gives hope for interpretations of the Earth's paleofield.

Another utility of stochastic models is their capacity to reproduce the statistics of field variations. This has been investigated in the context of numerical simulations (Kuipers et al., 2009; Buffett et al., 2014; Buffett and Matsui, 2015; Meduri and Wicht, 2016; Bouligand et al., 2016) as well as the Earth's magnetic field (Buffett et al., 2013; Gillet et al., 2013). If stochastic models are able to accurately reflect the statistics of field variations, then such models might be useful in predictive settings (Buffett and Davis, 2018; Buffett et al., 2019).

One possibility is to use stochastic models built from short numerical dynamo simulations to predict asymptotic statistical quantities. This might enable the estimation of quantities of interest, such as reversal rates, from high-resolution simulations without excessive computational cost, greatly aiding systematic searches for Earth-like geodynamo simulations (e.g., Kutzner and Christensen, 2002; Christensen and Aubert, 2006; Christensen, 2011).

Finally, with regard to analysis of the Earth's magnetic field, a range of paleomagnetic records have been studied through the use of stochastic models. The timescales in these records range from thousands of years (e.g., Constable et al., 2016), millions of years (e.g., Ziegler et al., 2011; Valet et al., 2005), to tens of millions of years (e.g., Ogg, 2020). Future work should attempt to bridge these with records of intermediate ranges of about $\sim 10^5$ years (e.g., Panovska et al., 2018). Records from both paleomagnetic and archaeomagnetic measurements should continue to be studied (Panovska et al., 2019). Particular effort should be made to investigate the effects of averaging that result from slow magnetic acquisition in sedimentary records (Buffett and Puranam, 2017). Related to this, the effects of measurement noise and temporal uncertainty should also be investigated carefully. Methods should also be developed to fit stochastic models from unevenly sampled records. Such methods would also help the integration of multiple diverse sets of data together into comprehensive models (e.g., Morzfeld and Buffett, 2019).

Chapter 4

Inferring Core Processes Using Stochastic Models of the Geodynamo

Foreward

In this chapter, I address the main focus of this thesis and investigate stochastic models of the geodynamo. I fit stochastic models to a set of numerical geodynamo simulations, and investigate how the underlying physical processes are represented in elements of the stochastic models. As the major work of this thesis, this chapter aims to lay the foundations for both the fitting of stochastic models of the geodynamo, the validation of such models, as well as the physical interpretations.

This work has been previously published in:

W. Davis and B. Buffett (2021). "Inferring core processes using stochastic models of the geodynamo". *Geophysical Journal International* 228.3, pp. 1478–1493, DOI: 10.1093/gji/ggab412.

Summary

Recent studies have represented time variations in the Earth's axial magnetic dipole field as a stochastic process, which comprises both deterministic and random elements. To explore how these elements are affected by the style and vigour of convection in the core, as well as the core-mantle boundary conditions, we fit stochastic models to a set of numerical dynamo simulations at low Ekman numbers. The deterministic part of the stochastic model, the drift term, characterises the slow relaxation of the dipole back to its time-average. We find that these variations are predominantly accommodated by the slowest decay mode, enhanced by turbulent diffusion to enable a faster relaxation. The random part—the noise term—is set by the amplitude and timescale of variations in dipole field generation, including contributions from both velocity and internal magnetic field variations. Applying these interpretations to the paleomagnetic field suggest that reversal rates are very sensitive to rms variations in the field generation. Less than a 50 per cent reduction in rms field generation variations is sufficient to prevent reversals for the recent magnetic field.

4.1 Introduction

The geodynamo is a complex and chaotic system. Its dynamics are governed by the equations of magnetohydrodynamics; the interplay between fluid motions in the liquid core and an existing magnetic field generate a self-sustaining magnetic field (Roberts and King, 2013). Paleomagnetic evidence shows this field has existed for most of Earth's history, whilst also exhibiting variations over a broad range of timescales. Linking variations in the field to core processes can give us insights into the state of the interior of the Earth throughout geological history. On these long timescales, compilations of paleomagnetic and archeomagnetic observations are insufficient in spatial and temporal resolution to reconstruct the full field. Instead, observations of magnetic direction and intensity are translated to virtual geomagnetic poles (VGPs) and the virtual axial dipole moments (VADMs) under the assumption that the geomagnetic field is represented as a time-averaged geocentric axial dipole (Valet et al., 2005; Ziegler et al., 2011). Furthermore, complete polarity reversals of the dipole field have occurred, and the rate of reversal frequency has been shown to change throughout geological time (Johnson et al., 1995). These reversal rates, along with variations in VGPs and VADMs, record valuable information about the interior of the core. However, direct links to physical processes are unclear.

One method of investigating field variations is through statistical models. Constable and Parker (1988) explored variations of the spherical harmonic components of the field through time. These components are described by Gaussian distributions with zero means for non-dipole components, and a bimodal distribution for the axial dipole. Refinements of this approach have been proposed (e.g., Quidelleur and Courtillot, 1996; Constable and Johnson, 1999; Bono et al., 2020, and references therein), however physical interpretations of the distributions and correlations between components has not been directly established.

Another approach interprets the changing VADM as a stochastic process (Brendel et al., 2007; Buffett et al., 2013; Morzfeld and Buffett, 2019). Stochastic models are commonly used to describe changes to a small set of variables in large and complex physical systems, including chemical reactions (Van Kampen, 1992; Haken, 2013), turbulent fluid flows (Renner et al., 2001), electrical systems (Friedrich et al., 2000), wind variability (Sura and Gille, 2003), and climate dynamics (Nicolis and Nicolis, 1981). For comprehensive review of applications, the reader is referred to Friedrich et al. (2011). Specifically, previous studies have interpreted VADM variations as the result of a stochastic differential equation (SDE). These SDEs have two main components. The first is an expression that governs the slow deterministic adjustment towards equilibrium states, often referred to as the drift term. The second expression governs the amplitude of random fast-scale fluctuations, and is called the noise term. Speculations that the physical causes of changes in VADM can be partitioned into these two components are motivated by the goals of finding a simple model of dynamics and to attach physical meaning to this model.

Insights into the physical significance of stochastic models of VADM variations can be gained by examining results from numerical dynamo models (Kuipers et al., 2009; Buffett et al., 2014; Meduri and Wicht, 2016). For numerical models—unlike the paleomagnetic record—we can directly access the details of the flow and magnetic field within the core. This information can be used to draw inferences as to how stochastic models link to physical processes in the geodynamo.

In this study, we examine the time variations in axial dipole moment (ADM) for a suite of numerical geodynamo simulations with different control parameters and boundary conditions. Specifically, we investigate two end-member cases: (1) dynamos driven by buoyancy at both the core-mantle boundary (CMB) and the inner core boundary (ICB); and (2) dynamos solely driven from the ICB. From these simulations we fit stochastic models, which are then compared with outputs of the internal dynamics of the geodynamo models, in the aim of developing tools to quantitatively interpret variations in the paleomagnetic record. Section 4.2 begins with a description of the numerical geodynamo model and outlines the set of regimes and parameters investigated. We use these data in Section 4.3 to fit stochastic models following a new method (Lehle and Peinke, 2018) that explicitly accounts for correlated noise. Results for the fitted stochastic models are presented in Section 4.4. Detailed outputs from the numerical models are then used to investigate the physical significance of the stochastic models in Section 4.5. We explore the implications for interpreting the paleomagnetic record in Section 4.6, and conclude in Section 4.7 with a summary of our findings.

4.2 Geodynamo Simulations using Calypso

Numerical geodynamo models are important tools for exploring the processes of convection and magnetic-field generation in the Earth's core. While these models operate at conditions far from those of the Earth, much of the underlying dynamics is thought to be representative (e.g., Aubert, 2019). Using the geodynamo model Calypso (Matsui et al., 2014) we

consider two end-member model configurations, which extend the boundary conditions and styles of convection explored in Buffett et al. (2014). In the first configuration, convection is driven by maintaining a fixed temperature difference, ΔT, across a spherical shell with thickness L. Buoyancy is generated at both boundaries, driving convection from above and below. The second configuration has convection driven solely by buoyancy at the lower boundary, and the heat flow is sustained across the lower boundary by using volumetric heat sink, Qt, in combination with a no-heat-flow condition at the top boundary.

Solutions are specified using five dimensionless parameters. The vigour of convection is specified by a modified Rayleigh number

$$\mathrm{Ra} = \frac{\alpha g(r_{\mathrm{cmb}})\Delta T L}{\nu \Omega}, \tag{4.2.1}$$

where α is the coefficient of thermal expansion, $g(r)$ is the radially dependent gravity, ν is the kinematic viscosity, and Ω is the angular velocity about the $\hat{z}$ axis. The Ekman number

$$\mathrm{Ek} = \frac{\nu}{\Omega L^2}, \tag{4.2.2}$$

defines the relative importance of viscous forces to the leading-order Coriolis force. The Prandtl number

$$\mathrm{Pr} = \frac{\nu}{\kappa}, \tag{4.2.3}$$

and magnetic Prandtl number

$$\mathrm{Pm} = \frac{\nu}{\eta}, \tag{4.2.4}$$

define the ratio of viscosity to thermal κ and magnetic η diffusivities, respectively. The final dimensionless parameter is the heat sink, Qt, which controls the style of convection (e.g., Kutzner and Christensen, 2002). Setting $\mathrm{Qt} = 0$ causes the heat flow at the top and bottom boundaries to be equal. Increasing the heat sink lowers the heat flow at the top boundary under constant temperature boundary conditions. Combining a heat sink with a no heat-flux condition at the top boundary ensures that convection is driven entirely from below. In this case the amplitude of the heat flow at the lower boundary is set by Qt. The mantle and inner core are assumed to be electrically insulating. In all experiments we let $\mathrm{Ek} = 5 \times 10^{-5}$, $\mathrm{Pr} = 1$, and $\mathrm{Pm} = 1$. Two different values of Ra are investigated for each configuration. The configuration is selected by the value of Qt and the choice of boundary conditions. Setting $\mathrm{Qt} = 0$ with constant temperature conditions defines the top and bottom-driven configuration. In the basal-driven configuration we set Qt to the value needed to reproduce the basal heat flow in the top and bottom-driven configuration. This choice facilitates comparisons between the two configurations.

Simulation time is scaled by the viscous diffusion time, L^2/ν. Conversion to physical time is accomplished by setting a realistic magnetic diffusivity $\eta = 0.8\ \mathrm{m^2\ s^{-1}}$, which gives $\nu = \eta \cdot \mathrm{Pm} = 0.8\ \mathrm{m^2\ s^{-1}}$ and a viscous diffusion time of 202 kyr. The magnetic field is

Table 4.1: Dynamo model control parameters

Run name	$\frac{\partial T}{\partial r}\big\vert_{r_{\rm cmb}}$	Ra	Qt	Δt	$t_{\rm max}$
TB0	-1.8	1000	0	2×10^{-4}	2.11
TB00	-1.8	1000	0	2×10^{-4}	2.01
TB1	-2.2	1200	0	2×10^{-4}	2.22
B2	0	1100	-3.66	5×10^{-4}	8.53
B3	0	1300	-4.32	2.5×10^{-4}	4.06

converted to physical units using the magnetic scale $\sqrt{\rho\mu\eta\Omega}$, where ρ is the fluid density, μ is the permeability of free space, and Ω is the rotation rate. Setting $\rho = 10^4$ kg m^{-3}, $\mu = 4\pi \times 10^{-7}$ H m^{-1}, and $\Omega = 0.73 \times 10^{-4}$ s^{-1}, gives a magnetic scale of 0.86 mT.

We run five dynamo simulations with different sets of control parameters (see Table 4.1). Cases with the prefix "TB" represent the first configuration, where convection is driven from the top and bottom boundaries. Cases with the prefix "B" represent the second configuration, where convection is driven from the bottom boundary. The numbers in each case distinguish between different values for Ra. The cases TB0, TB00 and B2 represent the lower value of Ra and are referred to as "low Ra states", whereas cases TB1 and B3 are run at higher Ra, and are referred to as "high Ra states". Cases TB0 and TB00 share the same control parameters but are initialized from a different starting conditions. We use these results to confirm that these stochastic models can be fitted from independent numerical solutions.

A fixed dimensionless time step δt is used for the calculations. A summary output is recorded every $\Delta t = 1000 \times \delta t$. Each solution is run until equilibrated and subsequently recorded after transients for at least 2 viscous diffusion times, indicated as $t_{\rm max}$ in Table 4.1. We found that 2 diffusion times was sufficient for the convergence of the system for the top and bottom driven dynamos, whereas the bottom driven cases required longer simulation time to achieve stable results.

All dynamo solutions produce a stable non-reversing but time-varying dominantly dipole field. We record the Gauss coefficient $g_1^0(r,t)$ at the Earth's surface $r = a$ and convert to ADM using

$$X(t) = \frac{4\pi}{\mu} g_1^0(a,t) a^3. \tag{4.2.5}$$

Fig. 4.1 shows the axial dipole moment for all simulations in this study. Diagnostic parameters are shown in Table 4.2. Although these dynamo models produce flows that are slow compared to the Earth, they are still in a realistic regime as there is a significant separation of timescales between slow magnetic diffusion and fast turbulent fluctuations. Furthermore, the ratios of magnetic to kinetic energies in the models spans the range $\sim$ 3–7. These are higher than unity, indicating that Lorentz forces are stronger than inertia or viscosity, suggesting that the models are in the suitable Magneto-Coriolis-Archimedes (MAC)

Table 4.2: Dynamo model diagnostic parameters. Here X is the ADM, $V_{\rm rms}$ is the volume averaged root mean squared (rms) velocity, $V^{\rm p}_{\rm rms}$ is the volume averaged rms poloidal velocity, $B_{\rm rms}$ is the volume averaged rms magnetic field, $T(r_{\rm cmb})$ is the temperature at the CMB, $\frac{\partial T}{\partial r}\big|_{r_{icb}}$ is radial temperature gradient at the ICB. The ADM has units of 10^{22}Am^2, and all other values are non-dimensional. Mean values are reported, with standard deviations in brackets. Reported units are 10^{22} A m^2 for ADM, and non-dimensional for the rest.

Run name	X	$V_{\rm rms}$	$V^{\rm p}_{\rm rms}$	$B_{\rm rms}$	$T(r_{\rm cmb})$	$\frac{\partial T}{\partial r}\big\|_{r_{icb}}$
TB0	14.12(0.69)	135.3(7.8)	73.6(4.9)	2.45(0.10)	-0.13	-14.8
TB00	14.36(0.74)	133.8(8.1)	72.4(5.0)	2.47(0.14)	-0.14	-14.7
TB1	14.35(0.84)	164.9(9.2)	91.6(5.8)	2.57(0.15)	-0.19	-18.0
B2	8.77(0.37)	129.2(6.8)	65.1(4.0)	1.719(0.088)	0.029	-14.7
B3	9.60(0.45)	150.2(7.8)	78.7(4.7)	1.853(0.093)	0.010	-17.3

force balance regime (Schwaiger et al., 2019; Aubert, 2019). We use these simulations in the next section to fit stochastic models.

4.3 Stochastic Model for Dipole Fluctuations

Stochastic models can be fitted to simulations of the underlying process by using statistical methods. We outline the basic methods in this section, explicitly accounting for correlated noise in the description of the stochastic model. We account for this complication in the methodology used to fit the parameters of a stochastic model.

Overview of Stochastic Models

Time evolution of the ADM, $X(t)$, is modeled by the stochastic differential equation

$$\frac{d}{dt}X = v(X) + g(X)\zeta(t), \tag{4.3.1}$$

where $v(x)$ and $g(x)$ are the drift and noise functions, respectively. The drift and noise functions are independent of time, reflecting the fact that the simulations have no long-term secular evolution or forcing. The $\zeta(t)$ term is the noise that drives the system; it is defined to have a vanishing time average

$$\langle \zeta(t) \rangle = 0. \tag{4.3.2}$$

The autocorrelation of the noise, $\langle \zeta(t)\zeta(t') \rangle$, defines the duration of fast-scale fluctuations. It is common to assume that the system is driven by white noise, where the correlation becomes $\delta(t-t')$. A more realistic description of the noise term for a geodynamo model allows for a short but finite duration fluctuation, where the autocorrelation of $\zeta(t)$ is set by

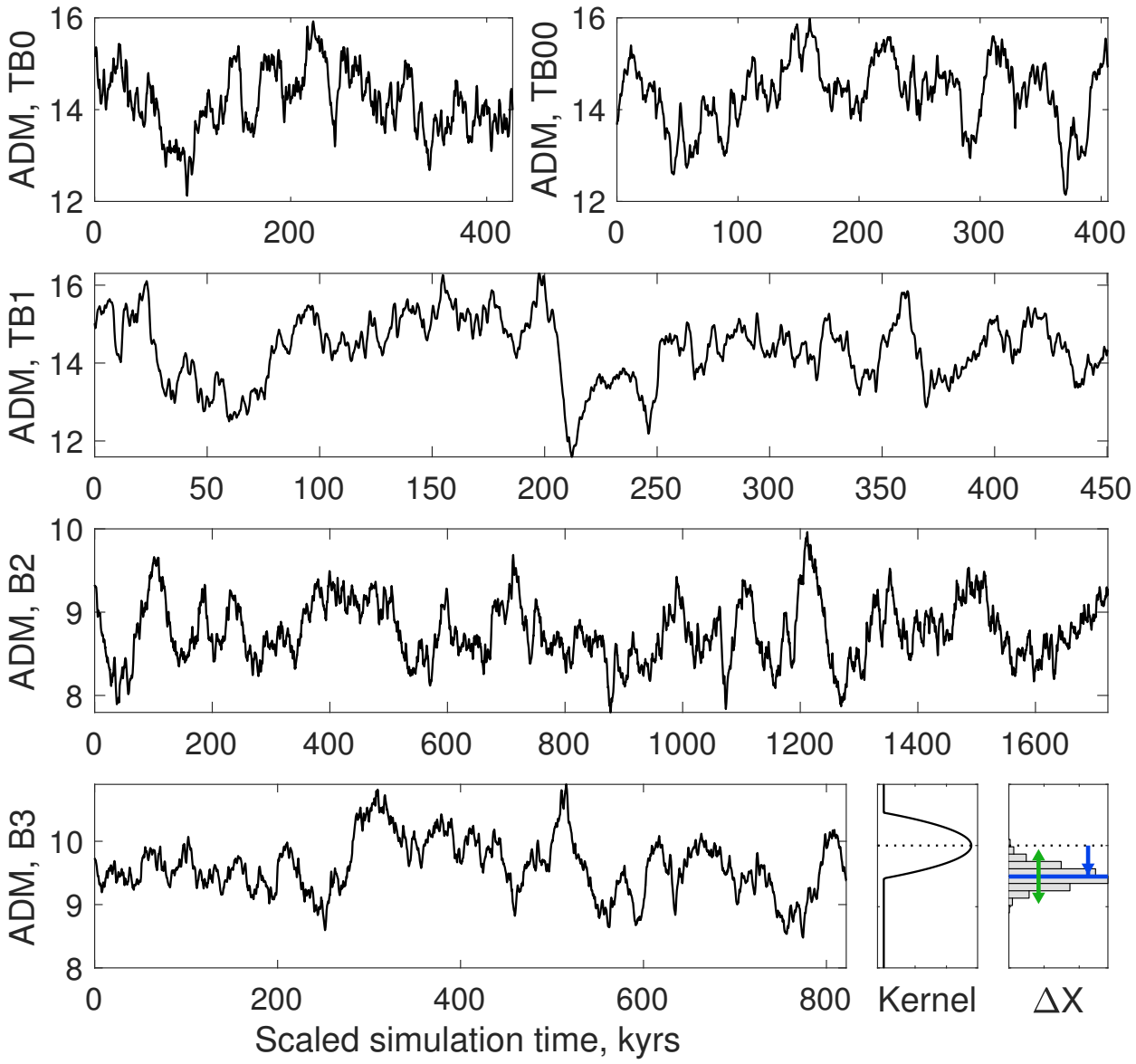

Figure 4.1: Axial dipole moment (in units $10^{22}\mathrm{Am}^2$) for all simulations in this study. The last two panels on the bottom right show a sketch of how moments (4.3.7)–(4.3.8) are estimated from the time-series data. The sketch illustrates calculations for conditioning on $x = 10$, indicated by a dashed line. The left panel shows the kernel used to weight the increments, equation (A.0.3). The right panel shows an example of increments ΔX that are subsequently weighted by the kernel and then averaged. The difference between mean, indicated by the blue arrow and line, is caused by the drift. The spread of the increments, indicated by the green arrows, is caused by the noise. The offset and spread of the increments has been exaggerated here for visual purposes.

$$\langle \zeta(t)\zeta(t')\rangle = \frac{1}{2\theta} e^{-|t-t'|/\theta}, \tag{4.3.3}$$

where θ defines the correlation time. In the limit $\theta \to 0$, the white noise model is recovered. Use of correlated noise gives (4.3.1) the desirable property of well defined time derivatives, and gives the appropriate high-frequency spectra (Buffett and Matsui, 2015; Bouligand et al., 2016). The time dependence of $\zeta(t)$ is given by (Jazwinski, 2007)

$$\frac{d}{dt}\zeta = -\frac{1}{\theta}\zeta + \frac{1}{\theta}\xi(t), \tag{4.3.4}$$

where $\xi(t)$ is Gaussian white noise with $\langle \xi(t)\rangle = 0$ and $\langle \xi(t)\xi(t')\rangle = \delta(t-t')$.

A simulation of the stochastic model for dipole fluctuations is obtained by numerically integrating (4.3.1) and (4.3.4) using a random realization of the white noise $\xi(t)$. The inverse problem fits $v(x)$, $g(x)$, and θ to time series of $\{X(t_j)\}$ $j = 1, \ldots, N$, where N denotes the number of data points, from the dynamo model.

Fitting Method

To fit drift and noise terms of ADM or VADM variations, many previous studies (e.g., Buffett et al., 2013, 2014; Buffett and Matsui, 2015; Meduri and Wicht, 2016) have used a method known as "direct estimation" (Siegert et al., 1998). However it is known that this method systematically underestimates the drift and noise terms in the presence of correlated noise in synthetic tests (Friedrich et al., 2002). Therefore we seek to investigate this problem using a robust non-parametric method that intrinsically accounts for correlated noise. We apply the method of Lehle and Peinke (2018) to fit the stochastic model. Sample increments in the time series are calculated using

$$\Delta X(t; x, \tau) \equiv \lfloor X(t+\tau) - X(t) \rfloor_{X(t)=x} \tag{4.3.5}$$

where τ defines the chosen sampling interval. We refer to ΔX as a conditional increment because it depends on the condition that $X(t) = x$. Statistical averages of these conditional increments will be governed by the drift and noise functions. To the first order, the means and variances of ΔX evaluated at a condition x are "directly" equal to the values of drift and noise functions at that condition, respectively (Siegert et al., 1998). For our purposes, a more robust alternative is to find optimal drift and noise functions by comparing averages of increments from data with theoretical expectations (Honisch and Friedrich, 2011; Lehle and Peinke, 2018). In practice the increments are grouped together when $X(t)$ lies within a prescribed bin (say $x_- < X(t) < x_+$). Each ΔX in the bin is usually assigned equal weight. Alternatively, we can compute sample increments using kernels that weight increments according to the difference between $X(t)$ and the condition $X(t) = x$ (Lamouroux and Lehnertz, 2009). In this case the increment is given by

$$\Delta X(t; x, \tau, h) = W(X(t); x, h)[X(t+\tau) - X(t)], \tag{4.3.6}$$

where the weight, $W(X(t); x, h)$, depends on the difference in x and $X(t)$, as well as the kernel bandwidth h (see Appendix A for details). The sample mean and variance of these conditional increments represent estimates of the first two moments

$$\widehat{M}^{(1)}(x,\tau;h) = \big\langle \Delta X(t;x,\tau,h) \big\rangle, \tag{4.3.7}$$

$$\widehat{M}^{(2)}(x,\tau;h) = \big\langle [\Delta X(t;x,\tau,h) - \widehat{M}^{(1)}(x,\tau;h)]^2 \big\rangle, \tag{4.3.8}$$

where the hat indicates these are estimates depending on time series $X(t)$ and kernel properties, and $\langle \dots \rangle$ indicates time averaging. The bottom right two panels of Fig. 4.1 give an illustration of how these moments are calculated. In the direct estimation method, these moments are directly related to the drift and noise functions, by

$$v(x) = \lim_{\tau \to 0} \frac{1}{\tau} \widehat{M}^{(1)}(x,\tau;h), \tag{4.3.9}$$

$$g(x) = \sqrt{\lim_{\tau \to 0} \frac{1}{\tau} \widehat{M}^{(2)}(x,\tau;h)}, \tag{4.3.10}$$

and the limit is approximated by evaluating the moments at some small evaluation time τ. However in the presence of correlated noise, the above method fails since moments (4.3.7-4.3.8) vanish as $\tau \to 0$ (see Fig. 4.2). Instead, Lehle and Peinke (2018) used a stochastic Itô-Taylor series expansion (Kloeden and Platen, 2013) of $X(t+\tau)$ to show that the expected value of the first two moments $M^{(k)}(x,\tau)$ of an arbitrary SDE defined by (4.3.1) and (4.3.4) can be represented in the form

$$M^{(k)}(x,\tau) \approx \sum_{i=1}^{3} \lambda_i^{(k)}(x) r_i(\tau;\theta), \quad k = 1, 2, \tag{4.3.11}$$

where terms $\mathcal{O}(\tau^4)$ and higher are omitted. Functions r_i are prescribed basis functions

$$\begin{aligned} r_1(\tau;\theta) &= \tau - \theta(1 - e^{-\tau/\theta}), \\ r_2(\tau;\theta) &= \tau^2/2 - \theta r_1(\tau;\theta), \\ r_3(\tau;\theta) &= \tau^3/6 - \theta r_2(\tau;\theta), \end{aligned} \tag{4.3.12}$$

and $\lambda_i^{(k)}(x)$ are the corresponding coefficients. A linear combination of these three basis functions approximate the first and second moments when the sampling interval is small. Note that basis function $r_1(\tau,\theta)$ depends linearly on the small time scales τ and θ, whereas $r_2(\tau,\theta)$ depends on τ^2, as well as $\tau\theta$ and θ^2. We can think of the basis functions in (4.3.12) as terms of a power series expansion in these two small timescales. The coefficients $\lambda_i^{(k)}(x)$ define the amplitude of the moments at different values for x. The goal is to recover estimates for $\lambda_i^{(k)}(x)$ when the moments are computed at discrete values for x and τ.

A separate estimation for θ is based on autocorrelation of $X(t)$. The procedure of Lehle and Peinke (2018) relies on an expansion of the autocorrelation function in terms of the same three basis functions (4.3.12). Details are deferred to Appendix B so we proceed with the estimation of the coefficients $\lambda_i^{(k)}(x)$ assuming that θ is known. When referring to a specific estimate of the correlation time, the symbol $\hat{\theta}$ will be used.

We compare the expected value of the moments in (4.3.11) against estimates (4.3.7-4.3.8) using a set of evaluation points in x and τ. Let the discrete vector of evaluation points in x be denoted by the vector

$$\mathcal{X} = (x_{\min}, \ldots, x_{\max}). \tag{4.3.13}$$

These evaluation points are analogous to bin centers. Similarly, we consider a discrete vector of sampling intervals, τ, starting with $\tau = \Delta t$. We denote the set of sampling times by

$$\mathcal{T} = (\Delta t, 2\Delta t, \ldots, \tau_{\max}) \tag{4.3.14}$$

where $\tau_{\max}$ should be large enough to separate the τ^1, τ^2 and τ^3 terms in the power series expansion of $M^{(k)}(x,\tau)$, but small enough to justify the neglection of $\mathcal{O}(\tau^4)$ and higher-order terms in (4.3.11).

Discrete values for estimates of the first two moments are computed from the time series using (4.3.7- 4.3.8) and are represented in matrix form by the symbol $M_{ij}^{(k)}$, which is defined by equation (C.0.1) in Appendix C. Similar notation is used for basis functions (4.3.12), R_{il}, and corresponding coefficients, $\lambda_{lj}^{(k)}$, which are defined by equations (C.0.2) and (C.0.3), respectively. This allows for (4.3.11) to be written in matrix form

$$M_{ij}^{(k)} = R_{il}\lambda_{lj}^{(k)} \tag{4.3.15}$$

where summation over the repeated index $l = 1, 2, 3$ refers to the three basis functions. Now the linear equations in (4.3.15) can be solved for coefficients $\lambda_{lj}^{(k)}$ using the method of least squares, e.g.,

$$\lambda_{lj}^{(k)} = \left(R_{li}R_{il}\right)^{-1} R_{li}M_{ij}^{(k)}. \tag{4.3.16}$$

The final step is to relate the coefficients $\lambda_{lj}^{(k)}$ to the terms in the SDE. Lehle and Peinke (2018) showed that the $l = 1$ coefficients are related to the drift and noise functions by

$$\begin{aligned} v(x) =& \lambda_1^{(1)}(x) - \frac{1}{2}g(x)g'(x) - \frac{1}{2}\theta\Big(v'(x)g(x)g'(x) - v(x)g'(x)^2\Big), \\ g(x) =& \sqrt{\lambda_1^{(2)}(x) - \theta\Big(v'(x)g(x)^2 - v(x)g(x)g'(x)\Big)}. \end{aligned} \tag{4.3.17}$$

These expressions are accurate to the order of the series expansion in (4.3.11). We solve the two differential algebraic equations in (4.3.17) for $v(x)$ and $g(x)$ using a fixed point iteration scheme. Spatial derivatives are evaluated using finite differences.

This fitting method has the advantage of intrinsically accounting for the correlation of the noise. This is in contrast to direct estimation method, where one can attempt to minimise the effects of correlation by selecting (*a posteriori*) a single evaluation time τ that is large compared to the correlation time. However, if the correlation time is not sufficiently small compared with the slow relaxation time the direct estimate will always underestimate the true values in synthetic tests (Friedrich et al., 2002). In the geodynamo models the correlation times are typically a few percent of the slow relaxation time, large enough to cause substantial discrepancies in the fitted stochastic model. It is important to note that the fitting method of Lehle and Peinke (2018) does not provide advantages regarding measurement noise or temporal averaging associated with paleomagnetic observations. For such data, methods tailored to be preferentially sensitive to longer period features (e.g., time-averaged mean, variance, power spectra, reversal rate, etc...) as opposed to small time increments are more suitable (Buffett and Puranam, 2017; Morzfeld and Buffett, 2019). However, a key advantage of the new method is that sampling over a range of time-lags greatly increases the amount of information used to determine outputs (Honisch and Friedrich, 2011). Lehle and Peinke (2018) showed that this method accurately recovers the drift and noise functions, as well as the correlation time, with typical mean relative errors of about 10^{-4} for numerically simulated SDEs. This method is now applied to the data from our dynamo simulations.

Application of Fitting Method

We apply the method described in the previous section to each ADM time-series from our dynamo simulations. Each calculation requires a choice for the bandwidth, h, and the maximum time-shift, $\tau_{\max}$. Values are reported in Table 4.3. Bandwidth h is selected using equation (A.0.7). The maximum time-shift $\tau_{\max}$ is chosen to be large enough to separate the τ^1, τ^2 and τ^3 terms in the power series expansion of $M^{(k)}(x,\tau)$, but small enough to justify the neglection of $\mathcal{O}(\tau^4)$ and higher-order terms in (4.3.11). The fitted stochastic model is not overly sensitive to the choice of h and $\tau_{\max}$. It suffices to round h to 2 significant figures and $\tau_{\max}$ to the nearest multiple of $50\Delta t$. For all cases, we choose the sampling of $\mathcal{X}$ as 50 evenly spaced points between $x_{\min}$ and $x_{\max}$, which are set by 2.5^{th} and 97.5^{th} percentiles of the time series, respectively. When comparing this method with the direct estimation method, we choose evaluation times τ in the range $[0, \tau_{\max}]$ that give maximal values for the resulting drift and noise functions.

Fig. 4.2 shows the sample moments for case B3 superimposed on the functional fit from (4.3.11), as well as the sample autocorrelation of B3 against the functional fit. Similar plots for the other simulations are available in the supplementary material (Figs D.1-D.3). For all cases the fit is excellent, having an average mean error comparable to the calculations of Lehle and Peinke (2018). In the next section the drift and noise functions will be determined from functional fits of $\lambda_i^{(k)}(x)$.

Table 4.3: SDE fit parameters

Run name	Bandwidth, h	$\tau_{\max}$
TB0/TB00	0.38	$400\Delta t$
TB1	0.54	$300\Delta t$
B2	0.16	$300\Delta t$
B3	0.24	$300\Delta t$

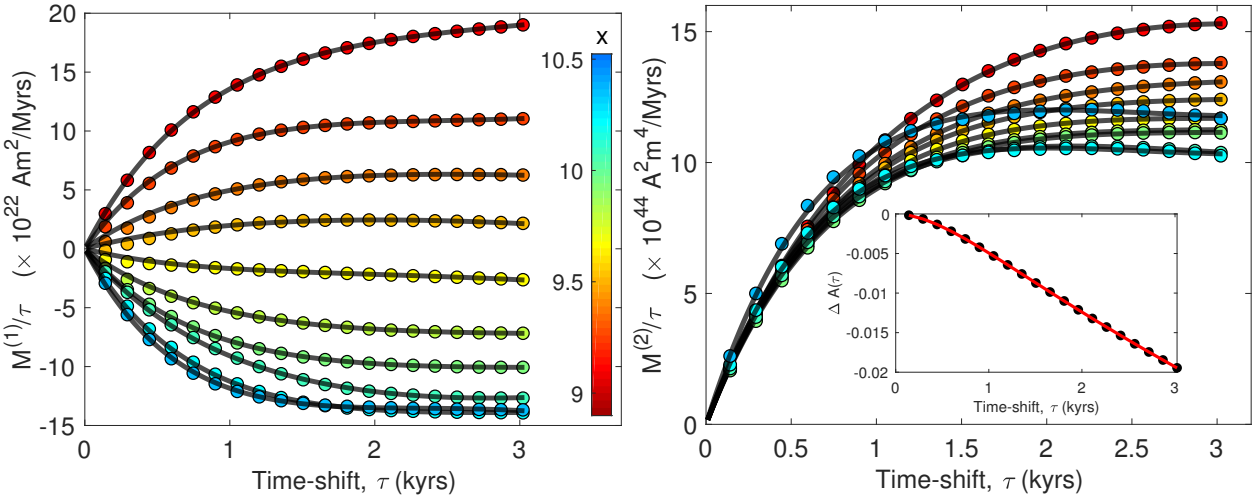

Figure 4.2: First (left) and second (right) moments for dynamo case B3. Colored circles indicate calculated moments from equations (4.3.7-4.3.8), and black lines indicate the model best fit by equation (4.3.11). The color of the circles in both plots corresponds to the evaluation point x for the moment calculation, and is indicated by the colorbar in the left plot. For plotting clarity, moment data from every 5th $\mathcal{X}$ evaluation point and every 15th $\mathcal{T}$ evaluation point are plotted. The inset in the right plot shows the sample autocorrelation increments calculated from equation (B.0.2) and the model best fit by equation (B.0.3), as black circles and a red line, respectively. Data from every 15th $\mathcal{T}$ evaluation point is plotted.

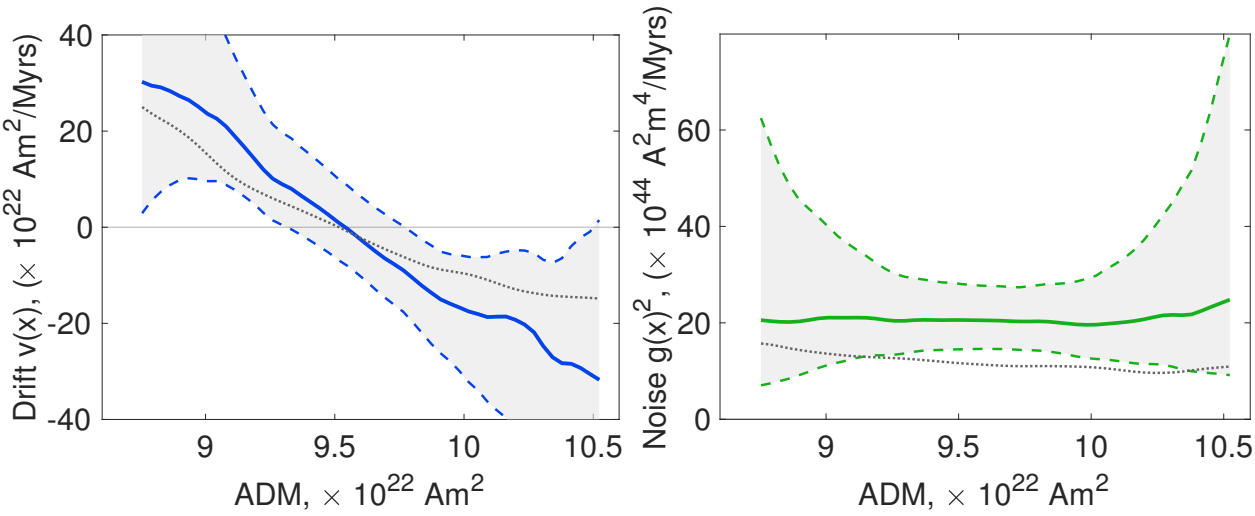

Figure 4.3: Drift (left) and noise (right) functions fitted from case B3. Solid colored lines indicate the fitted functions, and dashed colored lines enclosing shaded areas indicate 95% confidence intervals, estimated with a block bootstrap algorithm using 10 000 resamples (Kunsch, 1989). Dotted grey lines indicate results calculated from the direct estimation method.

4.4 Results

Broadly similar stochastic models are found for each dynamo simulation. We show the drift and noise for case B3 as a representative example (see Fig. 4.3). Similar plots for the other simulation are available in the supplementary material (Figs D.4-D.6). Separate analysis of the shorter TB0 and TB00 cases produced results that were consistent within the uncertainties. Consequently, we combined these cases and analyzed them together.

These results here can be compared with fits using the direct estimation method (Buffett et al., 2013, 2014; Buffett and Matsui, 2015; Meduri and Wicht, 2016). Since the correlation times are not small, the direct estimation predicts drift and noise functions that are at all points absolutely lower than the fits derived from the method of Lehle and Peinke (2018). For the drift term, these fits are usually within the 95% bootstrapped confidence intervals (Kunsch, 1989). On the other hand, fits for the noise term are often outside the confidence intervals. Similar results are observed when using the average between pairs of fits (Stanton, 1997), as in Buffett et al. (2013).

All cases are well approximated by a linear drift term and a constant noise term. A finite correlation time is found for the noise source, which confirms that a white noise approximation is not suitable at these short sampling intervals. The form of the drift and noise terms suggest a parameterised model for the variations in ADM

$$\frac{d}{dt}X = -\gamma(X(t) - \bar{X}) + \bar{g}\zeta(t), \tag{4.4.1}$$

with four model parameters: γ, the gradient of the drift term; $\bar{X}$, the x-intercept; $\bar{g}$, the

Table 4.4: SDE model fit parameters. Sub/superscripts indicate estimated 95% confidence intervals based on 10 000 bootstrap resample models (Kunsch, 1989). The R^2 value refers to the linear fit of the drift term and the normalised root mean squared errors (NRMSE) corresponds to the fit of the constant noise term.

Run name	γ, Myr^{-1}	$\bar{g}^2$, $\times 10^{44}$ $\mathrm{A}^2\ \mathrm{m}^4\ \mathrm{Myr}^{-1}$	$\hat{\theta}$, kyr	$\bar{g}^2$ NRMSE %	γ R^2 %
TB0/TB00	74^{+30}_{-28}	109^{+25}_{-27}	$0.51^{+0.13}_{-0.11}$	4.5	98
TB1	99^{+42}_{-35}	226^{+83}_{-54}	$0.69^{+0.21}_{-0.14}$	6.0	94
B2	26^{+18}_{-10}	$10.0^{+1.9}_{-2.0}$	$0.43^{+0.12}_{-0.10}$	3.2	95
B3	38^{+31}_{-19}	$20.5^{+5.9}_{-4.2}$	$0.58^{+0.15}_{-0.10}$	2.5	98

average noise amplitude; and θ, the characteristic timescale of correlated noise $\zeta(t)$ in (4.3.4). Table 4.4 lists the best fit model parameters for each case. In this table and henceforth, noise amplitude $\bar{g}$ is squared to have more physically meaningful units, as well as being comparable to different definitions of the noise term $D(x)$ from previous studies, $\bar{g}^2 \equiv 2D$ (e.g., Buffett et al., 2014).

In the dynamo solutions with top and bottom-driven convection we observe high values for the gradient of the drift, γ, compared with the values for bottom-driven case. A larger γ corresponds to shorter timescales for the dipole to relax back to the time-averaged state. Fits for the squared noise amplitude $\bar{g}^2$, are an order of magnitude larger in the top and bottom driven dynamos than the bottom driven dynamos. In contrast, fitted noise correlation times $\hat{\theta}$ are similar in magnitude for the four cases, relative to the uncertainties. The bottom driven cases have a slightly lower correlation time, although this effect is marginal (about 15%). A small change to γ is observed in the dynamo solutions when changing Ra from the initial values to the higher values. For example, the change from case B2 to B3 increases γ by 46%. A smaller increase is observed for cases TB0/TB00 and TB1. Furthermore, the high Ra cases show a roughly doubled noise amplitude compared to their low Ra case counterparts. The uncertainties in $\bar{g}^2$ also increase with increasing amplitude. The high Ra dynamos also have a 20-35% longer correlation time compared to the low Ra cases.

Power Spectra

Calculations of the power spectra affords a useful test of the stochastic models because no information on timescales longer than $\tau_{\max}$ are used in fitting the stochastic models. This means that the long-period part of the power spectra is an independent check on the fitted model. The form of the stochastic model in (4.4.1) permits an analytical solution for the power spectrum (e.g., Buffett and Matsui, 2015)

$$S_X(f) = \frac{2\bar{g}^2/\theta^2}{(\gamma^2 + 4\pi^2 f^2)(1/\theta^2 + 4\pi^2 f^2)}, \tag{4.4.2}$$

where f is frequency. Since the spectrum is symmetric about $f = 0$, a factor of two is included in the theory to allow direct comparisons to numerical calculations, which assume positive frequencies when the signals are real. For each solution, we compare this prediction with the power spectrum computed numerically from the ADM time series using a multi-taper technique (Constable and Johnson, 2005). A comparison between calculated and predicted power spectrum for case B3 is shown in Fig. 4.4. Similar plots for other cases are available in the supplementary materials (Figs D.7–D.9).

There is a close match between the calculated and theoretical power spectra, despite the fact that the time increments used to fit model (4.4.1) are restricted to $\tau \leq \tau_{\max}$. In particular the corner frequencies—where the power changes from $\propto f^0$ to f^{-2} (set by $\gamma/2\pi$), and from $\propto f^{-2}$ to f^{-4} (set by $1/2\pi\theta$)—are matched well. This suggests that the stochastic model (4.4.1) is a suitable description of ADM variations in quasi-steady dynamo models on a wide range of timescales. In the next section we interpret the drift gradient and noise amplitudes for each case, and relate changes between models to physical features in the geodynamo.

4.5 Interpretation: Links to Physical Processes in the Core

Only four parameters are needed to specify the stochastic model in (4.4.1), yet this simple representation is sufficient to predict power spectra that are in good agreement with those computed from the output of the dynamo simulations. An important question is whether these four parameters can be related to physical processes in the geodynamo. To facilitate comparisons we use $\overline{\mathbf{B}}$ to denote the dipole field, which is obtained by projecting the total magnetic field onto the $l = 1$, $m = 0$ poloidal part of the vector spherical harmonic expansion. Now we seek to find an equivalent stochastic representation of dipole variations, in a similar manner to Buffett et al. (2014). The time evolution of $\overline{\mathbf{B}}$ can then be expressed as

$$\frac{\partial}{\partial t}\overline{\mathbf{B}} = \nabla \times (\overline{\mathbf{V} \times \mathbf{B}}) + \eta \nabla^2 \overline{\mathbf{B}}, \tag{4.5.1}$$

where $\hat{z}$ is the unit vector in the direction of the axis of the Earth. The first term on the right-hand side represents the generation of the dipole field by convection, whereas the second terms describes the influence of magnetic diffusion. The ADM can be expressed as an integral over the volume of the core, V_c, (e.g., Davidson, 2013)

$$X(t) = \frac{3}{2\mu} \int_{V_c} \hat{\mathbf{z}} \cdot \overline{\mathbf{B}}(t)\, dV_c, \tag{4.5.2}$$

so the rate of change of the ADM can be partitioned to sources due to fluid motion, $S(t)$, and losses due to diffusion, $\Phi(t)$,

$$\frac{d}{dt}X(t) = S(t) - \Phi(t), \tag{4.5.3}$$

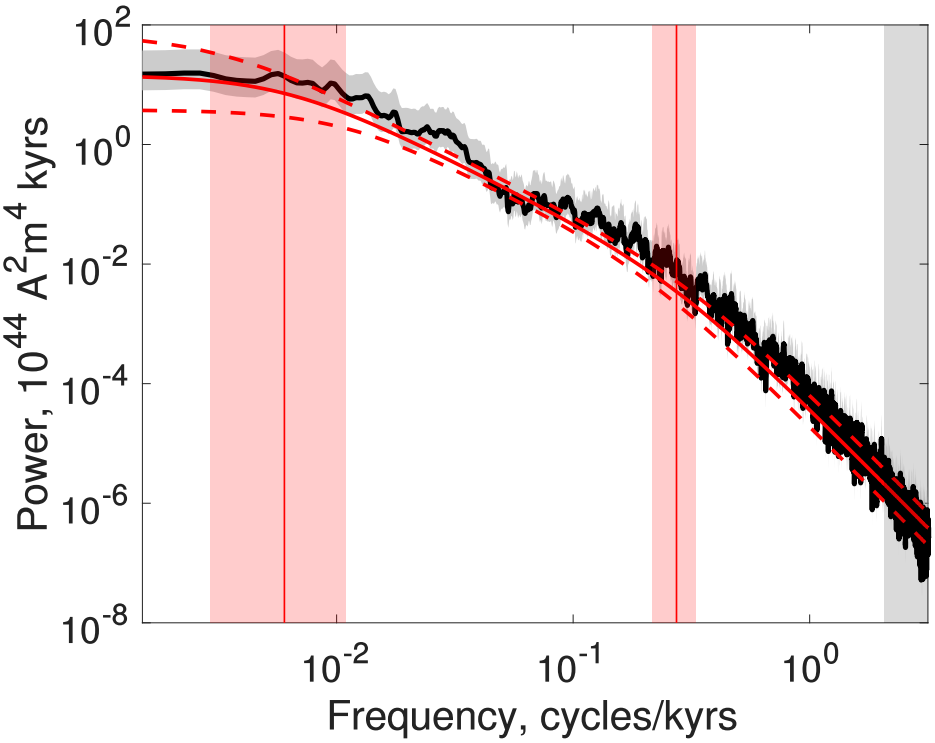

Figure 4.4: Power spectrum for the axial dipole moment from case B3. The black line indicates the calculated ADM power spectrum, with grey shaded region indicating 95% confidence intervals. The solid red line indicates the theoretical spectrum from equation (4.4.2), with red dashed lines indicating 95% confidence intervals. The left and right vertical red lines indicate corner frequencies relating to the drift gradient γ and the correlation time θ, respectively, and shaded red vertical bars indicate 95% confidence intervals. The right grey shaded box indicates the frequencies that corresponds to a sampling interval times $\tau \leq \tau_{\max}$ (see Table 4.3).

where

$$S(t) = \frac{3}{2\mu} \int_{V_c} \hat{\mathbf{z}} \cdot \nabla \times (\overline{\mathbf{V} \times \mathbf{B}}) \, dV_c, \tag{4.5.4}$$

$$\Phi(t) = -\frac{3}{2\mu} \int_{V_c} \hat{\mathbf{z}} \cdot \eta \nabla^2 \overline{\mathbf{B}} \, dV_c. \tag{4.5.5}$$

We separate the source in (4.5.3) into average and complimentary parts

$$S(t) = \langle S \rangle + \Delta S(t), \text{ such that } \langle \Delta S \rangle = 0, \tag{4.5.6}$$

which gives

$$\frac{d}{dt}X(t) = \langle S \rangle - \Phi(t) + \Delta S(t). \tag{4.5.7}$$

When the dipole is represented as a linear combination of decay modes (Gubbins and Roberts, 1987) the diffusion term can be approximated by

$$-\eta \nabla^2 \overline{\mathbf{B}} \approx \overline{\mathbf{B}}/\tau_{\text{eff}}, \tag{4.5.8}$$

where τ_{eff} is the effective decay timescale; see Section 4.5 for details. Using (4.5.2) and (4.5.8) in (4.5.5) gives

$$\Phi(t) \approx \frac{3}{2\mu} \int_{V_c} \hat{\mathbf{z}} \cdot \frac{\overline{\mathbf{B}}}{\tau_{\text{eff}}} \, dV_c = \frac{X(t)}{\tau_{\text{eff}}}, \tag{4.5.9}$$

which allows us to write the time dependence of $X(t)$ as

$$\frac{d}{dt}X(t) = \langle S \rangle - \frac{X(t)}{\tau_{\text{eff}}} + \Delta S(t). \tag{4.5.10}$$

Taking the time average of (4.5.10) yields a steady-state balance between the source and sink,

$$\langle S \rangle = \langle X \rangle / \tau_{\text{eff}}. \tag{4.5.11}$$

Combining (4.5.11) and (4.5.10) gives

$$\frac{d}{dt}X(t) = -\frac{1}{\tau_{\text{eff}}}\big(X(t) - \langle X \rangle\big) + \Delta S(t), \tag{4.5.12}$$

which is the starting point for interpreting the SDE in (4.4.1).

The first term in (4.5.12) has the same form as the drift term in (4.4.1). The time average $\langle X \rangle$ must coincide with drift x-intercept $\bar{X}$ to ensure that the slow relaxation rate vanish at the same value of X, but the relationship between τ_{eff} and γ is not immediately clear. Similarly, a correspondence between $\Delta S(t)$ and the noise term in the SDE is plausible, but not yet demonstrated. To clarify these connections, we use the results of the dynamo simulations to assess the physical significance of the terms in (4.4.1). This analysis is a new framework, based on Buffett et al. (2014), that encompasses a wider range of conditions in the style and vigour of convection in our dynamo models. We show that each term in the SDE can be quantitatively evaluated using the output of the dynamo simulations.

Noise Amplitude: Turbulent Fluctuations

Short-term ADM fluctuations are represented by the noise term in the stochastic model (4.4.1), and by departures in source $S(t)$ from the time average $\langle S \rangle$ in the physical model (4.5.12). To relate the statistics of source fluctuations $\Delta S(t)$ to the amplitude of the noise term

in (4.4.1), we need to establish how these terms contribute to fluctuations in ADM. A typical fluctuation in ADM occurs over a short timescale relative to the characteristic timescale of relaxation. We denote this short timescale by τ_f. When $\tau_f \ll \tau_{\text{eff}}$ we can safely neglect the contribution from the drift term and express the fluctuation solely in terms of $\Delta S(t)$ as

$$\Delta X(\tau_f) = \int_0^{\tau_f} \Delta S(t)\ dt. \tag{4.5.13}$$

For small τ_f the variance of ADM fluctuations can be approximated as

$$\langle \Delta X(\tau_f)^2 \rangle \approx \tau_f^2 \langle \Delta S^2 \rangle. \tag{4.5.14}$$

We can now compare the typical fluctuation in (4.5.13) with the fluctuation due to the noise term in (4.4.1),

$$\Delta X(\tau_f) = \int_0^{\tau_f} \bar{g}\zeta(t)\ dt, \tag{4.5.15}$$

where $\zeta(t)$ is correlated noise (4.3.4). The variance of this process for arbitrary τ_f is (e.g., Uhlenbeck and Ornstein, 1930)

$$\langle \Delta X(\tau_f)^2 \rangle = \bar{g}^2 \tau_f + \frac{\bar{g}^2 \theta}{2}\left(4e^{-\tau_f/\theta} - e^{-2\tau_f/\theta} - 3\right). \tag{4.5.16}$$

Comparing (4.5.14) and (4.5.16) suggests that the variance of the source fluctuation is

$$\langle \Delta S^2 \rangle \approx \frac{\bar{g}^2}{\tau_{f\theta}}, \qquad \text{where} \qquad \tau_{f\theta} = \tau_f \Big/ \left(1 + \frac{1}{2}\frac{\theta}{\tau_f}\left(4e^{-\tau_f/\theta} - e^{-2\tau_f/\theta} - 3\right)\right), \tag{4.5.17}$$

which reduces to expression (42) given in Buffett et al. (2014) when $\theta \ll \tau_f$. Here $\tau_{f\theta}$ can be interpreted as a "correlation corrected" timescale. We take τ_f as short as possible to ensure the accuracy of (4.5.14), but require $\theta < \tau_f$ to average over the correlations in $\Delta S(t)$. A natural choice for τ_f is the convective overturn time, which is approximately 4θ for all dynamo simulations. We adopt this value below, but varying τ_f in the range $[3\theta, 5\theta]$ makes little difference for the results presented below.

A direct calculation of $S(t)$ from the numerical simulation is not possible because the integral for $S(t)$ in (4.5.4) vanishes when the flow satisfies no-slip conditions at the core-mantle boundary. This outcome can be confirmed by direct calculation, and it is not altered by removing a thin viscous boundary layer from the volume integral of $S(t)$. Instead, we quantify the statistics of $S(t)$ using a physical model for the generation of the dipole field (Buffett et al., 2014). Dipole generation is assumed to be the result of the α-effect from helical flows inside the core, where the induction term can be approximated by

$$\overline{V \times B} = \epsilon B_\phi V_{\text{rms}}^2 l/\eta, \tag{4.5.18}$$

and l is the width of a convection column, and B_ϕ is the azimuthal magnetic field (Moffatt, 1970). The factor ϵ was introduced in Buffett et al. (2014) to represent the fraction of field generation that contributes to the external dipole field. This approximation can be justified through a rough agreement between the total induction efficiency and that inferred from (4.5.18) (Buffett et al., 2014). Consequently the source term (4.5.4) becomes

$$S \approx \frac{3}{2\mu}\Big(\frac{\epsilon B_\phi V_{\rm rms}^2 l}{L\eta}\Big)V_c, \tag{4.5.19}$$

where L represents the characteristic length-scale of $\overline{V \times B}$. Parameters l, L and ϵ represent average properties of the convective system of the convective system, and are defined in a time-averaged sense. Local variations in l and L are likely to be small (e.g., Aubert et al., 2017). Considering variations in (4.5.19) from $V_{\rm rms}$ and B_ϕ gives

$$\frac{\langle \Delta S^2\rangle^{\frac{1}{2}}}{\langle S\rangle} = 2\frac{\langle \Delta V_{\rm rms}^2\rangle^{\frac{1}{2}}}{\langle V_{\rm rms}\rangle} + \frac{\langle \Delta B_{\rm rms}^2\rangle^{\frac{1}{2}}}{\langle B_{\rm rms}\rangle} \tag{4.5.20}$$

for the time average when $\Delta V_{\rm rms}^2$ and $\Delta B_{\rm rms}^2$ are assumed to be statistically independent. Values for the terms in (4.5.20) for the dynamo models are reported in Table 4.2. Estimating the amplitude of the source $\langle S\rangle$ from equation (4.5.11) with $\tau_{\rm eff}=1/\gamma$ allows for the calculation of the amplitude of the source fluctuations, $\langle \Delta S^2\rangle^{\frac{1}{2}}$. These calculations are compared to the result from (4.5.17) for each of the dynamo cases in Fig. 4.5. The estimates and fits for each model agree reasonably well, despite the order of magnitude difference in $\bar{g}^2$ over the two dynamo regimes. Replacing $V_{\rm rms}$ with the variation in the poloidal field $V_{\rm rms}^{\rm p}$ gives similar results. Although within uncertainties, there is a small underestimate for the bottom driven cases. This may be due to the no heat-flux boundary condition suppressing velocity variations in the upper part of the core. The velocity variations in the remaining part of the core would preferentially contribute to the fluctuations in the source, resulting in estimates of $\langle \Delta S^2\rangle^{\frac{1}{2}}$ from $V_{\rm rms}$, the full core volume average, being an underestimate.

Noise Correlation: Integral Time Scale

Source variations $\Delta S(t)$ are attributed to a turbulent flow with a finite correlation time; however, the link between these correlations, physical quantities in the dynamo, and terms in a stochastic model, have not been previously studied. One measure of the correlation timescale of a process $y(t)$ is the integral of the normalised autocorrelation function

$$P_y(\tau) = \frac{1}{{\rm Var}(y)}\Big\langle \big(y(t)-\langle y\rangle\big)\big(y(t+\tau)-\langle y\rangle\big)\Big\rangle, \tag{4.5.21}$$

over $[0,\infty]$ (Hänggi and Jung, 1995). This is expressed by the functional

$$\Theta[y(t)] = \int_0^\infty P_y(\tau)\ d\tau. \tag{4.5.22}$$

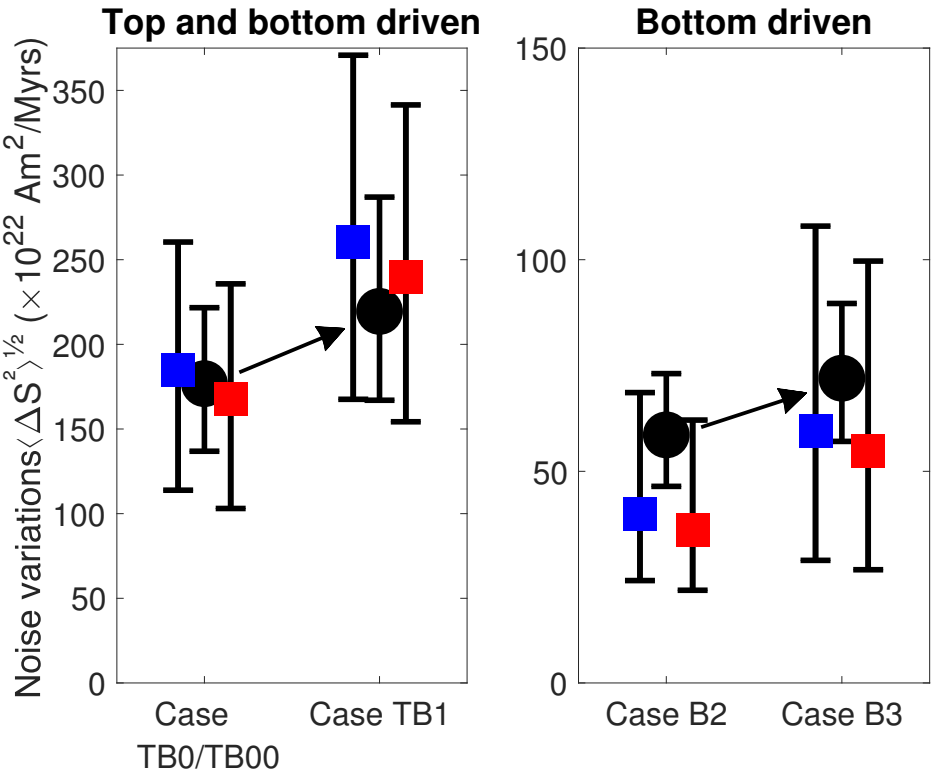

Figure 4.5: Noise variation amplitude from each dynamo simulation. Black circles and error bars represent values determined from SDE analysis and 95% confidence intervals, respectively, from Table 4.3. Red (shifted right) and blue (shifted left) squares represent estimates taken from diagnostic parameters, based on $V_{\rm rms}$ and $V^{\rm p}_{\rm rms}$, respectively, in the dynamo simulations. Error bars represent 95% confidence intervals. Note the change in y-limits for the two plots.

Noise in the stochastic model, $\zeta(t)$, was formulated specifically to have an autocorrelation (4.3.3) with correlation time equal to θ,

$$\Theta[\zeta(t)] = \int_0^\infty P_\zeta(\tau)\, d\tau = \int_0^\infty e^{-|\tau|/\theta}\, d\tau = \theta. \tag{4.5.23}$$

The corresponding correlation time of physical fluctuations $\Delta S(t)$,

$$\Theta[\Delta S(t)] = \int_0^\infty P_{\Delta S}(\tau)\, d\tau, \tag{4.5.24}$$

is defined by variations in the terms in (4.5.19) that contribute significantly to its amplitude, i.e., $V_{\rm rms}$ and B_ϕ. The effective correlation time is set by the fastest varying term (Van Kampen, 1992), which corresponds to $V_{\rm rms}$ in the dynamo simulations. Accordingly we replace the autocorrelation $P_{\Delta S}$ with $P_{V_{\rm rms}}$ in (4.5.24), where $V_{\rm rms}(t)$ is extracted from the

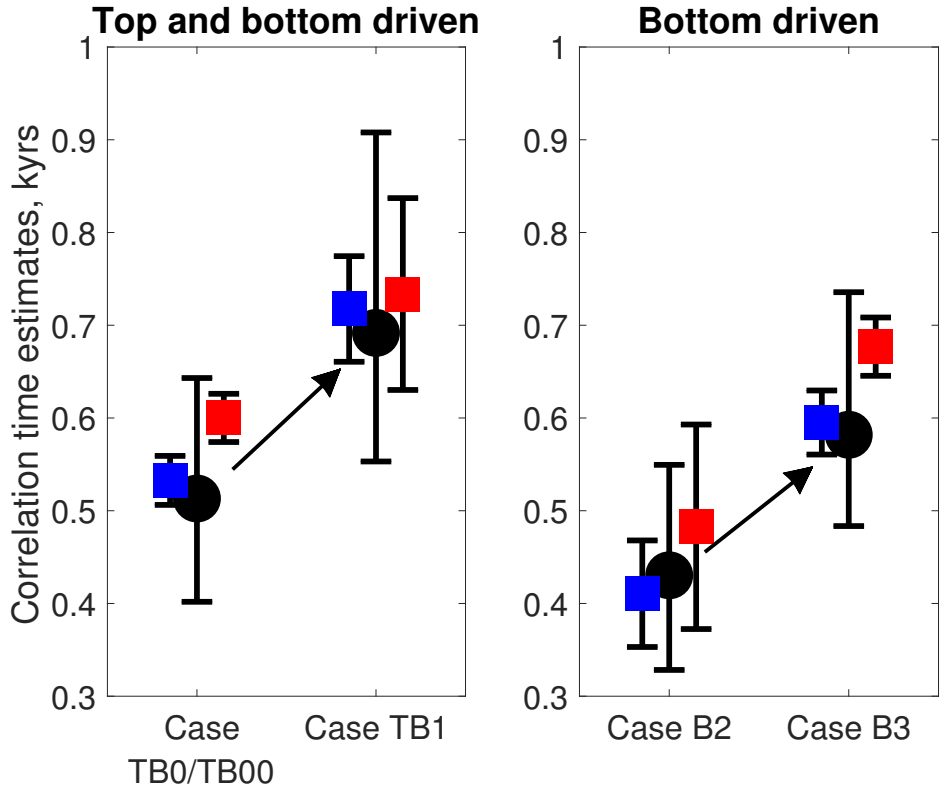

Figure 4.6: Correlation time of noise from each dynamo simulation. Black circles and error bars represent values determined from SDE analysis, $\hat{\theta}$, and 95% confidence intervals, respectively, from Table 4.3. Red (shifted right) and blue (shifted left) squares represent estimates taken from diagnostic parameters $\Theta[V_{\rm rms}(t)]$ and $\Theta[V^{\rm p}_{\rm rms}(t)]$, respectively. Error bars on the colored squares represent an estimate of the uncertainties due to finite integration lengths of $\Theta[\dots]$ (see text).

dynamo simulations. The integral over time is limited to a finite T to allow for numerical calculation. The sample correlation time is

$$\Theta[V_{\rm rms}(t)] = \int_0^T P_{V_{\rm rms}}(\tau)\ d\tau. \tag{4.5.25}$$

In practice as τ increases $P_{V_{\rm rms}}(\tau)$ decays rapidly then fluctuates around zero. Choosing the limit $T \sim 8$ kyr yields a representative estimate for θ. The integral is repeated for a range $T \sim 8 \pm 1$ kyr, and variance in results gives an estimate of the uncertainty associated with the correlation time, shown in Fig. 4.6.

These calculations are compared with fits of the correlation time from Table 4.4 for each dynamo case (see Fig. 4.6). All models show good agreement between fits and estimates from the stochastic and physical interpretations. Replacing $V_{\rm rms}$ with poloidal $V^{\rm p}_{\rm rms}$ gives comparable correlation times, as it did in the interpretation of the amplitude of the noise.

Drift Gradient: Slow Adjustment of the Dipole Field

Slow relaxation of the axial dipole to its time average is described by the drift term in the stochastic model. For all dynamo simulations in this study, fits of the drift are approximately linear, defined in (4.4.1). This provides three important pieces of information:

1. The drift vanishes at the time average, $\bar{X}$, where the ADM is no more likely to increase or decrease.

2. The rate of change of the ADM is proportional to the displacement from the average, and the magnitude of the rate is independent of the sign of this displacement.

3. This response drives the ADM towards the time average.

Point 1 verifies that there exists one ADM state where, on average, $S(t)$ and $\Phi(t)$ balance. This condition defines the time average $\langle X \rangle$. The second and third points are more subtle. Naively, the inverse of the drift gradient γ^{-1} may be interpreted as the slow relaxation timescale of the stochastic process (e.g., Strogatz, 2018). However this offers little physical insight. To determine the physical origins of these observations, we proceed by analyzing processes in the dynamo that govern the time-averaged adjustment of the dipole field to $\langle X \rangle$.

We start our analysis in a similar manner to Buffett et al. (2014), but focus on the imbalance between generation and decay of the dipole field. In the absence of any source mechanism the field $\overline{\mathbf{B}}$ decays according to

$$\frac{\partial}{\partial t}\overline{\mathbf{B}} = \eta \nabla^2 \overline{\mathbf{B}}. \tag{4.5.26}$$

Solutions of (4.5.26) define the decay modes of the dipole field. It is customary to represent the dipole field in terms of a poloidal scalar

$$\overline{\mathbf{B}}(r,\theta,t) = \nabla \times \nabla \times [\mathcal{P}(r,\theta,t)\hat{r}], \tag{4.5.27}$$

where $\mathcal{P}(r,\theta,t) = \mathcal{P}(r,t)\cos\theta$ is the $l = 1, m = 0$ poloidal scalar field, defined in terms of colatitude θ. At any instant in time, $\mathcal{P}$ may be decomposed into a set of orthogonal modes

$$\mathcal{P}(r,t) \approx \sum_{n=1}^{N} A_n \mathcal{P}_n(r,t) \tag{4.5.28}$$

where the n^{th} decay mode

$$\mathcal{P}_n(r,t) = \widetilde{\mathcal{P}}_n(r) e^{-t/\tau_n}, \tag{4.5.29}$$

is associated with a characteristic timescale τ_n and A_n is a constant coefficient (Gubbins and Roberts, 1987). The first few modes in a spherical shell have dimensional decay times of $(47.9, 10.7, 4.1, \dots)$ kyr. When $\overline{\mathbf{B}}$ has the structure of a single mode $\mathcal{P}_n$, the rate of change of the dipole field is given by $-\overline{\mathbf{B}}/\tau_n$. A more general field can be represented by a linear superposition of modes, so an effective decay time τ_{eff} would be defined by

differentiating (4.5.28). It follows that the diffusive term in (4.5.26) can be approximated by equation (4.5.8). This approximation is best when the field can be well represented by the first few long wavelength modes, which is valid for our simulations.

Next, we need to explicitly consider the long-term balance between decay and sources in $\overline{\mathbf{B}}$. The time average of (4.5.1) requires

$$\nabla \times \langle \overline{V \times \mathbf{B}} \rangle = -\eta \nabla^2 \langle \overline{\mathbf{B}} \rangle. \tag{4.5.30}$$

Using this result in the definition of $S(t)$ in (4.5.4) gives an expression for the time-averaged source

$$\langle S \rangle = -\frac{3}{2\mu} \int_{V_c} \hat{\mathbf{z}} \cdot \eta \nabla^2 \langle \overline{\mathbf{B}} \rangle \, dV_c. \tag{4.5.31}$$

Recalling the definition of $\Phi(t)$ from (4.5.5), we can now write the *im*balance between decay and average source as

$$\langle S \rangle - \Phi(t) = \frac{3}{2\mu} \int_{V_c} \hat{\mathbf{z}} \cdot \eta \nabla^2 \Big(\overline{\mathbf{B}}(t) - \langle \overline{\mathbf{B}} \rangle \Big) \, dV_c, \tag{4.5.32}$$

which depends on deviations of $\overline{\mathbf{B}}(t)$ from the time average. This imbalance between $\Phi(t)$ and $\langle S \rangle$ controls the rate at which $X(t)$ adjusts toward $\langle X \rangle$ due to diffusion, satisfying point 3. This is precisely what the drift term is intended to represent.

Both $\overline{\mathbf{B}}(t)$ and $\langle \overline{\mathbf{B}} \rangle$ can be represented as a linear combination of decay modes, so the slow adjustment of $X(t)$ can be related to the amplitudes of the linear superposition of decay modes. To illustrate this, suppose that the dipole field can be represented at time t_0 by a linear combination of coefficients $A_n(t_0)$. The change in coefficients at later times due to the influence of diffusion can be expressed in the form

$$A_n(t) = \langle A_n \rangle + \big(A_n(t_0) - \langle A_n \rangle \big) e^{-(t-t_0)/\tau_n}, \tag{4.5.33}$$

where $\langle A_n \rangle$ are the coefficients of time-averaged field $\langle \overline{\mathbf{B}} \rangle$. Note that this formulation predicts relaxation to the mean on a timescale that is independent of whether the adjustment involves growth or decay, as noted in point 2. Random fluctuations due to $\Delta S(t)$ cause deviations from this expected relaxation, but by averaging over a large ensemble of solutions we can expect the slow adjustment to the mean to emerge because the random fluctuations should average to zero.

We can test this expectation using samples of the poloidal scalar field $\mathcal{P}(r,t)$ from the dynamo simulations. Samples were extracted from each dynamo simulation (except TB0) and mode amplitudes $A_n(t)$ in (4.5.28) were determined at each time-step using least squares regression. To capture the large-scale field structures, we truncate the sum in (4.5.28) to $N = 3$ modes. The slowest decay mode accounts for most of the radial variation in snapshots of the poloidal scalar. This is true of all our dynamo simulations. Trajectories are defined as

$$A_n(t; x) := \lfloor A_n(t - t_0) \rfloor_{X(t_0)=x}, \tag{4.5.34}$$

where the conditioning on $X(t_0)$ is set by a small bin around x. In order to verify (4.5.33), we perform two tests for each dynamo simulation: $X(t_0)$ starting from above the mean, and $X(t_0)$ starting from below the mean. To facilitate this, the center of the bin in (4.5.34) is chosen to be ADM values either 2 standard deviations above or below the mean. For each test, 20 trajectories were extracted for each dynamo simulation, and the ensemble mean path and confidence intervals were calculated. We would expect individual trajectories to fluctuate due to noise from the magnetic induction term (4.5.1), and the ensemble should display a relaxation to the mean value. If (4.5.33) holds, the relaxation of the nth mode should be symmetric above or below the mean, and on a timescale set by τ_n. Sample trajectories and ensemble averages are shown for case TB1 in Fig. 4.7. Similar plots for the other simulations are available in the supplementary material (Figs D.10-D.12).

Fig. 4.7 shows that the slowest mode accommodates the majority of the changes to the full field. Higher order modes seem unaffected by conditioning on $X(t_0)$, and do not differ significantly from the time-averaged field. On average the slowest mode relaxes to the mean *faster* than the characteristic decay timescale τ_n in (4.5.33) predicts, suggesting that diffusion in (4.5.32) is enhanced by fluid motion at small scales (Braginsky and Meytlis, 1990). This validates the second point of proportional response. Furthermore, the average relaxation for the ensemble is within the confidence intervals of exponential decay with a timescale γ^{-1}, predicted by the stochastic model. This suggests that the characteristic timescale of the drift function can be interpreted as representing the turbulence enhanced diffusion of the $l = 1$ poloidal field, which is the dominant magnetic structure in the core.

For the uniformly conducting spherical shell in our dynamo models, the slowest decay time is $\tau_1 = r_{\rm cmb}^2/(k^2\eta)$, where $k \approx 3.1688$. By setting $\tau_1 = \gamma^{-1}$ we can estimate the effective diffusivity implied by the drift term, which comprises both molecular and turbulent contributions, i.e., $\eta_{\rm eff} = \eta + \eta_{\rm tur}$. Table 4.5 shows these inferred diffusivities and the ratio of turbulent to molecular diffusivity ($\eta = 0.8$ m^{2}s^{-1}) for each dynamo model. The turbulent diffusivities are also shown in Fig. 4.8. Diffusion is enhanced by turbulence most significantly in the top-and-bottom driven dynamo models, but is a minor effect for the bottom-driven models. This suggests why, for the bottom-driven cases, the average model amplitudes relax to the mean only marginally faster than (4.5.33) predicts. Indeed the uncertainties on $\eta_{\rm tur}$ for the bottom-driven cases means that these dynamo models are compatible with no turbulent enhancement of diffusivity, and magnitudes of estimated values are comparable to their uncertainties. Plotting $\eta_{\rm tur}$ as a function of (dimensionless) rms velocity in Fig. 4.8 is effectively a plot using the magnetic Reynolds number when Pm = 1. Extrapolating $\eta_{\rm tur}$ to a realistic value of Rm ≈ 1000 would give $\eta_{\rm tur} \sim 5 - 10$ m^2 s^{-1}.

These interpretations demonstrate that random motions of the fluid are responsible for both the drift and noise terms. Turbulent diffusion enhances the slowest decay mode, which contributes to the drift term; small-scale helical turbulence contributes to the noise term. The phenomena of turbulence contributing in both a constructive and destructive way has been previously investigated in the context of mean field electrodynamics, through analysis of the turbulent electromotive force arising from the induction term $\overline{V \times B}$ (e.g., Tobias, 2021). Contributions to the induction arise from helical flows—the α-effect—which act to

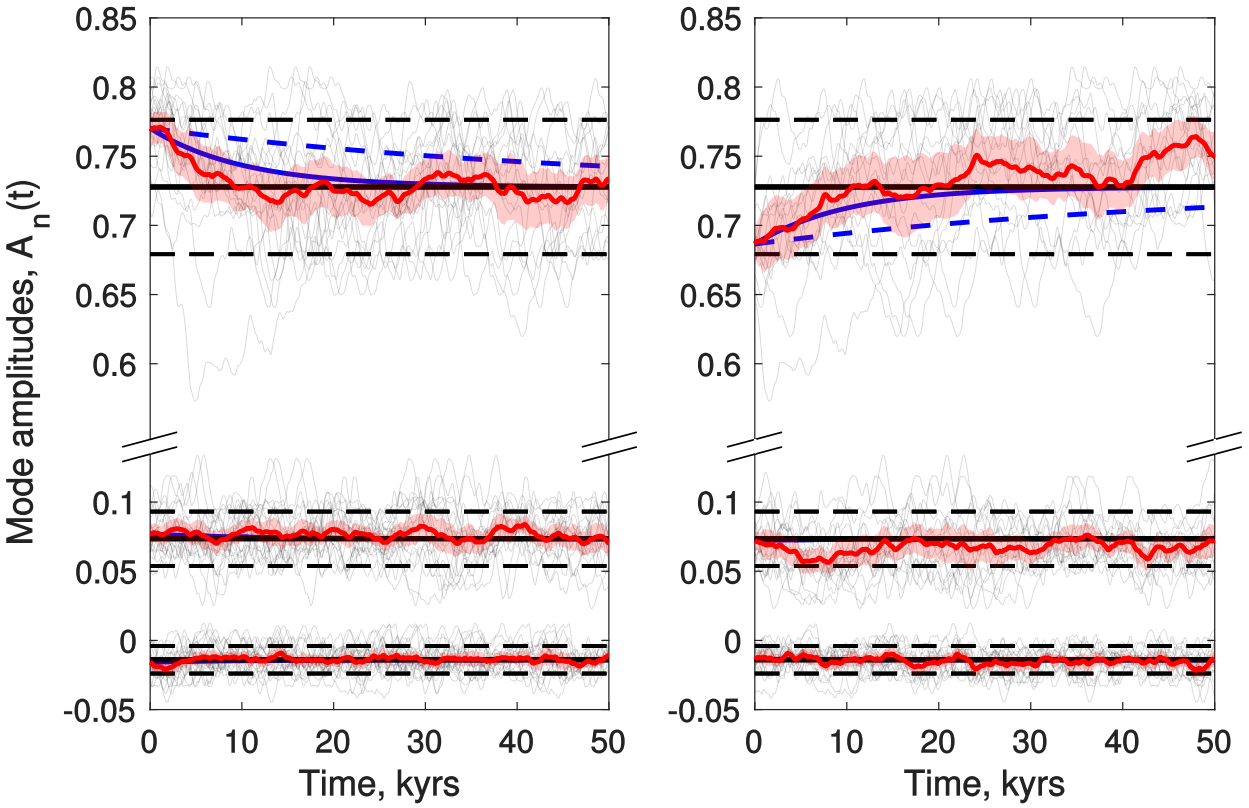

Figure 4.7: Relaxation of decay mode amplitudes (n=1, 2 and 3) extracted from case TB1. Plots show trajectories of individual mode trajectories with n=1 at the top and n=3 at the bottom. Left and right plots are conditional on sample points starting two standard deviations above and below the mean, respectively. The thin black lines show a sample of individual conditioned trajectories (4.5.34). The thick red line and shaded red area show the ensemble mean and 95% confidence intervals on the mean of trajectories, respectively. The solid and dashed thick black lines show the total mean ± two standard deviations, respectively, for the mode amplitudes $A_n(t)$. The solid blue line shows relaxation predicted by timescale γ^{-1}. The dashed blue line shows the theoretical relaxation (4.5.33), for the imposed magnetic diffusivity in the dynamo solution.

Table 4.5: Effective diffusivity from dynamo models. Sub/superscripts indicate approximate 95% confidence intervals based on 10 000 bootstrap resamples (Kunsch, 1989).

Run name	γ^{-1}, kyr	η_{eff}, m^2 s^{-1}	η_{tur}, m^2 s^{-1}	η_{tur}/η
TB0/TB00	$13.5^{+8.2}_{-3.9}$	$2.8^{+1.1}_{-1.1}$	$2.0^{+1.1}_{-1.1}$	$2.5^{+1.4}_{-1.3}$
TB1	$10.1^{+5.5}_{-3.0}$	$3.8^{+1.6}_{-1.3}$	$3.0^{+1.6}_{-1.3}$	$3.7^{+2.0}_{-1.7}$
B2	38^{+24}_{-16}	$1.00^{+0.67}_{-0.38}$	$0.20^{+0.67}_{-0.20}$	$0.24^{+0.86}_{-0.24}$
B3	26^{+26}_{-12}	$1.45^{+1.19}_{-0.73}$	$0.65^{+1.19}_{-0.65}$	$0.82^{+1.48}_{-0.82}$

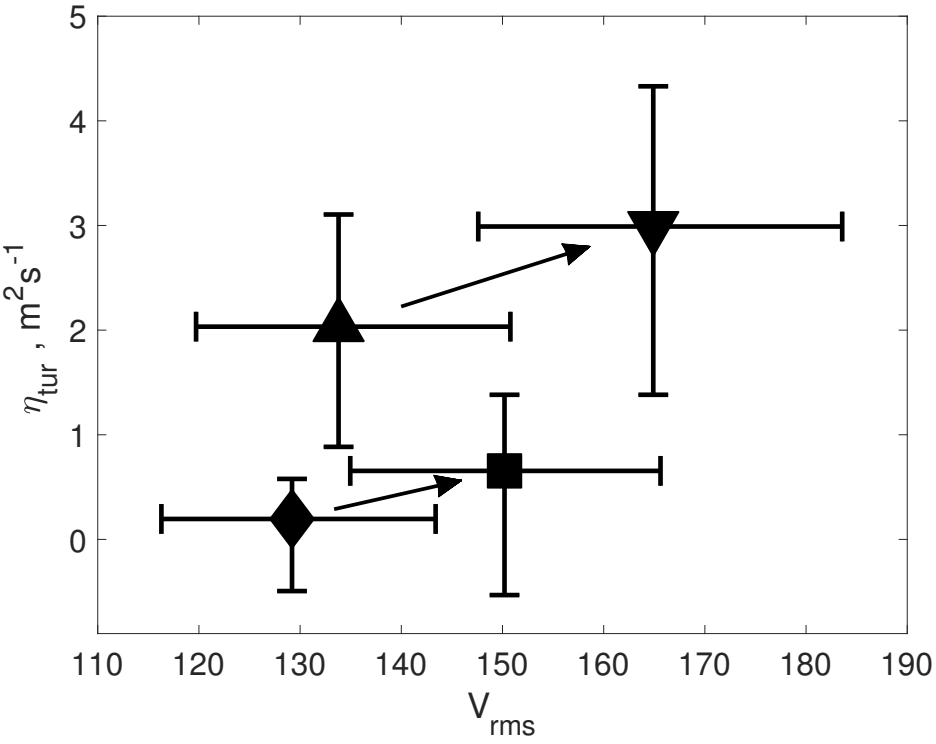

Figure 4.8: Root mean squared (dimensionless) velocities and turbulent diffusivities for dynamo models. Values for models TB0/TB00, TB1, B2, and B3 are displayed with a triangle, inverted triangle, diamond, and square respectively. Arrows from case TB0/TB00 to TB1 and from B2, B3 are for visual distinction between the two convection regimes. Error bars for V_{rms} show 95% percentiles of the distribution of data. Error bars for η_{tur} indicate approximate 95% confidence intervals based on 10 000 bootstrap resamples (Kunsch, 1989).

alter the poloidal field on the timescale of V (Parker, 1955; Steenbeck and Krause, 1966). On the other hand, second spatial derivatives of the mean field gives, in its simplest form known as the β-effect, a net effect of enhancing magnetic diffusivity (Moffatt, 1978; Krause and Raedler, 1980). Buffett et al. (2014) showed that the smallest scales in the velocity field (spherical harmonic degrees $\ell \gtrsim 47$) did not significantly contribute towards induction, indicating that effects of turbulent diffusivity are not restricted to small scales. In general, the properties found from the SDE fitting are consistent with statistical properties extracted from the dynamo simulations. These physical inferences can be used to interpret fluctuations in virtual axial dipole moment (VADM) from the paleomagnetic record.

4.6 Implications for the Paleomagnetic Record

As the physical inferences developed in the previous section apply for general dynamo processes, we can use them in conjunction with stochastic models of the paleomagnetic field to

infer the internal state of the core. Stochastic models of variations in the recent geomagnetic field have been previously fitted to paleomagnetic observations of the VADM. In order to conduct a meaningful comparison, it is necessary to focus on studies that explicitly account for the finite correlation time of the noise. Paleomagnetic estimates of the VADM were analyzed in this way in the study of Buffett and Puranam (2017). More recently, Morzfeld and Buffett (2019) fitted the drift and noise functions for the last 2 million years based on a variety of paleomagnetic VADM models, as well as recent reversal rates. Broadly similar results were obtained for the amplitude of the noise term, gradient of the drift term, and correlation time, so we will use these fits in conjunction with the physical inferences developed in Section 4.5 to infer physical quantities in the core.

Morzfeld and Buffett (2019) fit a drift function with two stable points (positive and negative polarity) at an absolute VADM of $|\bar{X}| = 5.23 \pm 0.04 \times 10^{22}$ A m^2. The drift gradient at these points is $\gamma = 100 \pm 3$ Myr^{-1} which corresponds to $\gamma^{-1} \approx 10$ kyr, a timescale comparable to the top and bottom driven dynamo models. Relating this timescale to the slowest decay mode of a uniformly conducting sphere, $\tau_1 = r_{\rm cmb}^2/(\pi^2\eta)$, we obtain an effective diffusivity of $\eta_{\rm eff} = 3.9$ m^2 s^{-1}. Typically this would correspond with an upper bound on effective diffusivity (Buffett et al., 2014) because modes other than the slowest decay mode could potentially contribute. Our results from the dynamo models suggest that slow variations in dipole field structure can be almost completely expressed by the slowest mode. If this structure is representative of the Earth's core, then we can assume that this estimate of effective diffusivity is a reasonable assumption. Assessing the partitioning of this diffusivity requires a choice for the core electrical conductivity. Adopting a value of $\sigma_e = 0.8 \times 10^6$ S m^{-1} would correspond to a molecular diffusivity of 1.0 m^2 s^{-1}, requiring an additional turbulent diffusivity of 2.9 m^2 s^{-1} to account for the drift term. A higher conductivity of $\sigma_e = 1.6 \times 10^6$ S m^{-1} entails a molecular diffusivity of 0.5 m^2 s^{-1} (Koker et al., 2012; Pozzo et al., 2012; Gomi et al., 2013), giving a turbulent diffusivity of 3.4 m^2 s^{-1}. These estimates give a ratio of turbulent to molecular diffusivity in a range from 2.9 to 6.8. Other fits for the gradient of the drift function report lower values of $\gamma = 75$ Myr^{-1} (Buffett and Puranam, 2017), which would correspond to $\eta_{\rm eff} = 2.9$ m^2 s^{-1}. This would result in lower values turbulent diffusivities, as well as lower proportions of turbulent to molecular diffusivities. Our dynamo simulations span a range of values for γ and result in ratios of turbulent to molecular diffusivities both above and below unity, so there is no reason to expect interpretations of the paleomagnetic record using stochastic models to promote or suppress the requirement for turbulent diffusivity.

The assumption of a constant noise term is supported by the paleomagnetic record (Buffett et al., 2013); there is some evidence for increased noise amplitudes at low VADM, however this may be due to measurement noise (Buffett and Puranam, 2017). Morzfeld and Buffett (2019) fit a constant noise term with amplitude $\bar{g}^2/2 \equiv D = 340 \pm 7 \times 10^{44}$ A^2 m^4 Myr^{-1} based on paleomagnetic estimates for the recent field (i.e., the last 2 million years). From equation (4.5.17) we predict that the rms variations in the dipole generation for the recent field is 9.6×10^{24} A m^2 Myr^{-1}. Comparing this with $\langle S \rangle = \gamma \bar{X}$ permits an estimate of rela-

tive source variations $\langle \Delta S^2 \rangle^{\frac{1}{2}} / \langle S \rangle$, defined in (4.5.20), about 180 per cent for the recent field. Source variations depend on both velocity and magnetic field variations in the core. In our dynamo models, these variations have roughly equal magnitudes. If these conditions are representative of Earth's core, convective velocity and magnetic field vary by about 60 per cent. We note that the noise amplitude for the Earth is higher than our dynamo models, indicating that the Earth is likely more strongly driven by fluid turbulence.

The drift term can be extended from a linear function to allow for two stable points at $\bar{X}$ and $-\bar{X}$, and one unstable point at the polarity crossing (Buffett and Puranam, 2017)

$$v(x) = -\frac{\gamma x}{\bar{X}}(|x| - \bar{X}). \tag{4.6.1}$$

This modification allows reversals of polarity. It also permits us to estimate the rate of reversals using Kramers' formula (Kramers, 1940). The reversal rate can be expressed as

$$r = \frac{\gamma}{2\pi} e^{-\gamma \bar{X}^2/(3\bar{g}^2)}, \tag{4.6.2}$$

Using values determined from Morzfeld and Buffett (2019) give a reversal rate of about 4.2 Myr^{-1}, which is comparable with recent observations (Lowrie and Kent, 2004). To facilitate the interpretation of the reversal rate in terms of our findings, we introduce a non-dimensional reversal rate

$$\tilde{r} = 2\pi \frac{r}{\gamma}. \tag{4.6.3}$$

which isolates the exponential term in Kramers' formula. Using (4.5.17) and (4.5.11) allows us to express $\tilde{r}$ in terms of physical timescales and relative source variations

$$\tilde{r} = \exp\left(-\frac{1}{3}\left(\frac{\langle S \rangle}{\langle \Delta S^2 \rangle^{\frac{1}{2}}} \right)^2 \left(\frac{\gamma^{-1}}{\tau_{f\theta}} \right) \right). \tag{4.6.4}$$

This connection to internal physical quantities contrasts with previous studies, where the reversal rate is related to external statistical quantities such as the mean and variance of the ADM (Buffett and Puranam, 2017). Changes in reversal rate can be attributed to relative changes in the source fluctuations or to changes in the overturn time relative to the slow relaxation time. Values for these quantities are extracted from each of the dynamo models and the resulting reversal rates $\tilde{r}$ are plotted in Fig. 4.9. We also show the location of the recent paleomagnetic field. The reversal rate for the recent field is nearly invariant with respect to changes in timescale ratio $\gamma^{-1}/\tau_{f\theta}$, whereas small changes in relative source fluctuations would produce substantial changes in the reversal rate.

These results yield a link between relative velocity and magnetic fluctuations to the reversal rate, and can provide further insight into the ultimate influence of the CMB on the dynamo (Biggin et al., 2012). Previous numerical studies indicate that reversal rates are linked to the local Rossby number (Aubert et al., 2009), a measure of the velocity of small scale flows (Christensen and Aubert, 2006). An empirical scaling relates these

velocities to the convective power to drive the dynamo (Olson and Christensen, 2006), and therefore the heat flux at the CMB (Aubert et al., 2009), showing that the amplitude of CMB heat flow is positively correlated with reversal frequency (Driscoll and Olson, 2009; Driscoll and Olson, 2011; Olson and Amit, 2014). Further influences of heterogeneous CMB heat flux, especially in the equatorial zones, seem to increase this effect (Olson et al., 2010; Amit and Olson, 2015; Olson and Amit, 2015). Our results show an order of magnitude higher noise amplitudes for models with active CMB boundaries, and therefore support a link between CMB heat flux and reversal rate. Furthermore, they additionally offer a physical interpretation to the connection between the small scale flows—through the relative velocity and magnetic fluctuations and source variations (4.5.20)—to reversal rates through equation (4.6.4). As indicated in Fig. 4.9, estimates for the recent field show preferential sensitivity to changes in relative source variations, indicating that variations in reversal rate may be largely controlled by the state of the CMB. Furthermore, by using (4.6.2) with (4.5.17) and (4.5.20) we can investigate the influence of relative convective velocity and magnetic field variations on observed reversal rate for a fixed timescale ratio. The dynamo solutions suggest that the relative fluctuations in velocity and magnetic field are comparable to each other, so the velocity variations contribute two-thirds of the relative source fluctuations. This allows us to plot reversal rate as a function of relative velocity variations for the recent paleomagnetic field (see Fig. 4.10). Interestingly, the recent reversal rate from the paleomagnetic record is close to the point of greatest variability. Raising relative rms velocity variations from 60 per cent to 90 per cent increases reversal rate by a factor of two. Decreasing variations to 40 per cent reduces the reversal rate by more than a factor of six. Furthermore, this formulation permits a value of velocity variations with a critical point

$$V_{\mathrm{rms}}^{\mathrm{crit}} = \frac{2}{27}\sqrt{\frac{2\gamma^{-1}}{\tau_{f\theta}}}, \tag{4.6.5}$$

below which the reversal rate is essentially zero. This corresponds to variations of about 38 per cent for the recent paleomagnetic field. With increasing velocity variations, the reversal rate eventually saturates to a value of $\gamma/2\pi$. The transition to this behavior is not as sharply defined as (4.6.5), but can be approximated as

$$V_{\mathrm{rms}}^{\mathrm{sat}} = \frac{1}{27}(2 + e^{3/2})\sqrt{\frac{2\gamma^{-1}}{\tau_{f\theta}}}. \tag{4.6.6}$$

These two transition points partition dynamics into three sections: non-reversing, reversing with a variable rate, and saturated reversing. These sections are illustrated in Fig. 4.9; the non-reversing/reversing transition line correctly discriminates between the non-reversing dynamo models and the reversing recent field, validating the predictions of (4.6.4). Validation of this transition from reversing numerical dynamo simulations deserves further investigation. Distinguishing between the dynamics of these three sections may be possible for the

longest paleomagnetic records, and can provide inferences on turbulent fluctuations in the core.

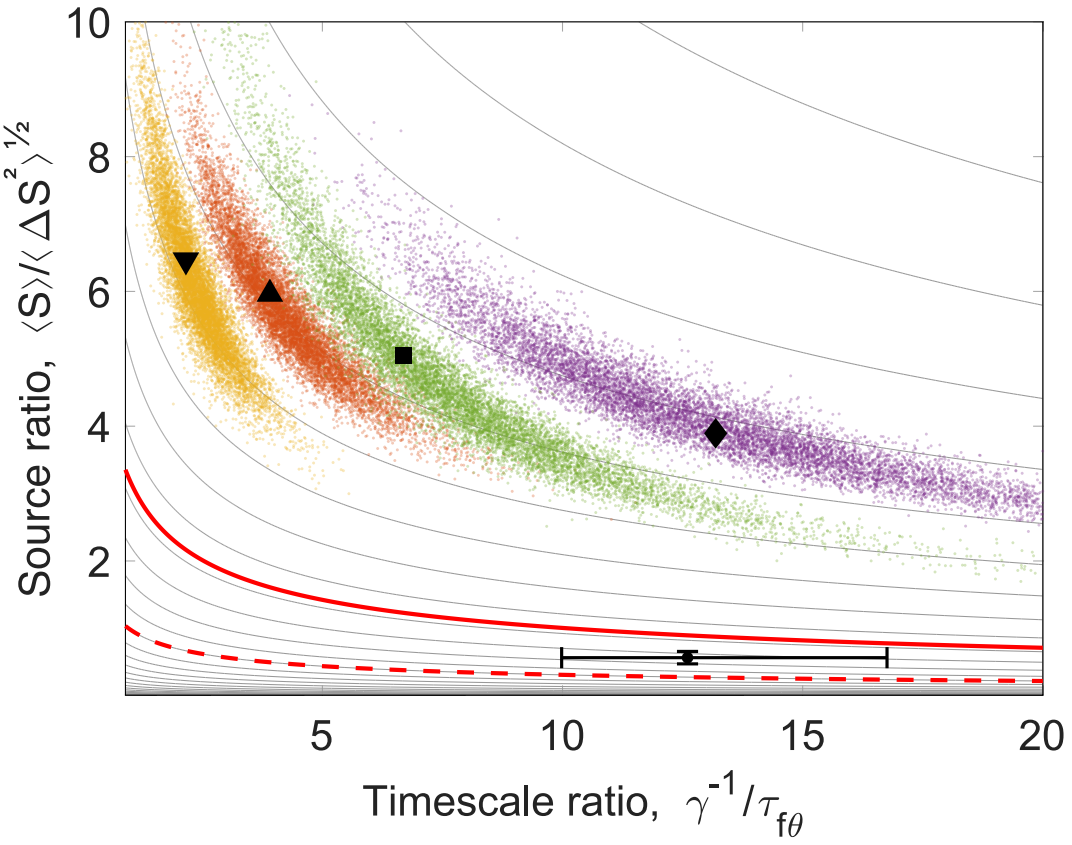

Figure 4.9: Correlation between source variations and timescale ratios for the four dynamo models. The location of the recent paleomagnetic field is identified by a small circle (with error bar uncertainties). Values found from models TB0/TB00, TB1, B2, and B3 are indicated with a triangle, inverted triangle, diamond, and square respectively. Nearby colored points indicate uncertainties from 10 000 bootstrap resamples (Kunsch, 1989). Use of different colors visually discriminates between the different cases. Thin grey contour lines indicate values of equal $\ln(\tilde{r})$. The thick solid red line corresponds to the critical value $V_{\mathrm{rms}}^{\mathrm{crit}}$, and the thick dashed red line corresponds to the saturation value $V_{\mathrm{rms}}^{\mathrm{sat}}$.

4.7 Conclusions

We use a set of numerical dynamo simulations to fit stochastic models of ADM variations, using a fitting method that intrinsically accounts for correlated noise. All of the stochastic models have the same general linear form (4.4.1) over a range of different configurations and

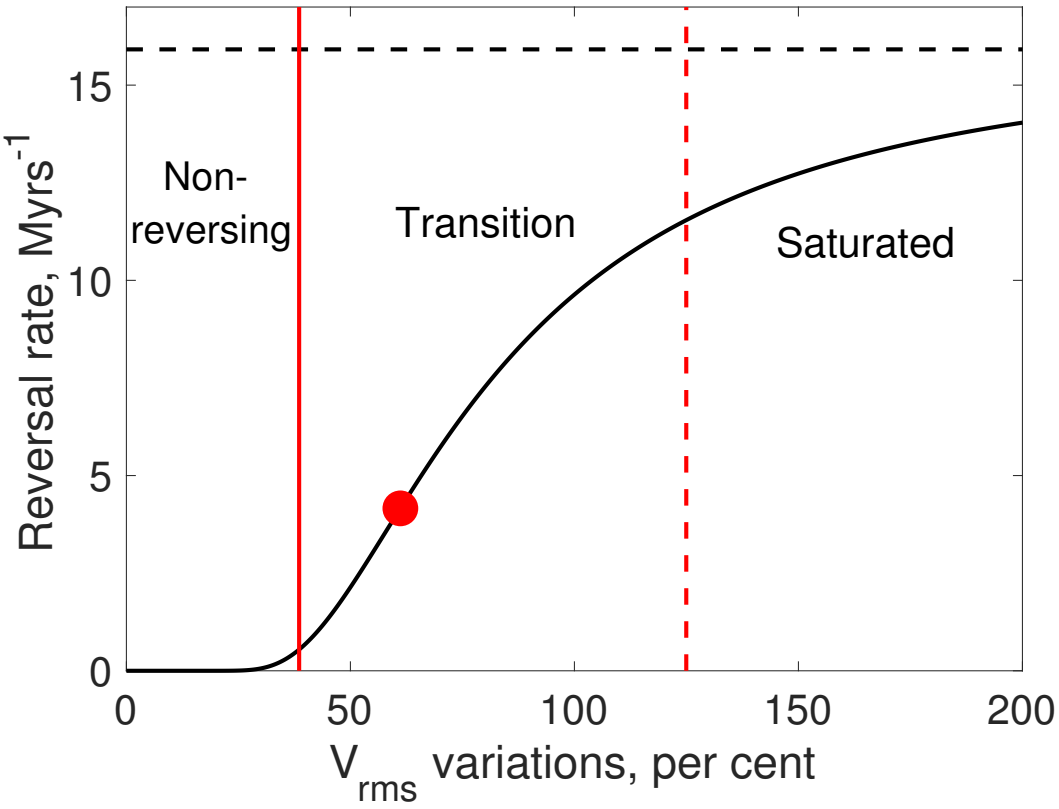

Figure 4.10: Predicted reversal rates for the recent paleomagnetic field as a function of $\langle \Delta V_{\rm rms}^2 \rangle^{\frac{1}{2}} / \langle V_{\rm rms} \rangle$, assuming that the relative variations in velocity and magnetic field are equal. The red circle indicates recent reversal rate, where the velocity variation is roughly 60%. The black dashed line indicates the asymptotic reversal rate. The red solid and red dashed lines indicate the critical and saturation reversal rate thresholds, (4.6.5) and (4.6.6), respectively.

convective vigour. Theoretical and numerical power spectra are in excellent agreement, even though no long timescale information was used to build the stochastic models.

Detailed output from the dynamo model is used to interpret the terms in the stochastic model. The drift term reflects the slow adjustment of the dipole field to its time average. Average variations in ADM are accommodated by the slowest decay mode, however the relaxation back to time average is enhanced by turbulent diffusion, giving a shorter timescale of relaxation than the molecular rate of decay (Gubbins and Roberts, 1987). The noise term characterises variations in the amplitude of dipole field generation, arising from velocity and magnetic field variations, whereas the correlation of this process is set by the lifetime of convective fluctuations. If the paleomagnetic field can be interpreted this way, the strength of such fluctuations would have a strong influence on the reversal rate. Small decreases in the rms velocity variation is sufficient to terminate reversals.

Chapter 5

Analysis of a Reversing Geodynamo Simulation

Foreward

In order to continue investigating stochastic models of geomagnetic field variations, I extend the analysis of the previous chapter to a reversing geodynamo simulation. Specifically, I construct a stochastic model from the results of a reversing numerical geodynamo simulation, and investigate whether variations in the axial dipole field can be accurately reproduced. Particular attention is paid to the statistics of polarity reversals. I also consider the possibility of using stochastic models that are fitted from short simulations to predict long-run reversal statistics.

This work was performed in collaboration with Bruce Buffett (University of California, Berkeley), Nathanaël Schaeffer (ISTerre, CNRS, Université Grenoble Alpes), and Alexandre Fournier (Université de Paris, Institut de Physique du Globe de Paris). Permission to present this work in this dissertation has been obtained from these co-authors.

Summary

Fluctuations in the Earth's magnetic field occur on a wide range of timescales. It has been proposed that stochastic models may be able to reproduce the statistics of variations in the Earth's axial magnetic dipole field. Here we analyze a stochastic model derived from the output of a reversing numerical geodynamo simulation. We find that the bimodal distribution of chron durations in the simulation is approximately reproduced by the stochastic model. The average reversal rates are almost comparable, suggesting that stochastic models can reproduce some bulk qualitative characteristics and quantitative properties of simulated axial dipole field variations. We also investigate the effect of the simulation length on the accuracy of the fitted stochastic model. The data used here were obtained from a computationally expensive, long-duration simulation. We thus investigate whether it could be possible to extract the same statistical information from the results of shorter simulations. We find that similar stochastic models can be fitted with the first $\sim 20\%$ of the simulation.

5.1 Introduction

The geodynamo is a complex and chaotic system. Its time evolution is governed by the interactions between fluid motions and the magnetic field in the outer core (Roberts and King, 2013). These interactions generate a magnetic field that is observable at the Earth's surface, which exhibits variations over a broad range of timescales, from historical secular variation to superchrons spanning tens of millions of years (Constable and Johnson, 2005). Observations of the external magnetic field represent one of the few methods we have to gain insight into the deep Earth; however, links between the dynamics of the geomagnetic field and physical processes within the core are still poorly understood. Numerical geodynamo simulations offer one way of exploring these connections (Wicht and Sanchez, 2019). These simulations solve the full magnetohydrodynamic equations in a 3D domain, and as such the internal details of the flow and magnetic field are directly accessible. Although numerical limitations necessitate that these simulations are conducted at parameters far from those of the Earth (Wicht and Sanchez, 2019), many properties of the external field can be reproduced (Christensen et al., 2010).

One property of particular interest in geodynamo models is the presence reversals, where the axial dipole field completely changes sign and attains a stable opposite polarity (Wicht et al., 2009; Amit et al., 2010; Glatzmaier et al., 2015). These are a first-order feature of paleomagnetic observations, which show that the Earth's field reversed polarity many times throughout of Earth's history (Valet and Fournier, 2016). As such, the presence and frequency of polarity reversals have been suggested as criteria for the indication of Earth-like geodynamo simulations (Sprain et al., 2019). Numerous studies have been able to produce numerical dynamos that exhibit reversals (see Glatzmaier et al., 2015, for a comprehensive review), and these simulations have enabled the investigation of links between the state of the core and the frequency and style of reversals. Connections have been made to the

role of the inner core (Lhuillier et al., 2013, 2019), thermal conditions at the core-mantle boundary (Olson and Amit, 2014), as well as the style and vigor of convection (Christensen and Aubert, 2006; Meduri et al., 2021). However, a recurring difficulty encountered in these studies relates to the typical rarity of reversals. Adequately constraining an accurate estimate of reversal rates generally requires a simulation to sample hundreds of reversals, requiring long integration times. For example, in order to adequately estimate the rate of reversals, Lhuillier et al. (2013) ran low-resolution simulations for 50 Myr in scaled time. This is particularly impracticable in the case of higher-resolution simulations, where long integration times come at great numerical expense, sometimes requiring millions of CPU hours (Roberts and King, 2013; Schaeffer et al., 2017). This poses the question: can asymptotic reversal rates can be predicted with more efficient methods than direct, brute-force simulation?

One option it to employ a "rare event sampling" technique, which forces a computer simulation to selectively sample states or transition paths of interest (e.g., Bouchet et al., 2019; Hussain and Haji-Akbari, 2020). Although such methods have seen great success in other areas of geophysics (e.g., Hoffman et al., 2006; Weare, 2009; Ragone et al., 2018; Webber et al., 2019), they have yet be used in the context of geodynamo simulations. An alternative approach is to use a suite of geodynamo simulations to search for correlations between asymptotic reversal rates and some other "proxy" attribute of the field. The hypothesis is that reversal rates might obey some sort of scaling law, which is reflected in other details of field variations. If the proxy attribute can be constrained with shorter simulation lengths, and assuming the proposed correlations can be extrapolated to simulations outside of the sample, this would allow for the prediction of reversals rates of new simulations with much shorter integration times. This approach was explored in Lhuillier and Gilder (2013), where the authors investigated the variabilities of the external field in dynamo simulations, as it would be observed from the Earth's surface. Specifically, relative fluctuations in surface field intensity and the dispersion of virtual geomagnetic poles were found to be good proxies for reversal rate in their set of simulations. A different approach was taken by Wicht and Meduri (2016), where the shape of the histograms of axial dipole intensity were investigated. They found that the absolute intensities of non-reversing simulations had approximately Gaussian distributions, whereas reversing simulations were more negatively skewed. Although these attempts showed some predictive power, they exclusively considered quantities that are agnostic to time-dependencies of the field, disregarding valuable information present in the time-dependent field.

Another possible option is to model the time-dependent variability of the external field as a stochastic processes (Brendel et al., 2007; Buffett et al., 2013; Meduri and Wicht, 2016; Bouligand et al., 2016; Morzfeld and Buffett, 2019). Stochastic processes are commonly used to describe the variability of a small set of representative quantities in large and complex physical systems (see Friedrich et al. (2011) for a comprehensive review). For the geomagnetic field, the time dependence of the axial dipole moment (ADM) is modeled as the result of a stochastic differential equation (SDE). The underlying assumption of the dynamics is a temporal separation of scales: that the internal memory of fluctuations is substantially shorter than macroscopic response timescales. These SDEs have two main components. The

first term—the drift function—governs the slow deterministic adjustment towards average stable states. The second term—the noise function—sets the amplitude of random fast-scale fluctuations. These functions are generally assumed to be independent of time, reflecting the fact that the simulations often have no long-term secular evolution or forcing. The drift and noise functions can be fitted from time-series data using established methods (e.g., Siegert et al., 1998; Friedrich et al., 2011). Recent studies have suggested that SDEs are able to reproduce some properties of non-reversing ADM fluctuations, including the power spectra (Buffett and Matsui, 2015; Davis and Buffett, 2021) and the variability of millennial-scale trends (Buffett et al., 2019). Although stochastic models were previously explored in the context of reversing dynamo simulations (Meduri and Wicht, 2016), the capacity of SDEs to reproduce reversal rates was not investigated. This poses the question: can stochastic models reproduce reversal statistics of numerical simulations? If so, then this raises a second question: can reversal rates be reliably predicted from SDEs built with short simulation times, perhaps only displaying a few reversals? This would be particularly useful for systematic parameter searches for Earth-like dynamo simulations (Lhuillier et al., 2013; Olson and Amit, 2014; Wicht and Meduri, 2016; Lhuillier et al., 2019; Meduri et al., 2021).

The purpose of this study is twofold. First, we aim to qualitatively and quantitatively compare the ADM of a reversing numerical dynamo simulation and a corresponding stochastic model. To do this, we begin by examining the ADM variations from a long-run reversing numerical dynamo simulation. Under the assumption that the ADM variations can be well described by an SDE model, we fit the corresponding drift and noise functions of that model. A time-series realization of this model is then produced, and compared with the original simulation data. Specific attention paid to the statistics of reversals, and we investigate whether the SDE model can reproduce the reversal rate of the dynamo simulation. The second aim is to investigate the effect of length of data on the fitted stochastic model, and whether a stochastic model can predict asymptotic reversal rates with only a short length of data.

5.2 Descriptions of the Geodynamo Simulation and Stochastic Model

We compare the time-series of ADM variations from a dynamo simulation with a reconstruction from an SDE. The geodynamo simulation, which is considered as the "ground truth", is a direct numerical simulation of the three-dimensional magnetohydrodynamic (3D MHD) equations. The reconstruction is a time-series realization of an SDE model, which is fitted from the statistics of the 3D MHD time-series. We briefly describe the numerical simulation and corresponding stochastic model.

3D MHD Geodynamo Simulation

Numerical geodynamo simulations solve the governing equations of thermal-chemical convection and magnetic field induction in the core. For this study, we consider a dynamo simulation

which exhibits polarity reversals and dipole excursions. The simulation is part of an ensemble of reversing simulations, and has been presented previously in Gwirtz et al. (2021). The set of equations governing rotating dynamo action in a spherical shell geometry are solved with a pseudo-spectral approximation using the `xshells`[1] code. The physical scales chosen to non-dimensionalize the governing equations are the same as those used by Schaeffer et al. (2017). The radius ratio of the inner-core boundary to the core-mantle boundary is set to its present-day value. The 3D simulation has no-slip boundary conditions on the inner-core and core-mantle boundaries, and it assumes that the inner core is electrically conducting. The solution is specified using four non-dimensional control parameters, including the Ekman number $\mathrm{Ek} = 10^{-4}$, the Prandtl number $\mathrm{Pr} = 1$, the magnetic Prandtl number $\mathrm{Pm} = 3$, and the Rayleigh number $\mathrm{Ra} = 1.5 \times 10^3$ (see Schaeffer et al. (2017) for definitions). In order to scale to physical time, the time-average power spectra of the magnetic field and its secular variation are computed for the non-dipole field up to spherical harmonic degree 13. Time is then scaled under the assumption that the dynamo simulation and the earth share the same secular-variation time scale, namely 415 years (Lhuillier et al., 2011). This approximately corresponds to advective scaling, as the secular variation is mostly due to flux transport. With this scaling the simulation has a sampling interval $\Delta t \sim 43$ years, and a total length of 172 million years. In this time frame, approximately 142 long-scale polarity changes occur. For further technical details of the simulation, and descriptions of its favourable physical and morphological attributes compared to the Earth's magnetic field (Christensen et al., 2010; Sprain et al., 2019), see Section 2.2.4 of Gwirtz et al. (2021). For this study, we will exclusively examine the time dependence of the ADM from this simulation, as shown in the left panels of Fig. 5.1. In the next section, we use this time-series to construct a stochastic model for ADM variations.

Stochastic Model for Axial Dipole Moment Variations

For the stochastic model of ADM variations, we use a scalar SDE driven by exponentially correlated noise (Davis and Buffett, 2021). The time evolution of the ADM $X(t)$, and its driving noise $\zeta(t)$, is written as

$$\frac{d}{dt}X(t) = v(X(t)) + g(X(t))\zeta(t), \tag{5.2.1}$$

$$\frac{d}{dt}\zeta(t) = -\frac{1}{\theta}\zeta(t) + \frac{1}{\theta}\xi(t), \tag{5.2.2}$$

where $v(x)$ is the drift function, $g(x)$ is the noise function, θ is the correlation time of the noise, and $\xi(t)$ is internal Gaussian white noise. The drift function governs the slow deterministic adjustment towards equilibrium states, whereas the noise function sets the amplitude of random fast-scale fluctuations. The drift and noise functions are independent

[1]This code is available at `https://nschaeff.bitbucket.io/xshells/`

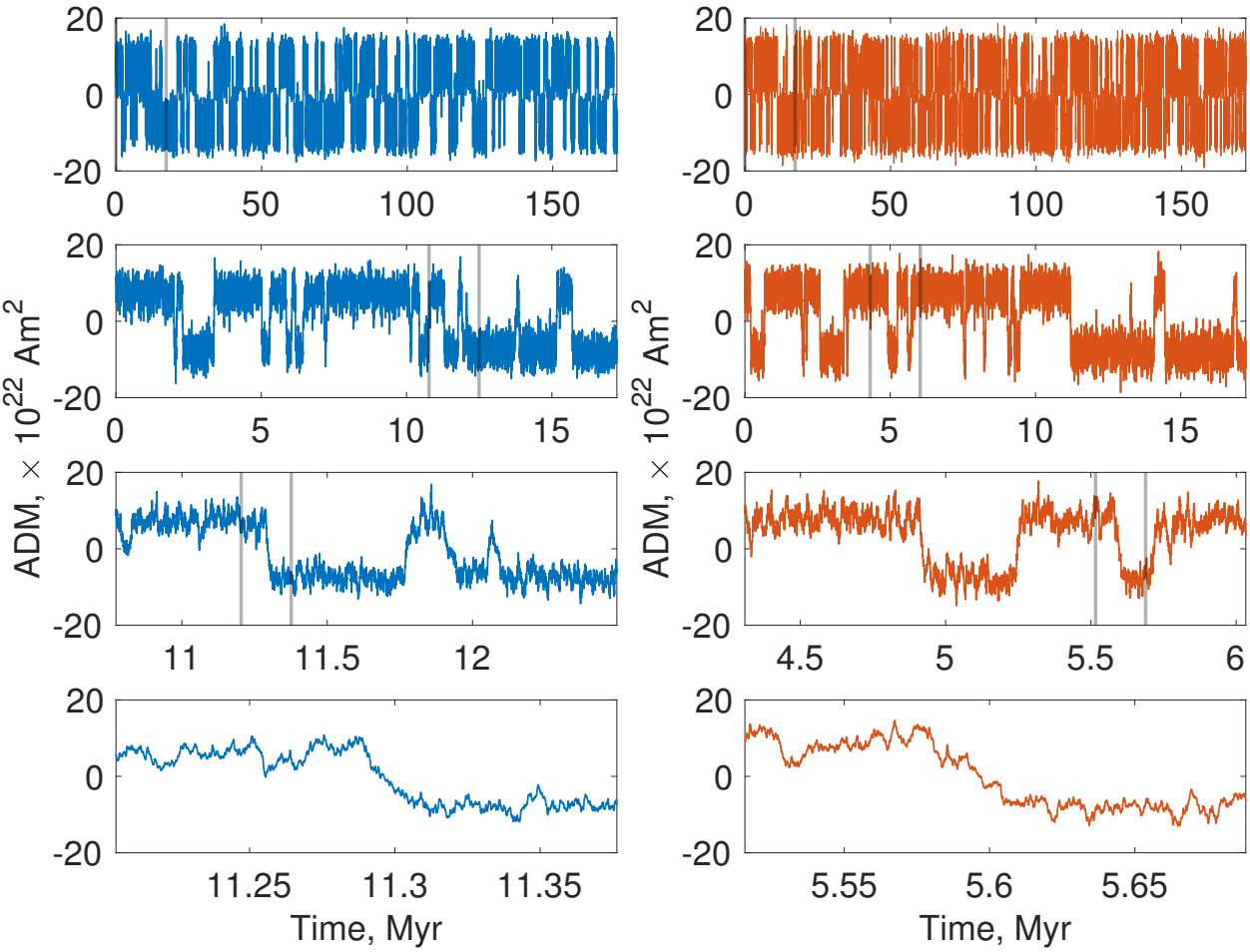

Figure 5.1: Time variations in axial dipole moment for the 3D MHD simulation (left, in blue) and the SDE realization (right, in orange). The top panels illustrate the full length of the data, and subsequent panels highlight increasingly smaller timescales (sections indicated with gray vertical lines).

of time, reflecting the fact that the 3D MHD simulation has no long-term secular evolution or forcing. The process $\zeta(t)$ drives the fast scale fluctuations in the system, and has a vanishing average

$$\langle \zeta(t) \rangle = 0, \tag{5.2.3}$$

and an autocorrelation of

$$\langle \zeta(t)\zeta(t') \rangle = \frac{1}{2\theta} e^{-|t-t'|/\theta}. \tag{5.2.4}$$

This form ensures well defined time-derivatives of $X(t)$ (Van Kampen, 1992), which is appropriate as we expect the rate of change of the ADM to converge to well defined values.

We fit the drift and noise functions, and correlation time θ, from the dimensional ADM time-series of the dynamo simulation using the method of Lehle and Peinke (2018). A full description of the implementation of this method is available in Section 3.2 of Davis and Buffett (2021), as well as Section 4.3 of this thesis. We give a brief summary here and reiterate the details relevant to this study. The first two conditional moments of the increments in $X(t)$ are calculated directly from the time-series data,

$$\widehat{M}^{(1)}(x,\tau;h) = \Big\langle \lfloor X(t+\tau) - X(t) \rfloor_{X(t)=x} \Big\rangle, \tag{5.2.5}$$

$$\widehat{M}^{(2)}(x,\tau;h) = \Big\langle [\lfloor X(t+\tau) - X(t) \rfloor_{X(t)=x} - \widehat{M}^{(1)}(x,\tau;h)]^2 \Big\rangle. \tag{5.2.6}$$

Here $\langle \dots \rangle$ indicates averaging over all times t, and $\lfloor \dots \rfloor_{X(t)=x}$ indicates state conditioning which is accomplished through kernel averaging (Lamouroux and Lehnertz, 2009). For example, evaluating equations (5.2.5–5.2.6) at $\tau = 15\Delta t$ involves averaging across all time-steps that are $15\Delta t$ apart. These two moments are calculated at a range of spatial evaluation points x, and time-difference evaluation points τ, for a set kernel bandwidth h. Lehle and Peinke (2018) showed that the expected conditional moments moments $M^{(k)}(x,\tau)$ of an arbitrary SDE defined by (5.2.1-5.2.2) can be represented in the form

$$M^{(k)}(x,\tau) \approx \sum_{i=1}^{3} \lambda_i^{(k)}(x) r_i(\tau;\theta), \quad k = 1, 2, \tag{5.2.7}$$

where terms $\mathcal{O}(\tau^4)$ and higher are omitted. Functions r_i are prescribed basis functions, and $\lambda_i^{(k)}(x)$ are the corresponding coefficients. We note that for relation (5.2.7), a prior fit of θ is required. This step follows a similar procedure as above, involving a comparison of the sample autocorrelation of $X(t)$ to theoretical predictions. Details of this step are present in Appendix B of Davis and Buffett (2021), as well as Appendix B of this thesis. Following from the expansions (5.2.7), the $i = 1$ coefficients of $\lambda_i^{(k)}(x)$ can be related to the drift and noise functions of the original SDE,

$$\begin{aligned}\lambda_1^{(1)}(x) &= v(x) + \frac{1}{2}g(x)g'(x) + \frac{1}{2}\theta\Big(v'(x)g(x)g'(x) - v(x)g'(x)^2\Big),\\ \lambda_1^{(2)}(x) &= g(x)^2 + \theta\Big(v'(x)g(x)^2 - v(x)g(x)g'(x)\Big),\end{aligned} \tag{5.2.8}$$

where $v'(x)$ and $g'(x)$ are the derivatives of the drift and noise functions evaluated at x, respectively. In summary, the overall method can outlined in the following steps:

1. Fit the correlation time, θ.
2. Calculate the conditional moments (5.2.5)–(5.2.6).
3. Posit that the conditional moments follow the relation (5.2.7), and extract coefficients $\lambda_i^{(k)}(x)$ at a range of evaluation points in x.
4. Finally, solve the differential-algebraic equations (5.2.8) for the drift and noise functions, $v(x)$ and $g(x)$.

This method intrinsically accounts for the effects of correlation in the noise, in contrast to the "direct estimation" method (Siegert et al., 1998; Friedrich et al., 2002) used in previous studies (Buffett et al., 2013; Meduri and Wicht, 2016).

For the 3D MHD data, conditional moments are calculated for a set of 50 equally spaced evaluation points in x, in the range $[-14, 14] \times 10^{22}$ Am^2, and we use a kernel bandwidth $h = 1.05$. The time-difference evaluation points τ are from the sampling interval Δt to $\tau_{\max} = 15\Delta t \approx 646$ years. The value of $\tau_{\max}$ is picked using a heuristic described in Lehle and Peinke (2018), however the fitted stochastic model is not overly sensitive to this choice. Fig. 5.2 shows the sample conditional moments extracted from the time-series data, as well the functional fit.

After the inversion process the fit to the data is excellent, having an average mean error comparable to the calculations of Lehle and Peinke (2018) and Davis and Buffett (2021). The fitted drift and noise functions are shown in Fig. 5.3. The correlation timescale is found to be $\theta = 70.7^{+1.1}_{-1.0}$ years (see Fig. 5.4). This bound is very far from overlapping with zero, suggesting that the process is not driven by white noise. We note that repeating the fitting process with the non-dimensional time-series and applying dimensional scaling afterwards gives almost identical results. Alternatively, if the white noise assumption is enforced by using the direct estimation method, we observe absolutely lower drift and noise functions (Fig. 5.3) which corresponds to inconsistent conditional moments (Fig. 5.2).

With the drift and noise functions of the SDE model now fitted, a time-series realization can be computed. Equations (5.2.1–5.2.2) are integrated forward in time using the Euler-Maruyama method (e.g., Kloeden and Platen, 2013) and a random sample of internal noise ξ. We use an internal time-step of $\delta t = 0.02 \times \Delta t = 0.86$ years. Arbitrary initial conditions for $X(0)$ and $\zeta(0)$ are imposed as the memory of these conditions are quickly forgotten. The realization is integrated until reaching steady state dynamics, and then subsequently recorded for a given time-span. In principle the realization could be integrated to any required length,

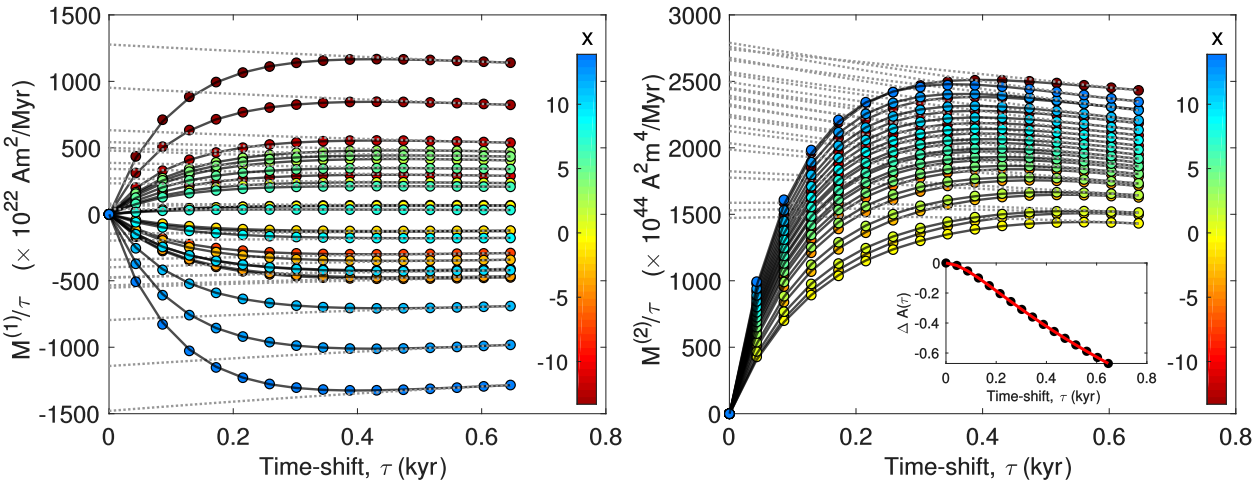

Figure 5.2: The first (left) and second (right) conditional moments calculated from the ADM of the dynamo simulation. Colored circles indicate calculated moments from equations (5.2.5–5.2.6). The color of the circles corresponds to the evaluation point x for the moment calculation, and is indicated by the colorbar. Solid black lines indicate the resulting best fit for a process driven by correlated noise (Lehle and Peinke, 2018; Davis and Buffett, 2021), whereas dashed gray lines indicate moments for a process driven by white noise, fit using the direct estimation method (Siegert et al., 1998). Note that the direct estimates diverge from the calculated moments at low time-shifts. For visual clarity, the moments have been downsampled to a set of 25 equally spaced points in x. The inset in the right plot shows the sample autocorrelation increments and its prediction, as black circles and a red line, respectively. Data from every 15th $\mathcal{T}$ evaluation point is plotted.

however for a fair comparison we choose to match the length and sampling interval of the 3D MHD simulation, as shown in the right panels of Fig. 5.1. With the stochastic model now defined, we proceed by comparing its realization to the time-series of the original dynamo simulation.

5.3 Comparison of Chron Durations and Reversal Rates

A comparison of the time-series of the 3D MHD simulation and the SDE realization in Fig. 5.1 shows that the two time-series look, qualitatively, similar on a range of timescales. For a more quantitative comparison, we investigate the distributions of chron durations for the two time-series.

The zero-crossing times of both the 3D MHD and SDE time-series are determined, and the durations of time between consecutive zero-crossings are defined as chrons. By this choice, excursions are not considered as a separate family of events. The left panel of Fig. 5.5 shows

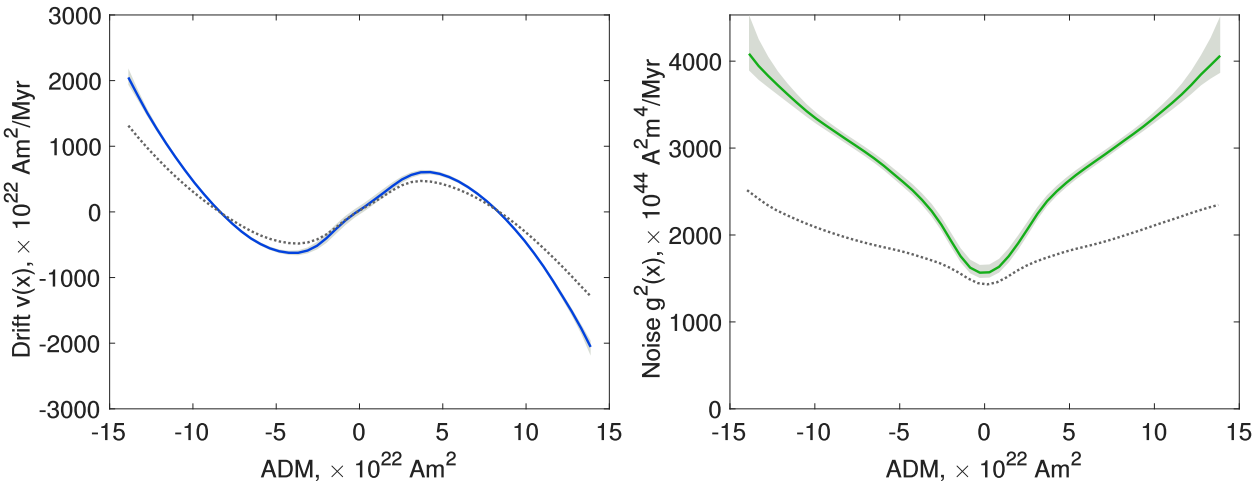

Figure 5.3: Drift (left) and noise (right) functions fitted to the ADM of the dynamo simulation. Solid colored lines indicate the fitted functions, and grey shaded areas indicate estimated 95% confidence intervals, calculated with a block bootstrap algorithm using 10 000 resamples (Kunsch, 1989). These uncertainties are very small, due to the great length of the time-series data. Dotted grey lines indicate functions calculated using the direct estimation method, evaluated at $\tau = \tau_{\max}$.

the distributions of these chron-durations for the two records. Two types of polarity reversals are present: (1) chrons related to the average transition from a mean state of one polarity to the alternate mean state; and (2) chrons corresponding to frequent fluctuations around zero (Constable and Parker, 1988; Wicht and Meduri, 2016). This dichotomy is apparent in chron durations as well as the average ADM strength during a chron, as shown in Fig. 5.6. The stochastic model recovers the bimodal distribution of chron durations in the dynamo simulation. For type 1 chrons the 3D MDH time-series has a modal duration of $\sim$ 350 kyr, while the SDE realization reproduces more chrons at a modal duration of $\sim$ 200 kyr. For type 2 chrons the 3D MDH and the SDE records both have a modal duration of $\sim$ 500 years, however the SDE model reproduces fewer chrons. It should be noted that type 1 chrons here correspond to what are commonly identified as a reversal, whereas type 2 chrons are expressions of reversal complexities, and would be masked by the slow magnetic acquisition process in marine magnetic anomalies (e.g., Lowrie and Kent, 2004). Smoothing both records by 25 kyr—representing the resolution of marine magnetic anomalies—indeed reduces the abundance of type 2 chrons, as shown in the right panel of Fig 5.5. To interpret these data in the same way as the paleomagnetic record, we interpret reversal rates as the inverse of chron durations, using the smoothed records. The 3D MHD simulation has a mean reversal rate of 0.82 Myr^{-1}, and the SDE realization has a rate of 2.00 Myr^{-1}.

The mean reversal rates of the 3D MHD simulation and the SDE model are not equivalent, showing greater than a factor of two difference. On the other hand, there is a overlap in the distribution of observed chron durations, Fig. 5.5. The chron durations of both records

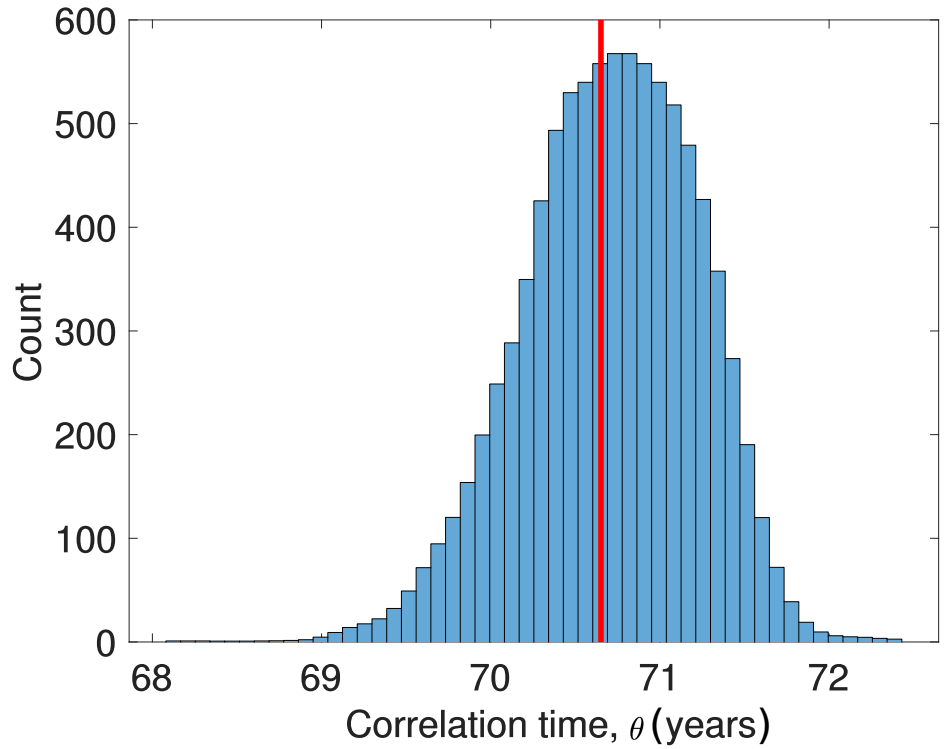

Figure 5.4: Fitted noise correlation time, θ, for the stochastic model of ADM variations. The red vertical line indicates the full data fit, and the histogram shows the distribution of the 10 000 bootstrap resamples.

show a bimodal distribution, indicating a qualitatively similar behavior over a wide range of timescales. This bimodal distribution is also reflected in the average absolute chron amplitudes, which is reproduced approximately by the SDE model (see Fig. 5.6). The SDE model is approximately able to reproduce some quantitative properties of the dynamo simulation, with similar short-scale polarity changes, but larger discrepancies for the long-scale reversals. Overall, the bulk qualitative characteristics of the ADM variations of the dynamo simulation are approximately reproduced by the form of the SDE (5.2.1–5.2.2).

Alternate SDE Approaches

Although some properties of the ADM variations of the dynamo simulation were somewhat reproduced by the stochastic model, the mean reversal rate was overpredicted. One question that arises is whether a stochastic model specially formulated to match the reversal statistics could also be consistent with the shorter time-scale statistics of the original data. As an illustrative example, we alter the fitted drift and noise functions such that the chron-duration distribution of the resulting stochastic realization matches that of the 3D MHD simulation. The characteristic shapes of the fitted drift and noise functions are kept the same, and we

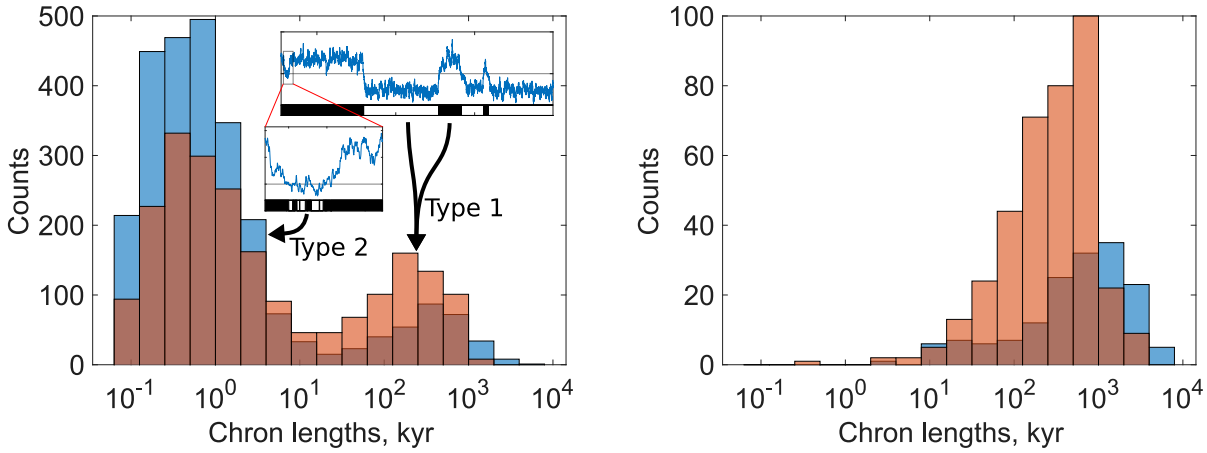

Figure 5.5: Chron-duration distributions for the 3D MHD time-series (blue) and the stochastic realization (orange). The chron durations for the original records (left) are compared with filtered records (right) to represent the typical resolution of marine magnetic anomalies (Lowrie and Kent, 2004). The filter is a moving average with a width of 25 kyr. A schematic is included in the left panel, depicting the typical behavior of type 1 and type 2 chrons.

only consider linear transformations. In order to encourage longer type 1 reversals, we reduce the drift function and correlation time by 50%. The empirical probability distribution of the time-series is kept similar to the original SDE model by applying an appropriate linear transformation to the noise function (e.g., Risken, 1996). A realization of this new SDE model is produced, and its chron-duration distribution is calculated similarly to the original SDE model. Fig. 5.7 shows the chron-duration distributions for the 3D MHD simulation as well as this new SDE model.

This comparison between the 3D MHD simulation and the new SDE model is excellent. The type 1 chrons of the new SDE model reproduced that of the 3D MHD simulation in both duration and quantity. For type 2 chrons, the new SDE model predicts the modal duration of ~ 300 years. This is a slight underprediction compared with the value from the 3D MHD time-series, ~ 350 years. Similar to the original SDE model, the new model also reproduces fewer type 2 chrons. Although this new SDE model is able to successfully reproduce the large-scale reversal statistics of the original 3D MHD simulation, it produces a very poor fit to the conditional moments of the original data, as shown in Fig. 5.8.

The poor fit of conditional moments reveals that the proposed drift and noise functions are not representative of the statistics of the original 3D MHD simulation at small time increments. This example shows that the replication of reversal rates does not necessarily guarantee a self-consistent stochastic model.

The original stochastic model was not able to accurately reproduce the average reversal rate of the dynamo simulation, overpredicting by approximately a factor of two. However,

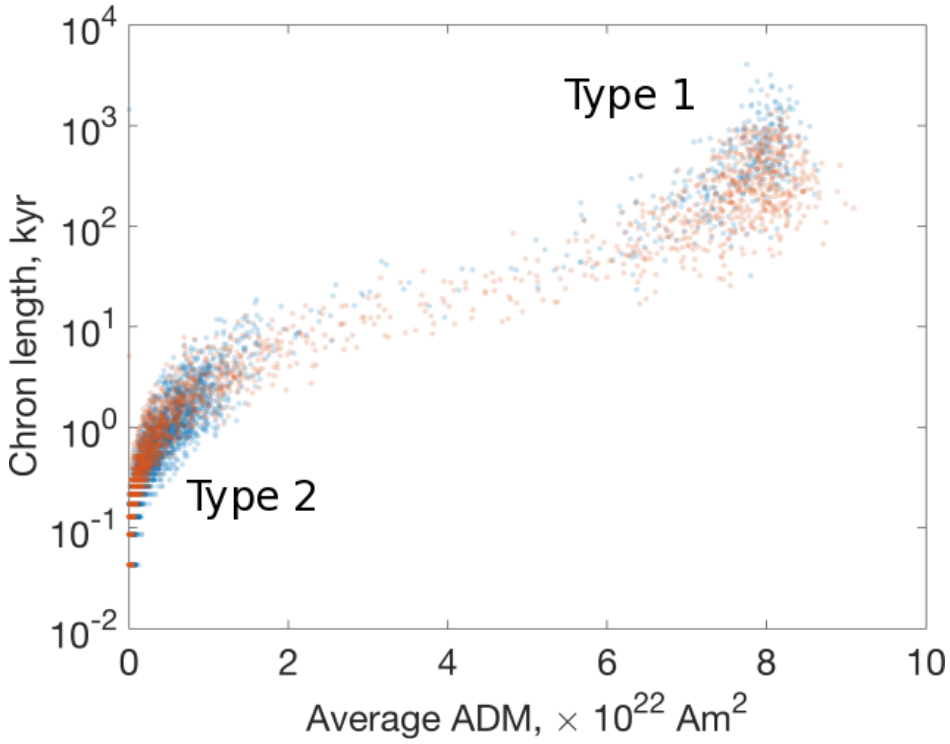

Figure 5.6: Distribution of average absolute chron amplitudes and chron-durations, for the 3D MHD time-series (blue) and the stochastic realization (orange). Each point represents a single chron. The bimidal dustribution of type 1 and 2 chrons are indicated.

as this prediction is the same order of magnitude, the bias might be tolerable and useful results may still be obtained. In particular, this suggests that SDEs may be used as a tool for predicting the asymptotic reversal rates of shorter dynamo simulations, which perhaps display only a few reversals. This is of interest to systematic searches of parameter space for Earth-like dynamo simulations (Lhuillier et al., 2013; Olson and Amit, 2014; Wicht and Meduri, 2016; Lhuillier et al., 2019; Meduri et al., 2021). In the next section, we ask the question: what is the critical amount of data required to estimate asymptotic reversal rates?

5.4 The Effect of Simulation Length on Model Reliability

The estimation of asymptotic reversal rates in numerical geodynamo models often necessitates long simulation lengths (e.g., Lhuillier et al., 2013). As numerical dynamo simulations are computationally intensive, this makes a direct assessment of reversal statistics difficult. On the other hand, estimation of reversal rates from shorter simulations may introduce bias.

In the previous section, we showed that a stochastic model can approximately repro-

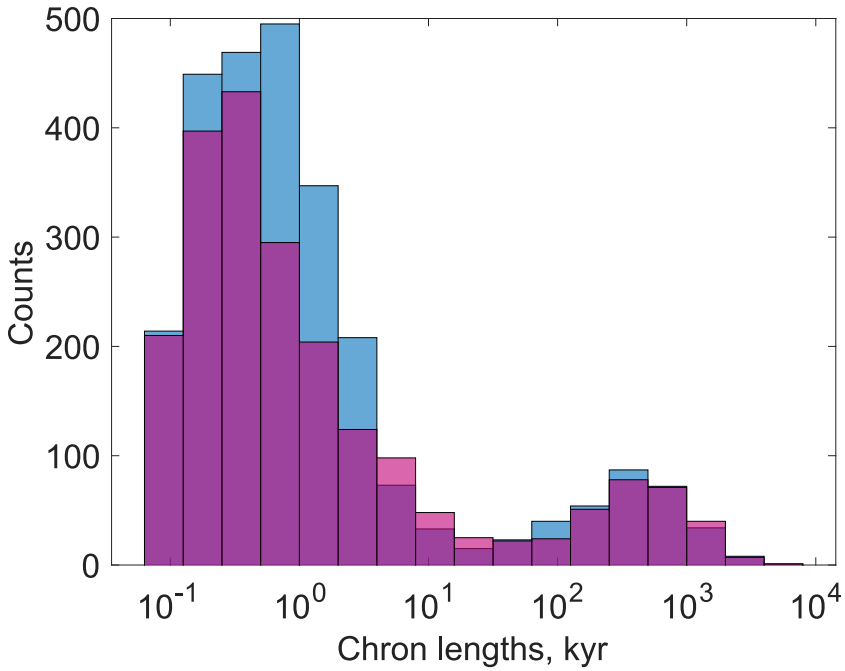

Figure 5.7: Chron-duration distributions for the 3D MHD time-series (blue) and a stochastic process formulated to produce a similar chron-duration distribution (purple).

duce the broad reversal statistics of a dynamo simulation, with about a factor of two error. As such, it may be possible to recover reversal statistics from stochastic models built from shorter simulations, displaying only a few reversals. Therefore it is important to investigate the effect of the length of data on estimated statistical properties. If the length of data is too short, then an estimate will not be representative of the asymptotic value. Alternatively, a long simulation will produce well-constrained results at the cost of excessive computational effort. A *post hoc*, qualitative comparison can be accomplished by repeating the drift and noise function fitting with a fraction of the length of the time-series. For example, repeating the fit with 10% of the data gives drift and noise functions that cannot be visually distinguished from the functions in Fig. 5.3. However we seek a quantitative assessment of this similarity. Ideally this assessment should also be applicable for determining an early-stopping point when running numerical simulations. In this case, the theoretical "ground truth" would not be known beforehand, so any assessment will have to be based off available data up until that current point. A lower limit to the minimum amount of data length necessary is at least enough time for the process to sufficiently explore its parameter space. In the case of a reversing dynamo simulation, this equates to having at least one polarity reversal. Previous research on the topic of data length for fitting SDE functions offers only recommendations on the number of data points used, suggesting counts of $\gtrsim 10^4 - 10^5$ for accurate results (Mourik et al., 2006; Kleinhans and Friedrich, 2007; Lamouroux and Lehnertz,

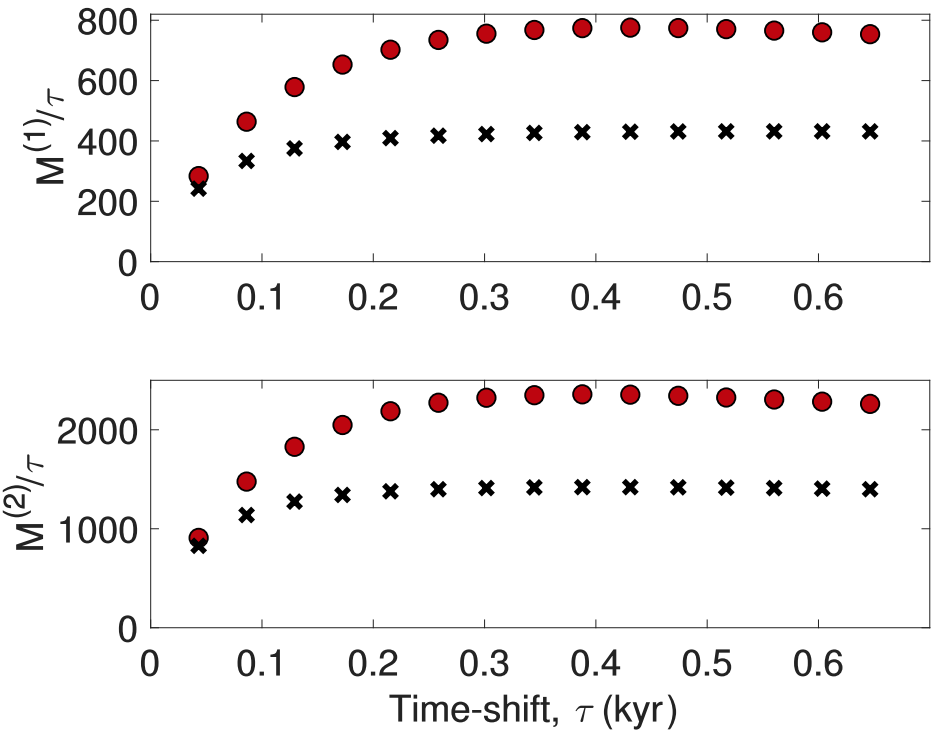

Figure 5.8: The first (top) and second (bottom) conditional moments for the dynamo model and the new SDE model. For visual clarity, only the moments conditioned at $x = -12$ are plotted. Colored circles indicate calculated moments from the ADM of the 3D MHD time-series, using equations (5.2.5–5.2.6). The color of the circles corresponds to the evaluation point x for the moment calculation, using the same color scale as Fig. 5.2. Black crosses indicate moments from the ADM of the new SDE model, evaluated at the same x and τ condition points. Only data from every 15th $\mathcal{T}$ evaluation point is plotted.

2009). These suggestions are conditional on the characteristic timescale of the process and the sampling interval. Furthermore, they are not appropriate for correlated noise, or when using multiple-timestep techniques (Honisch and Friedrich, 2011; Lehle and Peinke, 2018). For this reason, we will focus on the effect of the length of data rather than the number of data points.

The first step is to define a measure of similarity between the drift and noise functions of the full length data, which will be assumed to be the "ground truth", and the functions fitted from shorter data. We consider the fitted drift and noise functions—and corresponding uncertainties estimated though block bootstrap resampling (Kunsch, 1989)—as distributions. As $v(x)$ and $g(x)$ are sampled at $n = 50$ points in x, these these values can be interpreted as two 50×1 column vectors, $\boldsymbol{\mu}_v$ and $\boldsymbol{\mu}_g$. These vectors represent the most likely values in 50-dimensional space for the drift and noise functions, respectively. Similarly, the bootstrap resamples represent 10 000 samples of the drift and noise distributions in 50-dimensional space. To facilitate calculations with these distributions, we use the assumption

that they are well represented by multivariate Gaussian distributions. We then estimate the two 50×50 sample covariance matrices, $\mathbf{S}_v$ and $\mathbf{S}_g$, corresponding to the drift and noise functions, respectively. Using these vectors and covariance matrices, we can measure how many standard deviations a given 50×1 vector, $\boldsymbol{x}$, is from its corresponding distribution,

$$D_v(\boldsymbol{x}) = \sqrt{(\boldsymbol{x} - \boldsymbol{\mu}_v)^\mathsf{T} \mathbf{S}_v^{-1} (\boldsymbol{x} - \boldsymbol{\mu}_v)}, \tag{5.4.1}$$

$$D_g(\boldsymbol{x}) = \sqrt{(\boldsymbol{x} - \boldsymbol{\mu}_g)^\mathsf{T} \mathbf{S}_g^{-1} (\boldsymbol{x} - \boldsymbol{\mu}_g)}. \tag{5.4.2}$$

This method of multivariate distance is sometimes referred to as the Mahalanobis distance (Mahalanobis, 1936). It would be possible to combine (5.4.1) and (5.4.2) into one distance, however it is revealing to keep them separate for comparison. To verify the multivariate Gaussian distribution assumption, we evaluate (5.4.1-5.4.2) for all 10 000 bootstrap samples and compare the distribution of these distances with the predicted form: the chi-squared distribution at 50 degrees of freedom (Slotani, 1964). The deviation from this distribution is very small for both the drift and noise functions, each giving a mean absolute error of about 10^{-3}, validating the assumption.

Now we focus on fits from shorter lengths of data by resampling the original ADM time-series. We choose to fix the start of the sample at the original starting point, to emulate the conditions of running a simulation. Using a fraction of the total data length, $0 < f < 1$, we repeat the fitting of the drift and noise functions, noted as $\boldsymbol{\mu}_{\hat{v},f}$ and $\boldsymbol{\mu}_{\hat{g},f}$. We then calculate the distance of the fitted drift and noise functions, from the full data distribution using (5.4.1–5.4.2), noted as $D_v(\boldsymbol{\mu}_{\hat{v},f})$ and $D_g(\boldsymbol{\mu}_{\hat{g},f})$. Uncertainties on these distances are calculated using 10 000 bootstrap resamples. If the fits from fractional data are similar to the ground truth, then distances (5.4.1–5.4.2) will be small. Otherwise, if the length of data is too short to produce accurate drift and noise functions, the multivariate distances will be large. To assess what distance is considered significantly different, we set up a hypothesis test. Under the null hypothesis, H_0, a candidate drift vector $\boldsymbol{\mu}_{\hat{v},f}$ is not significantly far from the distribution $N(\boldsymbol{\mu}_v, \mathbf{S}_v)$. However, we can reject H_0 with significance p if

$$D_v(\boldsymbol{\mu}_{\hat{v},f}) > F^{-1}_{\chi^2}(1 - p, 50), \tag{5.4.3}$$

where $F^{-1}_{\chi^2}(x, 50)$ is the inverse cumulative distribution function of the chi-squared distribution with 50 degrees of freedom evaluated at x. An equivalent hypothesis and inequality is used for the noise function. We resample the original time-series and calculate distances (5.4.1-5.4.2) for a range of fractions f in the interval $(0, 1)$, shown in the top panel of Fig. 5.9. To assess the sharpness of acceptance/rejection transition, we consider two significance levels of $p = 0.05$ and $p = 0.001$.

For the fitted drift and noise functions with f close to 1, distances D_v and D_g are very small and not significantly different from $N(\boldsymbol{\mu}_v, \mathbf{S}_v)$ or $N(\boldsymbol{\mu}_g, \mathbf{S}_g)$, as expected. This "closeness" continues for decreasing f until approximately $f \lesssim 0.2$ for the drift function, and $f \lesssim 0.1$ for the noise function. At these points, the distances are greater than both

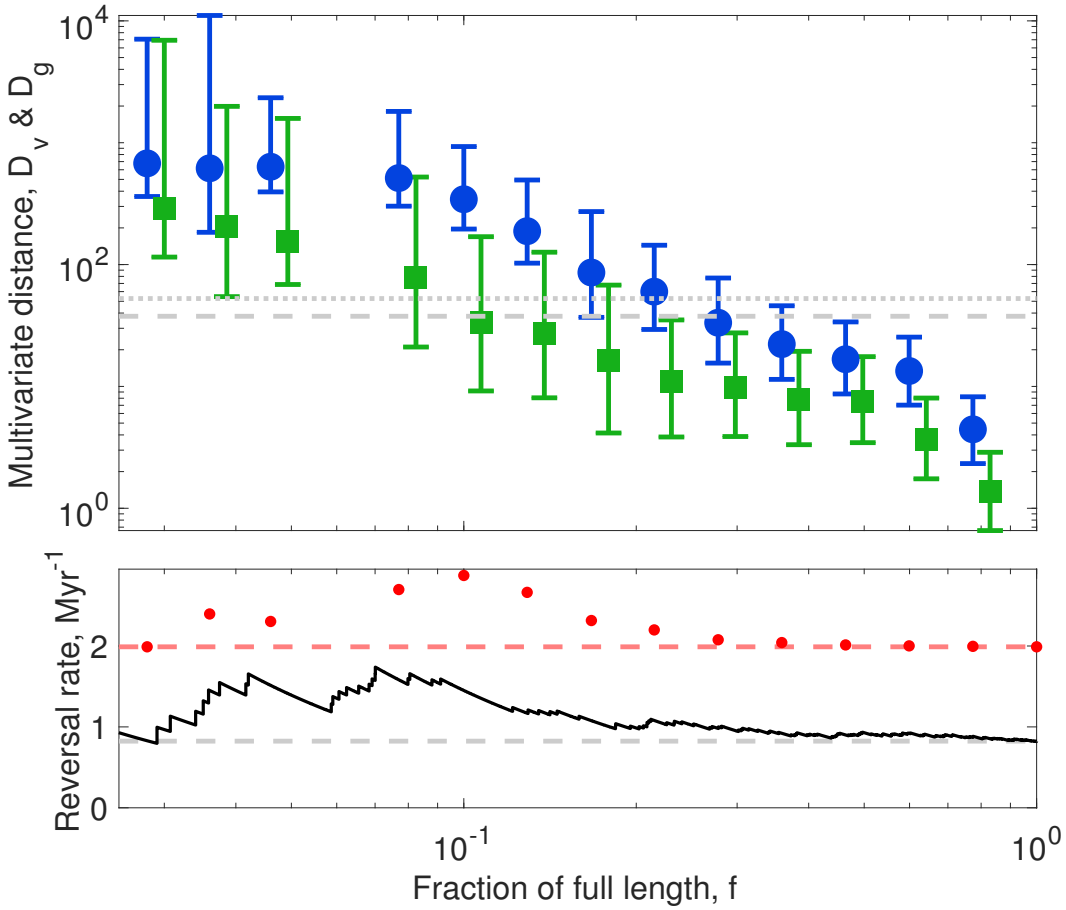

Figure 5.9: Cumulative multivariate distances and reversal rates. The top panel shows multivariate distances for drift and noise functions fit at partial lengths compared with the full length counterparts. Blue circles and green squares indicate the distances for the drift and noise functions, respectively. These points share the same abscissa, so values for the noise functions have been shifted slightly to the right, for visual clarity. Error bars indicate estimated 95% confidence intervals. Horizontal gray dashed and dotted lines indicate distances at $p = 0.05$ and $p = 0.001$ significance, respectively. The bottom panel shows cumulative reversal rates of the dynamo simulation and stochastic models. The black solid line indicates the mean reversal rate for the dynamo simulation calculated using a fraction of the full length of the data. The horizontal grey dashed line indicates the estimated reversal rate using the full length of data. The red circles indicate the predicted asymptotic reversal rate from a stochastic model fit to a fraction of the simulation data. The horizontal red dashed line indicates the predicted reversal rate from a stochastic model fitted to the full length of data.

critical levels and the null hypotheses can be rejected. A realization of an SDE with drift and noise functions fitted with $f = 0.2$ of the data indeed reproduces the chron-duration distributions and mean reversal rate of the full data SDE, see the bottom panel of Fig. 5.9). Repeating this method using several different discretizations of the drift and noise functions (e.g., sampling at $n = 20$ points) has little effect on these results. These results show that stochastic models fitted from the ADM time-series are reliably resolved when $f \gtrsim 0.2$.

5.5 Conclusions

We use a reversing numerical dynamo simulation to construct a stochastic model for variations in ADM. The correlation of the noise is explicitly accounted for—as opposed to previous studies (Buffett et al., 2013; Meduri and Wicht, 2016)—allowing for a model that accurately reproduces the conditional moments. The ADM variations of the dynamo simulation and the stochastic model look visually similar on a broad range of timescales, and both records show bimodal chron-duration distributions, relating to large-scale reversals as well as fast polarity changes at low ADM. The stochastic model approximately reproduces the distribution of shorter reversals, however there is a discrepancy for the longer reversals. At low ADM states the observable field would be dominated by the non-dipole part of the field, and a change in sign of the dipole would have a limited impact on the intensity or direction recorded in paleomagnetic observations (Constable and Parker, 1988). Such fast-scale polarity changes are masked by the gradual acquisition of magnetization in marine magnetic anomalies (Cande and Labreque, 1974; Buffett and Avery, 2019). The average reversal rate of the stochastic model approaches that of the dynamo simulation, overpredicting by a factor of about two. Despite this error, the stochastic model compares to some degree with the dynamo simulation, and this study represents the first attempt at a reconciliation of reversal rates between numerical simulations and stochastic models of ADM variations. Further work should investigate alternate SDE models to (5.2.1–5.2.2), which may be able to better reproduce reversal rates.

We show that a stochastic model specifically constructed to reproduce reversal statistics is not guaranteed to be internally consistent with short-time-scale variations. This lack of consistency indicates that, in such a case, the fitted drift and noise functions are unlikely to reflect any physical processes in the dynamo simulation. Attempts at links to internal mechanisms have been present in previous studies of stochastic models of ADM fluctuations. For example, for stochastic models of non-reversing dynamo simulations, both long-scale properties (e.g., power spectral densities) and shorter scale statistics (e.g., conditional moments) are well represented, allowing the investigation of links between the drift and noise functions and internal field generation mechanisms (Davis and Buffett, 2021). Future work should aim to create stochastic models that can reproduce both shorter timescale statistics—such as the conditional moments—as well as longer scale properties—such as reversal rates—before attempting to investigate links to internal processes in the simulations.

We also investigate the effect of length of data on the fitted stochastic model, with the

aim to predict asymptotic reversal rates from shorter data. Visually similar drift and noise function can be fitted with 10% of the original data. We attempt to further quantify this by developing similarity criteria, which account for uncertainties in the fitted drift and noise functions. However, as this method relies on bootstrap resampling to estimate uncertainties, its accuracy is questionable (Schenker, 1985). From this method, we find that the drift and noise functions fitted from this dynamo simulation are similarly resolved from $\gtrsim 20\%$ of the time-series data, which reproduces the reversal rate of the stochastic model fitted from the full data. For the dynamo simulation discussed here, the first 20% of the data corresponds to approximately 29 large-scale polarity reversals, giving an estimated reversal rate of 1.02 Myr^{-1}. This compares with the full-record rate of 0.82 Myr^{-1}, meaning that the stochastic model shows little advantage to simply estimating the reversal rate directly from a shorter simulation. Together with the bias present in the stochastic model prediction of the reversal rate, the usefulness of this perspective has yet to be demonstrated.

Chapter 6

Estimation of Drift and Diffusion Functions from Unevenly Sampled Time-Series Data

Foreward

When interpreting complex systems like the geomagnetic field as stochastic processes, it is important to quantitatively fit appropriate models. To facilitate this fitting, various top-down statistical methods have been developed. However, paleomagnetic and archaeomagnetic observations of the geomagnetic field are often not compatible with these methods, as they are sampled irregularly in time. In order to analyse geomagnetic observations, I develop a set of techniques for the inference of stochastic processes that allows for irregular sampling. The following chapter introduces these new methods, and demonstrates their validity for a set of numerical and empirical data.

This work has been previously published in:

W. Davis and B. Buffett (2022). "Estimation of drift and diffusion functions from unevenly sampled time-series data". *Phys. Rev. E* 106 (1), p. 014140, DOI: 10.1103/-PhysRevE.106.014140.

Summary

Complex systems can often be modeled as stochastic processes. However, physical observations of such systems are often irregularly spaced in time, leading to difficulties in fitting appropriate models from data. Here we present extensions of two methods for fitting drift and diffusion functions from irregularly sampled time-series data. Our methods are flexible and applicable to a variety of stochastic systems, including non-Markov processes or systems with measurement noise. To demonstrate applicability, we use this approach to analyse an irregularly sampled paleoclimatological isotope record, giving insights into underlying physical processes.

6.1 Introduction

The time-dependent behavior of complex systems consisting of a large number of subsystems can often be described by low-dimensional order parameter equations (Haken, 2004). In many cases, a separation between slow adjustments and fast fluctuations allows such systems to be described by a Langevin-type equation,

$$\frac{d}{dt}X(t) = f(X,t) + g(X,t)\Gamma(t), \tag{6.1.1}$$

where $\Gamma(t)$ denotes the stochastic forcing, with $\langle\Gamma(t)\rangle = 0$ and $\langle\Gamma(t)\Gamma(t')\rangle = \delta(t-t')$ (Risken, 1996). The same information is expressed in the corresponding Fokker-Planck equation,

$$\frac{\partial}{\partial t}p(x,t|x',t') = \left[-\frac{\partial}{\partial x}D^{(1)}(x,t) + \frac{\partial^2}{\partial x^2}D^{(2)}(x,t)\right]p(x,t|x',t'), \tag{6.1.2}$$

which contains the Kramers-Moyal (KM) coefficients

$$D^{(n)}(x,t) = \lim_{\tau\to 0}\frac{1}{n!\tau}\int_{-\infty}^{\infty}\left[x'-x\right]^n p(x',t+\tau|x,t)\;dx', \tag{6.1.3}$$

where $p(\circ|\circ)$ is the transition probability. Here, the first two coefficients are called the drift and diffusion,[1] respectively, connecting to (6.1.1) in $f(x,t) = D^{(1)}(x,t)$ and $g(x,t) = \sqrt{2D^{(2)}(x,t)}$.

It has been shown that it is possible to fit the forms of such processes directly from regularly sampled time-series data using a technique called "direct estimation" (Siegert et al., 1998; Gottschall and Peinke, 2008). This approach has been applied to various fields of science (Friedrich et al., 2011).

There are two main difficulties associated with applying this approach to "real-world" time-series data. The first occurs when observations are contaminated by another undesirable

[1]The diffusion term is also sometimes referred to as the noise term. However, since I will also refer to measurement noise in this chapter, I will exclusively refer to this term as the diffusion.

signal, or measurement noise. In this case, Böttcher et al. (2006) introduced a method to parametrically fit drift and diffusion functions as well as the amplitude of the measurement noise, an approach has been expanded in subsequent studies (Lind et al., 2010; Lehle, 2011; Scholz et al., 2017).

The other difficulty involves the discrete sampling of the time-series data. For low sampling frequencies, is can be difficult to perform or infer the limit $\tau \to 0$ required for direct estimation. In this case, Honisch and Friedrich (2011) proposed a finite-τ prediction/optimization method that correctly recovers drift and diffusion functions even at large, regular sampling. However a related impediment is irregular sampling. In this case, there is no obvious way to calculate averages in (6.1.3). This is commonly encountered in geoscientific measurements (e.g., Schulz and Stattegger, 1997; Rehfeld et al., 2011), but also is encountered in turbulence measurements (Tropea, 1995; Broersen et al., 2000; Harteveld et al., 2005), astrophysical observations (Scargle, 1981; Scargle, 1982; Edelson and Krolik, 1988; Scargle, 1989), and biological systems (Liew et al., 2007). In some cases, interpolation is used to side-step these difficulties; however such methods can introduce a significant and hard-to-quantify bias (Scholes and Williams, 1977; Hayashi and Yoshida, 2005; Rehfeld et al., 2011; Eckner, 2014). This motivates a method for fitting drift and diffusion functions directly from the unaltered time-series data.

In the next section we review the currently available estimation techniques, and propose two extensions for irregular sampling. Section 6.3 gives three numerical examples where we demonstrate the functionality of our new methods. In Section 6.4 we apply this framework to an empirical data-set, namely a paleoclimatological isotope record (Westerhold et al., 2020). Discussion and conclusions are given in Section 6.5, where further applications are proposed.

6.2 Estimation of Conditional Moments

We consider a *stationary* scalar process $X(t)$ that is observed at a set of N increasing points in time, $\{t_1, t_2, \ldots, t_N\}$, with no guarantee of a regular sampling frequency. Observations at these points are denoted as $\{X(t_1), X(t_2), \ldots, X(t_N)\}$. The finite-time KM coefficients of $X(t)$ are defined as (Honisch and Friedrich, 2011)

$$D_\tau^{(n)}(x) = \frac{1}{n!\tau} M^{(n)}(x, \tau), \tag{6.2.1}$$

which are calculated using the finite-time conditional moments

$$M^{(n)}(x, \tau) = \int_{-\infty}^{\infty} [x' - x]^n p(x', t + \tau | x, t)\, dx'. \tag{6.2.2}$$

The task is to estimate these conditional moments from data $X(t)$. These estimates will subsequently be used as finite-time KM coefficients (e.g., Honisch and Friedrich, 2011) in an appropriate method in order to fit drift and diffusion functions of the underlying process.

Conditional moment estimates are denoted as $\hat{M}^{(n)}(x_i, \tau_j)$, and are evaluated at a set of evaluation points in $x_i \in \{x_1, x_2, \ldots, x_{\max}\}$, and $\tau_j \in \{\tau_1, \tau_2, \ldots, \tau_{\max}\}$.

Histogram Based Regression

The simplest way of estimating conditional moments is by means of regressogram, (e.g., Tukey, 1961), also known as histogram based regression (HBR). This estimator can be written as, (e.g., Lamouroux and Lehnertz, 2009),

$$\hat{M}^{(n)}(x_i, \tau_j) = \frac{\sum_{k=1}^{N} I\big(X(t_k) \in B^{(x)}(x_i)\big)\big[X(t_k + \tau_j) - X(t_k)\big]^n}{\sum_{k=1}^{T} I\big(X(t_k) \in B^{(x)}(x_i)\big)}, \tag{6.2.3}$$

where $I(\circ)$ is the indicator function, and binning is indicated with the half closed interval $B^{(x)}(x_i) := [x_i - \frac{1}{2}b_x, x_i + \frac{1}{2}b_x)$, where b_x is the width of the bin.

Histogram Time-Based Regression

One simple way to extend HBR to account for uneven time-sampling is to average over all pairs of increasing times, and also bin data by timestep. We shall refer to this method as histogram time-based regression (HTBR). This approach, when applied to estimators of the autocorrelation function, has been called "slotting" (Edelson and Krolik, 1988). The estimator for conditional moments can be written as

$$\hat{M}^{(n)}(x_i, \tau_j) = \frac{\sum_{k=1}^{N-1} \sum_{l=k+1}^{N} \overbrace{I\big(X(t_k) \in B^{(x)}(x_i)\big)}^{x\text{-conditioning}} \overbrace{I\big(\Delta t_{l,k} \in B^{(\tau)}(\tau_j)\big)}^{\tau\text{-conditioning}} \big[X(t_l) - X(t_k)\big]^n}{\sum_{k=1}^{T-1} \sum_{l=k+1}^{T} I\big(X(t_k) \in B^{(x)}(x_i)\big) I\big(\Delta t_{l,k} \in B^{(\tau)}(\tau_j)\big)} \tag{6.2.4}$$

where $\Delta t_{l,k} := t_l - t_k (> 0)$, and binning in τ is facilitated with a bounded half closed interval $B^{(\tau)}(\tau_j) := [\max(0, \tau_j - \frac{1}{2}b_\tau), \tau_j + \frac{1}{2}b_\tau)$.

Both HBR and HTBR provide simple methods of estimating conditional moments. However the histogram based nature of both methods results in undesirable properties.

1. Histograms assign the same weight to every point inside each bin, resulting in the undesirable property of a sharp cut-off between data across the edge of a bin.

2. The width of the bins sets the resolution length scale, however this length scale dependence is not explicit, it is indirectly determined by the number and range of bins.

Kernel Based Regression

To address the deficiencies of the histogram based approach, Lamouroux and Lehnertz (2009) extended HBR using a kernel based regression (KBR) method. For this, each value of conditional moments at x is assigned an estimate by averaging over all observations according to the distance of the observation $X(t)$ to x. Moments are then estimated with

$$\hat{M}^{(n)}(x_i, \tau_j) = \frac{\sum_{k=1}^{N} K_h(x_i - X(t_k))[X(t_k + \tau_j) - X(t_k)]^n}{\sum_{k=1}^{T} K_h(x_i - X(t_k))} \tag{6.2.5}$$

where $K_h(\circ) = K(\circ/h)/h$ is a scaled kernel, h is the bandwidth, and $K(\circ)$ is the kernel function. Here we use the Epanechnikov kernel (Epanechnikov, 1969)

$$K(x) = \begin{cases} \frac{3}{4}(1 - x^2) & \text{if } x^2 < 1, \\ 0 & \text{otherwise.} \end{cases} \tag{6.2.6}$$

for its computationally desirable properties (Härdle et al., 2004).

Kernel-based methods have a number of advantages over histogram-based approaches. They show a higher convergence rate in the limit of a large number of data points (Härdle et al., 2004). Also, the introduction of a bandwidth gives an explicit indication of the length scale of averaging. However, as points are indexed at set time-shifts τ_j in the future, this method is unsuitable for unevenly spaced data.

Kernel Time-Based Regression

To extend KBR to unevenly spaced data, kernel density estimation is applied to the τ component as well as the x component. We shall refer to this method as kernel time-based regression (KTBR). A similar approach has been used for estimators of the autocorrelation function (Babu and Stoica, 2010). A bivariate kernel density estimation is used

$$\hat{M}^{(n)}(x_i, \tau_j) = \frac{\sum_{k=1}^{T-1} \sum_{l=k+1}^{T} K_h^{(2)}(x_i - X(t_k), \tau_j - \Delta t_{l,k}) \left[X(t_l) - X(t_k)\right]^n}{\sum_{k=1}^{T-1} \sum_{l=k+1}^{T} K_h^{(2)}(x_i - X(t_k), \tau_j - \Delta t_{l,k})}, \tag{6.2.7}$$

where $K_h^{(2)}(\circ, \circ)$ is a bandwidth scaled, Euclidian distance 2D kernel

$$K_h^{(2)}(x, \tau) = \frac{C}{h_x h_\tau} K\left(\left((x/h_x)^2 + (\tau/h_\tau)^2\right)^{\frac{1}{2}}\right) \tag{6.2.8}$$

where h_x and h_τ and the bandwidths in x and τ, respectively. The prefactor C is defined such that the kernel integrates to unity over the whole domain. In this example we continue

to use the Epanechnikov kernel (6.2.6), in which case $C = 8/3\pi$. This choice is equivalent to a diagonal bandwidth matrix (Wand and Jones, 1993).

As the domain in τ only has positive support, kernel estimations at $\tau < h_\tau$ can be biased. To account for this, we use a boundary correction method (Jones, 1993) that replaces the application of kernel (6.2.8) inside (6.2.7) in the following way

$$K_h^{(2)}(x_i - X(t_k), \tau_j - \Delta t_{l,k}) \to \left[K_h^{(2)}(x_i - X(t_k), \tau_j - \Delta t_{l,k}) + K_h^{(2)}(x_i - X(t_k), \tau_j + \Delta t_{l,k})\right]. \tag{6.2.9}$$

We note that it is not simple to express estimator (6.2.7) in the traditional multivariate vector form, as $\Delta t_{l,k}$ values are dependent on pairs of $(X(t_k), X(t_l))$.

6.3 Numerical Examples

To validate the presented methods, we test them on a set of three synthetic data-sets. These examples each have difficult aspects, and hence require different estimation methods from the conditional moments, illustrating the flexibility and versatility of HTBR and KTBR.

Example A: Ornstein-Uhlenbeck Process

Here we test the method on an Ornstein-Uhlenbeck process given by the drift and diffusion functions

$$D^{(1)}(x) = -x, \tag{6.3.1a}$$
$$D^{(2)}(x) = 1. \tag{6.3.1b}$$

For this process, we consider a discrete time-series sampling of $X(t)$ consisting of 10^7 points with uneven time-sampling, with a distribution of time-samples, $\Delta t \sim \mathcal{N}(5\times10^{-3}, 3.2\times10^{-7})$. The solution is integrated using the Milstein method (Mil'shtejn, 1975) with an internal time-step of at most $\delta t \leq 10^{-4}$, to ensure numerical accuracy.

To estimate the conditional moments of this data, we use three separate methods. First, the moments are estimated using HTBR (6.2.3). Sampling in x is performed by 11 evenly spaced bins in the range $[-2, 2]$. Sampling in τ is performed by a single bin with limits $[0, 0.01]$. Here τ is small enough that the drift and diffusion functions can be directly estimated from the conditional moments

$$\hat{D}^{(n)}(x) \approx \frac{1}{n!\tau}\hat{M}^{(n)}(x, \tau). \tag{6.3.2}$$

Second, the moments are estimated using KTBR (6.2.7). Evaluation points in x are 30 evenly spaced points in $[-2, 2]$, with a kernel bandwidth of $h_x = 0.3$. Sampling in τ is performed with a single evaluation point at $\tau = 5\times10^{-3}$, with a kernel bandwidth of $h_\tau = 2.5\times10^{-3}$. As with

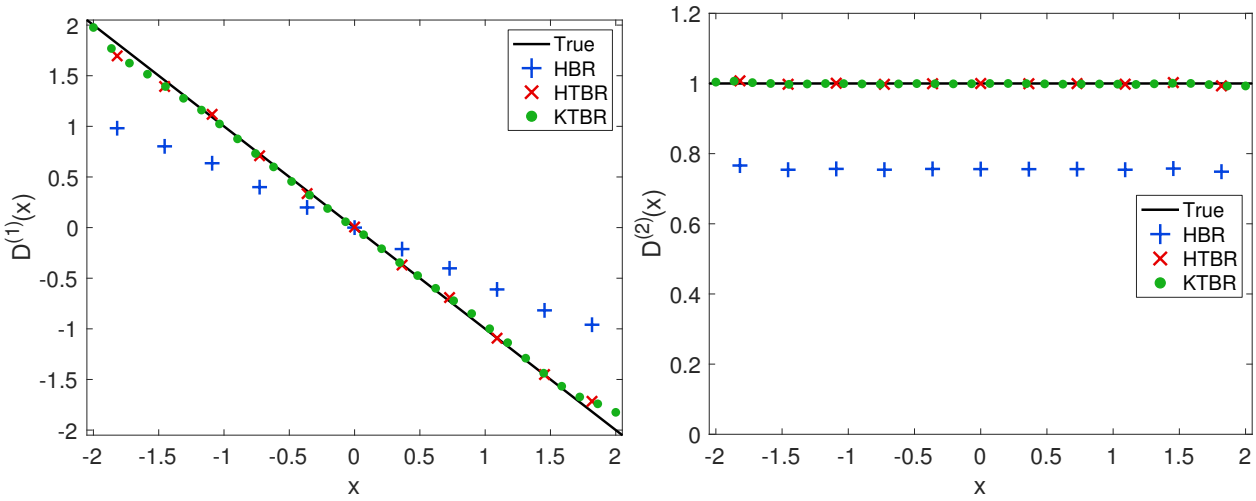

Figure 6.1: Results for example A: Ornstein-Uhlenbeck process. Estimated finite-time coefficients for $D^{(1)}(x)$ and $D^{(2)}(x)$ are shown in the left and right plots, respectively. True coefficients are plotted as black lines. Estimates from the HTBR method and KTBR method are plotted with red crosses and green circles lines, respectively. Estimates from the HBR method with interpolated data are plotted with blue plusses. KBR performed similarly to HBR except with finer resolution, and is not shown for conciseness.

HTBR, the direct estimation method (6.3.2) is used to estimate the KM coefficients. Finally, to compare with the two previous methods, naive resampling is performed on the time-series data. The data $X(t)$ is linearly interpolated to a regular sampling of $\Delta t = 5 \times 10^{-3}$, and then traditional direct estimation is applied with the sample bin sampling as the HTBR estimate. The drift and diffusion functions are shown in Fig. 6.1.

We find that the estimates of drift and diffusion functions are in good accordance with the true values for both HTBR and KTBR. These functions are systematically underestimated when using HBR with interpolated time-sampling.

Example B: Multiplicative Process with Measurement Noise

Next we examine a multiplicative process with measurement noise. The drift and diffusion functions are set as

$$D^{(1)}(x) = -x, \tag{6.3.3a}$$

$$D^{(2)}(x) = 1 + x^2. \tag{6.3.3b}$$

Unevenly spaced time-series data $X(t)$ is produced in the same way as example A, however we now also add Gaussian δ-correlated measurement noise

$$Y(t) = X(t) + \sigma\zeta(t), \tag{6.3.4}$$

where σ denotes the standard deviation of the measurement noise, and $\zeta \sim \mathcal{N}(0,1)$. We seek to estimate coefficients of parameterised drift and diffusion functions

$$\hat{D}^{(1)}(x) = p_1 + p_2 x, \tag{6.3.5a}$$
$$\hat{D}^{(2)}(x) = p_3 + p_4 x + p_5 x^2, \tag{6.3.5b}$$

using the method of Lind et al. (2010). The time-series $Y(t)$ is used to estimate noisy moments, $\hat{M}^{(n)}(y,\tau)$. These moments are then separated by linear regression

$$\hat{M}^{(1)}(y_i,\tau_j) \approx \hat{m}_1(y_i)\tau_j + \hat{\gamma}_1(y_i), \tag{6.3.6a}$$
$$\hat{M}^{(2)}(y_i,\tau_j) \approx \hat{m}_2(y_i)\tau_j + \hat{\gamma}_2(y_i) + \sigma^2, \tag{6.3.6b}$$

along with uncertainties $\sigma^2_{\hat{m}_1}(y_i), \sigma^2_{\hat{\gamma}_1}(y_i)$, etc... These estimates are compared with theoretical values of $m_1(y), \gamma_1, m_2(y)$, and γ_2, which depend solely on parameters $p_1, \ldots, p_5$, and σ, see Lind et al. (2010) for more details. The parameters vary the fit function

$$F = \sum_{i=1}^{8} \left\{ \frac{[\hat{m}_1(y_i) - m_1(y_i)]^2}{\sigma^2_{\hat{m}_1}(y_i)} + \frac{[\hat{\gamma}_1(y_i) - \gamma_1(y_i)]^2}{\sigma^2_{\hat{\gamma}_1}(y_i)} + \frac{[\hat{m}_2(y_i) - m_2(y_i)]^2}{\sigma^2_{\hat{m}_2}(y_i)} + \frac{[\hat{\gamma}_2(y_i) - \gamma_2(y_i) - \sigma^2]^2}{\sigma^2_{\hat{\gamma}_2}(y_i)} \right\}, \tag{6.3.7}$$

which is minimised using simulated annealing (Carvalho et al., 2011).

As in example A, we compare three methods to estimate the conditional moments. For HTBR, sampling in y is performed with 50 equally spaced bins in the range $[-6, 6]$. Sampling in τ is performed by 8 equally spaced bins with centers from $\tau_1 = 5 \times 10^{-3}$ to $\tau_8 = 4 \times 10^{-2}$, with bin-widths of $b_\tau = 5 \times 10^{-3}$. For KTBR, evaluation points in x are 50 equally spaced points in the range $[-6, 6]$, and the bandwidth is $h_x = 0.18$. Sampling in time is performed with 8 equally spaced points from $\tau_1 = 5 \times 10^{-3}$ to $\tau_8 = 4 \times 10^{-2}$, with a bandwidth of $b_\tau = 2.5 \times 10^{-3}$. Finally, the data $Y(t)$ is also linearly interpolated to a regular sampling of $\Delta t = 5 \times 10^{-3}$ and then sampled in the same way as the HTBR example. The optimized parameters from these three results are shown in Table 6.1 and the drift and diffusion functions are shown in Fig. 6.2.

The parameters of the drift and diffusion functions are very close to the true values for both HTBR and KTBR. For HBR with interpolated time sampling, the intercept of the drift and the linear term in the diffusion are estimated well. However the magnitude of gradient of the drift term, the constant diffusion term, and the quadratic term are all overestimated. Finally the measurement noise amplitude σ is underestimated. We note that entering the true parameter values into function (6.3.7) with estimates gathered from the interpolated HBR method result in a value of F two orders of magnitude higher than the optimized minimum.

Table 6.1: True and optimized parameter values for example B: multiplicative process with measurement noise. Parameters are rounded to either 2 significant figures or at least 2 decimal places. The HBR column represents results from interpolated $Y(t)$ data. KBR performed similarly to HBR, and is not shown for conciseness.

Parameter	True	HTBR	KTBR	HBR
p_1	0	-0.0050	-0.0040	-0.014
p_2	-1	-0.99	-1.00	-1.48
p_3	1	0.99	1.00	1.62
p_4	0	0.0062	0.013	0.0020
p_5	1	0.97	0.98	1.11
σ	1	1.00	1.00	0.76

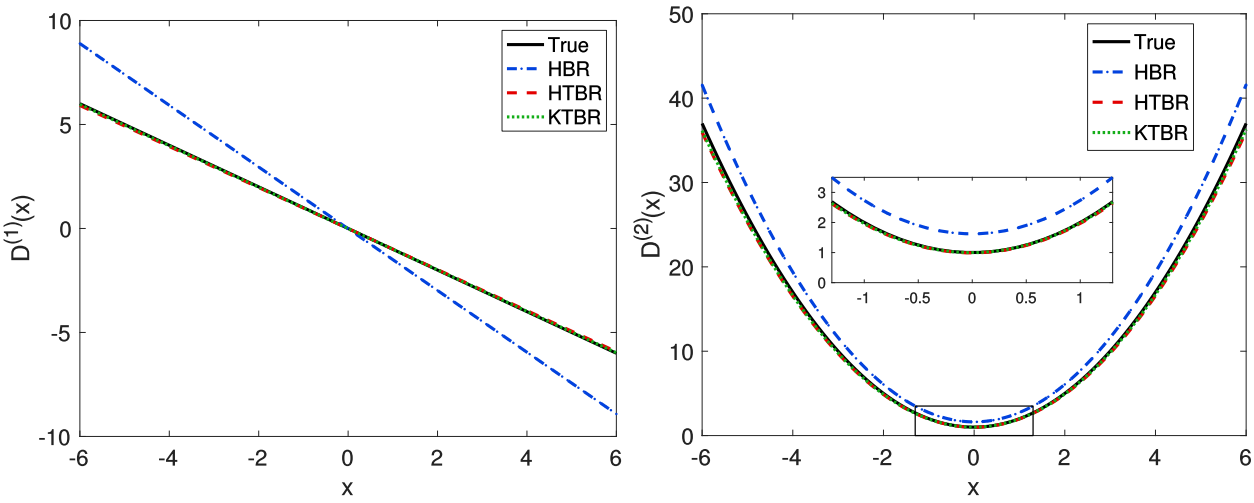

Figure 6.2: Results for example B: multiplicative process with measurement noise. Estimated finite-time coefficients for $D^{(1)}(x)$ and $D^{(2)}(x)$ are shown in the left and right plots, respectively. True coefficients are plotted as black lines. Estimates from the HTBR method and KTBR method are plotted with red dashed lines and green dotted lines, respectively. Estimates from the HBR method with interpolated data are plotted with blue dot-dashed lines. KBR performed similarly to HBR, and is not shown for conciseness.

Example C: Bistable System with Correlated Noise

Finally we test the method on a bistable process $X(t)$ driven by a correlated noise $\eta(t)$ (Lehle and Peinke, 2018). This system is defined as

$$\frac{d}{dt}X = D^{(1)}(X) + \sqrt{2D^{(2)}(X)}\eta(t), \tag{6.3.8a}$$

$$\frac{d}{dt}\eta = -\frac{1}{\theta}\eta + \frac{1}{\theta}\xi(t), \tag{6.3.8b}$$

where θ is the correlation time of the noise. The drift and diffusion functions are

$$D^{(1)}(x) = x - \frac{1}{2}x^3, \tag{6.3.9a}$$

$$\text{and} \qquad D^{(2)}(x) = 1 + \frac{1}{20}\ln\cosh 2x, \tag{6.3.9b}$$

and the correlation time is $\theta = 0.01$. An unevenly spaced timeseries is produced in the same way as example 1, however only $X(t)$ is observed.

We seek to estimate these drift and diffusion functions using the non-parametric method of (Lehle and Peinke, 2018). This method involves comparing estimates of conditional moments, $\hat{M}^{(n)}(x,\tau)$, with theoretical estimates

$$M^{(n)}(x,\tau) \approx \sum_{i=1}^{3} \lambda_i^{(n)}(x) r_i(\tau,\theta), \tag{6.3.10}$$

where functions r_i are prescribed basis functions and $\lambda_i^{(n)}(x)$ are the corresponding coefficients. Coefficients are found through least squares inversion, and then $\lambda_1^{(n)}(x)$ are directly related to estimates of the drift and diffusion functions at points in x. For a detailed description of the method, see Lehle and Peinke (2018).

As in the two previous examples, we compare three methods of estimating conditional moments. For HTBR, sampling in x is performed by 16 equally spaced bins in the range $[-2, 2]$. Sampling in τ is performed by 30 spaced bins with from $\tau_1 = 5 \times 10^{-3}$ to $\tau_{30} = 1.5 \times 10^{-1}$, with bin-widths of $b_\tau = 5 \times 10^{-3}$. For KTBR, evaluation points in x are 50 equally spaced points in the range $[-2, 2]$, and the bandwidth is $h_x = 0.24$. Sampling in time is performed with 30 equally spaced points from $\tau_1 = 5 \times 10^{-3}$ to $\tau_{30} = 1.5 \times 10^{-1}$, with a bandwidth of $b_\tau = 2.5 \times 10^{-3}$. Finally, the data $X(t)$ is also linearly interpolated to a regular sampling of $\Delta t = 5 \times 10^{-3}$ and then sampled in the same way as the HTBR example. For all examples, we assume that the correlation time θ has been accurately estimated *a priori* (Edelson and Krolik, 1988; Rehfeld et al., 2011). For all methods, the mean absolute error between estimated moments $\hat{M}^{(n)}(x,\tau)$ and fitted moments (6.3.10) is on the order of 10^{-5}. The drift and diffusion functions from these three estimates are shown in Fig. 6.3.

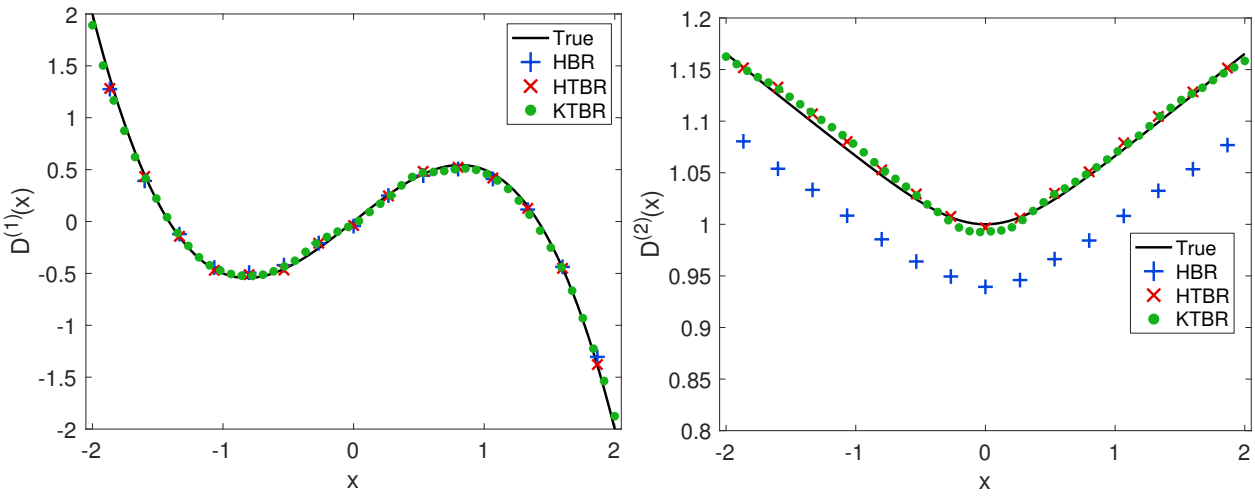

Figure 6.3: Results for example C: bistable system with correlated noise. As Fig. 6.1.

The estimates of the drift and diffusion functions compare well with the true values for both HTBR and KTBR. For the interpolated HBR the drift function is reproduced well, whilst the diffusion function is systematically underestimated.

6.4 Application to Paleoclimatological Data

Paleoclimate proxies preserve a record of Earth's climate variability. This variability is commonly studied through carbon and oxygen isotopes records from benthic foraminifera (Zachos et al., 2001; Westerhold et al., 2020). Of particular interest are large and rapid negative excursions in carbon isotope ratios, δ^{13}C, throughout the Cenozoic (Cramer et al., 2003; Lourens et al., 2005; Nicolo et al., 2007; Sexton et al., 2011; Lauretano et al., 2015). These excursions have been interpreted as "hyperthermal" warming events, and are speculated to be linked to the release of isotopically depleted organic carbon from permafrost or methane clathrates into the surface environment (Dickens, 2003; Lunt et al., 2011; DeConto et al., 2012). Such records offer insights to Earth's climate response to hyperthermal events, and provide an analogue to modern anthropogenic forcing (Bowen et al., 2006; Zachos et al., 2008; Dunkley Jones et al., 2010; Zeebe and Zachos, 2013). Recently Arnscheidt and Rothman (2021) suggested that the time-variability of these records can be modeled as stochastic processes, invoking a single-variable correlated additive-multiplicative (CAM) process

$$\frac{d}{dt}X = -\frac{1}{\tau_{\text{eff}}}X + v\,(X - c)\,\Gamma(t), \tag{6.4.1}$$

where τ_{eff}, v, and c are constants (Sura and Sardeshmukh, 2008; Sardeshmukh and Sura, 2009; Sura, 2011; Penland and Sardeshmukh, 2012; Sardeshmukh and Penland, 2015). This conclusion was reached through a short-time-scale agnostic analysis of the probability density

of the record. A non-parametric verification of the CAM hypothesis has been unreachable with previous methods, as the δ^{13}C record is unevenly sampled in time. In this section, we apply KTBR to a section of this unevenly sampled paleoclimate record.

We choose a section of the record, from 53 Ma to 46 Ma, containing a series of representative excursions but excluding the anomalous Paleocene-Eocene Thermal Maximum (McInerney and Wing, 2011), shown in Fig. 6.4. This section was previously found to have stationary statistics (Arnscheidt and Rothman, 2021). The sampling in this timespan is approximately log-normally distributed, with $\log_{10}\Delta t \sim \mathcal{N}(-2.7, 0.2)$. To calculate conditional moments using KTBR, evaluation points in x are 50 equally spaced points in the range $[-0.8, 0.5]$, and the bandwidth is $h_x = 0.4$. Sampling in time is performed with 30 equally spaced points from $\tau_1 = 3.5$ kyr to $\tau_{30} = 116$ kyr, with a bandwidth of $h_\tau = 5$ kyr. The higher order moments in $M^{(4)}(x,\tau) \simeq 3\left(M^{(2)}(x,\tau)\right)^2$ are evaluated using (6.2.7) and are comparable, showing a small error of $\sim 5\times10^{-3}$, validating the continuity of the record (Lehnertz et al., 2018; Tabar, 2019). To fit the drift and diffusion functions from these moments, we use the approach of Lehle and Peinke (2018), while the correlation time is fitted through a grid search and is found to be small but finite, $\theta \approx 0.4$ kyr. The moments are fit well, with an absolute error between calculated moments $\hat{M}^{(n)}(x,\tau)$ and fitted moments (6.3.10) on the order of 10^{-4}. The fitted drift and diffusion functions are shown in Fig. 6.5.

The drift function has a strongly linear form, and is well approximated by the CAM model (6.4.1) with $\tau_{\text{eff}} = 47$ kyr ($R^2 = 0.98$). For the diffusion function, while a CAM model (6.4.1) with the coefficients $v = -3.2$ and $c = -1.2$ falls within the confidence intervals ($R^2 = 0.67$), we cannot reject a likely piecewise diffusion of

$$D^{(2)}(x) = \begin{cases} p_1 + p_2(x - p_3), & x \le p_3, \\ p_1, & \text{otherwise}, \end{cases} \tag{6.4.2}$$

with best fitting coefficients of $p_1 = 3.30, p_2 = -11.50$, and $p_3 = -0.36$ ($R^2 = 0.99$).

To demonstrate that this linear drift and piecewise diffusion cannot be rejected by the data, we numerically integrate a sample path with these functions. The timeseries and probability density functions (PDF) of the original data and the SDE simulation are shown in Fig. 6.4. The SDE matches the skewed distribution of the original record, and also displays characteristic excursions to low δ^{13}C values.

This model qualitatively displays temporally similar negative excursions, and has an overall negatively skewed distribution. Note that if the drift function were constant, then the system would behave approximately like an Ornstein-Uhlenbeck process and display no skew. Beyond reproducing observations, the form of the fitted drift and diffusion functions can give insight into the physical processes in Earth's climate that are reflected in the record. The linear drift term indicates an average relaxation timescale of $\tau_{\text{eff}} = 47^{+14}_{-17}$ kyr, with uncertainties estimated from the bootstrap confidence intervals. This possibly reflects the stabilizing feedback of weathering of silicate rocks (e.g., Walker et al., 1981; Bowen, 2013). The piecewise nature of the diffusion suggests a critical "tipping-point" at ~ 0.36 below the time average. Beyond this point fluctuations are amplified, which may indicate an imbalance

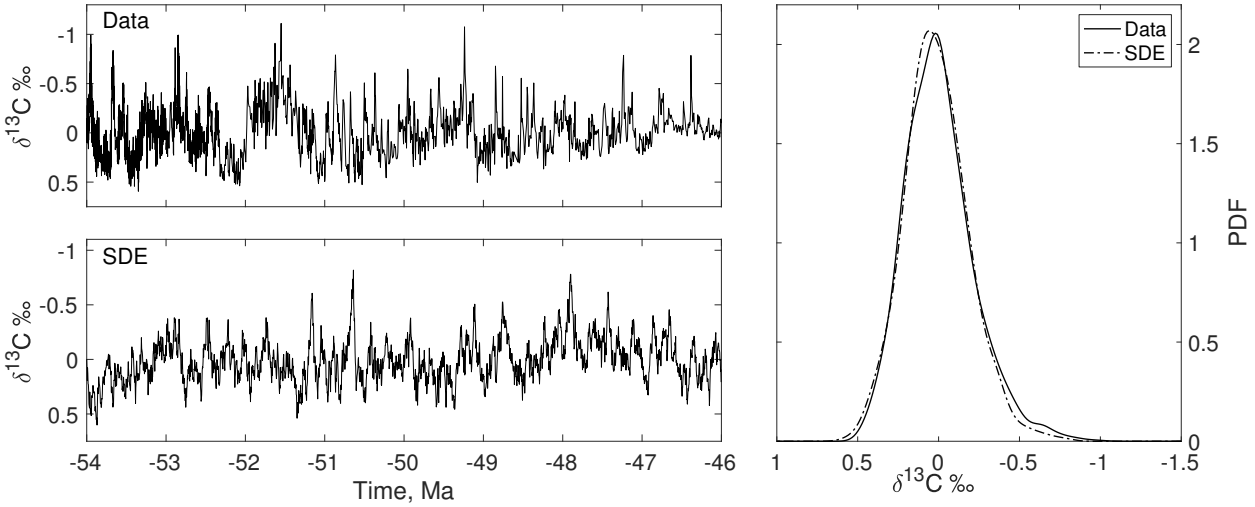

Figure 6.4: Carbon cycle variations in the Early Eocene, as recorded in benthic foraminiferal δ^{13}C data (Westerhold et al., 2020). A running mean of 1-Ma has been subtracted from the data to remove longer scale effects and isolate sub-million-year fluctuations. The top left plot shows the time-series data, while the right plot shows the histogram. A simulated trajectory is shown in the bottom left plot. By convention, the vertical axes are reflected.

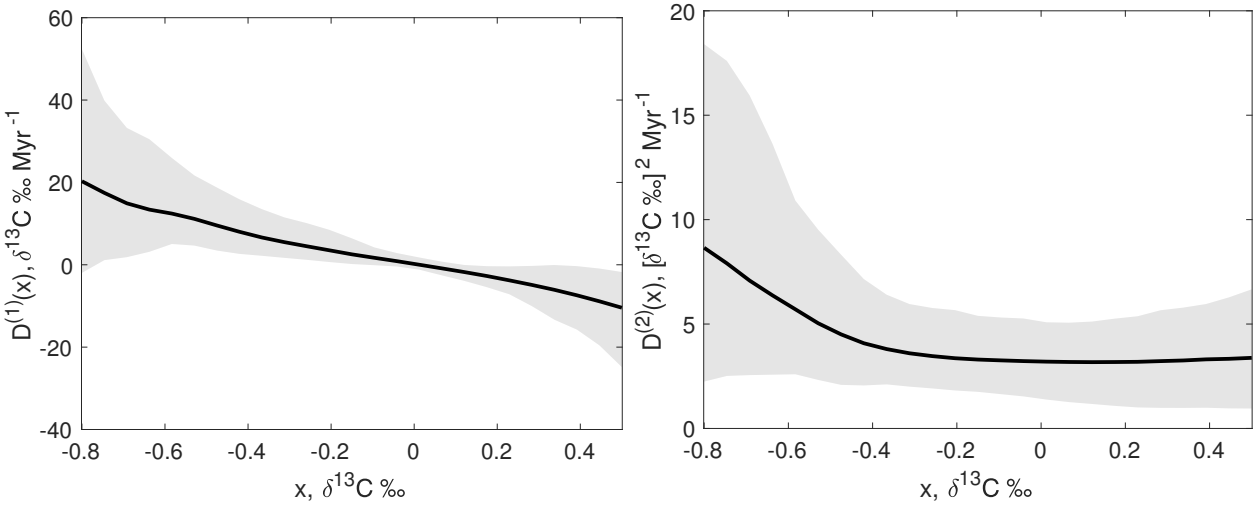

Figure 6.5: Results for early Eocene δ^{13}C record. Fitted drift and diffusion functions $D^{(1)}(x)$ and $D^{(2)}(x)$ are shown in the left and right plots, respectively. Best fits are plotted as black lines, and approximate 95% confidence intervals based on bootstrapping are shown as grey regions (Kunsch, 1989).

in the typical weathering feedback mechanism (Lenton et al., 2008; Rothman, 2017, 2019). Further work should investigate whether this behavior reflected in related oxygen isotope records, as well as other epochs in the Cenozoic.

6.5 Discussion and Conclusion

We present two methods to estimate conditional moments from irregularly spaced time series data. These moments are used alongside parametric or non-parametric methods to facilitate the accurate estimation of drift and diffusion functions of stochastic differential equations. We demonstrate this for three numerical examples, in a number of settings. Even in the presence of measurement noise (example B) or non-Markovian processes (example C), both HTBR and KTBR are able to produce moments that result in accurate estimates of the original drift and diffusion functions. Additionally, KTBR is applied to a series of irregularly spaced paleoclimatological measurements. We show that the fitted model is able to produce qualitatively similar time-dependent behavior, in addition to reproducing the broad statistics of the original data. Insights into the underlying dynamics are revealed, including an indication of the characteristic timescale of recovery, as well as a sign of an inflection point indicating an imbalance in the expected weathering feedback mechanism.

This study also illustrates the dangers of interpolating time-series observations for estimating stochastic processes. The effects of interpolation on regression results often can be difficult to predict or quantify (e.g., Eckner, 2014; Rehfeld et al., 2011). Indeed, while example A shows that interpolation results in an absolute underestimate in the magnitude of estimated drift and diffusion functions, the parametric estimation in example B shows the opposite bias (with an underestimated measurement noise amplitude estimate). Example C shows that interpolation has no apparent effect on the estimated drift function, but the same cannot be said for the diffusion function. In this case the bias may be small because of the longer scale time information that is included in the inversion method. In other words, the interpolation bias may be masked by the non-Markovian nature of the process. It is possible that these smaller errors average out for the drift function, as is the case with weak measurement noise (Siefert et al., 2003).

In addition to being applicable to a wide class of stochastic systems, these methods could allow for the handling of other non-ideal sampling conditions. Data with sporadic missing values or inconvenient gaps, for example, can be approached by this outlook when framed as irregularly sampled processes. These methods are also capable of estimating higher-order moments ($n > 2$ in (6.2.4) and (6.2.7)), which are useful for analysis of jump-diffusion processes (Anvari et al., 2016). On the effect of number of data points on the accuracy of the estimated drift and noise functions, as HTBR and KTBR are inherently frequency based calculations we expect them to perform similarly to previous methods (Mourik et al., 2006; Kleinhans and Friedrich, 2007; Lamouroux and Lehnertz, 2009). The methods here are demonstrated in one dimension, however extensions to higher dimensions is straightforward. On a technical note, both HTBR and KTBR require a double summation when indexing

Table 6.2: An overview of moment estimation techniques. Spaces marked as "?" have, to our knowledge, not been investigated.

	x-condition	
τ-condition	Histogram	Kernel
Index	HBR[1]	KBR[2]
Histogram	HTBR[3]	?
Kernel	?	KTBR[3]

[1] In Siegert et al. (1998).
[2] In Lamouroux and Lehnertz (2009).
[3] This study.

through $X(t)$, resulting in a computation time that scales with the square of the length of $X(t)$. Alternatively, equations (6.2.4) and (6.2.7) can be trivially expressed as rolling time-series operators, reducing the time to the product of length of $X(t)$ and the average number of observations in each time window. As with many statistical operators, it may be possible to devise a more efficient algorithm with a complexity proportional only on the length of $X(t)$ (Eckner, 2019).

In the broader picture for stochastic processes, the methods presented here extend time-shift conditioning from index-based methods to regressogram and kernel based methods. An overview of these methods is shown in Table 6.2. This reflects similar work that has been done for calculating the sample autocorrelation (or power spectra) from irregular data (Edelson and Krolik, 1988; Babu and Stoica, 2010; Rehfeld et al., 2011). In those examples conditioning in only one dimension is necessary, whereas state dependent statistics require conditioning also on the ordinate. We note that it is not strictly required to match histogram conditioning in x with histogram conditioning in τ—and similarly for kernels. In theory, hybrid methods could be used, for example, kernel conditioning in x combined with histogram conditioning in τ. To our knowledge such methods have not been investigated, however it is not clear if such approaches would have significant advantages over HTBR or KTBR.

Chapter 7

Conclusions and Outlook

Variations in the geomagnetic field occur over a broad range of timescales; however the physical origins of many of these variations remain poorly understood. This thesis has sought to investigate stochastic models of the geodynamo, using data produced by numerical geodynamo simulations. This represents a connection between the magnetohydrodynamic field generation in the planetary cores, and the modeling of complex systems through the lens of stochastic differential equations.

The material presented in Chapter 4—and previously published in Davis and Buffett (2021)—is the main focus of this thesis. It investigated the use of stochastic differential equations as models for variations in axial dipole moment. This analysis was performed on a set of numerical geodynamo simulations. The work was conducted in an inductive manner, without any prior assumption of a particular field generation mechanism. The numerical simulations were conducted at high numerical resolutions, and considered a wide range of styles of convection and different boundary conditions. As such, they represent significant extensions to previous studies (Kuipers et al., 2009; Buffett et al., 2014; Meduri and Wicht, 2016). From these simulations, the time-varying axial dipole moment was modeled as the trajectory of a stochastic differential equation. The drift and noise functions were fitted using a sophisticated inversion technique (Lehle and Peinke, 2018). This method enabled the relaxation of the white noise approximation, and instead used a more suitable exponentially-correlated noise. This represents a major improvement compared with previous studies, where the white noise approximation was inappropriately adopted. The axial dipole moment variations were modeled more accurately than in previous studies with this stochastic differential equation, which is non-Markov and has a noise with a finite correlation time. This new technique enabled self-consistency of the conditional moments and autocorrelation (see e.g., Fig. 4.2), as well as producing models with the realistic property of well-defined time derivatives. The stochastic models that were derived all had a remarkably simple form, consisting of a linear drift term and a constant noise term, and were compared with the numerical power spectra of the original data. Qualitatively good fits were found, especially at very low frequencies, suggesting that these simple stochastic models are representative of a wide range of axial dipole moment variabilities in the simulations. These results were interpreted in the con-

text of proposed magnetic field generation mechanisms for planetary dynamos, including the Earth's (e.g., Buffett et al., 2014). Specifically, links between the stochastic models and proposed field generation mechanisms were investigated and re-evaluated. Through re-analysis of the magnetic induction mechanism, the amplitude of the noise was linked to helical turbulent fluctuations that contribute towards the axial dipole field (e.g., Parker, 1955; Moffatt, 1970). A further extension also associated the characteristic time-scale of the stochastic noise with the integral time-scale of helical turbulent fluctuations. A major extension to previous studies was made with regard to the interpretation of the drift term. Contrary to previous hypotheses, the drift was not only representative of ohmic dissipation and absolute decreases in axial dipole moment (Buffett et al., 2013; Avery et al., 2017, 2019). Instead, the drift reflected symmetric imbalances between ohmic dissipation and average inductive field generation. Furthermore, these imbalances were almost exclusively accommodated by the slowest decay mode, rather than combinations of modes (Buffett et al., 2014). The discrepancy between the characteristic decay time of the axial dipole moment, compared with the expected decay rate, may reflect turbulently enhanced magnetic diffusion of the slowest magnetic mode.

The Earth's magnetic field has reversed polarity numerous times in the geologic past. As stochastic models in Chapter 4 were shown to be good representations of stable dipole variations, Chapter 5 investigated whether stochastic models can also adequately reproduce reversals. This question was investigated using the axial dipole moment data from a single reversing numerical geodynamo simulation. The simulation represents a significant extension of previous studies, as it is both high-resolution and substantially longer than previous simulations (Kuipers et al., 2009; Meduri and Wicht, 2016). From this simulation, the time-varying axial dipole moment was modeled as the trajectory of a stochastic differential equation. Like the analysis of Chapter 4, this work also relaxed the assumption of white noise in the stochastic process (Lehle and Peinke, 2018). It was found that, although the stochastic model was able to reproduce some statistics of the original axial dipole moment, there were slight discrepancies in the statistics of polarity reversals (see Fig. 5.5). Although the stochastic model could be altered to remedy this inconsistency, that resulted in inconsistencies in other places. In particular, the conditional moments were no longer self-consistent. Despite this failure, the stochastic model still predicted a reversal rate that was approximately a factor of two different than the true rate. One possibility that was explored was that, if the bias in the predicted reversal rate could be tolerated, then perhaps a stochastic model fitted from a short numerical geodynamo simulation could be used to gain an (admittedly biased) asymptotic reversal rate of that simulation. The motivation of this was to aid systematic searches through parameter space for Earth-like geodynamo simulations (e.g., Kutzner and Christensen, 2002; Christensen and Aubert, 2006; Christensen, 2011). With regard to the example simulation in Chapter 5, it was found that statistically indistinguishable drift and noise functions could be attained from approximately the first $\sim 20\%$ of the original data. Therefore, the stochastic differential equation prediction of the reversal rate could be attained from fewer data. However, a direct calculation of the reversal rate with $\sim 20\%$ of the data produced a number that was close to the full data value, negating the utility of the

stochastic model. Together with the bias present in the stochastic model prediction of the reversal rate, the usefulness of this of this perspective has yet to be demonstrated.

Paleomagnetic observations show that Earth's magnetic field has had long periods of relative stability and quiescence, and periods of more frequent reversals. In order to interpret paleomagnetic models of these observations in the framework of stochastic processes, as has been done in, e.g., Buffett et al. (2013), sampling complications from the geologic record must be considered (e.g., Buffett and Puranam, 2017). In particular, most paleomagnetic records have been irregularly sampled, and thus the data must be approached carefully (Rehfeld et al., 2011). This problem was considered in Chapter 6, where statistical methods for fitting drift and noise functions from irregularly sampled time-series data were developed. Two methods were introduced, and validated on a set of synthetic examples. The examples considered comprise a variety of Langevin-like systems, including processes contaminated with measurement noise, and non-Markov processes—complications that are present in the analysis of paleomagnetic models (Buffett and Puranam, 2017).

7.1 Future Directions

The work in this thesis has advanced the understanding of mechanisms and representations of magnetic field generation in fluid dynamos, as well as developed new techniques for the fitting of stochastic differential equations from irregularly sampled time-series data. As such, this work motivates a few possibilities for new and continued research.

The investigation of stable-polarity geodynamo simulations presented in Chapter 4 can be continued in a few directions. A particularly interesting set of simulations for further study would sample the transition between stable and reversing dipole fields. An ideal regime to explore is geodynamo simulations with a fixed inner core boundary heat flux, fixed core-mantle boundary temperature, and between 0% and 50% internal heating, i.e., models along paths 3, 4 and 5 in Kutzner and Christensen (2002). This can be investigated through increasing the Rayleigh number, as long as the stability of the simulations is permitted with adequate increases to the numerical resolution, and multipolar configurations can be avoided (Olson and Christensen, 2006). This path would likely increase the magnetic Reynolds number, reflecting more geophysically relevant flows. These changes could also be performed in conjunction with moderate increases to the magnetic Prandtl number (Wicht and Sanchez, 2019). The mode of linear drift and constant noise might continue onward to higher magnetic Reynolds numbers, further than has been explored in this thesis. However, such a configuration must surely break down when reversals initiate, and the role of magnetic induction becomes dominant at low dipolar states. In my opinion, the most scientifically valuable simulations will be those just beyond the critical Rayleigh number for the onset of reversals. As the influence of convective fluctuations continues to increase, a transition from stable to reversing states occur. At that point, reversals should be present but rare, allowing for a careful investigation of deviations from the linear drift and constant noise stochastic hypothesis. However it is not clear how this would be reflected in the field genera-

tion mechanisms identified in Chapter 4. Such an investigation would also test the predicted sharp dependency of the strength of convective fluctuations on reversal rate (e.g., Fig. 4.10), which has been previously indicated in simulations (Olson and Amit, 2014). Similarly, the role of turbulent diffusion of the magnetic field would likely be altered (Braginsky and Meytlis, 1990; Jones, 2008; Tobias, 2021), and may be reflected differently in the drift term at low dipole moment. Exploring the nature of these deviations from the stochastic models of Chapter 4 will assist in future insights into the nature of field generation in planetary magnetic fields and fluid dynamos (Jones, 2011).

Another geophysically relevant regime that can be explored comprises dynamo simulations at low Rayleigh numbers and moderate magnetic Prandtl numbers (Dormy, 2016). This branch of solutions is typically characterized by particularly strong, dipole-dominated fields; however, the physical mechanism for magnetic field generation at these conditions has not been investigated (Dormy et al., 2018). The interpretation of the dipole evolution of these simulations as stochastic models would enable a partitioning the dynamics into slow decay and fast fluctuations, facilitating investigation of the field generation mechanisms.

In the stable-polarity geodynamo simulations presented in Chapter 4, the noise term was found to reflect helical convective action that contributes towards the axial dipole field, through the α-effect (Moffatt, 1970). This does not rule out other mechanisms of magnetic induction in other fluid dynamos; for example, dynamos where the ω-effect is more efficient for field generation (Roberts, 2015). This would be present in dynamos with strong toroidal fields, which may be relevant for the Earth (e.g., Buffett and Bloxham, 2002). To my knowledge, geodynamo simulations where this effect is important have not been investigated in a stochastic differential equation model. As was the case with the geodynamo simulations in Chapter 5, such a model may be useful for linking internal field generation to the external field.

Focusing on stochastic modeling, there are many avenues for future research. The most immediately obvious direction is extending the scalar stochastic differential equation to include an appropriate order parameter for the toroidal field. This could be, for example, the amplitude of the slowest fundamental toroidal decay mode. The interaction between these poloidal and toroidal order parameters is likely complicated and non-linear, and will require careful non-parametric fitting and verification. This direction is of particular interest because, as pointed out by Scullard and Buffett (2018), the ratio between the slowest toroidal and poloidal modes is only $\sim 1/3$. Such a high fraction suggests an incomplete separation of fast and slow timescales necessary for the validity of single-variable Langevin models (e.g., Risken, 1996). This investigation would be particularly interesting because the toroidal field cannot exit the core (Roberts and Lowes, 1961). If the poloidal and toroidal order parameters are not completely uncorrelated, it may be possible to infer attributes of the unobservable toroidal field from the exterior poloidal field.

Stochastic models could also be used as time-dependent descriptions of higher order Gauss coefficients. This approach has been previously explored for individual Gauss coefficients on short timescales (Gillet et al., 2013; Bouligand et al., 2016). However cross-dependencies of coefficients—like that of the covariances described by giant Gaussian processes (e.g., Bono

et al., 2020)—have not been considered. In this case, a vector-valued stochastic differential equation describing the evolution of a number of Gauss coefficients would serve as a statistical representation of field variation. Even just the addition of equatorial dipole components would allow for the investigation of directional variations. This may prove useful for paleomagnetic modeling (Constable, C., personal communication).

For analyses of variations in the virtual axial dipole inferred from paleomagnetic models (e.g., Buffett et al., 2013), investigations into sources of measurement effects should be continued (e.g., Buffett and Puranam, 2017). Rather than turning to heavily regularized models built from continuous paleomagnetic measurements, an alternative direction could be a direct analysis of the irregularly spaced, discrete measurements from igneous sources. This may be explored using the new fitting techniques developed in Chapter 6, along with the recently-updated compilation of paleomagnetic intensity measurements present in the PINT database (Bono et al., 2022). Such an analysis may be incorporated into a wider, comprehensive model for paleofield fluctuations (e.g., Morzfeld and Buffett, 2019), and may enable the fitting of stochastic models for field variations through geologic time. If the proposed links between stochastic models and interior geodynamo mechanisms suggested in numerical simulations are applicable for the Earth, then this approach may allow inference of core dynamics through geologic history.

Another application of the new modeling methods of Chapter 6 is the analysis of marine magnetic anomalies (Gee and Kent, 2007). Although traditionally only viewed in the perspective of dipole polarity (Cande and Kent, 1995), continued work has revealed subtle signals that reflect shorter-scale field variations (Gee et al., 1996; Gee et al., 2000; Avery et al., 2017). Preliminary stochastic models for this record have been investigated (Gee et al., 2016); however, new analysis may be enabled by recently available high-resolution, irregularly-sampled near-bottom magnetic intensity measurements (Maher et al., 2021). These measurements may provide additional constraints for comprehensive stochastic models of field variations (e.g., Morzfeld and Buffett, 2019). Additionally, if the paleofield can be adequately established from other independent sources, then analysis into the emergent measurement effects present (e.g., in the style of Buffett and Puranam, 2017) may provide a window into understanding mid-ocean ridge magmatic processes.

For many of these proposed applications of stochastic modeling, attempting an inductive investigation requires more complicated fitting techniques. This is especially true if one wants to avoid the unrealistic properties of the white noise idealization. For instance, in the fitting of scalar SDEs in Lehle and Peinke (2018), relaxation of the white noise approximation to exponentially correlated noise required substantial effort. It is not clear whether similar approaches are possible for two-, three-, or N-dimensional stochastic differential equations. One drastic, but perhaps necessary option is to abandon the inverse modeling approach altogether. The alternative is to use optimization-based forward modeling methods. This approach would start with parameterized drift and noise functions and latent random variables representing the noise, and compare the resulting pathwise trajectory with empirical data. The parameterized functions and latent states could then be optimized with respect to the misfit between the prediction and data. This approach may not be completely im-

practical if the gradient of the misfit with respect to parameters can be efficiently calculated. In fact, this approach has been realized in the field of machine learning, where it is referred to as "neural SDEs" (e.g., Movellan et al., 2002). Although previous implementations of this approach have had to resort to computationally inefficient methods (Yang and Kushner, 1991; Gobet and Munos, 2005; Giles and Glasserman, 2006), recent research promises feasible scaling to high dimensions (Li et al., 2020). If these methods prove to be flexible and computationally efficient, they may provide a promising direction for future investigation of stochastic models of the geodynamo and geomagnetic field.

Bibliography

Amit, H., Leonhardt, R., and Wicht, J. (2010). "Polarity reversals from paleomagnetic observations and numerical dynamo simulations". *Space science reviews* 155.1, pp. 293–335.

Amit, H. and Olson, P. (2015). "Lower mantle superplume growth excites geomagnetic reversals". *Earth and Planetary Science Letters* 414, pp. 68–76.

Anvari, M., Tabar, M., Peinke, J., and Lehnertz, K. (2016). "Disentangling the stochastic behavior of complex time series". *Scientific reports* 6.1, pp. 1–12.

Arnscheidt, C. W. and Rothman, D. H. (2021). "Asymmetry of extreme Cenozoic climate–carbon cycle events". *Science Advances* 7.33, eabg6864.

Aubert, J. (2019). "Approaching Earth's core conditions in high-resolution geodynamo simulations". *Geophysical Journal International* 219, pp. 137–151.

Aubert, J., Gastine, T., and Fournier, A. (2017). "Spherical convective dynamos in the rapidly rotating asymptotic regime". *Journal of Fluid Mechanics* 813, pp. 558–593.

Aubert, J., Labrosse, S., and Poitou, C. (2009). "Modelling the palaeo-evolution of the geodynamo". *Geophysical Journal International* 179.3, pp. 1414–1428.

Avery, M. S., Constable, C. G., Davies, C. J., and Gubbins, D. (2019). "Spectral methods for analyzing energy balances in geodynamo simulations". *Physics of the Earth and Planetary Interiors* 286, pp. 127–137.

Avery, M. S., Gee, J. S., and Constable, C. G. (2017). "Asymmetry in growth and decay of the geomagnetic dipole revealed in seafloor magnetization". *Earth and Planetary Science Letters* 467, pp. 79–88.

Babu, P. and Stoica, P. (2010). "Spectral analysis of nonuniformly sampled data–a review". *Digital Signal Processing* 20.2, pp. 359–378.

Backus, G. (1986). "Poloidal and toroidal fields in geomagnetic field modeling". *Reviews of Geophysics* 24.1, pp. 75–109.

Backus, G. E. (1983). "Application of mantle filter theory to the magnetic jerk of 1969". *Geophysical Journal International* 74.3, pp. 713–746.

Backus, G., George, B., Parker, R. L., Parker, R., and Constable, C. (1996). *Foundations of geomagnetism*. Cambridge University Press.

Biggin, A. J., Steinberger, B., Aubert, J., Suttie, N., Holme, R., Torsvik, T. H., Meer, D. G. van der, and Van Hinsbergen, D. (2012). "Possible links between long-term geomagnetic variations and whole-mantle convection processes". *Nature Geoscience* 5.8, pp. 526–533.

Biggin, A. J., McCormack, A., and Roberts, A. (2010). "Paleointensity Database Updated and Upgraded". *EOS Transactions* 91.2, pp. 15–15.

Birch, F. (1952). "Elasticity and constitution of the Earth's interior". *Journal of Geophysical Research* 57.2, pp. 227–286.

Birch, F. (1964). "Density and composition of mantle and core". *Journal of geophysical research* 69.20, pp. 4377–4388.

Bono, R. K., Biggin, A. J., Holme, R., Davies, C. J., Meduri, D. G., and Bestard, J. (2020). "Covariant giant Gaussian process models with improved reproduction of palaeosecular variation". *Geochemistry, Geophysics, Geosystems* 21.8, e2020GC008960.

Bono, R. K., Paterson, G. A., Boon, A. van der, Engbers, Y. A., Michael Grappone, J., Handford, B., Hawkins, L. M., Lloyd, S. J., Sprain, C. J., Thallner, D., et al. (2022). "The PINT database: a definitive compilation of absolute palaeomagnetic intensity determinations since 4 billion years ago". *Geophysical Journal International* 229.1, pp. 522–545.

Borland, L. and Haken, H. (1992a). "Learning the dynamics of two-dimensional stochastic Markov processes". *Open Systems & Information Dynamics* 1.3, pp. 311–326.

Borland, L. and Haken, H. (1992b). "Unbiased determination of forces causing observed processes". *Zeitschrift für Physik B Condensed Matter* 88.1, pp. 95–103.

Borland, L. and Haken, H. (1992c). "Unbiased estimate of forces from measured correlation functions, including the case of strong multiplicative noise". *Annalen der Physik* 504.6, pp. 452–459.

Borland, L. and Haken, H. (1993). "On the constraints necessary for macroscopic prediction of time-dependent stochastic processes". *Reports on Mathematical Physics* 33.1-2, pp. 35–42.

Böttcher, F., Peinke, J., Kleinhans, D., Friedrich, R., Lind, P. G., and Haase, M. (2006). "Reconstruction of complex dynamical systems affected by strong measurement noise". *Physical Review Letters* 97.9, p. 090603.

Bouchet, F., Rolland, J., and Wouters, J. (2019). *Rare event sampling methods*.

Bouligand, C., Hulot, G., Khokhlov, A., and Glatzmaier, G. (2005). "Statistical palaeomagnetic field modelling and dynamo numerical simulation". *Geophysical Journal International* 161.3, pp. 603–626.

Bouligand, C., Gillet, N., Jault, D., Schaeffer, N., Fournier, A., and Aubert, J. (2016). "Frequency spectrum of the geomagnetic field harmonic coefficients from dynamo simulations". *Geophysical Supplements to the Monthly Notices of the Royal Astronomical Society* 207.2, pp. 1142–1157.

Bowen, G. J. (2013). "Up in smoke: A role for organic carbon feedbacks in Paleogene hyperthermals". *Global and Planetary Change* 109, pp. 18–29.

Bowen, G. J., Bralower, T. J., Delaney, M. L., Dickens, G. R., Kelly, D. C., Koch, P. L., Kump, L. R., Meng, J., Sloan, L. C., Thomas, E., et al. (2006). "Eocene hyperthermal event offers insight into greenhouse warming". *Eos, Transactions American Geophysical Union* 87.17, pp. 165–169.

Braginskii, S. (1964). "Self-excitation of a magnetic field during the motion of a highly-conducting fluid". *JETP* 20, pp. 726–735.

Braginsky, S. and Meytlis, V. (1990). "Local turbulence in the Earth's core". *Geophysical & Astrophysical Fluid Dynamics* 55.2, pp. 71–87.

Braginsky, S. I. and Roberts, P. H. (1995). "Equations governing convection in Earth's core and the geodynamo". *Geophysical & Astrophysical Fluid Dynamics* 79.1-4, pp. 1–97.

Brendel, K., Kuipers, J., Barkema, G., and Hoyng, P. (2007). "An analysis of the fluctuations of the geomagnetic dipole". *Physics of the Earth and Planetary Interiors* 162.3-4, pp. 249–255.

Broersen, P., De Waele, S., and Bos, R. (2000). "The accuracy of time series analysis for laser-doppler velocimetry". In: *Proceedings of the 10th International Symposium on Applications of Laser Techniques to Fluid Dynamics, Lisbon, Portugal*.

Buffett, B. and Avery, M. (2019). "How Does Temporal Resolution Influence Geomagnetic Reversal Statistics?" *Geophysical Research Letters* 46.10, pp. 5146–5152.

Buffett, B., Davis, W., and Avery, M. (2019). "Variability of Millennial-Scale Trends in the Geomagnetic Axial Dipole". *Geophysical Research Letters* 46.24, pp. 14450–14458.

Buffett, B., Avery, M., and Davis, W. (2022). "A Physical Interpretation of Asymmetric Growth and Decay of the Geomagnetic Dipole Moment". *Geochemistry, Geophysics, Geosystems* 23.3, e2021GC010239.

Buffett, B. and Bloxham, J. (2002). "Energetics of numerical geodynamo models". *Geophysical journal international* 149.1, pp. 211–224.

Buffett, B. (2015). "Dipole fluctuations and the duration of geomagnetic polarity transitions". *Geophysical Research Letters* 42.18, pp. 7444–7451.

Buffett, B. A., King, E. M., and Matsui, H. (2014). "A physical interpretation of stochastic models for fluctuations in the Earth's dipole field". *Geophysical Journal International* 198.1, pp. 597–608.

Buffett, B. A., Ziegler, L., and Constable, C. G. (2013). "A stochastic model for palaeomagnetic field variations". *Geophysical Journal International* 195.1, pp. 86–97.

Buffett, B. and Davis, W. (2018). "A probabilistic assessment of the next geomagnetic reversal". *Geophysical Research Letters* 45.4, pp. 1845–1850.

Buffett, B. and Matsui, H. (2015). "A power spectrum for the geomagnetic dipole moment". *Earth and Planetary Science Letters* 411, pp. 20–26.

Buffett, B. and Puranam, A. (2017). "Constructing stochastic models for dipole fluctuations from paleomagnetic observations". *Physics of the Earth and Planetary Interiors* 272, pp. 68–77.

Bullard, E. (1955). "The stability of a homopolar dynamo". In: *Mathematical proceedings of the Cambridge philosophical society*. Vol. 51. 4. Cambridge University Press, pp. 744–760.

Bullard, E. C. and Gellman, H. (1954). "Homogeneous dynamos and terrestrial magnetism". *Philosophical Transactions of the Royal Society of London. Series A, Mathematical and Physical Sciences* 247.928, pp. 213–278.

Bullen, K. (1954). "Composition of the Earth's outer core". *Nature* 174.4428, pp. 505–505.

Cande, S. C. and Kent, D. V. (1995). "Revised calibration of the geomagnetic polarity timescale for the Late Cretaceous and Cenozoic". *Journal of Geophysical Research: Solid Earth* 100.B4, pp. 6093–6095.

Cande, S. C. and Labreque, J. L. (1974). "Behaviour of the Earth's palaeomagnetic field from small scale marine magnetic anomalies". *Nature* 247.5435, pp. 26–28.

Carbone, V., Sorriso-Valvo, L., Vecchio, A., Lepreti, F., Veltri, P., Harabaglia, P., and Guerra, I. (2006). "Clustering of polarity reversals of the geomagnetic field". *Physical Review Letters* 96.12, p. 128501.

Carvalho, J., Raischel, F., Haase, M., and Lind, P. (2011). "Evaluating strong measurement noise in data series with simulated annealing method". In: *Journal of Physics: Conference Series*. Vol. 285. IOP Publishing, p. 012007.

Chandrasekhar, S. (1943). "Stochastic problems in physics and astronomy". *Reviews of modern physics* 15.1, p. 1.

Chandrasekhar, S. (1981). *Hydrodynamic and Hydromagnetic Stability*. Courier Corporation.

Chapman, S. and Bartels, J. (1940). "Geomagnetism, vol. II: Analysis of the data, and physical theories". *Geomagnetism*.

Chi-Durán, R., Avery, M. S., and Buffett, B. A. (2021). "Signatures of High-Latitude Waves in Observations of Geomagnetic Acceleration". *Geophysical Research Letters* 48.20, e2021GL094692.

Christensen, U., Olson, P., and Glatzmaier, G. (1999). "Numerical modelling of the geodynamo: a systematic parameter study". *Geophysical Journal International* 138.2, pp. 393–409.

Christensen, U. R. (2011). "Geodynamo models: Tools for understanding properties of Earth's magnetic field". *Physics of the Earth and Planetary Interiors* 187.3-4, pp. 157–169.

Christensen, U. R. and Aubert, J. (2006). "Scaling properties of convection-driven dynamos in rotating spherical shells and application to planetary magnetic fields". *Geophysical Journal International* 166.1, pp. 97–114.

Christensen, U. R., Aubert, J., and Hulot, G. (2010). "Conditions for Earth-like geodynamo models". *Earth and Planetary Science Letters* 296.3-4, pp. 487–496.

Christensen, U. R. and Tilgner, A. (2004). "Power requirement of the geodynamo from ohmic losses in numerical and laboratory dynamos". *Nature* 429.6988, pp. 169–171.

Christensen, U. R. and Wicht, J. (2015). "Numerical dynamo simulations". In: *Treatise on Geophysics (Second Edition)*. Ed. by G. Schubert. Vol. 8. Elsevier, pp. 245–277.

Christensen, U. (2010). "Dynamo scaling laws and applications to the planets". *Space science reviews* 152.1, pp. 565–590.

Clement, B. M. (1991). "Geographical distribution of transitional VGPs: evidence for non-zonal equatorial symmetry during the Matuyama-Brunhes geomagnetic reversal". *Earth and Planetary Science Letters* 104.1, pp. 48–58.

Clement, B. M. (2004). "Dependence of the duration of geomagnetic polarity reversals on site latitude". *Nature* 428.6983, pp. 637–640.

Constable, C. and Korte, M. (2015). "Centennial-to Millennial-Scale Geomagnetic Field Variations". In: *Treatise on Geophysics (Second Edition)*. Elsevier, pp. 309–341.

Constable, C. (1990). "A simple statistical model for geomagnetic reversals". *Journal of Geophysical Research: Solid Earth* 95.B4, pp. 4587–4596.

Constable, C. (2000). "On rates of occurrence of geomagnetic reversals". *Physics of the Earth and Planetary Interiors* 118.3-4, pp. 181–193.

Constable, C. G. and Johnson, C. L. (1999). "Anisotropic paleosecular variation models: implications for geomagnetic field observables". *Physics of the Earth and Planetary Interiors* 115.1, pp. 35–51.

Constable, C. and Johnson, C. (2005). "A paleomagnetic power spectrum". *Physics of the Earth and Planetary Interiors* 153.1-3, pp. 61–73.

Constable, C. and Korte, M. (2006). "Is Earth's magnetic field reversing?" *Earth and Planetary Science Letters* 246.1-2, pp. 1–16.

Constable, C., Korte, M., and Panovska, S. (2016). "Persistent high paleosecular variation activity in southern hemisphere for at least 10 000 years". *Earth and Planetary Science Letters* 453, pp. 78–86.

Constable, C. and Parker, R. (1988). "Statistics of the geomagnetic secular variation for the past 5 my". *Journal of Geophysical Research: Solid Earth* 93.B10, pp. 11569–11581.

Courtillot, V. and Le Mouël, J. (1984). "Geomagnetic secular variation impulses". *Nature* 311.5988, pp. 709–716.

Cowling, T. G. (1933). "The magnetic field of sunspots". *Monthly Notices of the Royal Astronomical Society* 94, pp. 39–48.

Cox, A. (1968). "Lengths of geomagnetic polarity intervals". *Journal of Geophysical Research* 73.10, pp. 3247–3260.

Cox, A. (1969). "Geomagnetic reversals". *Science* 163.3864, pp. 237–245.

Cox, A. (1981). "A stochastic approach towards understanding the frequency and polarity bias of geomagnetic reversals". *Physics of the Earth and Planetary Interiors* 24.2-3, pp. 178–190.

Cramer, B. S., Wright, J. D., Kent, D. V., and Aubry, M.-P. (2003). "Orbital climate forcing of δ^{13}C excursions in the late Paleocene–early Eocene (chrons C24n–C25n)". *Paleoceanography* 18.4.

Davidson, P. (2013). "Scaling laws for planetary dynamos". *Geophysical Journal International* 195.1, pp. 67–74.

Davies, C. J. and Constable, C. G. (2014). "Insights from geodynamo simulations into long-term geomagnetic field behaviour". *Earth and Planetary Science Letters* 404, pp. 238–249.

Davis, W. and Buffett, B. (2021). "Inferring core processes using stochastic models of the geodynamo". *Geophysical Journal International* 228.3, pp. 1478–1493.

Davis, W. and Buffett, B. (2022). "Estimation of drift and diffusion functions from unevenly sampled time-series data". *Phys. Rev. E* 106 (1), p. 014140.

De Santis, A., Qamili, E., and Wu, L. (2013). "Toward a possible next geomagnetic transition?" *Natural Hazards and Earth System Sciences* 13.12, pp. 3395–3403.

DeConto, R. M., Galeotti, S., Pagani, M., Tracy, D., Schaefer, K., Zhang, T., Pollard, D., and Beerling, D. J. (2012). "Past extreme warming events linked to massive carbon release from thawing permafrost". *Nature* 484.7392, pp. 87–91.

Dias, V., Franco, J., and Papa, A. (2008). "Simulation of geomagnetic reversals through magnetic critical models". *Brazilian Journal of Physics* 38, pp. 12–19.

Dickens, G. R. (2003). "Rethinking the global carbon cycle with a large, dynamic and microbially mediated gas hydrate capacitor". *Earth and Planetary Science Letters* 213.3-4, pp. 169–183.

Dormy, E. (2016). "Strong-field spherical dynamos". *Journal of Fluid Mechanics* 789, pp. 500–513.

Dormy, E., Oruba, L., and Petitdemange, L. (2018). "Three branches of dynamo action". *Fluid Dynamics Research* 50.1, p. 011415.

Driscoll, P. and Olson, P. (2011). "Superchron cycles driven by variable core heat flow". *Geophysical Research Letters* 38.9.

Driscoll, P. and Olson, P. (2009). "Effects of buoyancy and rotation on the polarity reversal frequency of gravitationally driven numerical dynamos". *Geophysical Journal International* 178.3, pp. 1337–1350.

Dunkley Jones, T., Ridgwell, A., Lunt, D., Maslin, M., Schmidt, D., and Valdes, P. (2010). "A Palaeogene perspective on climate sensitivity and methane hydrate instability". *Philosophical Transactions of the Royal Society A: Mathematical, Physical and Engineering Sciences* 368.1919, pp. 2395–2415.

Dunlop, D. and Özdemir, Ö. (2015). "Magnetizations in rocks and minerals". In: *Treatise on Geophysics (Second Edition)*. Ed. by G. Schubert. Vol. 5. Elsevier, pp. 277–336.

Eckner, A. (2014). "A framework for the analysis of unevenly spaced time series data". *Preprint.* Available at: `http://www.eckner.com/papers/unevenly_spaced_time_series_analysis.pdf`. Last accessed 06-June-2022.

Eckner, A. (2019). "Algorithms for unevenly-spaced time series: Moving averages and other rolling operators". *Preprint.* Available at: `http://www.eckner.com/papers/Algorithms\%20for\%20Unevenly\%20Spaced\%20Time\%20Series.pdf`. Last accessed 06-June-2022.

Edelson, R. and Krolik, J. (1988). "The discrete correlation function-A new method for analyzing unevenly sampled variability data". *The Astrophysical Journal* 333, pp. 646–659.

Elsasser, W. M. (1946). "Induction effects in terrestrial magnetism part II. The secular variation". *Physical Review* 70.3-4, p. 202.

Elsasser, W. M. (1947). "Induction effects in terrestrial magnetism. Part III. Electric modes". *Physical Review* 72.9, p. 821.

Elsasser, W. M. (1950). "The Earth's interior and geomagnetism". *Reviews of Modern Physics* 22.1, p. 1.

Epanechnikov, V. A. (1969). "Non-parametric estimation of a multivariate probability density". *Theory of Probability & Its Applications* 14.1, pp. 153–158.

Fan, J. and Gijbels, I. (1996). *Local polynomial modelling and its applications: monographs on statistics and applied probability 66*. Vol. 66. CRC Press.

Finlay, C., Dumberry, M., Chulliat, A., and Pais, M. (2010a). "Short timescale core dynamics: theory and observations". *Space science reviews* 155.1, pp. 177–218.

Finlay, C. C., Maus, S., Beggan, C., Bondar, T., Chambodut, A., Chernova, T., Chulliat, A., Golovkov, V., Hamilton, B., Hamoudi, M., et al. (2010b). "International geomagnetic reference field: the eleventh generation". *Geophysical Journal International* 183.3, pp. 1216–1230.

Friedrich, R., Peinke, J., Sahimi, M., and Tabar, M. R. R. (2011). "Approaching complexity by stochastic methods: From biological systems to turbulence". *Physics Reports* 506.5, pp. 87–162.

Friedrich, R., Renner, C., Siefert, M., and Peinke, J. (2002). "Comment on "Indispensable finite time corrections for Fokker-Planck equations from time series data"". *Physical Review Letters* 89.14, p. 149401.

Friedrich, R., Siegert, S., Peinke, J., Siefert, M., Lindemann, M., Raethjen, J., Deuschl, G., Pfister, G., et al. (2000). "Extracting model equations from experimental data". *Physics Letters A* 271.3, pp. 217–222.

Gardiner, C. W. et al. (1985). *Handbook of stochastic methods*. Vol. 3. springer Berlin.

Gauss, C. F. (1877). "Allgemeine theorie des erdmagnetismus". In: *Werke*. Springer, pp. 119–193.

Gee, J., Schneider, D. A., and Kent, D. V. (1996). "Marine magnetic anomalies as recorders of geomagnetic intensity variations". *Earth and planetary science letters* 144.3-4, pp. 327–335.

Gee, J. S., Cande, S. C., Hildebrand, J. A., Donnelly, K., and Parker, R. L. (2000). "Geomagnetic intensity variations over the past 780 kyr obtained from near-seafloor magnetic anomalies". *Nature* 408.6814, pp. 827–832.

Gee, J. S., Cande, S. C., and Kent, D. V. (2016). "Lava Accumulation Patterns at Fast-Spread Ridges and the Fidelity of Marine Magnetic Anomalies". In: *AGU Fall Meeting Abstracts*. Vol. 2016, GP31D–01.

Gee, J. and Kent, D. (2007). "Source of Oceanic Magnetic Anomalies and the Geomagnetic Polarity Timescale". In: *Treatise on Geophysics*. Elsevier, pp. 455–507.

Giles, M. and Glasserman, P. (2006). "Smoking adjoints: Fast monte carlo greeks". *Risk* 19.1, pp. 88–92.

Gillet, N., Jault, D., Canet, E., and Fournier, A. (2010). "Fast torsional waves and strong magnetic field within the Earth's core". *Nature* 465.7294, pp. 74–77.

Gillet, N., Jault, D., Finlay, C., and Olsen, N. (2013). "Stochastic modeling of the Earth's magnetic field: Inversion for covariances over the observatory era". *Geochemistry, Geophysics, Geosystems* 14.4, pp. 766–786.

Gissinger, C., Dormy, E., and Fauve, S. (2010). "Morphology of field reversals in turbulent dynamos". *EPL (Europhysics Letters)* 90.4, p. 49001.

Gissinger, C. (2012). "A new deterministic model for chaotic reversals". *The European Physical Journal B* 85.4, pp. 1–12.

Glatzmaier, G., Coe, R., and Schubert, G. (2015). "Magnetic polarity reversals in the core". *Treatise on geophysics* 2, pp. 283–298.

Glatzmaier, G. A. (2013). "Introduction to Modeling Convection in Planets and Stars". In: *Introduction to Modeling Convection in Planets and Stars*. Princeton University Press.

Glatzmaier, G. A. and Roberts, P. H. (1995). "A three-dimensional convective dynamo solution with rotating and finitely conducting inner core and mantle". *Physics of the Earth and Planetary Interiors* 91.1-3, pp. 63–75.

Glatzmaier, G. A. and Roberts, P. H. (1996). "An anelastic evolutionary geodynamo simulation driven by compositional and thermal convection". *Physica D: Nonlinear Phenomena* 97.1-3, pp. 81–94.

Glatzmaiers, G. A. and Roberts, P. H. (1995). "A three-dimensional self-consistent computer simulation of a geomagnetic field reversal". *Nature* 377.6546, pp. 203–209.

Gobet, E. and Munos, R. (2005). "Sensitivity Analysis Using Itô–Malliavin Calculus and Martingales, and Application to Stochastic Optimal Control". *SIAM Journal on control and optimization* 43.5, pp. 1676–1713.

Gomi, H., Ohta, K., Hirose, K., Labrosse, S., Caracas, R., Verstraete, M. J., and Hernlund, J. W. (2013). "The high conductivity of iron and thermal evolution of the Earth's core". *Physics of the Earth and Planetary Interiors* 224, pp. 88–103.

Gottschall, J. and Peinke, J. (2008). "On the definition and handling of different drift and diffusion estimates". *New Journal of Physics* 10.8, p. 083034.

Graur, D. et al. (2021). "Stop using 'master–slave'terminology in biology". *Nature* 593.7858, pp. 195–195.

Gubbins, D. and Roberts, P. (1987). "Magnetohydrodynamics of the Earth's core." In: *Geomagnetism*. Ed. by J. A. Jacobs. Vol. 2. Academic Press, pp. 1–183.

Gubbins, D. and Herrero-Bervera, E. (2007). *Encyclopedia of geomagnetism and paleomagnetism*. Springer Science & Business Media.

Guyodo, Y. and Valet, J.-P. (1999). "Global changes in intensity of the Earth's magnetic field during the past 800 kyr". *Nature* 399.6733, pp. 249–252.

Gwirtz, K., Morzfeld, M., Fournier, A., and Hulot, G. (2021a). "Can one use Earth's magnetic axial dipole field intensity to predict reversals?" *Geophysical Journal International* 225.1, pp. 277–297.

Gwirtz, K., Morzfeld, M., Kuang, W., and Tangborn, A. (2021b). "A testbed for geomagnetic data assimilation". *Geophysical Journal International* 227.3, pp. 2180–2203.

Haken, H. (2004). *Synergetics: Intoduction and advanced topics Spinger-Verlag*.

Haken, H. (1985). *Laser light dynamics*. Vol. 2. North-Holland Amsterdam.

Haken, H. (1989). "Synergetics: an overview". *Reports on Progress in Physics* 52.5, p. 515.

Haken, H. (2006). *Information and self-organization: A macroscopic approach to complex systems*. Springer Science & Business Media.

Haken, H. (2013). *Synergetics: Introduction and advanced topics*. Springer Science & Business Media.

Haken, H. (2020). "Synergetics: basic concepts". *Synergetics*, pp. 5–30.

Haken, H., Kelso, J. S., and Bunz, H. (1985). "A theoretical model of phase transitions in human hand movements". *Biological cybernetics* 51.5, pp. 347–356.

Hänggi, P. and Jung, P. (1995). "Colored noise in dynamical systems". *Advances in chemical physics* 89, pp. 239–326.

Härdle, W., Müller, M., Sperlich, S., and Werwatz, A. (2004). *Nonparametric and semiparametric models*. Vol. 1. Springer.

Harteveld, W., Mudde, R., and Van den Akker, H. (2005). "Estimation of turbulence power spectra for bubbly flows from Laser Doppler Anemometry signals". *Chemical engineering science* 60.22, pp. 6160–6168.

Hayashi, T. and Yoshida, N. (2005). "On covariance estimation of non-synchronously observed diffusion processes". *Bernoulli* 11.2, pp. 359–379.

Hoffman, R. N., Henderson, J. M., Leidner, S. M., Grassotti, C., and Nehrkorn, T. (2006). "The response of damaging winds of a simulated tropical cyclone to finite-amplitude perturbations of different variables". *Journal of the atmospheric sciences* 63.7, pp. 1924–1937.

Holme, R. and Olsen, N. (2006). "Core surface flow modelling from high-resolution secular variation". *Geophysical Journal International* 166.2, pp. 518–528.

Honisch, C. and Friedrich, R. (2011). "Estimation of Kramers-Moyal coefficients at low sampling rates". *Physical Review E* 83.6, p. 066701.

Hoyng, P. (2009). "Statistical dynamo theory: Mode excitation". *Physical Review E* 79.4, p. 046320.

Hoyng, P. and Duistermaat, J. (2004). "Geomagnetic reversals and the stochastic exit problem". *EPL (Europhysics Letters)* 68.2, p. 177.

Hoyng, P., Ossendrijver, M., and Schmitt, D. (2001). "The geodynamo as a bistable oscillator". *Geophysical & Astrophysical Fluid Dynamics* 94.3-4, pp. 263–314.

Hoyng, P., Schmitt, D., and Ossendrijver, M. (2002). "A theoretical analysis of the observed variability of the geomagnetic dipole field". *Physics of the Earth and Planetary Interiors* 130.3-4, pp. 143–157.

Hulot, G. and Bouligand, C. (2005). "Statistical palaeomagnetic field modelling and symmetry considerations". *Geophysical Journal International* 161.3, pp. 591–602.

Hulot, G. and Le Mouël, J. (1994). "A statistical approach to the Earth's main magnetic field". *Physics of the Earth and Planetary Interiors* 82.3-4, pp. 167–183.

Hussain, S. and Haji-Akbari, A. (2020). "Studying rare events using forward-flux sampling: Recent breakthroughs and future outlook". *The Journal of Chemical Physics* 152.6, p. 060901.

I.N.I. (2022). *Inclusive Naming Initiative*. URL: `https://inclusivenaming.org/%20%5Ctextnormal%7BLast%20accessed%2006-June-2022.%7D`.

Ising, E. (1924). "Beitrag zur theorie des ferro-und paramagnetismus". PhD thesis. Grefe & Tiedemann.

Ito, H. (1988). "Stochastic disk dynamo as a model of reversals of the Earth's magnetic field". *Journal of statistical physics* 53.1, pp. 19–39.

Ito, K. (1980). "Chaos in the Rikitake two-disc dynamo system". *Earth and Planetary Science Letters* 51.2, pp. 451–456.

Jackson, A., Jonkers, A. R., and Walker, M. R. (2000). "Four centuries of geomagnetic secular variation from historical records". *Philosophical Transactions of the Royal Society of London. Series A: Mathematical, Physical and Engineering Sciences* 358.1768, pp. 957–990.

Jackson, J. D. (1998). *Classical Electrodynamics*. John Wiley & Sons.

Jacobs, J. A. (1994). *Reversals of the Earth's magnetic field*. Vol. 63. Cambridge University Press.

Jazwinski, A. H. (2007). *Stochastic processes and filtering theory*. Courier Corporation.

Johnson, H. P., Van Patten, D., Tivey, M., and Sager, W. W. (1995). "Geomagnetic polarity reversal rate for the Phanerozoic". *Geophysical Research Letters* 22.3, pp. 231–234.

Jones, C. A. (2008). "Course 2 dynamo theory". In: *Les Houches*. Vol. 88. Elsevier, pp. 45–135.

Jones, C. A. (2011). "Planetary magnetic fields and fluid dynamos". *Annual Review of Fluid Mechanics* 43, pp. 583–614.

Jones, M. C. (1993). "Simple boundary correction for kernel density estimation". *Statistics and Computing* 3.3, pp. 135–146.

Kageyama, A. and Sato, T. (1997). "Generation mechanism of a dipole field by a magnetohydrodynamic dynamo". *Physical review E* 55.4, p. 4617.

Kageyama, A., Sato, T., and Groupa), C. S. (1995). "Computer simulation of a magnetohydrodynamic dynamo. II". *Physics of Plasmas* 2.5, pp. 1421–1431.

Khokhlov, A., Hulot, G., and Bouligand, C. (2006). "Testing statistical palaeomagnetic field models against directional data affected by measurement errors". *Geophysical Journal International* 167.2, pp. 635–648.

Kleinhans, D. and Friedrich, R. (2007). "Quantitative estimation of drift and diffusion functions from time series data". In: *Wind Energy*. Springer, pp. 129–133.

Kloeden, P. E. and Platen, E. (2013). *Numerical solution of stochastic differential equations*. Vol. 23. Springer Science & Business Media.

Knobloch, E. (1980). "Stochastic phenomena in astrophysics". *Vistas in Astronomy* 24, pp. 39–58.

Koker, N. de, Steinle-Neumann, G., and Vlček, V. (2012). "Electrical resistivity and thermal conductivity of liquid Fe alloys at high P and T, and heat flux in Earth's core". *Proceedings of the National Academy of Sciences* 109.11, pp. 4070–4073.

Kono, M. (2015). "Geomagnetism". In: *Treatise on Geophysics (Second Edition)*. Ed. by G. Schubert. Vol. 8. Elsevier.

Kono, M. and Roberts, P. H. (2002). "Recent geodynamo simulations and observations of the geomagnetic field". *Reviews of Geophysics* 40.4, pp. 4–1.

Korte, M., Genevey, A., Constable, C., Frank, U., and Schnepp, E. (2005). "Continuous geomagnetic field models for the past 7 millennia: 1. A new global data compilation". *Geochemistry, Geophysics, Geosystems* 6.2.

Kramers, H. A. (1940). "Brownian motion in a field of force and the diffusion model of chemical reactions". *Physica* 7.4, pp. 284–304.

Krause, F. and Raedler, K.-H. (1980). "Mean-field magnetohydrodynamics and dynamo theory". *Oxford: Pergamon Press*.

Kuang, W. and Bloxham, J. (1999). "Numerical modeling of magnetohydrodynamic convection in a rapidly rotating spherical shell: weak and strong field dynamo action". *Journal of Computational Physics* 153.1, pp. 51–81.

Kuipers, J., Hoyng, P., Wicht, J., and Barkema, G. (2009). "Analysis of the variability of the axial dipole moment of a numerical geodynamo model". *Physics of the Earth and Planetary Interiors* 173.3-4, pp. 228–232.

Kunsch, H. R. (1989). "The jackknife and the bootstrap for general stationary observations". *The Annals of Statistics*, pp. 1217–1241.

Kutzner, C. and Christensen, U. (2002). "From stable dipolar towards reversing numerical dynamos". *Physics of the Earth and Planetary Interiors* 131.1, pp. 29–45.

Laj, C. and Channell, J. E. (2015). "Geomagnetic excursions". In: *Treatise on Geophysics (Second Edition)*. Vol. 5. Elsevier, pp. 343–383.

Laj, C. and Kissel, C. (2015). "An impending geomagnetic transition? Hints from the past". *Frontiers in Earth Science* 3, p. 61.

Lamouroux, D. and Lehnertz, K. (2009). "Kernel-based regression of drift and diffusion coefficients of stochastic processes". *Physics Letters A* 373.39, pp. 3507–3512.

Larmor, J. (1919). "How could a rotating body such as the sun become a rotating magnet? Rep". *Britt. Assoc. Adv. Sci.*

Lauretano, V., Littler, K., Polling, M., Zachos, J. C., and Lourens, L. J. (2015). "Frequency, magnitude and character of hyperthermal events at the onset of the Early Eocene Climatic Optimum". *Climate of the Past* 11.10, pp. 1313–1324.

Laymon, R. (1985). "Idealizations and the Testing of Theories by Experimentation". *Observation, experiment, and hypothesis in modern physical science*, pp. 127–146.

Laymon, R. (1995). "Experimentation and the Legitimacy of Idealization". *Philosophical Studies: An International Journal for Philosophy in the Analytic Tradition* 77.2/3, pp. 353–375.

Lehle, B. and Peinke, J. (2018). "Analyzing a stochastic process driven by Ornstein-Uhlenbeck noise". *Physical Review E* 97.1, p. 012113.

Lehle, B. (2011). "Analysis of stochastic time series in the presence of strong measurement noise". *Physical Review E* 83.2, p. 021113.

Lehmann, I. (1936). "P". *Publications du Bureau Central International de la Sêismologique* A14.3, pp. 87–115.

Lehnertz, K., Zabawa, L., and Tabar, M. R. R. (2018). "Characterizing abrupt transitions in stochastic dynamics". *New Journal of Physics* 20.11, p. 113043.

Lenton, T. M., Held, H., Kriegler, E., Hall, J. W., Lucht, W., Rahmstorf, S., and Schellnhuber, H. J. (2008). "Tipping elements in the Earth's climate system". *Proceedings of the national Academy of Sciences* 105.6, pp. 1786–1793.

Lhuillier, F., Fournier, A., Hulot, G., and Aubert, J. (2011). "The geomagnetic secular-variation timescale in observations and numerical dynamo models". *Geophysical research letters* 38.9.

Lhuillier, F. and Gilder, S. A. (2013). "Quantifying paleosecular variation: insights from numerical dynamo simulations". *Earth and Planetary Science Letters* 382, pp. 87–97.

Lhuillier, F., Hulot, G., and Gallet, Y. (2013). "Statistical properties of reversals and chrons in numerical dynamos and implications for the geodynamo". *Physics of the Earth and Planetary Interiors* 220, pp. 19–36.

Lhuillier, F., Hulot, G., Gallet, Y., and Schwaiger, T. (2019). "Impact of inner-core size on the dipole field behaviour of numerical dynamo simulations". *Geophysical Journal International* 218.1, pp. 179–189.

Li, X., Wong, T.-K. L., Chen, R. T., and Duvenaud, D. (2020). "Scalable gradients for stochastic differential equations". In: *International Conference on Artificial Intelligence and Statistics*. PMLR, pp. 3870–3882.

Liew, A. W.-C., Xian, J., Wu, S., Smith, D., and Yan, H. (2007). "Spectral estimation in unevenly sampled space of periodically expressed microarray time series data". *BMC bioinformatics* 8.1, pp. 1–19.

Lind, P. G., Haase, M., Böttcher, F., Peinke, J., Kleinhans, D., and Friedrich, R. (2010). "Extracting strong measurement noise from stochastic time series: applications to empirical data". *Physical Review E* 81.4, p. 041125.

Lorenz, E. N. (1963). "Deterministic nonperiodic flow". *Journal of atmospheric sciences* 20.2, pp. 130–141.

Lourens, L. J., Sluijs, A., Kroon, D., Zachos, J. C., Thomas, E., Röhl, U., Bowles, J., and Raffi, I. (2005). "Astronomical pacing of late Palaeocene to early Eocene global warming events". *Nature* 435.7045, pp. 1083–1087.

Lowes, F. (1966). "Mean-square values on sphere of spherical harmonic vector fields". *Journal of Geophysical Research* 71.8, pp. 2179–2179.

Lowrie, W. and Kent, D. V. (2004). "Geomagnetic Polarity Timescales and Reversal Frequency Regimes". *Timescales Of The Paleomagnetic Field* 145, pp. 117–129.

Lunt, D. J., Ridgwell, A., Sluijs, A., Zachos, J., Hunter, S., and Haywood, A. (2011). "A model for orbital pacing of methane hydrate destabilization during the Palaeogene". *Nature Geoscience* 4.11, pp. 775–778.

Mahalanobis, P. C. (1936). "On the generalized distance in statistics". In: National Institute of Science of India.

Maher, S. M., Gee, J. S., Cheadle, M. J., and John, B. E. (2021). "Three-dimensional magnetic stripes require slow cooling in fast-spread lower ocean crust". *Nature* 597.7877, pp. 511–515.

Majda, A., Abramov, R. V., and Grote, M. J. (2005). *Information theory and stochastics for multiscale nonlinear systems*. Vol. 25. American Mathematical Soc.

Malin, S. (1987). "Historical introduction to geomagnetism". In: *Geomagnetism*. Ed. by J. A. Jacobs. Vol. 1. Academic Press London, pp. 1–49.

Mandea, M., Holme, R., Pais, A., Pinheiro, K., Jackson, A., and Verbanac, G. (2010). "Geomagnetic jerks: rapid core field variations and core dynamics". *Space science reviews* 155.1, pp. 147–175.

Marzocchi, W. (1997). "Missing reversals in the geomagnetic polarity timescale: Their influence on the analysis and in constraining the process that generates geomagnetic reversals". *Journal of Geophysical Research: Solid Earth* 102.B3, pp. 5157–5171.

Matsui, H., King, E., and Buffett, B. (2014). "Multiscale convection in a geodynamo simulation with uniform heat flux along the outer boundary". *Geochemistry, Geophysics, Geosystems* 15.8, pp. 3212–3225.

Matsui, H., Heien, E., Aubert, J., Aurnou, J. M., Avery, M., Brown, B., Buffett, B. A., Busse, F., Christensen, U. R., Davies, C. J., et al. (2016). "Performance benchmarks for a next generation numerical dynamo model". *Geochemistry, Geophysics, Geosystems* 17.5, pp. 1586–1607.

Mauersberger, P. (1956). "Das mittel der energiedichte des geomagnetischen hauptfeldes an der erdoberflache und seine saulare anderung". *Gerlands Beitr. Geophys.* 65, pp. 207–215.

Mazaud, A. and Laj, C. (1989). "Simulation of geomagnetic polarity reversals by a model of interacting dipole sources". *Earth and planetary science letters* 92.3-4, pp. 299–306.

McDonough, W. (2003). "3.16–Compositional model for the Earth's core". *Treatise on geochemistry* 2, pp. 547–568.

McElhinny, M. W. and McFadden, P. L. (1999). *Paleomagnetism: continents and oceans*. Elsevier.

McFadden, P. and Merrill, R. (1984). "Lower mantle convection and geomagnetism". *Journal of Geophysical Research: Solid Earth* 89.B5, pp. 3354–3362.

McInerney, F. A. and Wing, S. L. (2011). "The Paleocene-Eocene Thermal Maximum: A perturbation of carbon cycle, climate, and biosphere with implications for the future". *Annual Review of Earth and Planetary Sciences* 39, pp. 489–516.

McMullin, E. (1968). "What do physical models tell us?" In: *Studies in Logic and the Foundations of Mathematics*. Vol. 52. Elsevier, pp. 385–396.

McMullin, E. (1985). "Galilean idealization". *Studies in History and Philosophy of Science Part A* 16.3, pp. 247–273.

Meduri, D. G., Biggin, A. J., Davies, C. J., Bono, R. K., Sprain, C. J., and Wicht, J. (2021). "Numerical dynamo simulations reproduce paleomagnetic field behavior". *Geophysical Research Letters* 48.5, e2020GL090544.

Meduri, D. G. and Wicht, J. (2016). "A simple stochastic model for dipole moment fluctuations in numerical dynamo simulations". *Frontiers in Earth Science* 4, p. 38.

Merrill, R., McElhinny, M., and McFadden, P. (1998). *The Magnetic Field of the Earth: Paleomagnetism, the Core, and the Deep Mantle*. International geophysics series. Academic Press. ISBN: 9780124912465.

Mil'shtejn, G. (1975). "Approximate integration of stochastic differential equations". *Theory of Probability & Its Applications* 19.3, pp. 557–562.

Moffatt, H. K. (1978). "Field generation in electrically conducting fluids". *Cambridge University Press, Cambridge, London, New York, Melbourne* 2, pp. 5–1.

Moffatt, H. (1970). "Turbulent dynamo action at low magnetic Reynolds number". *Journal of Fluid Mechanics* 41.2, pp. 435–452.

Molina-Cardín, A., Dinis, L., and Osete, M. L. (2021). "Simple stochastic model for geomagnetic excursions and reversals reproduces the temporal asymmetry of the axial dipole moment". *Proceedings of the National Academy of Sciences* 118.10.

Mori, N., Schmitt, D., Wicht, J., Ferriz-Mas, A., Mouri, H., Nakamichi, A., and Morikawa, M. (2013). "Domino model for geomagnetic field reversals". *Physical Review E* 87.1, p. 012108.

Morzfeld, M. and Buffett, B. A. (2019). "A comprehensive model for the kyr and Myr timescales of Earth's axial magnetic dipole field". *Nonlinear Processes in Geophysics* 26.3, pp. 123–142.

Morzfeld, M., Fournier, A., and Hulot, G. (2017). "Coarse predictions of dipole reversals by low-dimensional modeling and data assimilation". *Physics of the Earth and Planetary Interiors* 262, pp. 8–27.

Mourik, A. M. van, Daffertshofer, A., and Beek, P. J. (2006). "Estimating Kramers–Moyal coefficients in short and non-stationary data sets". *Physics Letters A* 351.1-2, pp. 13–17.

Movellan, J. R., Mineiro, P., and Williams, R. J. (2002). "A Monte Carlo EM approach for partially observable diffusion processes: theory and applications to neural networks". *Neural computation* 14.7, pp. 1507–1544.

Naidu, P. (1971). "Statistical structure of geomagnetic field reversals". *Journal of Geophysical Research* 76.11, pp. 2649–2662.

Nakamichi, A., Mouri, H., Schmitt, D., Ferriz-Mas, A., Wicht, J., and Morikawa, M. (2012). "Coupled spin models for magnetic variation of planets and stars". *Monthly Notices of the Royal Astronomical Society* 423.4, pp. 2977–2990.

Narteau, C., Blanter, E., Le Mouël, J.-L., Shirnman, M., and Allègre, C. (2000). "Reversal sequence in a multiple scale dynamo mechanism". *Physics of the Earth and Planetary Interiors* 120.4, pp. 271–287.

Nickerson, R. S. (1998). "Confirmation bias: A ubiquitous phenomenon in many guises". *Review of general psychology* 2.2, pp. 175–220.

Nicolis, C. and Nicolis, G. (1981). "Stochastic aspects of climatic transitions–additive fluctuations". *Tellus* 33.3, pp. 225–234.

Nicolo, M. J., Dickens, G. R., Hollis, C. J., and Zachos, J. C. (2007). "Multiple early Eocene hyperthermals: Their sedimentary expression on the New Zealand continental margin and in the deep sea". *Geology* 35.8, pp. 699–702.

Nijsse, F. J., Cox, P. M., Huntingford, C., and Williamson, M. S. (2019). "Decadal global temperature variability increases strongly with climate sensitivity". *Nature Climate Change* 9.8, pp. 598–601.

Nimmo, F. (2015). "Energetics of the core". In: *Treatise on Geophysics (Second Edition)*. Ed. by G. Schubert. Vol. 8. Elsevier, pp. 27–55.

Nozières, P. (1978). "Reversals of the Earth's magnetic field: an attempt at a relaxation model". *Physics of the Earth and Planetary Interiors* 17.2, pp. 55–74.

Ogg, J. (2020). "Geomagnetic polarity time scale". In: *Geologic Time Scale 2020*. Elsevier, pp. 159–192.

Oldham, R. D. (1906). "The constitution of the interior of the Earth, as revealed by earthquakes". *Quarterly Journal of the Geological Society* 62.1-4, pp. 456–475.

Olsen, N., Hulot, G., and Sabaka, T. (2007). "The present field". *Geomagnetism* 5, pp. 33–75.

Olsen, N., Lühr, H., Sabaka, T. J., Mandea, M., Rother, M., Tøffner-Clausen, L., and Choi, S. (2006). "CHAOS—a model of the Earth's magnetic field derived from CHAMP, Ørsted, and SAC-C magnetic satellite data". *Geophysical Journal International* 166.1, pp. 67–75.

Olsen, N. and Mandea, M. (2008). "Rapidly changing flows in the Earth's core". *Nature geoscience* 1.6, pp. 390–394.

Olson, P. L. (2015). "Core Dynamics". In: *Treatise on Geophysics (Second Edition)*. Ed. by G. Schubert. Vol. 8. Elsevier.

Olson, P. L., Coe, R. S., Driscoll, P. E., Glatzmaier, G. A., and Roberts, P. H. (2010). "Geodynamo reversal frequency and heterogeneous core–mantle boundary heat flow". *Physics of the Earth and Planetary Interiors* 180.1-2, pp. 66–79.

Olson, P. and Amit, H. (2014). "Magnetic reversal frequency scaling in dynamos with thermochemical convection". *Physics of the Earth and Planetary Interiors* 229, pp. 122–133.

Olson, P. and Amit, H. (2015). "Mantle superplumes induce geomagnetic superchrons". *Frontiers in Earth Science* 3, p. 38.

Olson, P. and Christensen, U. R. (2006). "Dipole moment scaling for convection-driven planetary dynamos". *Earth and Planetary Science Letters* 250.3-4, pp. 561–571.

Olson, P., Christensen, U., and Glatzmaier, G. A. (1999). "Numerical modeling of the geodynamo: mechanisms of field generation and equilibration". *Journal of Geophysical Research: Solid Earth* 104.B5, pp. 10383–10404.

Panovska, S., Constable, C., and Korte, M. (2018). "Extending global continuous geomagnetic field reconstructions on timescales beyond human civilization". *Geochemistry, Geophysics, Geosystems* 19.12, pp. 4757–4772.

Panovska, S., Korte, M., and Constable, C. (2019). "One hundred thousand years of geomagnetic field evolution". *Reviews of Geophysics* 57.4, pp. 1289–1337.

Parker, E. N. (1955). "Hydromagnetic dynamo models." *The Astrophysical Journal* 122, p. 293.

Pavliotis, G. A. (2014). *Stochastic processes and applications: diffusion processes, the Fokker-Planck and Langevin equations*. Vol. 60. Springer.

Peinke, J., Tabar, M. R., and Wächter, M. (2019). "The Fokker–Planck approach to complex spatiotemporal disordered systems". *Annual Review of Condensed Matter Physics* 10, pp. 107–132.

Penland, C. and Sardeshmukh, P. D. (2012). "Alternative interpretations of power-law distributions found in nature". *Chaos: An Interdisciplinary Journal of Nonlinear Science* 22.2, p. 023119.

Pétrélis, F., Fauve, S., Dormy, E., and Valet, J.-P. (2009). "Simple mechanism for reversals of Earth's magnetic field". *Physical Review Letters* 102.14, p. 144503.

Poirier, J.-P. (1994). "Light elements in the Earth's outer core: A critical review". *Physics of the Earth and Planetary Interiors* 85.3-4, pp. 319–337.

Pozzo, M., Davies, C., Gubbins, D., and Alfe, D. (2012). "Thermal and electrical conductivity of iron at Earth's core conditions". *Nature* 485.7398, pp. 355–358.

Prévot, M., Derder, M. E.-M., McWilliams, M., and Thompson, J. (1990). "Intensity of the Earth's magnetic field: Evidence for a Mesozoic dipole low". *Earth and Planetary Science Letters* 97.1-2, pp. 129–139.

Quidelleur, X. and Courtillot, V. (1996). "On low-degree spherical harmonic models of paleosecular variation". *Physics of The Earth and Planetary Interiors* 95.1-2, pp. 55–77.

Ragone, F., Wouters, J., and Bouchet, F. (2018). "Computation of extreme heat waves in climate models using a large deviation algorithm". *Proceedings of the National Academy of Sciences* 115.1, pp. 24–29.

Redhead, M. (1980). "Models in physics". *The British Journal for the Philosophy of Science* 31.2, pp. 145–163.

Rehfeld, K., Marwan, N., Heitzig, J., and Kurths, J. (2011). "Comparison of correlation analysis techniques for irregularly sampled time series". *Nonlinear Processes in Geophysics* 18.3, pp. 389–404.

Renner, C., Peinke, J., and Friedrich, R. (2001). "Experimental indications for Markov properties of small-scale turbulence". *Journal of Fluid Mechanics* 433, pp. 383–409.

Rikitake, T. (1958). "Oscillations of a system of disk dynamos". In: *Mathematical Proceedings of the Cambridge Philosophical Society*. Vol. 54. 1. Cambridge University Press, pp. 89–105.

Risken, H. (1996). *The Fokker-Planck equation*. Springer, pp. 63–95.

Roberts, A. P. (2008). "Geomagnetic excursions: knowns and unknowns". *Geophysical Research Letters* 35.17.

Roberts, P. H. and King, E. M. (2013). "On the genesis of the Earth's magnetism". *Reports on Progress in Physics* 76.9, p. 096801.

Roberts, P. (2015). "Theory of the geodynamo". In: *Treatise on Geophysics (2nd Edition)*. Ed. by G. Schubert. Vol. 8. Elsevier, pp. 67–105.

Roberts, P. and Lowes, F. (1961). "Earth currents of deep internal origin". *Journal of Geophysical Research* 66.4, pp. 1243–1254.

Rothman, D. H. (2017). "Thresholds of catastrophe in the Earth system". *Science Advances* 3.9, e1700906.

Rothman, D. H. (2019). "Characteristic disruptions of an excitable carbon cycle". *Proceedings of the National Academy of Sciences* 116.30, pp. 14813–14822.

Ryan, D. A. and Sarson, G. R. (2007). "Are geomagnetic field reversals controlled by turbulence within the Earth's core?" *Geophysical research letters* 34.2.

Sadhasivan, M. and Constable, C. (2022). "A new power spectrum and stochastic representation for the geomagnetic axial dipole". *Geophysical Journal International* 231.1, pp. 15–26.

Sakuraba, A. and Roberts, P. H. (2009). "Generation of a strong magnetic field using uniform heat flux at the surface of the core". *Nature Geoscience* 2.11, pp. 802–805.

Sardeshmukh, P. D. and Penland, C. (2015). "Understanding the distinctively skewed and heavy tailed character of atmospheric and oceanic probability distributions". *Chaos: An Interdisciplinary Journal of Nonlinear Science* 25.3, p. 036410.

Sardeshmukh, P. D. and Sura, P. (2009). "Reconciling non-Gaussian climate statistics with linear dynamics". *Journal of Climate* 22.5, pp. 1193–1207.

Scargle, J. D. (1981). "Studies in astronomical time series analysis. I-Modeling random processes in the time domain". *The Astrophysical Journal Supplement Series* 45, pp. 1–71.

Scargle, J. D. (1982). "Studies in astronomical time series analysis. II-Statistical aspects of spectral analysis of unevenly spaced data". *The Astrophysical Journal* 263, pp. 835–853.

Scargle, J. D. (1989). "Studies in astronomical time series analysis. III-Fourier transforms, autocorrelation functions, and cross-correlation functions of unevenly spaced data". *The Astrophysical Journal* 343, pp. 874–887.

Schaeffer, N., Jault, D., Nataf, H.-C., and Fournier, A. (2017). "Turbulent geodynamo simulations: a leap towards Earth's core". *Geophysical Journal International* 211.1, pp. 1–29.

Schenker, N. (1985). "Qualms about bootstrap confidence intervals". *Journal of the American Statistical Association* 80.390, pp. 360–361.

Schmitt, D. and Schüssler, M. (1989). "Non-linear dynamos. I-One-dimensional model of a thin layer dynamo". *Astronomy and Astrophysics* 223, pp. 343–351.

Schmitt, D., Ossendrijver, M., and Hoyng, P. (2001). "Magnetic field reversals and secular variation in a bistable geodynamo model". *Physics of the Earth and Planetary Interiors* 125.1-4, pp. 119–124.

Scholes, M. and Williams, J. (1977). "Estimating betas from nonsynchronous data". *Journal of financial economics* 5.3, pp. 309–327.

Scholz, T., Raischel, F., Lopes, V. V., Lehle, B., Wächter, M., Peinke, J., and Lind, P. G. (2017). "Parameter-free resolution of the superposition of stochastic signals". *Physics Letters A* 381.4, pp. 194–206.

Schulz, M. and Stattegger, K. (1997). "SPECTRUM: Spectral analysis of unevenly spaced paleoclimatic time series". *Computers & Geosciences* 23.9, pp. 929–945.

Schwaiger, T., Gastine, T., and Aubert, J. (2019). "Force balance in numerical geodynamo simulations: a systematic study". *Geophysical Journal International* 219.Supplement_1, S101–S114.

Scullard, C. R. and Buffett, B. A. (2018). "Probabilistic structure of the geodynamo". *Physical Review E* 98.6, p. 063112.

Seki, M. and Ito, K. (1993). "A phase-transition model for geomagnetic polarity reversals". *Journal of geomagnetism and geoelectricity* 45.1, pp. 79–88.

Seki, M. and Ito, K. (1999). "A coupled map lattice model for geomagnetic polarity reversals that exhibits realistic scaling". *Earth, planets and space* 51.6, pp. 395–402.

Sexton, P. F., Norris, R. D., Wilson, P. A., Pälike, H., Westerhold, T., Röhl, U., Bolton, C. T., and Gibbs, S. (2011). "Eocene global warming events driven by ventilation of oceanic dissolved organic carbon". *Nature* 471.7338, pp. 349–352.

Shimizu, M. and Honkura, Y. (1985). "Statistical nature of polarity reversals of the magnetic field in coupled-disk dynamo models". *Journal of geomagnetism and geoelectricity* 37.4, pp. 455–497.

Siefert, M., Kittel, A., Friedrich, R., and Peinke, J. (2003). "On a quantitative method to analyze dynamical and measurement noise". *EPL (Europhysics Letters)* 61.4, p. 466.

Siegert, S., Friedrich, R., and Peinke, J. (1998). "Analysis of data sets of stochastic systems". *Physics Letters A* 243.5-6, pp. 275–280.

Silverman, B. W. (1986). *Density estimation for statistics and data analysis*. Vol. 26. CRC press.

Slotani, M. (1964). "Tolerance regions for a multivariate normal population". *Annals of the Institute of Statistical Mathematics* 16.1, pp. 135–153.

Sprain, C. J., Biggin, A. J., Davies, C. J., Bono, R. K., and Meduri, D. G. (2019). "An assessment of long duration geodynamo simulations using new paleomagnetic modeling criteria (QPM)". *Earth and Planetary Science Letters* 526, p. 115758.

Stanton, R. (1997). "A nonparametric model of term structure dynamics and the market price of interest rate risk". *The Journal of Finance* 52.5, pp. 1973–2002.

Stark, P. (2004). "Geophysics, Statistics in". *Encyclopedia of Statistical Sciences* 4.

Steenbeck, M. and Krause, F. (1966). "Erklärung stellarer und planetarer Magnetfelder durch einen turbulenzbedingten Dynamomechanismus". *Zeitschrift für Naturforschung A* 21.8, pp. 1285–1296.

Steenbeck, M., Krause, F., and Rädler, K.-H. (1966). "Berechnung der mittleren Lorentz-Feldstärke für ein elektrisch leitendes Medium in turbulenter, durch Coriolis-Kräfte beeinflußter Bewegung". *Zeitschrift für Naturforschung A* 21.4, pp. 369–376.

Strogatz, S. H. (2018). *Nonlinear dynamics and chaos: with applications to physics, biology, chemistry, and engineering*. CRC press.

Sura, P. (2011). "A general perspective of extreme events in weather and climate". *Atmospheric Research* 101.1-2, pp. 1–21.

Sura, P. and Gille, S. T. (2003). "Interpreting wind-driven Southern Ocean variability in a stochastic framework". *Journal of marine research* 61.3, pp. 313–334.

Sura, P. and Sardeshmukh, P. D. (2008). "A global view of non-Gaussian SST variability". *Journal of Physical Oceanography* 38.3, pp. 639–647.

Tabar, R. (2019). *Analysis and data-based reconstruction of complex nonlinear dynamical systems*. Vol. 730. Springer.

Tarduno, J. and Cottrell, R. (2005). "Dipole strength and variation of the time-averaged reversing and nonreversing geodynamo based on Thellier analyses of single plagioclase crystals". *Journal of Geophysical Research: Solid Earth* 110.B11.

Tauxe, L. and Yamazaki, T. (2015). "Paleointensities". In: *Treatise on Geophysics (Second Edition)*. Ed. by G. Schubert. Vol. 5. Elsevier, pp. 461–509.

Tauxe, L. (2010). *Essentials of paleomagnetism*. University of California Press.

Tobias, S. (2021). "The turbulent dynamo". *Journal of Fluid Mechanics* 912.

Tropea, C. (1995). "Laser Doppler anemometry: recent developments and future challenges". *Measurement Science and Technology* 6.6, p. 605.

Tukey, J. W. (1961). "Curves as parameters, and touch estimation". In: *Proceedings of the Fourth Berkeley Symposium on Mathematical Statistics and Probability, Volume 1: Contributions to the Theory of Statistics*. Vol. 4. University of California Press, pp. 681–695.

Uhlenbeck, G. E. and Ornstein, L. S. (1930). "On the theory of the Brownian motion". *Physical review* 36.5, p. 823.

Valet, J.-P. and Fournier, A. (2016). "Deciphering records of geomagnetic reversals". *Reviews of Geophysics* 54.2, pp. 410–446.

Valet, J.-P., Fournier, A., Courtillot, V., and Herrero-Bervera, E. (2012). "Dynamical similarity of geomagnetic field reversals". *Nature* 490.7418, pp. 89–93.

Valet, J.-P., Meynadier, L., and Guyodo, Y. (2005). "Geomagnetic dipole strength and reversal rate over the past two million years". *Nature* 435.7043, pp. 802–805.

Van Kampen, N. G. (1992). *Stochastic processes in physics and chemistry*. Vol. 1. Elsevier.

Walker, J. C., Hays, P., and Kasting, J. F. (1981). "A negative feedback mechanism for the long-term stabilization of Earth's surface temperature". *Journal of Geophysical Research: Oceans* 86.C10, pp. 9776–9782.

Wand, M. P. and Jones, M. C. (1993). "Comparison of smoothing parameterizations in bivariate kernel density estimation". *Journal of the American Statistical Association* 88.422, pp. 520–528.

Weare, J. (2009). "Particle filtering with path sampling and an application to a bimodal ocean current model". *Journal of Computational Physics* 228.12, pp. 4312–4331.

Webber, R. J., Plotkin, D. A., O'Neill, M. E., Abbot, D. S., and Weare, J. (2019). "Practical rare event sampling for extreme mesoscale weather". *Chaos: An Interdisciplinary Journal of Nonlinear Science* 29.5, p. 053109.

Westerhold, T., Marwan, N., Drury, A. J., Liebrand, D., Agnini, C., Anagnostou, E., Barnet, J. S., Bohaty, S. M., De Vleeschouwer, D., Florindo, F., et al. (2020). "An astronomically dated record of Earth's climate and its predictability over the last 66 million years". *Science* 369.6509, pp. 1383–1387.

Wicht, J. and Meduri, D. G. (2016). "A Gaussian model for simulated geomagnetic field reversals". *Physics of the Earth and Planetary Interiors* 259, pp. 45–60.

Wicht, J. and Sanchez, S. (2019). "Advances in geodynamo modelling". *Geophysical & Astrophysical Fluid Dynamics* 113.1-2, pp. 2–50.

Wicht, J., Stellmach, S., and Harder, H. (2009). "Numerical models of the geodynamo: From fundamental Cartesian models to 3D simulations of field reversals". In: *Geomagnetic field variations*. Springer, pp. 107–158.

Yang, J. and Kushner, H. J. (1991). "A Monte Carlo method for sensitivity analysis and parametric optimization of nonlinear stochastic systems". *SIAM journal on control and optimization* 29.5, pp. 1216–1249.

Zachos, J. C., Dickens, G. R., and Zeebe, R. E. (2008). "An early Cenozoic perspective on greenhouse warming and carbon-cycle dynamics". *Nature* 451.7176, pp. 279–283.

Zachos, J., Pagani, M., Sloan, L., Thomas, E., and Billups, K. (2001). "Trends, rhythms, and aberrations in global climate 65 Ma to present". *Science* 292.5517, pp. 686–693.

Zeebe, R. E. and Zachos, J. C. (2013). "Long-term legacy of massive carbon input to the Earth system: Anthropocene versus Eocene". *Philosophical Transactions of the Royal Society A: Mathematical, Physical and Engineering Sciences* 371.2001, p. 20120006.

Ziegler, L. and Constable, C. (2011). "Asymmetry in growth and decay of the geomagnetic dipole". *Earth and Planetary Science Letters* 312.3-4, pp. 300–304.

Ziegler, L., Constable, C., Johnson, C., and Tauxe, L. (2011). "PADM2M: a penalized maximum likelihood model of the 0–2 Ma palaeomagnetic axial dipole moment". *Geophysical Journal International* 184.3, pp. 1069–1089.

Appendix A

Kernel Estimation

Conditional increments in expression (4.3.5) are commonly calculated through histogram methods (e.g., Siegert et al., 1998). Typically the evaluation range of x is divided into n non-overlapping and equal width bins B_l. A bin counting function such as

$$B(X(t);x,n) = \frac{\sum_{l=1}^{n} I(x \in B_l) I(X(t) \in B_l)}{N\left\langle \sum_{l=1}^{n} I(x \in B_l) I(X(t) \in B_l) \right\rangle}, \tag{A.0.1}$$

where I is the indicator function, assigns weights to the data. The expression for a conditional increment becomes

$$B(X(t);x,n)[X(t+\tau) - X(t)]. \tag{A.0.2}$$

Although this method is computationally inexpensive, it has undesirable properties such as only offering estimates at the center of the bins, and sharp cutoffs between data just outside a bin. Alternatively, density estimation kernels can be evaluated at arbitrary points, and have a well defined scale parameter through explicit choice of bandwidth. For these reasons, we use the kernel based method of Lamouroux and Lehnertz (2009) to estimate the conditional increments.

For an arbitrary evaluation point on x, the influence of a single increment at $X(t)$ is weighted by their scaled distance (the Nadaraya-Watson estimator)

$$W(X(t);x,h) = \frac{K(x - X(t);h)}{\big\langle K(x - X(t);h) \big\rangle}. \tag{A.0.3}$$

The length scaling of choice is made explicit by the bandwidth, h, that modulates the range of the kernel

$$K(\circ;h) = \frac{1}{h}\kappa(\circ/h). \tag{A.0.4}$$

We use the Epanechnikov kernel

$$\kappa(x) = \begin{cases} \frac{3}{4\sqrt{5}}(1 - x^2/5), & \text{if } x^2 \leq 5 \\ 0, & \text{otherwise} \end{cases} \tag{A.0.5}$$

for its computationally desirable properties (Silverman, 1986). Conditional increments indicated in expression (4.3.5) that are calculated through this method are now defined by

$$\Delta X(t; x, \tau, h) = W(X(t); x, h)[X(t + \tau) - X(t)]. \tag{A.0.6}$$

To choose a bandwidth, we use a modified version of the normal reference selector of Fan and Gijbels (1996)

$$\hat{h}_{\text{opt}} = 2.34 s_n n^{-1/5}, \tag{A.0.7}$$

where s_n is the sample standard deviation and n is the number of data points divided by the estimated number of correlated time-steps, see Appendix B.

Appendix B

Correlation Time Fitting

Lehle and Peinke (2018) showed that for a process $X(t)$ with autocorrelation

$$A(\tau) = \langle X(t+\tau)X(t)\rangle, \tag{B.0.1}$$

the increments of this function

$$\Delta A(\tau) = A(\tau) - A(0), \tag{B.0.2}$$

can be represented by basis functions (4.3.12) in the form

$$\Delta A(\tau) \approx \sum_{i=1}^{3} \lambda_i r_i(\tau;\theta), \tag{B.0.3}$$

accurately up to $\mathcal{O}(\tau^3)$.

To fit correlation time θ, we first calculate sample autocorrelation increments (B.0.2) on time-shift evaluation points $\mathcal{T}$,

$$(\Delta A)_i = \widehat{\Delta A}(\mathcal{T}_i), \tag{B.0.4}$$

where index i refers to the ith element of the $\mathcal{T}$ vector, and the hat symbol on ΔA denotes this is sample statistic. Using matrix $R_{ij}(\theta)$ defined by (C.0.2), we find the optimum correlation time $\hat{\theta}$ from a grid search on

$$\arg\min_{\theta} \sum_{i} \left[(\Delta A)_i - R_{ij}\lambda_j\right]^2, \tag{B.0.5}$$

where λ_j is found through the method of least squares

$$\lambda_j = \left(R_{ji}R_{ij}\right)^{-1} R_{ji}(\Delta A)_j. \tag{B.0.6}$$

Appendix C

Compact Notation of Moments and Related Quantities

Discrete values for estimates of the first two moments are computed using (4.3.7)–(4.3.8) and are represented in matrix form as

$$M_{ij}^{(k)} = \widehat{M}^{(k)}(\mathcal{X}_j, \mathcal{T}_i; h), \quad k = 1, 2. \tag{C.0.1}$$

where index i refers to the ith element of the $\mathcal{T}$ vector and j refers to the jth element of the $\mathcal{X}$ vector. Similarly, the matrices of basis functions (4.3.12) and corresponding coefficients are written in matrix form as

$$R_{il} = r_l(\mathcal{T}_i; \theta), \tag{C.0.2}$$

$$\lambda_{lj}^{(k)} = \lambda_l^{(k)}(\mathcal{X}_j), \tag{C.0.3}$$

respectively.

Appendix D

Supplementary Material for Chapter 4

Contents

1. Figures D.1 to D.12.

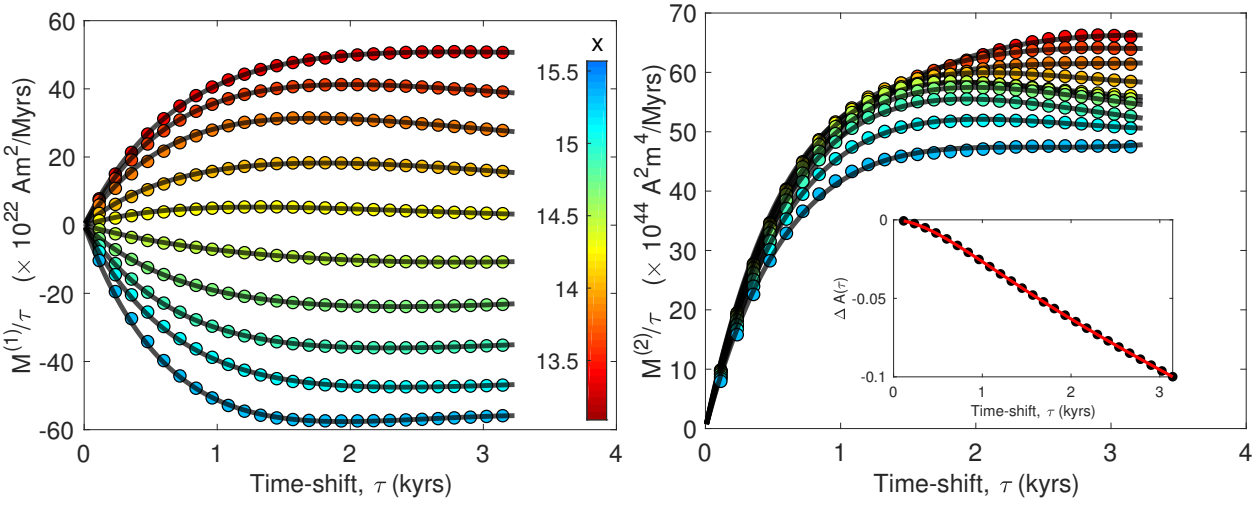

Figure D.1: Conditional moments and sample autocorrelation for combined cases TB0 and TB00, as Fig. 4.2.

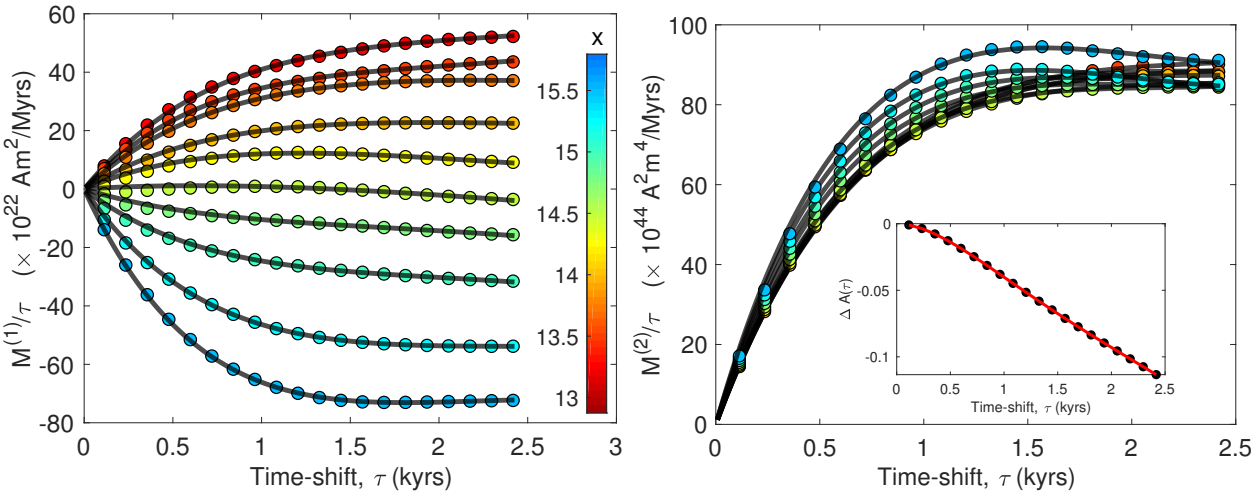

Figure D.2: Conditional moments and sample autocorrelation for case TB1, as Fig. 4.2.

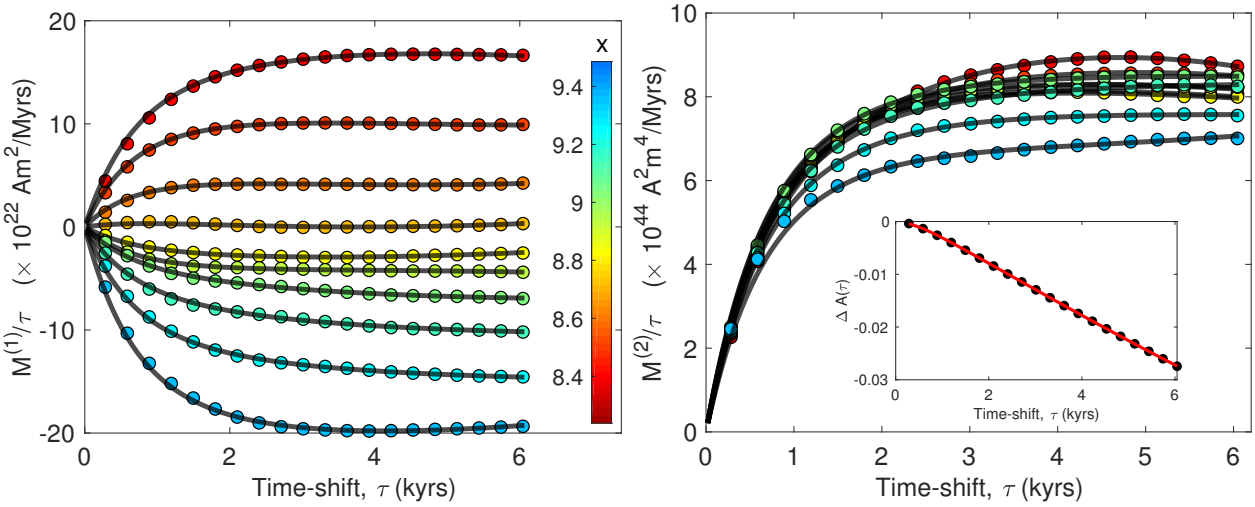

Figure D.3: Conditional moments and sample autocorrelation for case B2, as Fig. 4.2.

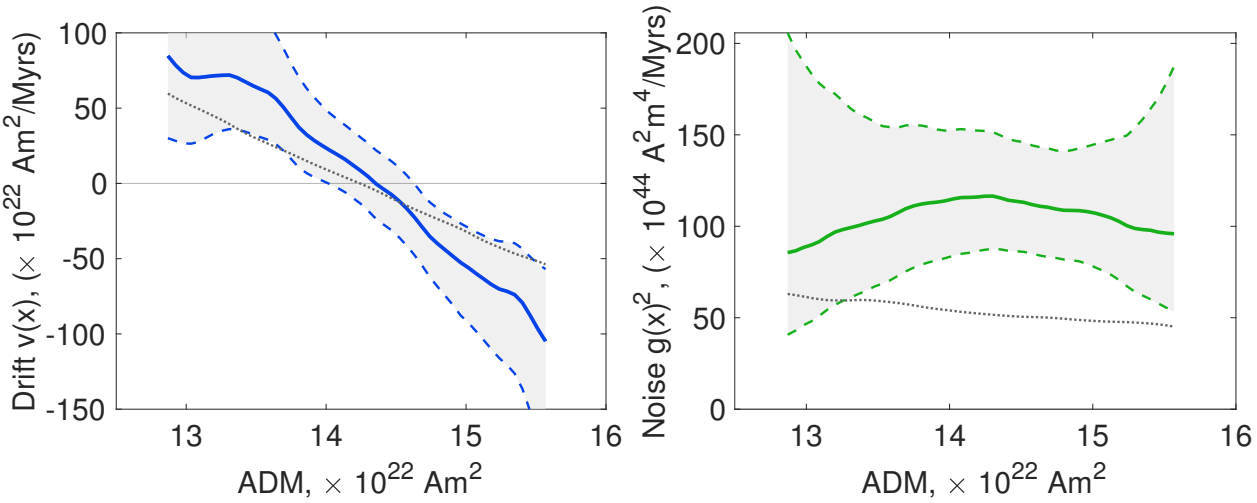

Figure D.4: Drift and noise functions fitted from combined cases TB0 and TB00, as Fig. 4.3.

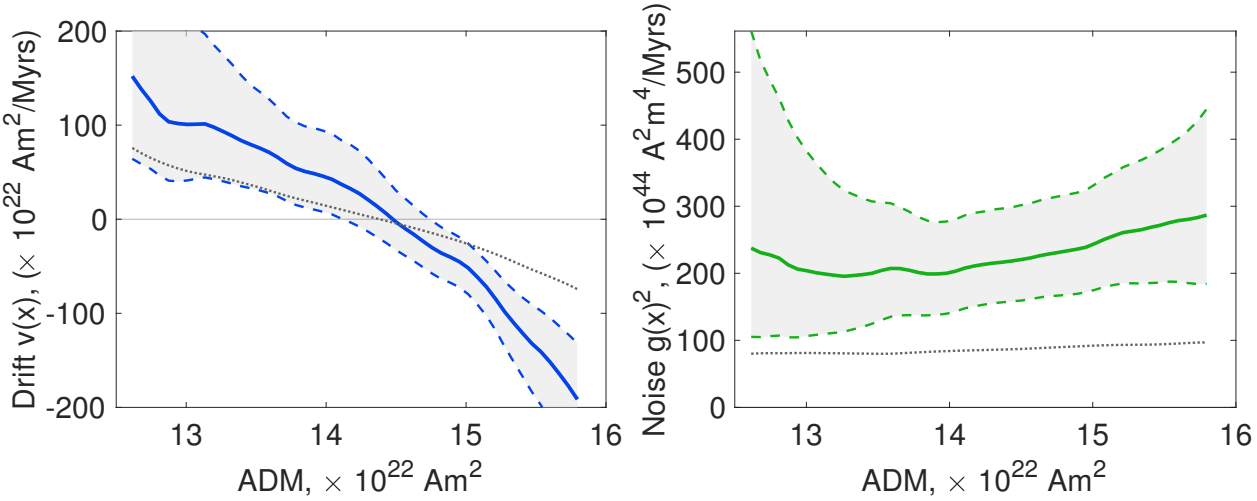

Figure D.5: Drift and noise functions fitted from case TB1, as Fig. 4.3.

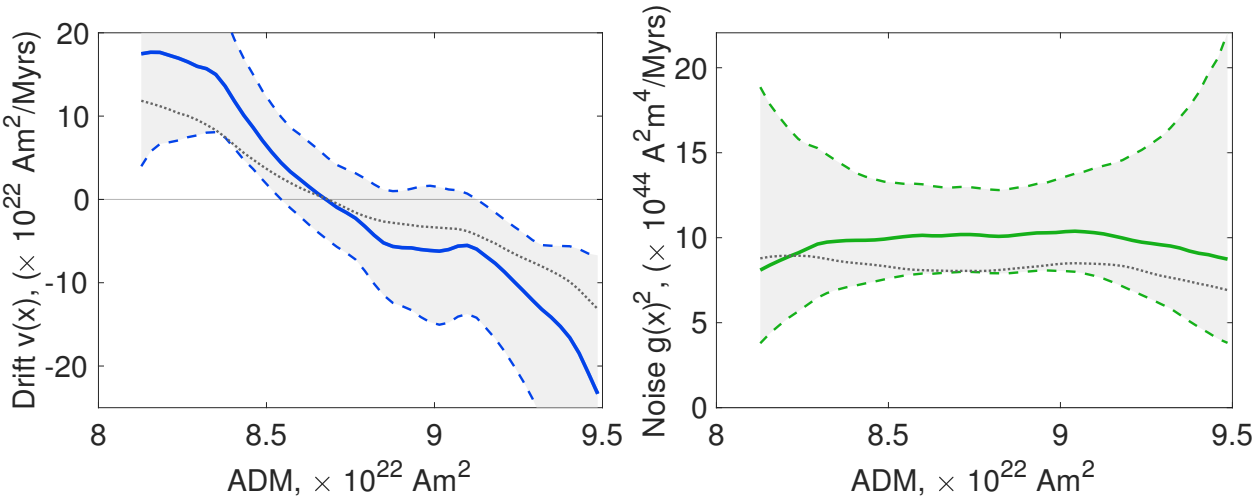

Figure D.6: Drift and noise functions fitted from case B2, as Fig. 4.3.

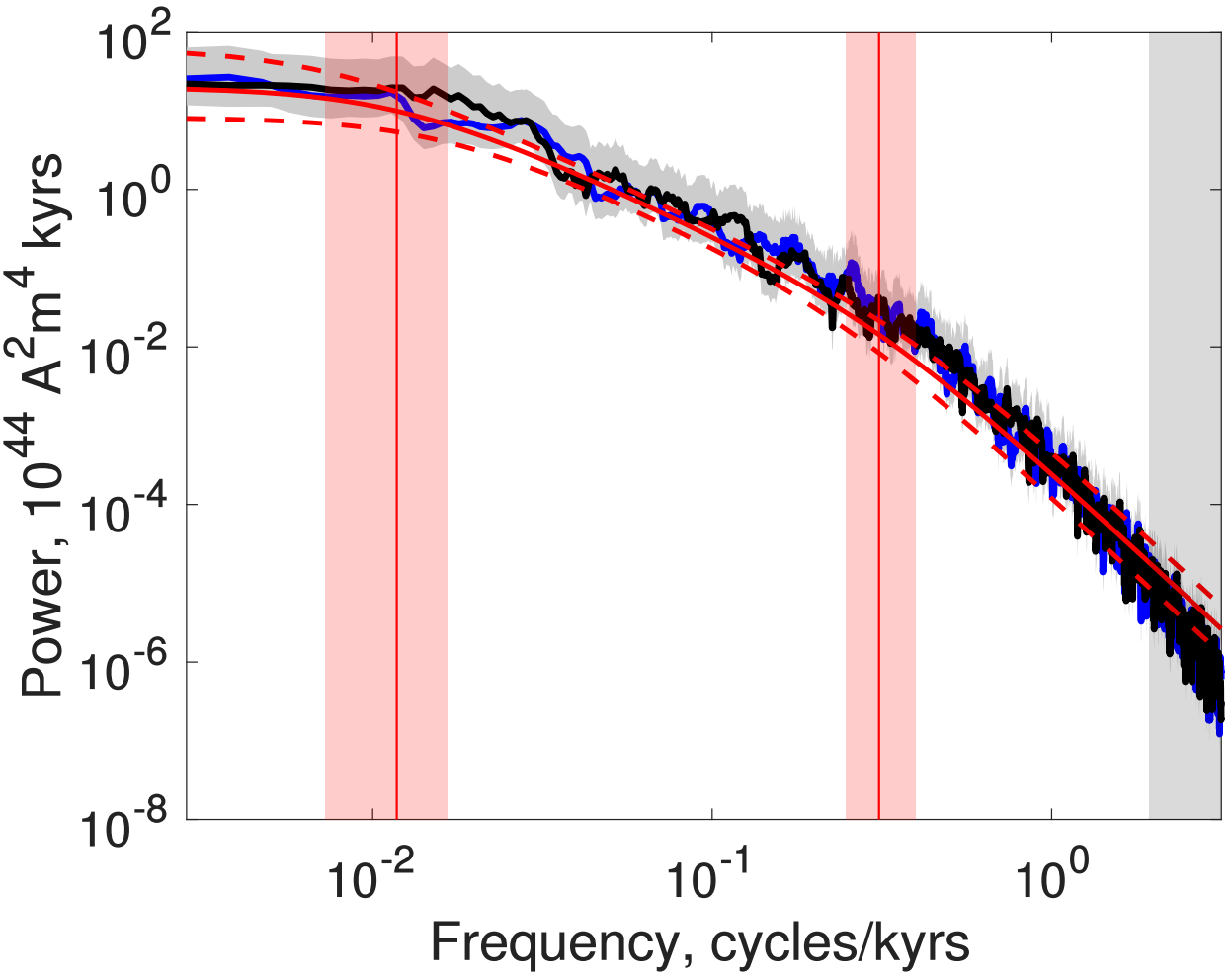

Figure D.7: Power spectra for cases TB0 and TB00. As Fig. 4.4, except cases TB0 and TB00 are shown with a black and blue line, respectively.

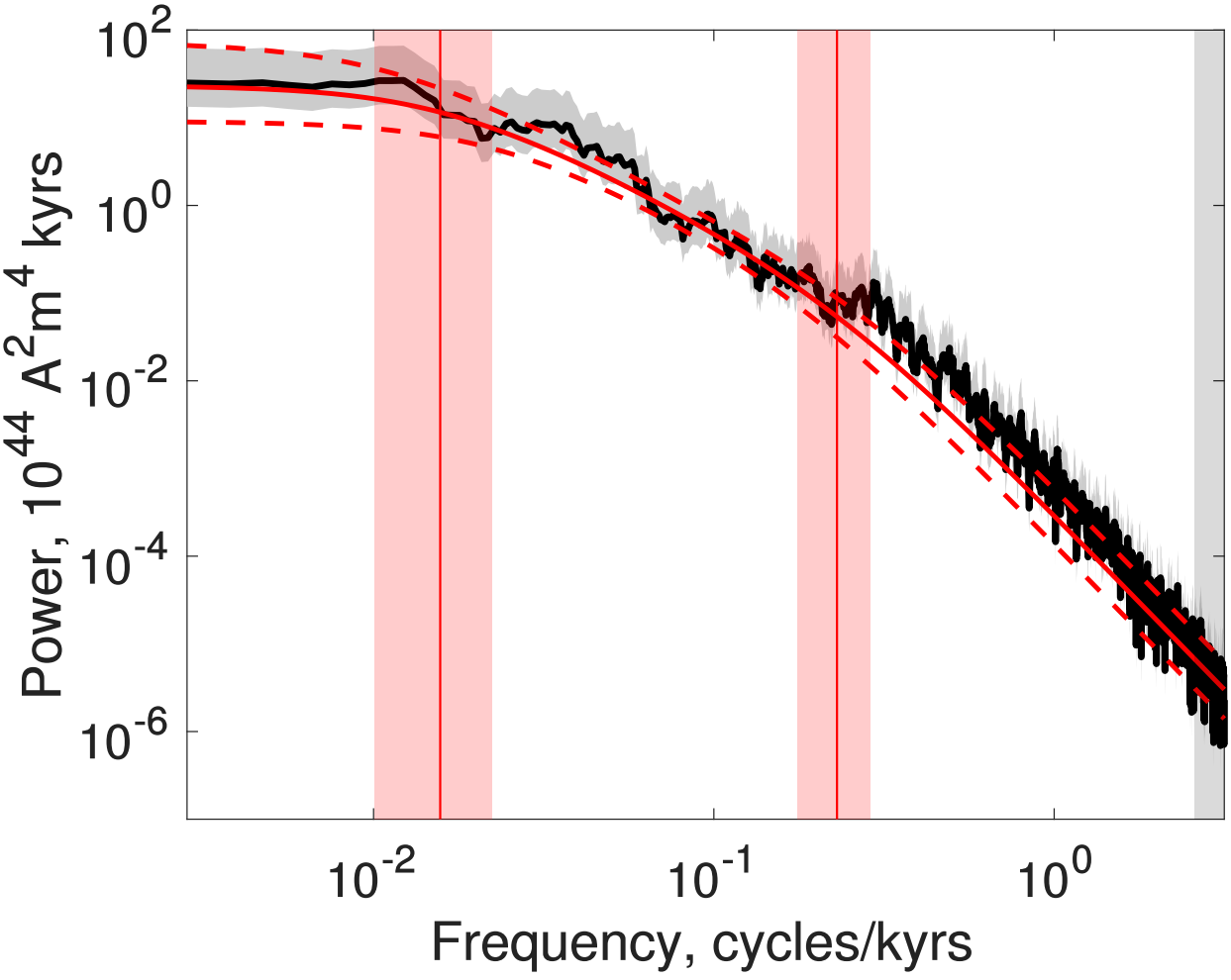

Figure D.8: Power spectrum for case TB1, as Fig. 4.4.

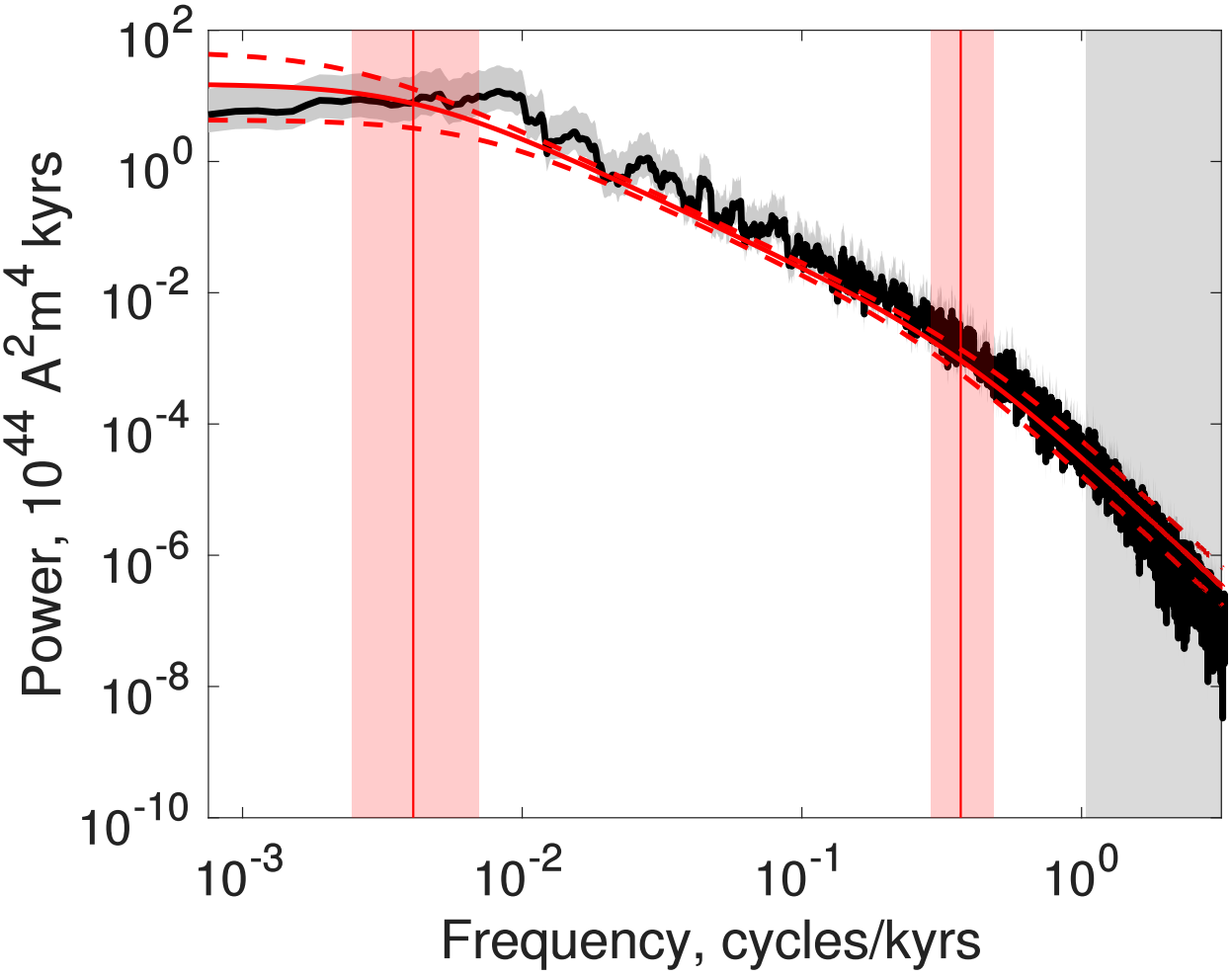

Figure D.9: Power spectrum for case B2, as Fig. 4.4.

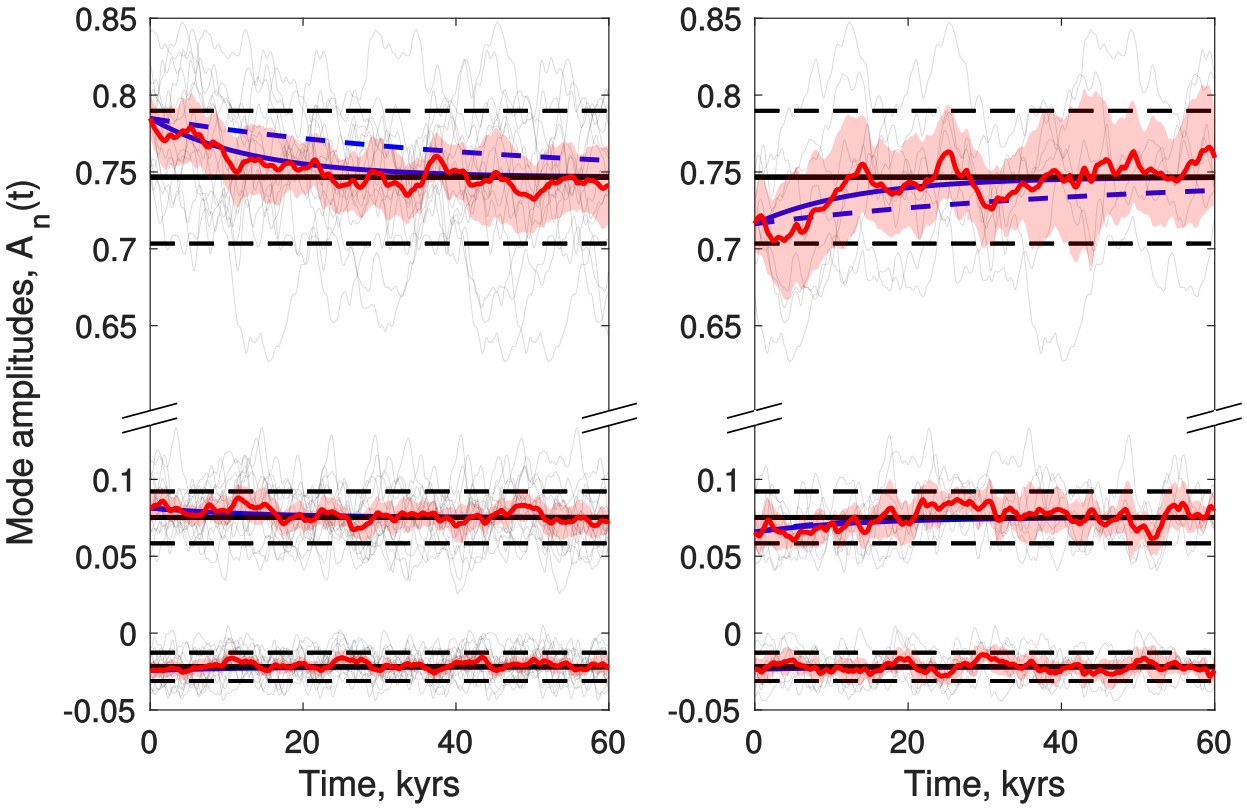

Figure D.10: Trajectories of individual mode amplitudes from case TB00, as Fig. 4.7.

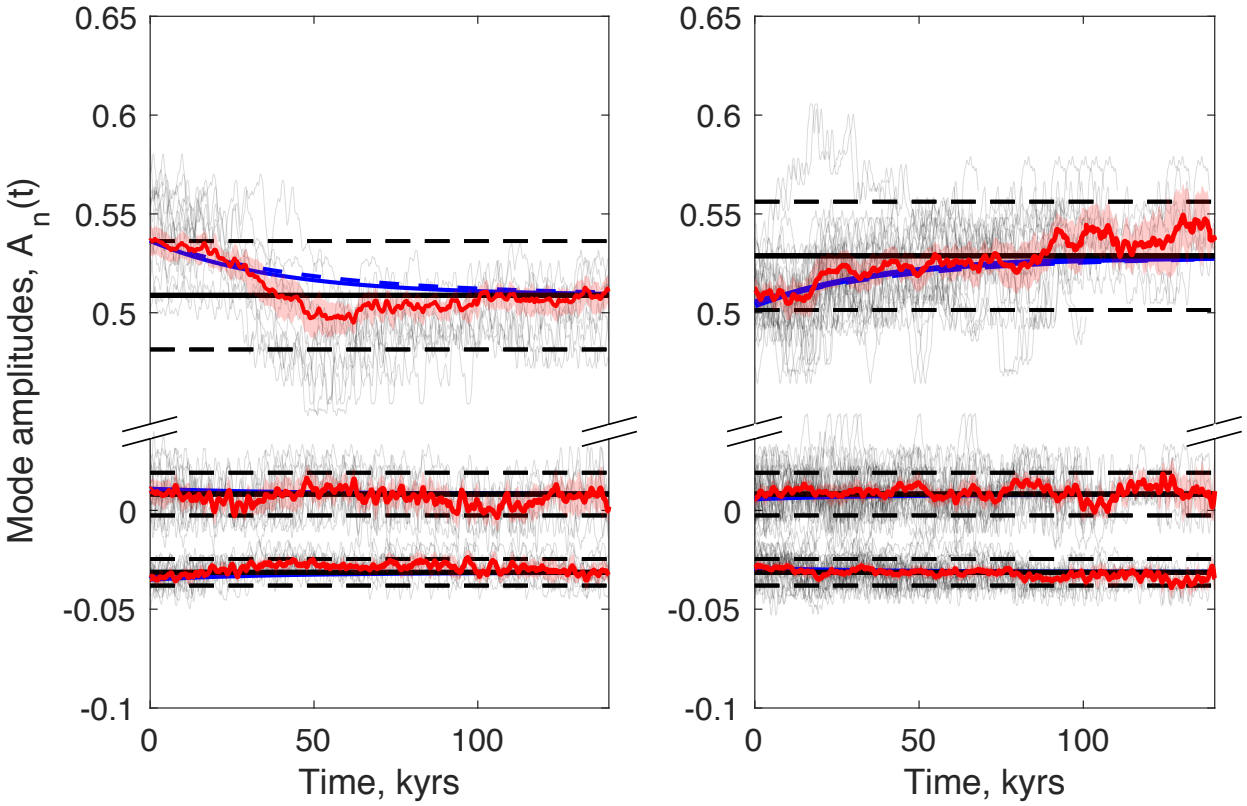

Figure D.11: Trajectories of individual mode amplitudes from case B2, as Fig. 4.7.

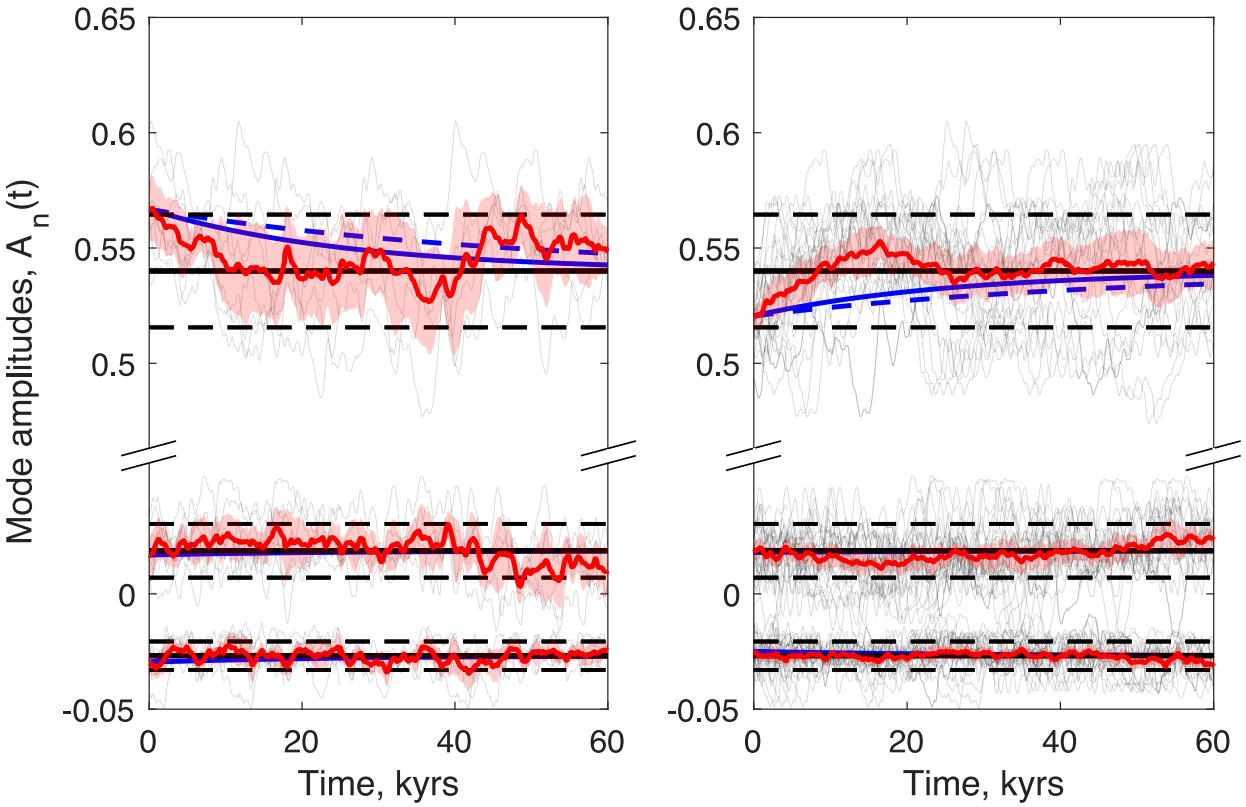

Figure D.12: Trajectories of individual mode amplitudes from case B3, as Fig. 4.7.